Simulations of charge transport in organic light emitting diodes

Martin, Simon James

Award date:
2002

Awarding institution:
University of Bath

Simulations of Charge Transport in Organic Light Emitting Diodes

Simon James Martin

October 2002

Submitted in partial fulfilment of the requirements for the degree of Doctor of Philosophy at the University of Bath, Bath, England

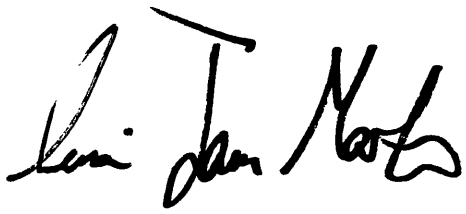

ProQuest LLC
789 East Eisenhower Parkway
P.O. Box 1346
Ann Arbor, MI 48106-1346

Abstract

In this thesis, two approaches to the modelling of charge transport in organic light emitting diodes (OLEDs) are presented. The first is a drift-diffusion model, normally used when considering conventional crystalline inorganic semiconductors (e.g. Si or III-V's) which have well defined energy bands. In this model, electron and hole transport is described using the current continuity equations and the drift-diffusion current equations, and coupled to Poisson's equation. These equations are solved with the appropriate boundary conditions, which for OLEDs are Schottky contacts; carriers are injected by thermionic emission and tunnelling. The disordered nature of the organic semiconductors is accounted for by the inclusion of field-dependent carrier mobilities and Langevin optical recombination. The second approach treats the transport of carriers in disordered organic semiconductors as a hopping process between spatially and energetically disordered sites. This method has been used previously to account for the observed temperature and electric field dependence of carrier mobilities in disordered organic semiconductors. A hopping transport model has been developed which accounts explicitly for the structure in highly ordered films of rigid rod liquid-crystalline conjugated polymers.

Chapter 2 discusses the formation of metal-semiconductor contacts, and current injection processes in OLEDs. If the barrier to carrier injection at a metal-semiconductor contact is small, or the contact is Ohmic, then the current may be space charge limited; this second limiting regime of current flow for OLEDs is also described. The remainder of Chapter 2 describes the drift-diffusion model used in this work in some detail.

Chapter 3 contains results obtained from modelling the J-V characteristics of single-layer OLEDs, which are compared to experimental data in order to validate the drift-diffusion model. Chapter 4 contains results of simulating bi-layer OLEDs; rather than examining J-V characteristics, the electric field distributions in bi-layer devices and the effect of layer thickness on quantum efficiency are investigated.

In Chapter 5, an introduction into modelling hopping transport in disordered

organic semiconductors is provided by considering the Gaussian disorder model (GDM). A Monte-Carlo model which was developed to investigate transport in liquid-crystalline conjugated polymer films is then described. Chapter 6 contains preliminary results obtained from the Monte-Carlo modelling of mobilities in liquid-crystalline conjugated polymer films as a function of electric field and temperature for various degrees of spatial and energetic disorder.

Chapter 7 concludes the thesis and summarises the findings made, and also suggests future directions in which the work could be taken.

For my parents, and for Karen.

Acknowledgements

Firstly, I should like to thank my supervisor, Alison Walker, for her unfailing help and support during the last three years, and all of the staff in the physics department at the University of Bath. I would like to thank Sharp Laboratories of Europe for their input, hospitality and financial support; a big thankyou goes to my industrial supervisor Dr. Geraldine Verschoor. I am also grateful to our collaborators, Professor Marshall Stoneham's group at University College London and Professor Donal Bradley's group at Imperial College, for their experimental data and useful discussions. I also thank John Lupton for providing experimental data and for his invaluable help.

A very big thankyou goes to all of my fellow group members, past and present. Chris Blades not only left me with a wonderful piece of software, the original drift-diffusion model, but helped me to understand the bigger picture, whilst Diego Oriato helped me with computer problems, physics problems, and shared my interest of looking out of the window. I am very grateful to my current fellow inmates Michael Cass and Matthew Webster for many things, mostly the frequent coffee breaks. I also thank Michael for his calming air in the office and his uncompromising approach to system administration, and Matthew for his entertaining turn of phrase. I would also like to thank Agapi Kambili for her help with, and for motivating, the Monte-Carlo work. I also thank all of the other postgraduates past and present I have known, including Faz, Ivan, David, Graham, Tom, Paul, Dejan, Matt, Dave, Will, and Jim, for relieving the tedium with coffee breaks, trips to the pub, and entertaining tales of the unexpected. Caffeine also deserves a special mention for getting me through the last 3 years, and probably the next 50.

Above all, I want to express my deep and probably hitherto unseen gratitude to my parents, for all of their support, financial and otherwise, over the years, and for believing in me.

Finally to Karen, thankyou for everything.

Contents

Chapter 1

Introduction

Electroluminescence (EL) in organic materials was first observed by Pope et al [1] in single crystals of anthracene, some 10-20 mm thick; however, the large voltages required (>100V) and the difficulty of single crystal growth hindered the progress of the technology. The demonstration of electroluminescence in thin-film organic devices (~100nm thick), initially in a bi-layer small-molecular material based device (consisting of a hole transporting layer of an aromatic diamine, and an emissive layer of 8-hydroxyquinoline aluminium (Alq), illustrated in Figure 1.1) in the late 1980s by Tang and VanSlyke [2][3], and subsequently in a single-layer conjugated polymer device (the emissive layer being poly(p-phenylene vinylene) (PPV), also illustrated in Figure 1.1) in 1990 by Burroughes et al [4] revived interest in organic electroluminescent devices. These devices catalysed a vast amount of academic and commercial research into investigating both the fundamental properties of light emitting organic semiconductors, and the fabrication of efficient devices, driven by the devices' numerous potential benefits, which are described below; organic LEDs (OLEDs) now have efficiencies and brightnesses rivalling those of other emissive display technologies [5]. Displays based on organic EL technology are imminently due in the commercial arena [6], using passive and active matrix technology, initially starting with low information content displays, such as mobile phones and car radios, and gradually moving towards use in high information content displays [7], for example in laptop computers [8] and personal digital assistants (PDAs). Organic semiconductors, particularly conjugated polymers, have also been shown to be excellent candidates for use in other electronic devices, including photovoltaics e.g. [9], FETs e.g. [10], and even lasers e.g. [11].

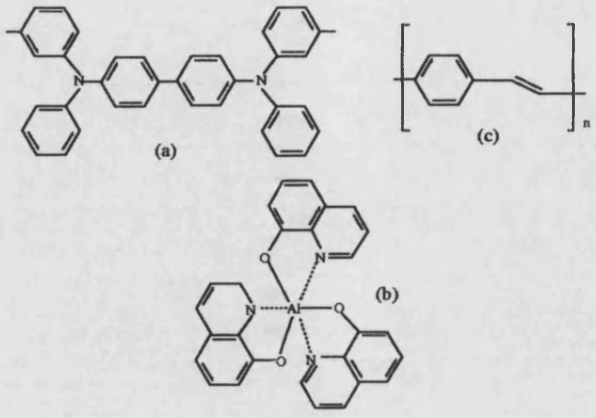

Figure 1.1: The chemical structure of the small molecules TPD, an aromatic diamine (N,N'-diphenyl-N,N'-bis-(3-methylphenyl)-(1,1')-biphenyl-4,4'diamine) (a) and Alq (8-hydroxyquinoline aluminium) (b), and a monomer unit of the conjugated polymer PPV (poly(p-phenylene vinylene)) (c).

1.1 Organic semiconductors

The semiconducting behaviour of both small molecules and conjugated polymers arises from the presence of conjugated molecules; the term conjugated refers to the existence of alternating single and double carbon-carbon bonds. In organic semiconductors, and other organic molecules e.g. benzene, the carbon atoms can form the so-called sp_2 hybrid orbitals, with each carbon atom having three sp_2 orbitals forming a triangle within a plane surrounding the carbon atom (Figure 1.2). In addition, each carbon atom also has a p_z orbital which is perpendicular to the plane of the sp_2 orbitals [12]. σ bonds between carbon atoms, essential to the molecular structure, are created when the sp_2 orbitals of neighbouring carbon atoms overlap; however, these orbitals do not provide the materials' semiconducting properties. The p_z orbitals of neighbouring carbon atoms can also overlap (Figure 1.2), forming π-bonds which are responsible for the semiconducting properties of these materials [13]. The π (bonding) orbital, the lower in energy, and π^* (anti-bonding) orbital, higher in energy, form delocalised valence and conduction wavefunctions, which support mobile charge carriers, resulting in a well defined $\pi - \pi^*$ bandgap. This bandgap is typically between 2-3eV [14], and hence emitted light is in the visible range. The valence and conduction wavefunctions are also known as the HOMO (Highest Occupied Molecular Orbital) and LUMO (Lowest Unoccupied Molecular Orbital) energy levels respectively. In reality, the existence of an electron or hole in an organic semiconductor causes a deformation of the surrounding molecule, forming negative or positive polarons respectively.

In this thesis, carriers will be referred to as electrons or holes for simplicity.

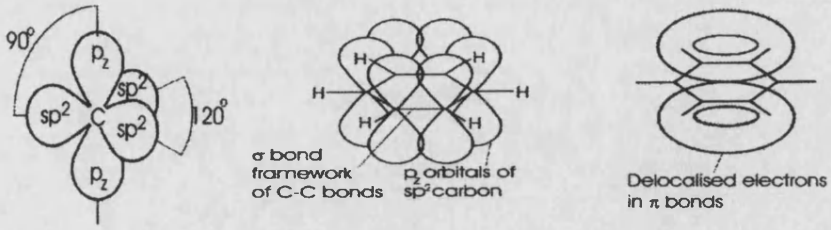

Figure 1.2: The sp^2 hybrid orbitals and the p_z orbitals of a carbon atom (left), a benzene ring with σ bonds formed by overlapping sp^2 orbitals (middle) and the delocalised electrons caused by overlapping p_z orbitals forming π bonds (right).

Since the semiconducting behaviour of both conjugated polymers and small molecule semiconductors is a consequence of the properties of the carbon atom, the physics of both classes of materials, in terms of electronic and optical properties, is very similar. As mentioned, the energy gap in both materials is typically between 2 and 3eV, and the density of states is typically $1 \times 10^{27} \mathrm{m}^{-3}$ e.g. [2]. Small molecule organic semiconductors typically have benzene rings with delocalised π orbitals as the basic unit, and can be prepared as molecular single crystals, with very high mobilities and band-like transport [12], or as amorphous films, with lower mobilities and hopping transport; these films are normally used in OLEDs e.g. [2]. In the case of conjugated polymers, the π bonds delocalise along the carbon 'backbone' of the polymer chain, forming a one-dimensional system. Transport in conjugated polymers is thus governed by inter-chain hopping, and defects in the polymers limiting intra-chain transport along the delocalised π orbitals. A common characteristic of transport in organic semiconductors is the field-dependence of the mobilities, which have the form:

$$\mu\left(\mathrm{E}\right) = \mu_0 \exp\left(\sqrt{\frac{\mathrm{E}}{\mathrm{E}_0}}\right) \tag{1.1}$$

where $\mu\left(\mathrm{E}\right)$ is the carrier mobility at a particular electric field, μ_0 is the zero field carrier mobility, E is the electric field strength, and E_0 is a material parameter which determines the field dependence of a carrier mobility in a particular organic semiconductor, and may often be sample dependent since it is related the amount of disorder in a material. The zero field mobility for electrons and holes, μ_0, is very low compared to mobilities in inorganic crystalline semiconductors (e.g. μ_n=1450 $\mathrm{cm}^2/\mathrm{Vs}$ and μ_p=450 $\mathrm{cm}^2/\mathrm{Vs}$ in Si [15]), with values ranging from 1×10^{-3} to $1 \times$

10^{-10} cm^2/Vs in small molecule and polymeric semiconductors e.g. [6]. Typically, the electric field applied to these devices is in the range from 10^4 to 10^6 V/cm. This field-dependent form for carrier mobilities is purely an empirical formula and has been frequently observed in experimental measurements of carrier mobilities as a function of electric field in both conjugated polymers e.g. [16] and small molecules e.g. [17] for all values of E. Such a field-dependence of the mobility has been shown to be a consequence of the disordered nature of these materials, and more specifically has been attributed to the energetic disorder present in a sample e.g. [18].

At the present time, there is no clear advantage to fabricating OLEDs from either small molecules or conjugated polymers; as well as their similar physics, all organic devices share a common core of advantages over competing technologies [6][7][13]. In terms of emission, OLEDs have several benefits over current technology; they do not require a backlight or polarisers, no colour filters are required for colour displays, making them relatively simple to fabricate, they are high contrast, and they have a wide viewing angle. All of these properties compare favourably to existing LCD technology. OLEDs have a low operating voltage, allowing battery operated devices to be feasible. Physically, advantages include flexibility (if the materials are deposited on a flexible substrate), low weight, and general ruggedness due to the lack of a vacuum and the fact that they are solid state devices. They also exhibit fast switching speeds, an important feature for video display capability, despite the low mobilities since the films are very thin and optical recombination is very fast. For typical material parameters, the carrier transit time can be calculated as $\tau = d^2/\mu V$, yielding $\tau \approx 10^{-6}$s, and the turn off time is much faster than this since carrier recombination times are between 1ns and 20ns [13]. One further benefit is the ability to modify the chemical structure of the molecules and physical structure of the films to enhance particular properties. For example, the the colour of emitted light can be altered by modifying the chemical structure, and adjusting the morphology of a film of the conjugated polymer PFO to improve the overall order has been shown to increase the mobility by reducing the positional disorder, hence enabling the carriers to take shorter paths through the film [19].

The main difference between the two classes of materials is in their methods of preparation. Thin films of small molecules are usually fabricated by vacuum evaporation, whereas films of conjugated polymers are formed by solution processing

methods such as spin casting. Perhaps one of the major advantages of conjugated polymer LEDs is that the films are cheaper and easier to fabricate; novel methods of polymer film deposition have been explored, notably using conventional ink jet printing technology [5].

Currently, the only major weakness of OLEDs is that of device lifetimes. Degradation of OLEDs is a significant problem which may have many causes e.g. [20][14], many of which are not understood, and degradation affects some materials more than others [21][22].

1.2 Device operation

An OLED consists of one or more layers of organic semiconductor (typically about 100nm thick) sandwiched between two electrodes; light emission can be considered as occurring in a sequence of steps. Firstly, charges are injected into the organic layer(s); electrons and holes are injected from the cathode and anode respectively. The electrons and holes are then transported through the material by drifting under the influence of an applied field. The carriers may then recombine to form a singlet or triplet exciton (a Coulombically bound electron-hole pair), which can decay radiatively (singlets) or non-radiatively (triplets). This overall process is shown schematically in Figure 1.3 for a single layer OLED.

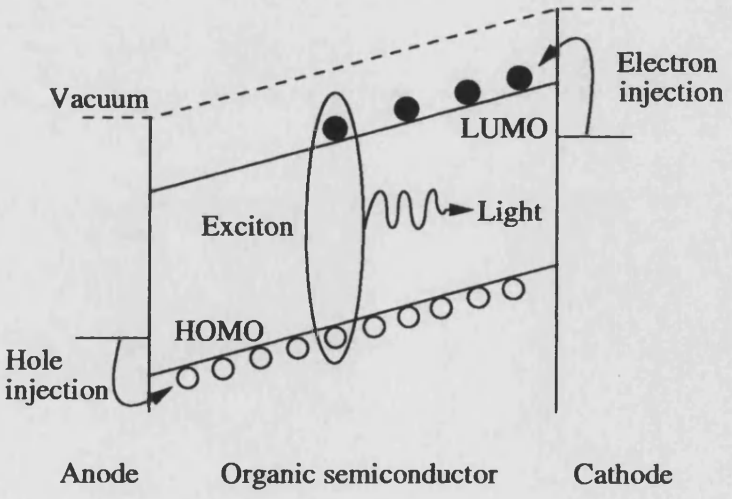

Figure 1.3: Schematic energy band diagram illustrating the principle of single-layer OLED operation.

Optimum efficiencies are achieved if carrier injection and transport are balanced

i.e. with the barrier to injection and the mobilities being similar for both carriers. However, this situation is usually difficult to obtain in a single layer device, since the majority of materials are hole transporters, and so multi-layer devices are often employed as they can balance both injection and transport; the benefits of bi-layer devices are discussed in Chapter 4.

The current-voltage (J-V) characteristics of OLEDs have been broadly considered to be either injection limited, or bulk limited, with space-charge effects dominating. In the case of injection limited J-V characteristics, both Fowler-Nordheim tunnelling currents [23], and thermionic emission of carriers over a metal-semiconductor barrier [24] have been cited as being responsible for carrier injection. In the case of bulk limited J-V characteristics, the contacts have been assumed to be Ohmic, with space charge limited current (SCLC) [16], or SCLC with traps [25] flowing. Although analytic expressions have previously been formulated for such currents [26], such formalisms cannot be easily applied to bipolar current flow with field dependent mobilities and recombination, or to multi-layer devices. For this reason, numerical models have been employed e.g. [27][28][29]. It is important to note that all of these approaches are based on conventional crystalline inorganic semiconductor theory [15], with transport occurring within energy bands as opposed to hopping between sites.

However, such models cannot investigate the fundamental nature of transport in disordered organic semiconductors, and in an attempt to understand the field and temperature dependence of carrier mobilities in organic semiconductors, hopping transport models have been devised which include the spatial and energetic disorder inherent in organic semiconductors e.g. [18]. The carrier mobilities generated by this method do qualitatively agree with the experimentally observed field and temperature dependence of the mobilities. There has also been a growing interest in investigating how the texture of thin films can affect transport and recombination; hopping models which incorporate the film morphology are being developed for this purpose [30]. For a recent review of both band and hopping transport models, see [31].

1.3 Overview

This thesis describes how two different types of device models have been employed to investigate charge carrier transport in OLEDs. The first model is a one-dimensional time-independent drift-diffusion model, of the type commonly employed in the simulation of inorganic semiconductor devices. The model presented is an extension of a model previously developed within the group [32], which although fully functioning and comparable to other models in the literature e.g. [27] [28], had not been thoroughly validated and required some minor functional additions, as well as some work to improve the numerical stability. The model includes both thermionic emission and Fowler-Nordheim tunnelling for carrier injection, along with Schottky barrier lowering, whilst the bulk transport incorporates field dependent carrier mobilities, and Langevin optical recombination. The model self-consistently solves the drift-diffusion equations, Poisson's equation, and the continuity equations, and can provide information including current-voltage characteristics, electric field profiles, and carrier density profiles. The main goals of this work were to use the model to investigate carrier transport in single and multi layer OLEDs by comparing simulated data to experimental data, to validate the model and discover any regimes in which it was ineffective as a tool. A potential benefit of such a model is to use it in a predictive capacity; such models are routinely used in the case of inorganic semiconductor devices to investigate the effect of varying material parameters or novel device geometries and reject or accept certain designs, which can then be investigated in more detail, without the time and financial costs of fabricating many extra devices. Chapter 2 discusses the formation of metal-semiconductor contacts, the injection and space-charge limited current regimes for OLEDs and describes the drift-diffusion model which has been developed. Chapters 3 and 4 contain the results obtained from the drift-diffusion model for single layer and bi-layer devices respectively. The actual computer code used has been omitted for brevity, along with the details of many aspects of the computer science and numerical methods employed, which formed a large part of the work undertaken.

The second approach taken was to develop a hopping transport Monte-Carlo model to investigate carrier transport in liquid crystalline conjugated polymers, by explicitly including details of the polymer morphology within the film, rather than simulating transport within a generic lattice of hopping sites (the model could easily be adapted for use with the low molecular weight materials or other

polymers). Again, the computational details and code have been omitted for brevity. Chapter 5 discusses the theory of charge transport in disordered organic semiconductors via hopping transport, and describes the Monte-Carlo hopping transport model which has been developed; Chapter 6 contains mobilities obtained from the Monte-Carlo hopping transport model for varying degrees of spatial and energetic disorder.

Chapter 7 concludes the thesis, summarising the findings made from both models. and suggests directions in which the work should be continued in order to answer any outstanding questions or investigate new issues which have become apparent from the work carried out.

References

[1] M Pope, H P Kallman and P Magnante, *J. Chem. Phys.*, **38**, 2042 (1963).

[2] C W Tang and S A VanSlyke, *Appl. Phys. Lett.*, **51**, 913 (1987).

[3] C W Tang, S A VanSlyke and C H Chen, *J. Appl. Phys.*, **65**, 3610 (1989).

[4] J H Burroughes, D D C Bradley, A R Brown, R N Marks, K MacKay, R H Friend, P L Burn and A B Holmes, *Nature*, **347**, 539 (1990).

[5] Information regarding device efficiencies, brightnesses and operating lifetimes is in a constant state of flux. See results from industry e.g. Cambridge Display Technology (www.cdtltd.co.uk) for the latest data.

[6] M T Bernius, M Inbasekaran, J O'Brien and W Wu, *Adv. Mater.*, **12**, 23, 1737 (2000).

[7] I D W Samuel, *Phil. Trans. R. Soc. Lond. A*, **358**, 193 (2000).

[8] R Troutman, *Synthetic Metals*, **91**, 31 (1997).

[9] G G Malliaras, J R Salem, P J Brock, and J C Scott, *J. Appl. Phys.*, **84**, 1583 (1988).

[10] H Sirringhaus, R J Wilson, R H Friend, M Inbasekaran, W Wu, E P Woo, M Grell, and D D C Bradley, *Appl. Phys. Lett.*, **77**, 406 (2000).

[11] N Tessler, *Adv. Mater.*, **11**, 363 (1999).

[12] K C Kao and W Hwang, *Electrical Transport In Solids: with particular reference to organic semiconductors*, Pergamon Press, Oxford (1981).

[13] I H Campbell and D L Smith, *Solid State Physics: Advances in Research and Applications*, **55**, 1 (2001).

[14] G Hadziioannou and P F van Hutten (eds.), *Semiconducting Polymers: Chemistry, Physics and Engineering*, 445, Wiley-VCH, Weinheim (2000).

[15] S M Sze, *Physics of Semiconductor Devices*, 2nd. ed., John Wiley and Sons, New York (1981).

[16] P W M Blom, H C F Martens, and J N Huiberts, *Synth. Met.*, **121**, 1621 (2001).

[17] W Brütting, S Berleb, and A G Mückl, *Organic Electronics*, **2**, 1 (2001).

[18] H Bässler, *Phys. Stat. Solidi B*, **175**, 15, (1993).

[19] M Redecker, D D C Bradley, M Inbasekaran, and E P Woo, *Appl. Phys. Lett.*, **74**, 1400 (1999).

[20] A Dodabalapur, *Solid State Communications*, **102**, 259 (1997).

[21] C Foden, *Private communication.*

[22] G L B Verschoor, *Private communication.*

[23] I D Parker, *J. App Phys.*, **75**, 3, 1656 (1994).

[24] A J Campbell, D D C Bradley, J Laubender, and M Sokolowski, *J. Appl. Phys.*, **8**, 5004 (1999).

[25] A J Campbell, D D C Bradley, and D G Lidzey, *J. Appl. Phys.*, **82**, 6326 (1997).

[26] M A Lampert and P Mark, *Current Injection In Solids*, Academic Press, New York (1970).

[27] P S Davids, I H Campbell, and D L Smith, *J. Appl. Phys.*, **82**, 6319 (1997).

[28] G G Malliaras and J C Scott, *J. Appl. Phys.*, **83**, 5399 (1998).

[29] C D J Blades and A B Walker, *Synth. Met.*, **111-112**, 335 (2000).

[30] A M Stoneham and M M D Ramos, *J. Phys.: Condens. Matt.*, **13**, 2411 (2001).

[31] A B Walker, A Kambili, and S J Martin, *J. Phys.: Condens. Matt.*, **14**, 9825 (2002).

[32] C D J Blades, *Ph.D. Thesis*, University of Bath (2000).

Chapter 2

Band Model of Charge Injection and Transport

As previously mentioned in Chapter 1, organic light emitting diodes consist of one or more layers of semiconductor sandwiched between two electrodes, which are usually two different metals. The asymmetry of the electrodes' workfunctions is the key to the operation of OLEDs; the proximity of the workfunction of the anode to the HOMO level allows hole injection into the device, and the proximity of the cathode workfunction to the LUMO level allows electrons to be injected into the device. The carriers are then transported through the layer(s), where they may recombine to emit light. However, the exact nature of injection and transport in OLEDs has long been the subject of debate, and in an attempt to elucidate the situation, the energy band model, as applied to crystalline inorganic semiconductors [1], has been applied to organic devices, despite their disordered and amorphous nature. As a rule, the materials in question are considered to be wide bandgap (>2eV), undoped semiconductors, which are fully depleted at zero bias [2]. Some unintentional doping is usually present in the films, but in well prepared materials the levels are usually low enough to ignore.

When a metal and semiconductor are brought into contact, a potential barrier may be formed due to the difference in their workfunctions; this barrier will act to limit the current flowing across the interface. Charges may cross such a potential barrier by either thermionic emission, whereby carriers acquire sufficient thermal energy to surmount the potential barrier, or by field emission, where carriers

tunnel through the potential barrier. Depending upon the size and nature of the potential barrier, the electrode-semiconductor interfaces are likely to have a significant impact upon the device performance, since limiting the injection of one type of carrier can drastically alter the device's efficiency, as well as determining the current-voltage characteristics. Metal-semiconductor contacts and the related carrier injection mechanisms are reviewed in sections 2.1 and 2.2. The basic operation of an OLED, which is a metal-semiconductor-metal device, is then outlined in section 2.3.1.

Alternatively, the bulk properties of the semiconductor may act to limit current flow if the barrier to injection is small or even non-existent (i.e. an Ohmic contact). In this case, the current carried by the injected carriers forms a space charge within the semiconductor which acts to control the current-voltage characteristics of the device. Space charge limited current (SCLC) is discussed in section 2.4.

In an attempt to understand injection and transport processes in OLEDs, current-voltage (J-V) characteristics from both analytical expressions and numerical models have been fitted to experimental data. However, analytical expressions are only usually formulated for unipolar conduction, and can only cope with simple cases, ignoring potentially crucial issues such as recombination, diffusion currents, and field dependent mobilities, whereas OLEDs by their very nature are bipolar. Analytical expressions for bipolar current flow are even more restricted, only applying to the case for Ohmic contacts, and cannot be applied to multi-layer devices. Additionally, when fitting analytical expressions to experimental J-V data, assumptions must be made as to whether the current is injection limited e.g. [3] or space charge limited e.g. [4]. The resulting J-V characteristics can often only be fitted to experimental current-voltage data over limited voltage ranges. While this fitting may yield parameters such as the carrier mobility or barrier height, such values have little use as the material parameters can be very sample dependent, and without simultaneous treatment of injection and bulk transport, no firm conclusions regarding injection and transport can be reached. Hence numerical models which can account for injection and bulk limited transport, without making explicit assumptions as to the nature of the contacts, are required. Using such a model, an unambiguous fit to the experimental data can often be made, yielding not only material parameters but insight into the injection and transport taking place within the device.

The results contained within this thesis for both single and multi-layer OLEDs (Chapters 3 and 4 respectively) have been obtained from a numerical drift-diffusion model, based on one previously instigated within the research group [5], but developed to incorporate new features, such as trapping and simultaneous barrier lowering and tunnelling injection, and also to eradicate bugs, to improve stability and speed, and to make the software more user-friendly. The model is one-dimensional and time independent, and is described in detail in section 2.5.

2.1 Metal-semiconductor contacts

When an isolated metal and an isolated semiconductor are brought into contact, thermal equilibrium will be established; the Fermi levels in both materials must be equal and continuous, and the vacuum level must also be continuous [1][6]. In order for this to occur, charge must be transferred from the semiconductor to the metal or vice-versa. In the case of an n-doped semiconductor, electrons flow from the semiconductor into the metal, leaving behind a positively charged depletion region, of width W, in the semiconductor, created by the positive donor ions. The energy bands in the semiconductor bend upwards in response to this depletion region, forming a barrier to the flow of electrons; the Fermi level in the semiconductor is lowered by an amount equal to the difference between the work-functions of the metal, ϕ_m, and semiconductor, ϕ_s. This situation is illustrated in Figure 2.1 for an ideal contact. In the case of a p-doped semiconductor, electrons flow into the semiconductor from the metal, causing a negatively charged region to build up in the semiconductor, again causing band bending (in the opposite direction to the n-type case). In this case, the Fermi level in the semiconductor is raised by an amount equivalent to the difference between the workfunctions. This is also illustrated in Figure 2.1. Such metal-semiconductor contacts are termed Schottky contacts, and are rectifying i.e. current flows easily in one direction only.

The barrier heights to electron and hole injection into the semiconductor from the metal are given by [1]:

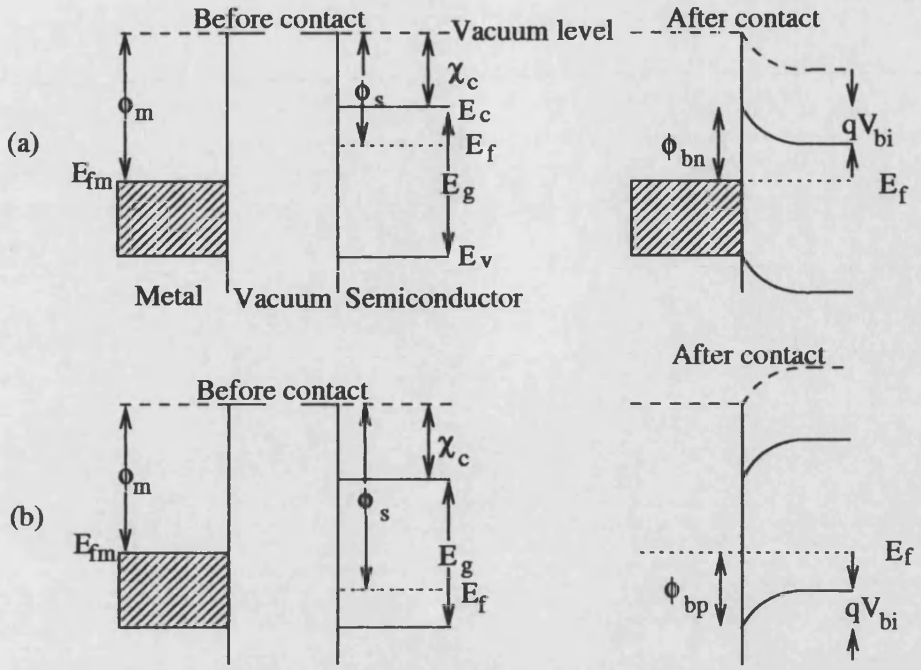

Figure 2.1: The formation of an ideal (a) n-type Schottky contact, and (b) p-type Schottky contact.

$$q\phi_{bn} = q\left(\phi_m - \chi_c\right) \tag{2.1}$$

$$q\phi_{bp} = E_g - q\phi_{bn} = E_g - q\left(\phi_m - \chi_c\right) \tag{2.2}$$

where q is the electronic charge, ϕ_{bn} and ϕ_{bp} are the barrier heights to electron and hole injection respectively, ϕ_m is the metal workfunction, E_g is the energy gap of the semiconductor, and χ_c is the electron affinity of the semiconductor. The metal workfunction is defined as the difference between the Fermi level of the metal, E_{fm}, and the vacuum level, whilst the electron affinity is the energy difference between the conduction band edge of the semiconductor and the vacuum level.

However, as previously mentioned, organic semiconductors are essentially undoped, and are therefore viewed as either intrinsic lightly doped semiconductors or insulators; metal-insulator and metal-intrinsic contacts are illustrated in Figure 2.2. A perfect insulator is simply defined as a material which contains no intrinsic conduction electrons or holes, and hence the electrical characteristics of insulators are determined by injected free charge. When organic semiconductors, or insulators, are brought into contact with a metal, a neutral contact is formed. The description neutral means that the regions adjacent to the interface on both

sides are electrically neutral, and so the conduction and valence bands are rigid i.e. there is no band bending [7]. At thermal equilibrium, this is known as the flat band condition, and the carrier concentration at the contact is deemed to be equal to that in the bulk of the semiconductor. In this thesis, the metal-semiconductor contacts in OLEDs are assumed to ideal metal-insulator contacts; the barrier heights calculated from equations 2.1 and 2.2 are equally valid in this case [8].

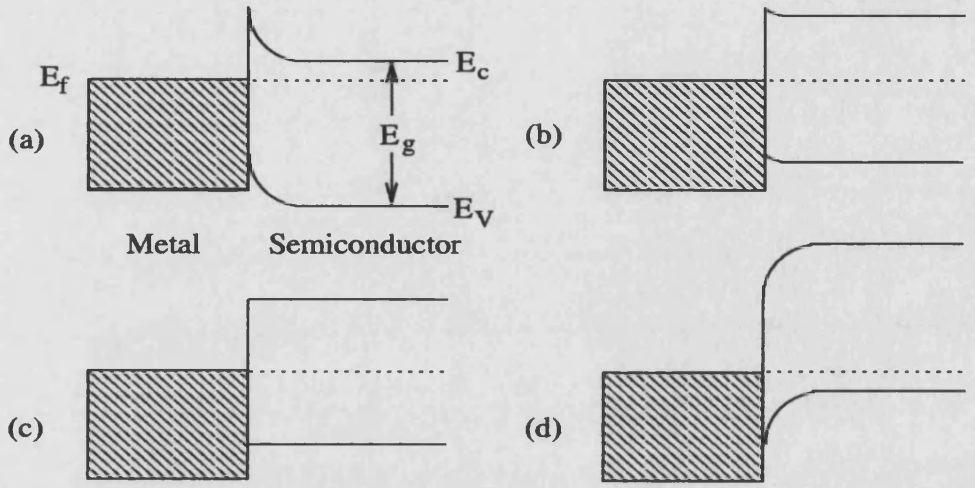

Figure 2.2: Schematic energy band diagrams of (a) a metal-n-type semiconductor contact, (b) a metal-intrinsic contact, (c) a metal-insulator contact, and (d) a metal-p-type semiconductor contact.

Although analytic expressions for the depletion width, W, and built-in potential, V_{bi}, in a metal-semiconductor contact are well known [1], such concepts are of little use in the case of organic semiconductors, which are considered to be fully depleted at thermal equilibrium; this has been experimentally verified e.g. [10]. However, the concept of a built-in potential is still very important in organic LEDs, and it arises due to the metal-semiconductor-metal structure of the devices, and is discussed in section 2.3.

2.1.1 Barrier height lowering

The barrier heights to carrier injection, ϕ_{bn} and ϕ_{bp}, obtained by considering the workfunctions of the metal and semiconductor (equations 2.1 and 2.2) apply to an ideal metal-semiconductor contact. However, for a real metal-semiconductor contact, there are three factors which can potentially affect the actual size of the barriers; interfacial layers, interface states, and image force lowering [6]. Of

these, only image force lowering will be considered here, and is discussed below. Interfacial regions have been hitherto largely neglected in the analysis of carrier transport in OLEDs, but there is some evidence suggesting their importance in the operation of OLEDs [2][9].

When an electric charge approaches a metal surface, charge of opposite polarity builds up on the metal surface and hence there is an attractive force between the charge approaching the metal surface and the charge built up on the metal surface. This effect can be analysed using the method of images and is called the image force [6]. The attractive image force, F, is given by:

$$F = \frac{-q^2}{4\pi(2x)^2\epsilon_s\epsilon_0} = \frac{-q^2}{16\pi\epsilon_s\epsilon_0 x^2} \tag{2.3}$$

where q is the electronic charge, x is the distance between the charge and the metal surface (hence the distance between the charge and its image is $2x$), ϵ_0 is the permittivity of free space and ϵ_s is the dielectric constant of the semiconductor.

The potential energy of an electronic charge, V, at a distance x from the metal surface is given by:

$$\mathrm{V}(x) = \frac{-q^2}{16\pi\epsilon_s\epsilon_0 x} \tag{2.4}$$

This image force potential modifies the shape of the potential barrier close to the interface (it is rounded off), and with the application of an electric field, E, it causes a reduction of the barrier height; this lowering is known as the Schottky effect, and is illustrated in Figure 2.3 for a neutral contact.

With the Schottky effect taken into account, the potential barrier height, ψ, measured from the Fermi level in the metal is given by:

$$\psi(x) = \phi_{bn} - q\mathrm{E}x - \frac{q^2}{16\pi\epsilon_s\epsilon_0 x} \tag{2.5}$$

It must be noted that this expression does not hold at $x = 0$. To avoid this

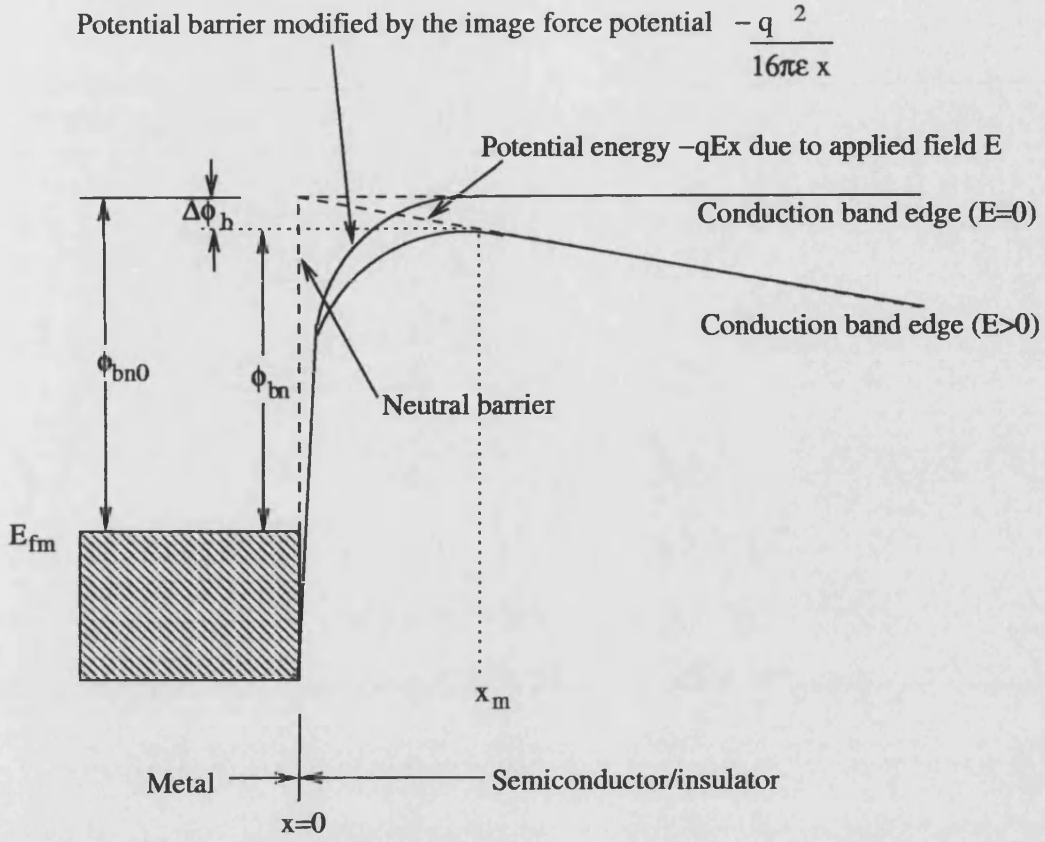

Figure 2.3: Energy band diagram for a neutral contact illustrating Schottky barrier lowering due to the combination of both image force and the applied field.

singularity, it is assumed that the expression is valid from the point x_0 to ∞, and that the image force is constant from $x = 0$ to $x = x_0$. The electron sea in the metal is also assumed to extend to x_0 [7].

The point at which the potential is a maximum, x_m, is found by setting $\frac{d\psi}{dx} = 0$, yielding:

$$x_m = \sqrt{\frac{q}{16\pi\epsilon_s\epsilon_0 \mathrm{E}}} \tag{2.6}$$

Substituting this value into equation 2.5 therefore gives the effective barrier height, ϕ_{bn}, at particular electric field, E:

$$\phi_{bn} = \phi_{bn0} - \sqrt{\frac{q^3 \mathrm{E}}{4\pi\epsilon_0\epsilon_s}} \tag{2.7}$$

where ϕ_{bn0} is the zero field electron barrier height.

Hence the electron and hole barrier heights are now given by these expressions:

$$\phi_{bn} = \phi_{bn0} - \Delta\phi_b \tag{2.8}$$

$$\phi_{bp} = E_g - (\phi_{bn0} - \Delta\phi_b) \tag{2.9}$$

where ϕ_{bn0} and ϕ_{bp0} are the zero field barrier heights, and $\Delta\phi_b = \sqrt{\frac{q^3 E}{4\pi\epsilon_0\epsilon_s}}$.

The value of ϵ_s is much lower in organic semiconductors (typically $\sim$ 3) than in inorganic semiconductors (ϵ_s is 11.9 in Si and 13.1 in GaAs [1]) and as can be seen from equation 2.7, this makes the effect of image force lowering more pronounced. In organic semiconductors, due to the thin films used, a typical electric field value might be of the order of $10^8 \mathrm{Vm}^{-1}$ or more, and so in an OLED the magnitude of the barrier lowering can be of the order of $\sim$ 0.2eV, and x_m would be $\sim$ 1nm, which is a significant distance within the device. An additional point which is important to consider is that in some OLEDs, the contacts are lightly doped polymers which are not metallic in nature and hence image force lowering is not applicable [11].

2.1.2 Forward and reverse bias operation

At thermal equilibrium, the net current density across a metal-semiconductor contact is zero since there is an equal and opposite flow of carriers, and hence current, from the metal into the semiconductor ($J_{m\to s}$ for holes and $J_{s\to m}$ for electrons) and vice-versa ($J_{s\to m}$ for holes, and $J_{m\to s}$ for electrons) [1]. If a positive bias is applied to an n-type Schottky barrier diode, as illustrated in Figure 2.4, then neglecting image barrier lowering, the potential barrier for carriers flowing from the semiconductor into the metal is reduced and hence $J_{m\to s}$ increases (since the electron current flows in the opposite direction to the electrons themselves). The barrier for carriers flowing from the metal into the semiconductor is field-independent, neglecting Schottky barrier lowering, and hence the current $J_{m\to s}$

dominates. In a p-type device, under forward bias conditions the flow of holes from the semiconductor to the metal increases i.e. $J_{s \to m}$ dominates. Under reverse bias conditions, the potential barrier for carriers traversing the interface from the semiconductor into the metal increases, whilst the barrier for carriers moving from the metal to the semiconductor is unchanged. Hence there is a net flow of carriers from the metal into the semiconductor, and the current saturates at $J_{m \to s}$ for p-type diodes, and $J_{s \to m}$ for n-type diodes.

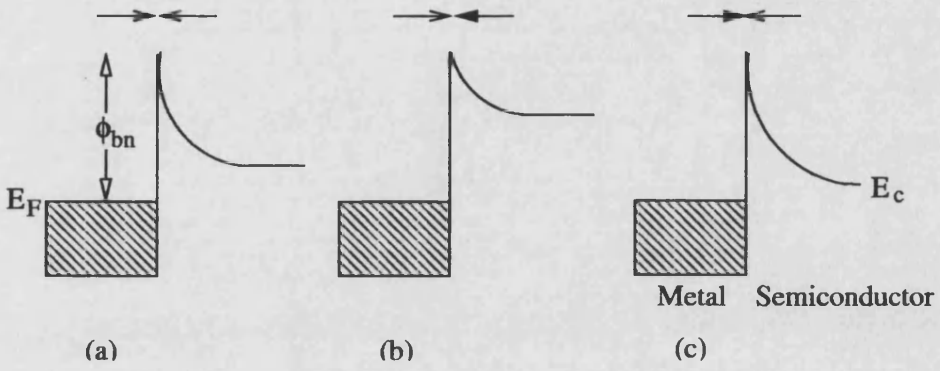

Figure 2.4: Current flow across an n-type Schottky barriers at (a) thermal equilibrium, (b) forward bias, and (c) reverse bias. The arrows represent the flow of electrons. The valence band has been omitted for clarity.

This results in an asymmetric current-voltage characteristic for a Schottky diode i.e. it is rectifying, (see Figure 2.5), similar to that for the pn junction diode; however, in the Schottky diode, majority carriers are largely responsible for conduction whereas in pn diodes, minority carriers are responsible for conduction [1].

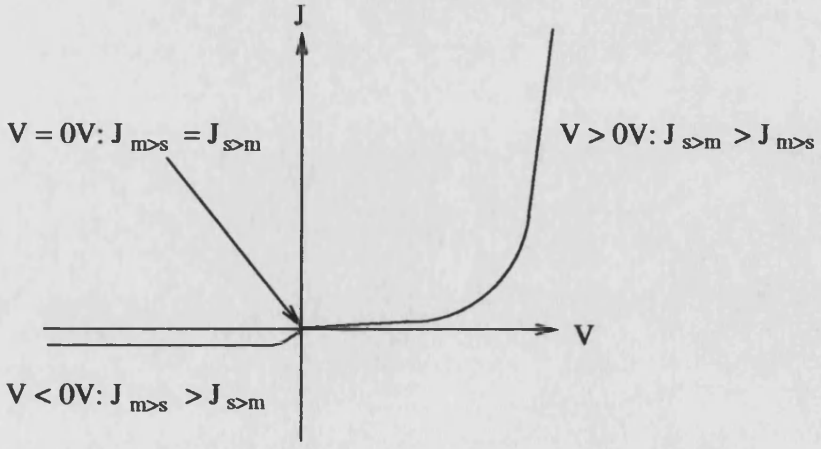

Figure 2.5: Schematic diagram of the forward and reverse bias current-voltage (J-V) characteristics of a Schottky barrier diode.

In practice, allowing for image barrier lowering and the field-dependent mobili-

ties means that the reverse bias current in a metal-organic semiconductor does not saturate, and this fact means that their operation is indeed possible, as is discussed in section 2.3.

2.2 Current transport processes across metal-semiconductor contacts

Several mechanisms are responsible for current transport across metal-semiconductor contacts [1][6][8]:

- Thermionic emission of carriers over the barrier
- Tunnelling emission of carriers through the barrier (field emission)
- Tunnelling via interface states (trap-assisted tunnelling)
- Interface generation and recombination
- Minority carrier transport

The contacts used in OLEDs are blocking contacts i.e. carriers must overcome a barrier to be injected from the metal into the semiconductor. Both thermionic emission and tunnelling (field emission) have been widely suggested as mechanisms for the injection of charge into OLEDs e.g. [1], and are discussed below.

2.2.1 Thermionic emission

Thermionic emission simply requires carriers with sufficiently high kinetic energy such that they can surmount the potential barrier at the metal-semiconductor interface. As the temperature increases, the number of carriers with high energies increases, thus increasing the rate of thermionic emission (hence the name). Similarly, if the barrier is decreased at a fixed temperature, again more carriers with adequate kinetic energy are available [8].

Pure thermionic emission theory makes the assumptions that the barrier height is greater than k_BT and that the carriers injected into the semiconductor from the metal are not influenced by space-charge effects or traps i.e. all the injected carriers are carried away from the contact [6]. For a metal-n type semiconductor contact, the thermionic emission current of carriers from the metal into the semiconductor is given by [1][6]:

$$J_{m\to s} = -A^*T^2 \exp\left(\frac{-\phi_{bn}}{k_BT}\right) \tag{2.10}$$

where $A^* = \frac{4\pi q m^* k_B^2}{h^3}$ is the Richardson constant, T is the temperature, k_B is Boltzmann's constant, q is the electronic charge, m^* is the effective mass of the electrons, h is Planck's constant, and ϕ_{bn} is the electron barrier height (neglecting image force lowering).

Similarly, the electron current flowing from the semiconductor into the metal is given by:

$$J_{s\to m} = A^*T^2 \exp\left(\frac{V_{app} - \phi_{bn}}{k_BT}\right) \tag{2.11}$$

where V_{app} is the applied bias.

Hence the net electron current, J_n, at a metal-semiconductor interface is given by the sum of $J_{s\to m}$ and $J_{m\to s}$:

$$J = A^*T^2 \exp\left(\frac{-\phi_{bn}}{k_BT}\right)\left[\exp\left[\frac{V_{app}}{k_BT}\right] - 1\right] \tag{2.12}$$

A similar expression can be derived for the net hole current, J_p.

However, if the carrier mobilities are low, as is the case in organic semiconductors, then carriers will not be efficiently removed from the locality of the contact. Hence charge may build-up in the proximity of the contact, and some will diffuse back into the metal; therefore the mobility of the carriers will determine the injection

current [7].

To account for this situation, Crowell and Sze proposed the so-called thermionic emission-diffusion theory [12]. This theory is a synthesis of pure thermionic emission theory (discussed above), which describes the current at the interface by assuming thermionic emission of carriers over the barrier and depletion region into the neutral region, and diffusion theory [1] which attempts to explain transport at metal-semiconductor interfaces by assuming drift-diffusion in the depletion region, with continuity of the Fermi-level at the metal-semiconductor interface. Thermionic emission-diffusion theory considers the current flow as the effects of thermionic emission over the barrier and drift-diffusion of carriers in the depletion region in series, and uses the concept of an effective recombination velocity, v_{rn}, at the potential energy maximum, x_m; v_{rn} was first implemented as a boundary condition in a numerical simulation of a Schottky barrier device by Choo [13].

In an n-type device the current in the depletion region ($x_m < x < W$) is given by the drift-diffusion current, J_D:

$$J_D = -q\mu_n n(x) \frac{\mathrm{d}\phi_n(x)}{\mathrm{d}x} \tag{2.13}$$

where μ_n is the electron mobility, ϕ_n is the electron quasi-Fermi level, and n is the electron density, given by:

$$n = N_c \exp\left(\frac{-[\psi(x) - \phi_n(x)]}{k_B T}\right) \tag{2.14}$$

where N_c is the density of states in the conduction band, and ψ is the electrostatic potential.

The barrier region between the metal-semiconductor contact and the potential energy maximum ($0 < x < x_m$) is assumed to be a perfect sink of electrons, such that the current flow in this region, J_B, is given by:

$$J_B = qv_{rn}(n_{eq} - n_m) \tag{2.15}$$

where q is the electronic charge, v_{Rn} is the effective recombination velocity, n_{eq} is the quasi-equilibrium electron density at x_m:

$$n_{eq} = N_c \exp\left(\frac{-\phi_{bn}}{k_B T}\right) \tag{2.16}$$

and n_m is the electron density at the point x_m when the current is flowing:

$$n_m = N_c \exp\left(-\left[\frac{\phi_{bn} - \phi_n(x_m)}{k_B T}\right]\right) \tag{2.17}$$

It can be shown that using the continuity of currents J_B and J_D yields [6][7]:

$$J = \frac{qN_c v_{rn}}{1 + (v_{rn}/v_D)} \exp\left[-\frac{\phi_{bn}}{k_B T}\right]\left[\exp\left(\frac{-qV_{app}}{k_B T}\right) - 1\right] \tag{2.18}$$

where v_D is the effective diffusion velocity associated with the diffusion of electrons from $x = W$ to $x = x_m$.

There exists then two limiting cases for the current density. If $v_{rn} \gg v_D$, diffusion dominates and equation 2.18 tends to the diffusion theory [1]:

$$J \approx qN_c \mu_n \mathrm{E}_{(x=0)} \exp\left(\frac{-\phi_{bn}}{k_B T}\right)\left[\exp\left(\frac{-V_{app}}{k_B T}\right) - 1\right] \tag{2.19}$$

where $\mathrm{E}_{(x=0)}$ is the electric field at the contact.

If $v_D \gg v_{rn}$, diffusion can be neglected and equation 2.18 reduces to thermionic emission theory:

$$J \approx qN_c v_{Rn} \exp\left(\frac{-\phi_{bn}}{k_B T}\right)\left[\exp\left(\frac{-V_{app}}{k_B T}\right) - 1\right] \tag{2.20}$$

$$\approx A^* T^2 \exp\left(\frac{-\phi_{bn}}{k_B T}\right)\left[\exp\left(\frac{-V_{app}}{k_B T}\right) - 1\right] \tag{2.21}$$

Despite any potential inaccuracies which may be involved with the concept of using thermionic emission as a mechanism for charge injection in OLEDs, it has been used widely in both numerical models as a boundary condition e.g. [5][15][16], or as an analytical expression which has been applied to experimental data e.g. [14][17][18], yielding values of the barrier height, carrier mobility and field dependence of the mobility. However, when fitting analytical expressions for the thermionic injection current to experimental, many authors use pure thermionic emission only e.g. [14]; neglecting the backflowing of carriers into the metal can lead to incorrect analysis of the data, as can neglecting barrier lowering.

2.2.2 Field emission (tunnelling)

If the barrier thickness becomes sufficiently small, the probability of quantum mechanical tunnelling through the barrier by a carrier increases dramatically. For a fixed barrier height, increasing the doping reduces the width of the barrier due to increased band bending; for highly doped Schottky contacts, the tunnelling current component may well exceed the thermionic emission current component, especially at low temperatures [1]. If the maximum component of the tunnelling current occurs at an energy approximately equal to the Fermi level, the tunnelling process is known as field emission; if the majority of the tunnelling carriers have energies between the Fermi level and the top of the barrier, the process is known as thermionic field emission [7].

In the case of metal-organic semiconductor devices, doping is negligible and hence tunnelling is only significant if the field is large, the barrier height is low, and the temperature is low. The tunnelling is considered to be of the field emission form only, and as such the Fowler-Nordheim formalism [19] for tunnelling at contacts is widely used for the analysis e.g. [3][21] and modelling of J-V characteristics e.g. [5][15].

The current density due to carriers tunnelling through a potential barrier of height C, depicted in Figure 2.6, can be expressed as [19]:

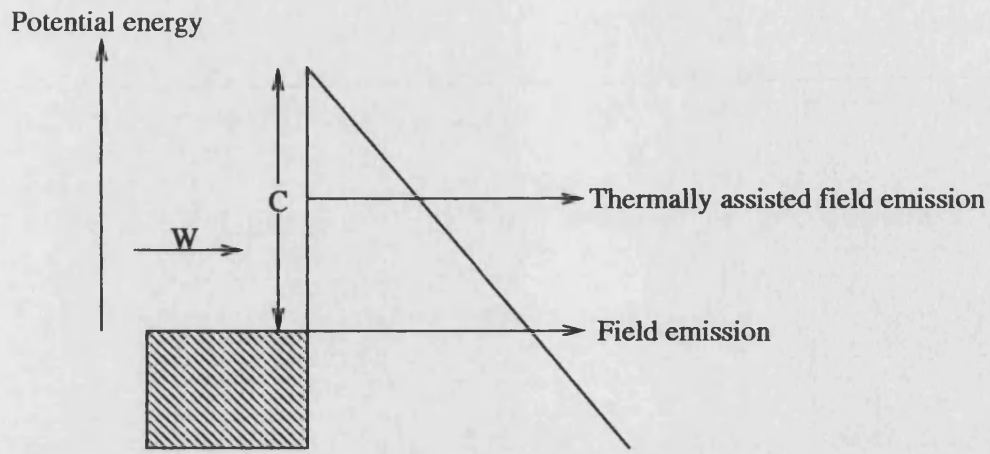

Figure 2.6: Illustration of potential barrier, of height C, to be tunnelled through.

$$J = \frac{16\pi mq}{Ch^3}\int_0^{\mu} W^{1/2}(C-W)^{1/2}(\mu - W)\exp\left(-\frac{4\kappa(C-W)^{3/2}}{3\mathrm{E}}\right)\mathrm{d}W \qquad (2.22)$$

where μ is the chemical potential, W is the electron kinetic energy normal to the barrier, m is the mass of the electron, q is the electronic charge, h is Planck's constant, $\kappa = 8\pi^2 m/h^2$, and E is the electric field.

Making the following substitutions [5][23]:

$$A = \frac{16\pi mq}{Ch^2} \qquad (2.23)$$

$$\beta = \frac{4\kappa}{3\mathrm{E}} \qquad (2.24)$$

$$f(W) = \exp(-\beta(C-W)^{3/2}) \qquad (2.25)$$

$$g(W) = \left(W^{1/2}\mu - W^{3/2}\right) \qquad (2.26)$$

allows equation 2.22 to be expressed in a more compact form:

$$J = \frac{2A}{3\beta}\int_0^{\mu} g(W)\frac{\mathrm{d}f}{\mathrm{d}W}\mathrm{d}W \qquad (2.27)$$

Integrating by parts yields:

$$J = -\frac{2A}{3\beta}\int_0^{\mu} \exp\left(-\beta(C-W)^{1/2}\right)\left(\frac{1}{2}W^{-1/2}\mu - \frac{3}{2}W^{-1/2}\right)\mathrm{d}W \tag{2.28}$$

which can be solved via the mean value theorem:

$$J = \int_a^b f(x)g(x)\mathrm{d}x \approx g(\xi)\int_a^b f(x)\mathrm{d}x (a \leq \xi \leq b) \tag{2.29}$$

to obtain:

$$J = -\frac{2A}{3\beta}\exp\left(-\beta\chi^{3/2}\right)\int_0^{\mu}\exp\left(-\frac{3\beta}{2}\chi^{1/2}(\mu - W)\right)\left(\frac{\mu W^{-1/2}}{2} - \frac{3W^{1/2}}{2}\right)\mathrm{d}W \tag{2.30}$$

Finally, this can be solved to give:

$$J \approx \frac{q}{2\pi h}\left(\frac{\mu^{1/2}}{(\chi+\mu)\chi^{1/2}}\right)(E)^2\exp\left(-\frac{4\kappa\chi^{3/2}}{3\mathrm{E}}\right) \tag{2.31}$$

This is commonly expressed as [22]:

$$J = \frac{q^3}{8\pi h\phi_{bn}}\mathrm{E}^2\exp\left[-\frac{8\pi\sqrt{2m^*}\phi_{bn}^{3/2}}{3\mathrm{E}qh}\right] \tag{2.32}$$

where ϕ_{bn} is the electron barrier height, E is the electric field at the contact, and m^* is the effective mass of the electron.

As mentioned, Fowler-Nordheim tunnelling has been widely used to analyse the current-voltage characteristics of unipolar single-layer OLEDs by fitting an analytical expression to experimental data. However, such fitting has yielded many problems including the fact that the fitted J-V characteristics typically only fit

the data over a very limited range, and the fitted barrier height increases with temperature e.g. [10]. There are several other criticisms levelled at the use of Fowler-Nordheim tunnelling in OLEDs, including the fact that it assumes a triangular barrier, it neglects temperature, and it assumes the existence of a continuum of unbound states for the carriers to tunnel into [20].

2.2.3 Ohmic contacts

An Ohmic metal-semiconductor contact is defined as one which has negligible resistance compared to the resistance of the bulk semiconductor to which the contact is applied [24]; there are several methods available for fabricating Ohmic contacts. Ohmic contacts are desirable for OLEDs as they mean the device will have a lower operating voltage and greater power efficiency.

If the bulk semiconductor is heavily doped, then the large band bending at the interface results in a very thin barrier which is easily tunnelled through, and high current densities result for relatively low voltage drops, and the current-voltage characteristic can be taken to be linear [1]. However, organic semiconductors cannot be easily or reproducibly doped and so this approach is not available as a means of achieving low resistance contacts. Instead, judicious choice of contact materials must be made in order to try and have the workfunctions of the cathode and anode close to the LUMO and HOMO levels respectively. For example, the workfunction of the default anode material, ITO, can vary upon preparation e.g. [25] and usually the higher the workfunction, the better. More recently, a heavily doped conducting polymer, PEDOT, has been used as an anode material [20]. PEDOT has a metallic nature, owing to the very high doping levels, and has a well known workfunction, which is very high and close to, or even above, the HOMO level of many materials. Hence using PEDOT as an anode means that the barrier to injection is very small or even non-existent.

The specific contact resistance, R_C, is an important figure of merit when considering ohmic contacts [1]. It is defined as the reciprocal of the derivative of the current with respect to voltage, evaluated at zero bias:

$$R_C = \left(\frac{\partial J}{\partial V}\right)^{-1}_{V=0} \tag{2.33}$$

For metal-semiconductor contacts with low to moderate doping, thermionic emission can be assumed to be the dominant current transport mechanism. Hence calculating the value of R_C by applying equation 2.33 to equation 2.12 yields:

$$R_C = \frac{k_B}{qA^*T} \exp\left(\frac{q\phi_{bn}}{k_B T}\right) \tag{2.34}$$

It can clearly be seen, then, that in order to minimise the contact resistance, R_C, the barrier height ϕ_{bn} must be kept as small as possible

In the case of the injection current being due to tunnelling, it can be shown that [1]:

$$R_C = \exp\left[\frac{2\sqrt{\epsilon_s m^*}}{\hbar}\left(\frac{\phi_{bn}}{\sqrt{N_D}}\right)\right] \tag{2.35}$$

This shows that the specific contact resistance depends strongly on doping, as is expected, and varies exponentially with the factor $\phi_{bn}/\sqrt{N_D}$. Hence for a fixed doping level, as is the case for OLEDs, the barrier again must be minimised in order to reduce the contact resistance. Alternatively, for a fixed barrier height, the doping must be increased; this is the approach taken in inorganic semiconductor devices, since doping is easily controlled and the barrier height is often independent of the contact metal.

2.3 Metal-semiconductor-metal device structures

Single layer organic LEDs have a simple metal-semiconductor-metal structure, and generally the workfunctions of the two metal contacts, ϕ_{m1} and ϕ_{m2}, and the semiconductor, ϕ_s, are all different. Assuming the semiconductor is fully depleted, then there will be a potential difference V_{bi} across the device, given by [2]:

$$V_{bi} = \frac{1}{q}[(\phi_{m2} - \chi) - (\phi_{m1} - \chi)] \tag{2.36}$$

$$= \frac{1}{q}(\phi_{m2} - \phi_{m1}) \tag{2.37}$$

Hence there is a corresponding built-in field in the device, E_{bi}, which is given by:

$$E_{bi} = -\frac{dV_{bi}}{dx} = -\frac{V_{bi}}{d} \tag{2.38}$$

where d is the film thickness. In a typical device, $d \sim$100nm, and the difference between the two workfunctions may be as much as 1.5eV, resulting in a built-in field of $1.5 \times 10^7 \mathrm{Vm}^{-1}$.

However, there is no guarantee that this is an accurate measure of V_{bi}, nor that the field is uniform across the device. Interfacial dipole layers and surface states may act to affect the metal workfunctions and hence V_{bi} [26]. The built-in potential can be obtained experimentally by techniques such as electroabsorption (EA) spectroscopy [27], or photovoltaic nulling [28].

This built-in field must be overcome before carrier injection can occur (Figure 2.7). Hence in the analysis of device data, care must be taken to ensure that the built-in field is removed from the applied field in order to obtain the correct internal field acting on the charge carriers.

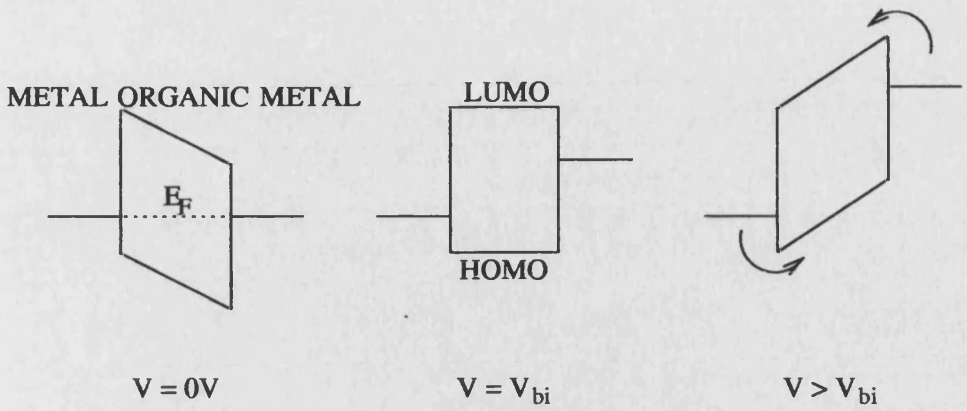

Figure 2.7: Schematic illustration of a single-layer OLED at 0V (left), V_{app}=V_{bi} (middle), and $V_{app} > V_{bi}$ (right). At 0V, the built-in potential exists and injection is impossible. When V_{app}=V_{bi}, the built-in potential is compensated for and the flat-band condition is reached. When $V_{app} > V_{bi}$, injection occurs (indicated by arrows) and device operates.

2.3.1 M-S-M device operation

Transport in metal-semiconductor-metal structures has been analysed in detail for inorganic semiconductors [29]; the case involving organic semiconductors is greatly simplified by the assumption that the device is fully depleted at zero bias, and that the bands are therefore rigid.

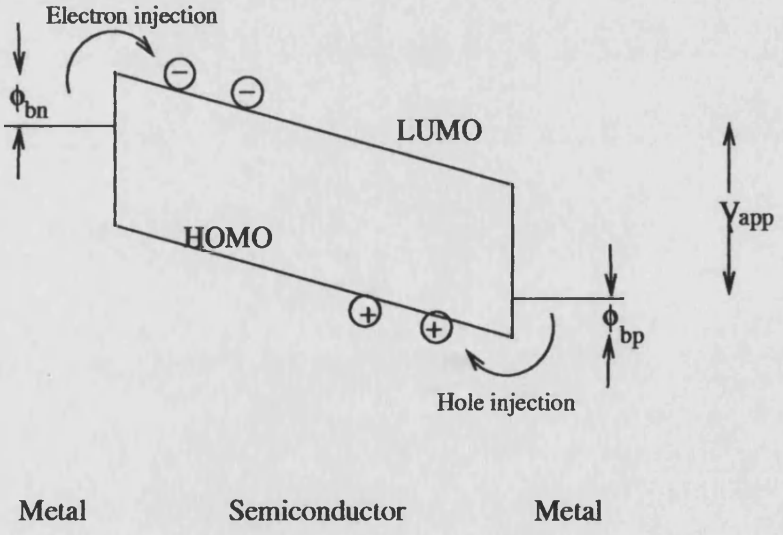

Figure 2.8: Band profile of a single layer OLED under an applied forward bias, V_{app}.

As can be seen in Figure 2.8, once a bias greater than V_{bi} is applied to the device, one Schottky contact becomes reverse biased, and the other forward biased. However, since the semiconductor is depleted, the current at the forward biased junction is not the high electron or hole current that might be expected, since

there are no intrinsic electrons or holes. Instead, the current at the forward biased junction is actually due to the carriers injected from the reverse biased contact. Consequently, the total current flowing through the device under large forward bias conditions is actually the sum of the thermionic emission reverse saturation currents (equation 2.10) of the electrons and holes at their respective injecting electrodes [30]:

$$J_{tot} = A_n^* T^2 \exp\left(\frac{-q\phi_{bn}}{k_B T}\right) + A_p^* T^2 \exp\left(\frac{-q\phi_{bp}}{k_B T}\right) \tag{2.39}$$

where A_n^* and A_p^* are the effective Richardson constants for electrons and holes respectively.

If a voltage is applied between the two electrodes, and electrode 1 (which is reverse biased) can supply an electron density n_0 to the semiconductor by thermionic emission from the metal, then the current which would flow out of the opposite electrode (assuming there is no recombination or generation of carriers) is:

$$J = qn_0\mu_n \mathrm{E} = qn_0\mu_n \frac{V}{d} \tag{2.40}$$

where q is the electronic charge, μ_n is the electron mobility, E is the electric field, V is the applied bias, and d is the device thickness.

Equation 2.40 obeys Ohm's law, with the current being proportional to the applied voltage, provided that there is no band bending so the field is constant across the device, the field-dependence of the mobility is neglected, and that the current J is not greater than the saturated reverse bias thermionic emission current. Once J is equal to the saturated reverse bias thermionic emission current, further increasing the applied bias does not result in an increased current since the contact cannot supply more carriers. Hence the contact ceases to be ohmic and the current is now contact limited. A similar situation applies to the hole current. In practice, however, the current does increase further with increasing applied bias due to barrier lowering, field-dependent mobilities, and with the onset of tunnelling current at high biases if the barrier is low enough.

2.4 Space-charge-limited current flow

The second limiting regime of OLED operation is that of space-charge limited current (SCLC), whereby the carriers in the bulk, rather than the contacts as described in the previous section, limit the maximum current flowing through the device. SCLC flow occurs when an electrode (normally an Ohmic contact) can supply an unlimited number of carriers into the bulk, causing a build-up of space charge in the device, which eventually acts to limit further carrier injection. Unipolar trap-free space-charge-limited current flow is a widely-used concept in the analysis of the current-voltage characteristics of single-layer devices, and is a useful method for determining the carrier mobility in a sample, particularly if other methods such as time-of-flight measurements fail e.g. [31][32]. However, many authors merely make the assumption that the injecting contact is indeed Ohmic without verification, leading to an erroneous evaluation of the majority carrier's mobility and field dependence. If both contacts are Ohmic, then a bi-polar SCL current may flow (section 2.4.3).

2.4.1 Unipolar SCLC

In order to develop an analytical expression for the single-carrier space-charge limited current into an insulator (with no traps and a negligible intrinsic carrier density), several simplifying assumptions are required (see [33] for more details). Firstly, one contact is assumed to be perfectly Ohmic for either electron or hole injection; the other acts as an efficient sink for the injected charge. Secondly, the electric field is assumed to be large enough such that the diffusion component of the carrier current can be neglected, leaving only the drift current component. Thirdly, the intrinsic charge density is assumed to be negligible, and the carrier mobilities are assumed to be field-independent. Finally, the electric field at the ohmic contact is taken to be zero.

If the insulator, of thickness d, has holes injected into it from the ohmic contact, then Poisson's equation becomes:

$$\frac{\mathrm{dE}}{\mathrm{d}x} = \frac{q}{\epsilon_0 \epsilon_s}(p(x)) \tag{2.41}$$

where $p(x)$ is the density of holes in the bulk, given by Boltzmann statistics, E is the electric field, and ϵ_S is the dielectric constant of the semiconductor. The hole drift current in the bulk is given by:

$$J = q\mu_p p(x)\,\mathrm{E}(x) \tag{2.42}$$

Substituting equation 2.42 into 2.41 yields:

$$\mathrm{E}\left(\frac{\mathrm{dE}}{\mathrm{d}x}\right) = \frac{J}{\mu_p \epsilon_0 \epsilon_s} \tag{2.43}$$

which can be integrated to give:

$$\mathrm{E}(x) = \left(\frac{2Jx}{\mu_p \epsilon_0 \epsilon_s}\right)^{1/2} \tag{2.44}$$

where the boundary condition E(0)=0 has been applied. Using the relation that E=$-$dV/dx:

$$V = \sqrt{\frac{2J}{\mu_p \epsilon_s \epsilon_0}} \int_0^d x^{1/2} \mathrm{d}x \tag{2.45}$$

Hence:

$$J = \frac{9}{8}\epsilon_0 \epsilon_s \mu_p \frac{V^2}{d^3} \tag{2.46}$$

This is the well-known Mott and Gurney equation, also known as the square law for trap-free SCLC [33].

Although one of the assumptions made in this formalism was that the density of intrinsic thermally generated carriers is negligible, in practice there will be some intrinsic carriers present in the device (p_0 for intrinsic holes). If these intrinsic

carriers dominate over the small number of injected carriers at low biases, then the current-voltage characteristics may be Ohmic due to the drift current of the intrinsic holes, p_0. If this is the case, then there exists a transition from the Ohmic regime to the onset of SCLC due to injected carriers at the applied voltage V_ω:

$$V_\omega = \frac{8}{9}\frac{qp_0d^2}{\epsilon_s\epsilon_0} \tag{2.47}$$

Another of the major assumptions made in obtaining an analytic expression for the space-charge limited current in an insulator was that the mobilities are field-independent, yet almost all organic semiconductors are characterised by field-dependent mobilities of the form:

$$\mu\,(\mathrm{E}) = \mu_0 \exp\left(\sqrt{\frac{\mathrm{E}}{\mathrm{E}_0}}\right) \tag{2.48}$$

where μ_0 is the zero-field carrier mobility, E is the electric field magnitude, and E_0 is a factor determining the field-dependence of the carrier mobility. Hence an expression incorporating such field-dependent mobilities is necessary when attempting to fit SCLC curves to experimental data. Such an expression has been calculated by [34]:

$$J_{SCLC} \approx \frac{9}{8}\epsilon_0\epsilon_s\mu_0\frac{V^2}{d^3}\exp\left(0.89\sqrt{\frac{V}{d\mathrm{E}_0}}\right) \tag{2.49}$$

2.4.2 Unipolar SCLC with traps

The presence of traps in a semiconductor has a significant effect on the space-charge limited current-voltage characteristics discussed in section 2.4.1. It is simplest to analyse the effect of a single discrete trap level on SCLC, but multiple trap levels and other distributions can also be analysed [33]. Two possible cases are considered here, for shallow and deep level traps.

In the case of shallow traps, the J-V curve has 3 separate regions (Figure 2.9).

The traps can be considered as being empty at thermal equilibrium, and the J-V curve is initially Ohmic, as in the trap-free case (section 2.4.1). Once significant amounts of charge are injected, then as in the trap-free case there is a transition from the Ohmic regime when the applied bias reaches V'_ω:

$$V'_\omega = \frac{8}{9}\frac{qp_0d^2}{\Theta\epsilon} \tag{2.50}$$

$$\Theta = \frac{p}{(p+p_t)} \tag{2.51}$$

where p_0 is the intrinsic hole density, d is the sample thickness, ϵ is the relative permittivity of the semiconductor, and Θ represents the ratio of free to trapped charge, where p_t is the density of trapped holes. V'_ω is larger than V_ω due to the reduced amount of free charge.

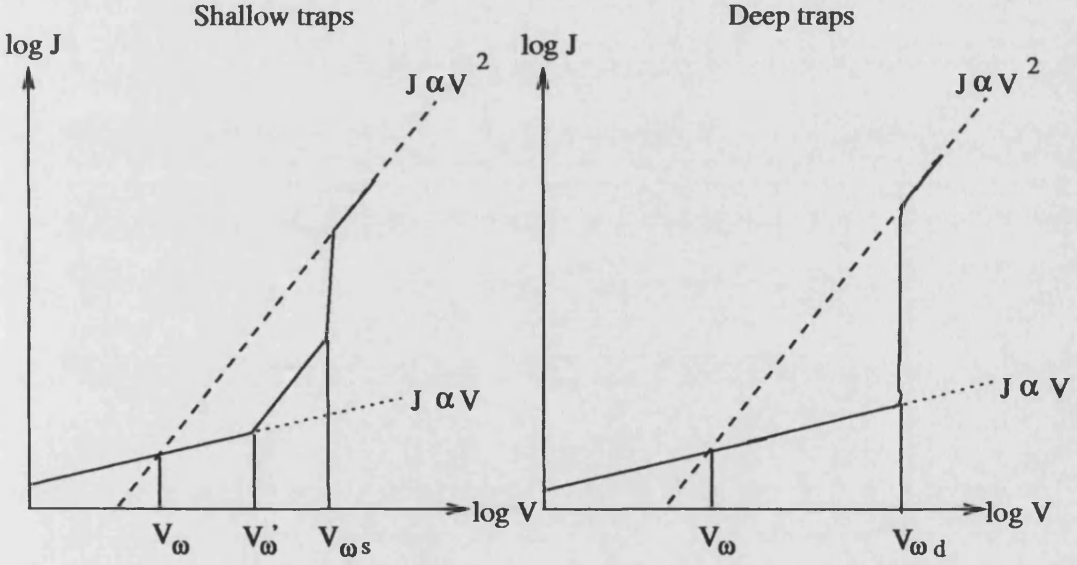

Figure 2.9: Illustration of the current-voltage characteristics for SCLC with shallow (left hand side) and deep (right hand side) traps.

At the transition point V'_ω, the current switches from Ohmic to the so-called shallow trap square law (STSL):

$$J_{STSL} = \frac{9}{8}\Theta\epsilon\mu_p\frac{V^2}{d^3} \tag{2.52}$$

As the bias is further increased, the quasi-Fermi level shifts (upwards in the case

of electrons, downwards in the case of holes), and as it reaches the trap energy level, the traps fill, a situation is reached whereby all traps are filled; the bias at which this occurs is the trap-filled limit ($V_{\omega s}$). Above this bias, all of the extra injected charge is free to carry current, and the current tends to the SCLC limit (equation 2.46) as the ratio of free to trapped charge becomes very large.

In the case of deep trap levels, the current-voltage characteristic has just two regions. Since the quasi-Fermi level is already close to or above the trap-level (for an electron trap) or below the trap level (for a hole trap), all injected carriers will be trapped until the traps are full. In this case the J-V curve will be Ohmic until the the trap-filled limit is reached at $V_{\omega d}$. Above this bias, all further injected carriers are free, and the J-V characteristic tends to the trap-free SCL situation ($J \propto V^2$). The modified J-V characteristics for SCLC with shallow and deep discrete trap levels are illustrated in Figure 2.9

In reality, traps are more likely to be distributed in energy rather than existing at discrete levels. If this is the case, then the traps will be filled from the bottom to the top of the distribution (for electron traps), or from the top to the bottom (for hole traps) with increasing applied bias, due to the quasi-Fermi level shifting upwards (downwards) for electrons (holes) as the field increases. Hence as the field increases, the ratio of free to trapped charge, Θ, increases as the traps are filled and more injected carriers remain as free carriers; the J-V characteristics become steeper before becoming quadratic, provided that the number of traps is less than the number of injected carriers. When trap states are distributed in energy, the J-V curves tend to follow $J \propto V^n$, where $n \geq 2$ [33].

Analytic expressions for trap-limited current with exponential or Gaussian distributions of traps have also been formulated [33], and although such distributions may well be more appropriate for disordered organic semiconductors e.g. [4][10], such expressions are difficult to fit to experimental J-V characteristics in order to obtain any information about the traps present in a particular device [35]. Furthermore, only discrete levels are included in the device model presented in section 2.5 owing to a lack of any firm evidence for any particular distribution.

2.4.3 Double carrier injection space-charge-limited current

In the situation of double carrier injection, even assuming Ohmic contacts, the formation of analytical expressions for the current flow is very complex due to the addition of the processes of electron-hole pair recombination and space-charge neutralisation, and other factors such as intragap states acting as recombination centres as well as the trap states which exist in the unipolar case [7] [33].

In the trap-free case (with no trapped charge or recombination centres), an expression for bi-polar space-charge limited current is given by [36]:

$$J = \frac{9}{8}\epsilon\mu_{eff}\frac{V^2}{d^3} \tag{2.53}$$

which is the analytic expression for unipolar SCLC but with the unipolar carrier mobility replaced by an effective mobility, μ_{eff}, which is a function of the electron and hole mobilities and the recombination rate:

$$\mu_{eff} = \frac{2}{3}\left[\frac{4\pi q\mu_n\mu_p\left(\mu_n+\mu_p\right)}{\epsilon < v\sigma_R >}\right]^{\frac{1}{2}} \tag{2.54}$$

where q is the electronic charge, μ_n is the electron mobility, μ_p is the hole mobility, ϵ is the relative permittivity of the semiconductor, v is the velocity of the carriers, and σ_R is the recombination cross-section.

Scott et al [37][38] extended the Parmenter-Ruppel approach (equation 2.53) by including Langevin recombination (section 2.5), but ignoring trapping, and more crucially, the field dependence of the mobilities. The Parmenter-Ruppel approach is therefore of little aid to analysing OLED current-voltage characteristics, since it is very unlikely that both contacts will be Ohmic, neither of the mobilities will known, and a value for σ_R must be established.

2.5 Drift-diffusion model

Although the current-voltage characteristics of unipolar OLEDs can be analysed as either injection limited or space-charge limited, such an approach clearly has its limitations. The main problems with applying analytical expressions to experimental data is that frequently an initial decision must be made as to whether the current is injection or space-charge limited, and that the fitted data often follows the experimental data only over a limited voltage range. Even if such expressions can be correctly fitted to experimental J-V data, they are still very limited in what they can actually achieve. For example, such expressions cannot predict potentially valuable information such as the recombination profile or quantum efficiency. As device technology improves, there is a tendency to use either multi-layer devices e.g. [39][40], or to modify electrodes e.g. [41] in an attempt to improve efficiency. Analytical expressions cannot cope with multi-layer devices, nor with the bi-polar currents in devices with enhanced injection. Therefore the only real use of such expressions is to analyse current-voltage characteristics of single-layer unipolar devices in order to try and investigate the nature of different contacts, and to obtain values for the mobilities and field-dependence of the mobilities for different materials.

In order to be able to fully investigate, and potentially predict device behaviour for a multitude of architectures and materials, comprehensive numerical models are required; for a review of OLED modelling see [42]. The drift-diffusion model describes the behaviour of excess injected charge carriers under the influence of an external electric field which causes them to deviate from thermal-equilibrium conditions [8]. The model consists of six equations, which can be split into three groups; the drift-diffusion equations themselves, representing the current density, Poisson's equation, relating the charge in the device to the electric field and electrostatic potential, and the continuity equations which relate spatial variations in current density with carrier recombination and generation. The one-dimensional form of these equations have been used, owing to the simple geometry of OLEDs.

In addition to these basic equations, the incorporation of traps into the model is dealt with in subsection 2.5.4 , and the issue of modelling multi-layer devices and the problems arising at the heterojunctions between layers are described in subsection 2.5.5.

These equations must be solved along with the appropriate boundary conditions, which represent the metal-semiconductor (Schottky) contacts; these are discussed in section 2.5.6. The overall set of equations, and boundary conditions, representing a particular device, are solved self-consistently using a finite-difference differential-equation solver routine called SOLVDE, which is taken from Numerical Recipes in Fortran [43]; details of the implementation of SOLVDE for the drift-diffusion model are contained in [5].

2.5.1 Drift-diffusion equations

$$J_n = q\mu_n n\mathrm{E} + qD_n\frac{\mathrm{d}n}{\mathrm{d}x} \tag{2.55}$$

$$J_p = q\mu_p p\mathrm{E} - qD_p\frac{\mathrm{d}p}{\mathrm{d}x} \tag{2.56}$$

J_n and J_p are the one-dimensional electron and hole current densities respectively [1], where q is the electronic charge, μ_n and μ_p are the electron and hole mobilities respectively, n and p are the electron and hole concentrations, E is the electric field, and D_n and D_p are the electron and hole diffusion coefficients. In non-degenerate semiconductors (i.e. assuming Boltzmann statistics), as is the case here, the diffusion coefficients are related to the mobilities via the Einstein relationship:

$$D_n = \left(\frac{k_B T}{q}\right)\mu_n \tag{2.57}$$

$$D_p = \left(\frac{k_B T}{q}\right)\mu_p \tag{2.58}$$

where k_B is the Boltzmann constant, and T is the temperature.

These current densities consist of a drift term (the first term on the right hand side of equations 2.55 and 2.56), caused by carriers moving under the influence of an

applied electric field, and a diffusion term (the second term on the right hand side of equations 2.55 and 2.56), due to the diffusion of carriers along a concentration gradient; these expressions can be fully derived from the Boltzmann transport equation [44]. However, the diffusion current in organic LEDs is assumed to be negligible by many authors [2] especially at typical operating biases. and the diffusion term is often omitted from some numerical models e.g. [45]. It has also been suggested that the Einstein relation described in equations 2.57 and 2.58 does not apply for organic semiconductors where the mobilities are strongly field dependent [2]; this possible inaccuracy is not critical due to the domination of the drift term at all biases of interest.

Substituting equations 2.57 and 2.58 into 2.55 and 2.56 respectively yields:

$$J_n = q\mu_n \left(n\mathrm{E} + \frac{k_B T}{q} \frac{\mathrm{d}n}{\mathrm{d}x} \right) \tag{2.59}$$

$$J_p = q\mu_p \left(p\mathrm{E} - \frac{k_B T}{q} \frac{\mathrm{d}p}{\mathrm{d}x} \right) \tag{2.60}$$

The electron and hole concentrations away from thermal equilibrium can be established by using Boltzmann statistics and quasi-Fermi levels [1]:

$$n = N_C \exp\left(\frac{-q\phi_n + q\psi + \chi_c}{k_B T} \right) \tag{2.61}$$

$$p = N_V \exp\left(\frac{q\phi_p - q\psi - \chi_c - E_g}{k_B T} \right) \tag{2.62}$$

where N_C and N_V are the conduction band and valence band density of states, χ_c is the electron affinity of the semiconductor, E_g is the energy gap of the semiconductor, and ϕ_n and ϕ_p are the electron and hole quasi-Fermi potentials within the device, related to the electron and hole quasi-Fermi levels respectively by $E_{fn} = -q\phi_n$ and $E_{fp} = -q\phi_p$.

If equations 2.61 and 2.62 are substituted into equations 2.59 and 2.60 respec-

tively, along with the relation $\mathrm{E} = -\nabla\psi$, more compact forms for the drift-diffusion equations can be obtained, which are more stable for numerical simulations [44]:

$$J_n = -qn\mu_n \frac{\mathrm{d}\phi_n}{\mathrm{d}x} \tag{2.63}$$

$$J_p = -qp\mu_p \frac{\mathrm{d}\phi_p}{\mathrm{d}x} \tag{2.64}$$

One final correction which must be made to these drift-diffusion equations, and which is exclusive to disordered organic semiconductors, is the inclusion of field-dependent carrier mobilities as mentioned in Chapter 1, where:

$$\mu(\mathrm{E}) = \mu_0 \exp\left(\sqrt{\frac{\mathrm{E}}{\mathrm{E}_0}}\right) \tag{2.65}$$

where μ_0 is the zero-field mobility at constant T, E is the electric field, and E_0 is the field-dependence of the mobility at a constant temperature.

2.5.2 Continuity equations

$$\frac{\partial n}{\partial t} = \frac{1}{q}\nabla \cdot \mathbf{J_n} + G - R \tag{2.66}$$

$$\frac{\partial p}{\partial t} = -\frac{1}{q}\nabla \cdot \mathbf{J_p} + G - R \tag{2.67}$$

Equations 2.66 and 2.67 are the continuity equations for electrons and holes respectively, where R and G are the electron-hole pair recombination and generation rates respectively [1]. Since the model is time-independent and one-dimensional, and by neglecting the generation term due to the large bandgap [2], equations 2.66 and 2.67 can be re-written as:

$$\frac{\mathrm{d}J_n}{\mathrm{d}x} = qR \tag{2.68}$$

$$\frac{\mathrm{d}J_p}{\mathrm{d}x} = -qR \tag{2.69}$$

In the case of organic semiconductors, the recombination term is taken to be an optical recombination term, R_{opt}. This optical recombination process is bimolecular:

$$R_{opt} = \gamma\,(np) \tag{2.70}$$

where γ is a Langevin recombination coefficient:

$$\gamma = \frac{4\pi q \mu_m}{\epsilon_0 \epsilon_s} \tag{2.71}$$

where μ_m is the larger of the electron and hole mobilities. Although this Langevin optical recombination process is widely cited and used in all device models e.g. [15], more recently an alternative electron-hole capture mechanism which is more accurate at high fields has been suggested [46].

In the case of inorganic semiconductors, the recombination of an electron-hole pair results in the emission of a photon with the energy of the bandgap. However, the recombination of an electron and hole in an organic semiconductor results in the formation of an exciton. The physics of excitons is complex [7] and omitted from the device model, but an essential concept is that excitons are formed as either singlet or triplet excitons; such excitons are formed in the ratio 1:3 according to spin statistics, and this accordingly has important consequences in terms of the potential maximum quantum efficiency of OLEDs. There has recently been some evidence, however, suggesting that singlets may be in fact formed in greater numbers in conjugated polymers [47].

2.5.3 Poisson's equation

Carrier transport in semiconductor devices must obey Maxwell's equations [1][44]; the most important is Poisson's equation:

$$\nabla \cdot \mathbf{D} = \rho \tag{2.72}$$

where **D** is the displacement field, and ρ is the electric charge density. The electric field displacement, D, is continuous at interfaces [44][48]. The electric field, E is related to the displacement field as:

$$\mathbf{D} = \epsilon_0 \epsilon_s \cdot \mathrm{E} \tag{2.73}$$

where ϵ_0 is the permittivity of a vacuum, and ϵ_s is the dielectric constant the semiconductor. The charge density, ρ, is given by:

$$\rho = q\left(p - n + N_D^+ - N_A^-\right) \tag{2.74}$$

where n is the electron density, p is the hole density, N_D^+ is the ionised dopant donor density, and N_A^- is the ionised dopant acceptor density.

Hence Poisson's equation can be expressed as:

$$\frac{\mathrm{dE}}{\mathrm{d}x} = -\frac{\mathrm{d}^2\psi}{\mathrm{d}x^2} = \frac{q}{\epsilon_0 \epsilon_s}\left(p - n + N_D^+ - N_A^-\right) \tag{2.75}$$

where E$= -\mathrm{d}\psi/\mathrm{d}x$.

2.5.4 Carrier trapping

Deep levels within the bandgap, depending on their location, can act as recombination centres, electron traps, or hole traps. An electron trap has a high probability of capturing an electron, then releasing it after a certain amount of time. Similarly, a hole trap has a high probability of capturing a hole and then releasing it after some time. A recombination centre has very similar probabilities of both electron and hole capture [33]. Recombination occurs when an electron is captured, swiftly followed by the capture of a hole, which results in the elimination of an electron-hole pair via a non-radiative process. It can be shown that an energy level at mid-gap is the most effective recombination centre, whilst the level of an electron trap will be near to the conduction band edge, and a hole trap will be nearer to the valence band edge [24].

Only discrete trap levels are included in the model. Using Fermi-Dirac statistics, the probability of a trap centre at energy level E_t being occupied, $f(E_t)$, is given by [24]:

$$f(E_t) = \frac{1}{1 + \exp\left(\frac{E_t - E_f}{k_B T}\right)} \tag{2.76}$$

where E_t is the trap energy level, E_f is the Fermi-level, k_B is the Boltzmann constant, and T is the temperature. Hence in the case of electron and hole traps, the number of trapped carriers in the j^{th} discrete trap level is given by:

$$n_{tj} = \frac{N_{tj}}{1 + (1/g)\exp\left(\frac{E_{tj} - E_{fn}}{k_B T}\right)} \tag{2.77}$$

$$p_{tj} = \frac{P_{tj}}{1 + (1/g)\exp\left(\frac{E_{fp} - E_{tj}}{k_B T}\right)} \tag{2.78}$$

where n_{tj} and p_{tj} are the trapped electrons and hole densities in the j^{th} trap level respectively, N_{tj} and P_{tj} are the total number of electron and hole trap sites in the j^{th} energy level respectively, g is the degeneracy of the traps, E_{tj} is the

energy of the trap level below the conduction band (E_C), and E_{fn} and E_{fp} are the electron and hole quasi-Fermi levels.

In order to implement trapping in the model, both Poisson's equation and the continuity equations must be modified. In the case of Poisson's equation, equation 2.75 must include the trapped charge carriers so that the overall charge density is unaltered. Such trapped charges represent a fixed charge affecting the electric field:

$$\frac{\mathrm{d}D}{\mathrm{d}x} = q\left(p - n + N_D^+ - N_A^- + \left(\sum_{j=1}^{N} p_{tj}\right) - \left(\sum_{j=1}^{N} n_{tj}\right)\right) \tag{2.79}$$

This includes the total numbers of electrons and holes trapped at each energy level.

The electron and hole continuity equations, equations 2.68 and 2.69, have only one recombination term, R_{opt}, in the absence of traps. In the presence of traps, recombination at trap centres must be considered in the continuity equations. The recombination rate is given by:

$$R_{trap} = \frac{np - n_i^2}{\tau_n\left(p + p_1\right) + \tau_p\left(n + n_1\right)} \tag{2.80}$$

where n and p are the electron and hole densities, n_i is the intrinsic carrier density (negligible in organic semiconductors due to their relatively large bandgaps, since $n_i = N_C N_V \exp(-E_g/k_B T)$), n_1 and p_1 are the equilibrium carrier densities that would result when the Fermi level lies at E_t, and τ_n and τ_p are the electron and hole lifetimes.

Hence the recombination rate, R, now has two components, R_{opt} and R_{trap}, and equations 2.68 and 2.69 become:

$$\frac{\mathrm{d}J_n}{\mathrm{d}x} = q\left(R_{opt} + R_{trap}\right) \tag{2.81}$$

$$\frac{\mathrm{d}J_p}{\mathrm{d}x} = -q\left(R_{opt} + R_{trap}\right) \tag{2.82}$$

2.5.5 Heterojunctions

As will be demonstrated in Chapter 4, single layer OLEDs are usually relatively inefficient due to an imbalance in terms of injection and transport of electrons and holes. For this reason, multi-layer devices, particularly those fabricated from small molecule semiconductors, are preferred as they can be engineered to give higher efficiencies, with different layers promoting the transport of electrons or holes. Hence the model should be able to simulate multi-layer devices, and so the issue of carrier transport at interfaces between layers of organic semiconductors (heterojunctions) needs to be properly addressed.

Although the drift-diffusion approach works well for modelling carrier transport in the bulk regions of a semiconductor device, it may cause problems at heterojunctions. The drift and diffusion current terms are related to the gradients of the band edges and the gradient in the carrier densities respectively, but at heterojunctions, these quantities may well be discontinuous. However, the discretised equations will approximate the infinite gradient due to a discontinuity with a high-value derivative, leading to an unphysically high current which, as well as being incorrect, can cause numerical instabilities [49]. The values of the derivatives at the heterojunction will also depend on the number of mesh points used, increasing as the mesh spacing is reduced.

Many inorganic semiconductor device models utilise the so-called diffusion model [44], in which the quasi-Fermi levels across the heterojunctions are assumed to be continuous, whilst ignoring any current transport mechanisms present, an approach initially taken with this model [5]. The implementation of an interface condition in drift-diffusion models, based on thermionic emission of carriers over band offsets at the heterojunction [50] represents an improvement over the diffusion model. This approach has been adapted by numerous authors to include effects such as tunnelling and barrier lowering at the heterojunction [8].

The interface is assumed to be ideal (Figure 2.10) i.e. free of dipoles, sheets of charge or recombination, and as such the electric displacement, D, the electro-

static potential, ψ, and the current densities, J_n and J_p, are continuous across the interface. Additionally, there is no band bending at the interface [51] Only thermionic emission of carriers over heterojunction barriers is considered, with the current at the interface given by [52] (c.f. section 2.2.1):

$$J_n = qn_2 v_{rn2} - qn_1 v_{rn1} \exp\left(\frac{-E_B}{k_B T}\right) \tag{2.83}$$

where $n_{1,2}$ is the electron density in layers 1 and 2 respectively at the interface, $v_{rn1,2}$ is the recombination velocity at the in layers 1 and 2 respectively at the interface, and E_B is the energetic difference between the conduction bands (Figure 2.10). An analogous expression exists for J_p at the interface.

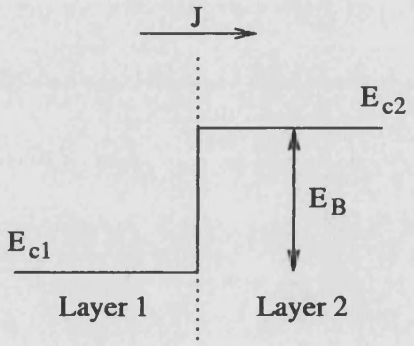

Figure 2.10: Energy diagram of the conduction bands at the heterojunction, with layer 1 on the left and layer 2 on the right.

2.5.6 Schottky contact boundary conditions

The Schottky contacts as described in section 2.1 are implemented within the drift-diffusion model as boundary conditions specifying the carrier currents at $x = 0$ and $x = d$, where d is the device thickness. Each carrier current consists of three components; a thermionic emission current of carriers being injected from the metal into the semiconductor, a backflowing interface recombination current (the time-reversed process of thermionic emission), and an athermal tunnelling current. So for example, the hole current at the left-hand electrode, $x = 0$, is given by:

$$J_p(0) = J_{th} - J_{ir} + J_{tp} \tag{2.84}$$

where J_{th} is the thermionic emission current, J_{ir} is the interface recombination current, and J_{tu} is the tunnelling current. The interface recombination current is caused by carriers on the organic side of the metal/organic interface falling back into the metal. There is an enhanced backflow of carriers in organic semiconductors due to the existence of disorder; carriers must overcome additional energetic barriers after they have been injected [14]. At thermal equilibrium, the thermionic emission and interface recombination currents cancel each other out.

The thermionic emission and interface recombination carrier currents at the interface are implemented using the form previously discussed in section 2.2.1:

$$J_n = qv_{rn}\left(n_0 - n_{eq}\right) \tag{2.85}$$

$$J_p = -qv_{rp}\left(p_0 - p_{eq}\right) \tag{2.86}$$

where p_0 and n_0 are the carrier densities evaluated at the boundaries rather than at x_m.

The recombination velocity, v_r, was calculated by Malliaras and Scott [53] based upon the assumption that the backflowing recombination current is analogous to the Langevin bimolecular recombination rate (section 2.5.2):

$$v_{rn} = \frac{16\pi\epsilon_s\epsilon_0\left(k_BT\right)^2\mu_n(\mathrm{E})}{q^3} \tag{2.87}$$

$$v_{rp} = \frac{16\pi\epsilon_s\epsilon_0\left(k_BT\right)^2\mu_p(\mathrm{E})}{q^3} \tag{2.88}$$

and has been implemented in the model.

The electron and hole tunnelling currents, J_{tn} and J_{tp}, are the Fowler-Nordheim tunnelling currents given in section 2.2.2:

$$J_{tn} = \alpha_1\left(\frac{B}{\phi_{bn}}\right)\mathrm{E}^2\exp\left[-\alpha_2 C\left(\frac{\left(q\phi_{bn}\right)^{3/2}}{\mathrm{E}}\right)\right] \tag{2.89}$$

$$J_{tp} = \alpha_1 \left(\frac{B}{\phi_{bp}}\right) \mathrm{E}^2 \exp\left[-\alpha_2 C \left(\frac{(q\phi_{bp})^{3/2}}{\mathrm{E}}\right)\right] \tag{2.90}$$

where B and C are given by:

$$B = \frac{q^3}{8\pi h} \tag{2.91}$$

$$C = \frac{8\pi\sqrt{2m}}{3hq} \tag{2.92}$$

α_1 and α_2 are fitting parameters added to the original F-N equations for the tunnelling current to allow for its inaccurate field and temperature dependence e.g. [10].

As carriers are injected by a combination of thermionic emission and tunnelling, a quasi-equilibrium carrier density is established by the superposition of the injection and interface recombination currents [15]. The device current is them determined by the drift of these carriers under the influence of the applied electric field.

Finally, the electrostatic potential at the boundary is specified by the condition that:

$$\psi(x = 0) = -\phi_{bn}(x = 0) \tag{2.93}$$

$$\psi(x = d) = -\phi_{bn}(x = d) \tag{2.94}$$

where ϕ_{bn} is the electron barrier height at the interface.

Barrier lowering as described in section 2.1.1 is included in all of the boundary conditions.

2.6 Conclusions

Despite the relatively simple structure of OLEDs, it is very difficult to analyse transport in these devices using simple analytical models, which assume that the current is either injection or bulk limited. Caution must prevail when attempting to fit analytic expressions to experimental current-voltage characteristics; although such expressions may well fit over a certain voltage range, this does not imply validity. Hence such erroneous fitting not only leads to obtaining incorrect material parameters, but also fails to correctly explain device operation or the injection mechanism responsible. Nevertheless, in some circumstances analytical expressions can provide a quick and useful method for analysing J-V characteristics.

Using the drift-diffusion model provides a useful method for understanding device operation. Such numerical device models provide a number of advantages over analytic expressions. Firstly, they can account for factors such as field dependent mobilities, Langevin optical recombination and internal interfaces in multi-layer devices. They can also provide better insight into the operation of a given device as they do not assume a specific type of contact or operating regime, and hence are more likely not to obscure the underlying physics. As well as the J-V characteristics of a particular device, numerical models can also provide a wealth of extra information such as carrier density and electric field profiles, which can be immensely useful not only in the understanding of device characteristics, but can also aid device design.

The drift-diffusion model which has been presented in this chapter is known to be very flexible, numerically quite stable, and a fast method for modelling OLEDs [5], and hence is a very useful tool for investigating the nature of injection and transport in OLEDs. In the following Chapters, 3 and 4, results from simulating both single and multi-layer devices are presented in order to demonstrate the validity, limits and potential value of such a model.

References

[1] S M Sze, *Physics of Semiconductor Devices*, 2^{nd} ed., J. Wiley and Sons, New York (1981).

[2] I H Campbell and D L Smith, *Solid State Physics*, **55**, 1 (2001).

[3] I D Parker, *J. Appl. Phys.*, **75**, 1656 (1994).

[4] P W M Blom, M J M de Jong, and J M Vleggaar, *Appl. Phys. Lett.*, **68**, 3308 (1996).

[5] C D J Blades, *Ph.D. Thesis*, University of Bath (2000).

[6] H K Hensich, *Semiconductor Contacts*, Clarendon Press, Oxford (1989).

[7] K C Kao, and W Hwang, *Electrical Transport In Solids: with particular reference to organic semiconductors*, Pergamon Press, Oxford (1981).

[8] D Schroeder, *Modelling of Interface Carrier Transport for Device Simulation*, Springer-Verlag, Vienna (1994).

[9] W R Salaneck, S Stafström, and J-L Brédas, *Conjugated Polymer Surfaces and Interfaces*, Cambridge University Press, Cambridge (1996).

[10] A J Campbell, D D C Bradley, and D G Lidzey, *J. Appl. Phys.*, **82**, 6326 (1997).

[11] N Tessler, Lecture notes available from http://www.ee.technion.ac.il/people/nir/Lectures.html (2002).

[12] C R Crowell and S M Sze, *Solid State Electronics*, **9**, 1035 (1966).

[13] S C Choo, *Solid State Electronics*, **38**, 2085 (1994).

[14] W Brütting, S Berleb, and A G Mückl, *Organic Electronics*, **2**, 1 (2001).

[15] P S Davids, I H Campbell, and D L Smith, *J. Appl. Phys.* , **82**, 6319 (1997).

[16] G G Malliaras and J C Scott, *J. Appl. Phys.*, **85**, 7426 (1999).

[17] A J Campbell, D D C Bradley, J Laubender, and M Sokolowski, *J. Appl. Phys.*, **86**, 5004 (1999).

[18] T Aernouts, W Geens, J Poortmans, J Nijs, and R Mertens, *Synthetic Metals*, **122**, 153 (2001).

[19] R H Fowler and L Nordheim, *Proc. Roy. Soc. London A*, **119**, 173 (1928).

[20] G Hadziioannou and P F van Hutten (eds.), *Semiconducting Polymers: Chemistry, Physics and Engineering*, Wiley-VCH, Weinheim (2000).

[21] M Koehler and I A Hümmelgen, *Appl. Phys. Lett.*, **70**, 3254 (1997).

[22] J G Simmons, *Phys. Rev. Lett.*, **15**, 967 (1965).

[23] A B Walker, *Private communication.*

[24] M S Tyagi, *Introduction to Semiconductor Materials and Devices*, J. Wiley and Sons, New York (1991).

[25] J C Scott, G G Malliaras, W D Chen, J-C Breach, J R Salem, P J Brock, S B Sachs, and C E D Chidsey, *Appl. Phys. Lett.*, **74**, 1510 (1999).

[26] J C Scott, P J Brock, J R Salem, S Ramos, G G Malliaras, S A Carter, and L Bozano, *Synth. Met.*, **111-112**, 289 (2000).

[27] T M Brown, J S Kim, R H Friend, F Cacialli, R Daik, and W J Feast, *Appl. Phys. Lett.*, **75**, 1679 (1999).

[28] G G Malliaras, J R Salem, P J Brock, and J C Scott, *J. Appl. Phys.*, **84**, 1583 (1998).

[29] S M Sze, D J Coleman, and A Loya, *Solid State Electronics*, **14**, 1209 (1971).

[30] J Singh, *Optoelectronics: An Introduction To Materials and Devices*, McGraw-Hill, Singapore (1996).

[31] P W M Blom, H C F Martens, and J N Huiberts, *Synthetic Metals*, **121**, 1621 (2001).

[32] L Bozano, S A Carter, J C Scott, G G Malliaras, and P J Brock, *Appl. Phys. Lett.*, **74**, 1132 (1999).

[33] M A Lampert and P Mark, *Current Injection In Solids*, Academic Press, London (1970).

[34] P N Murgatroyd, *J. Phys. D: Appl. Phys.*, **3**, 151 (1970).

[35] A J Campbell, *Private communication.*

[36] R H Parmenter and W Ruppel, *J. Appl. Phys.*, **30**, 1548 (1959).

[37] J C Scott, S Karg, and S A Carter, *J. Appl. Phys.*, **82**, 1454 (1997).

[38] G G Malliaras and J C Scott, *J. Appl. Phys.*, **83**, 5399 (1998).

[39] C Hochfilzer, G Leising, Y Gao, E Forsythe, and C W Tang, *Appl. Phys. Lett.*, **73**, 2254 (1998).

[40] D D Gebler, Y Z Wang, J W Blatchford, S W Jessen, D K Fu, T M Swager, A G MacDiarmid, and A J Epstein, *Appl. Phys. Lett.*, **70**, 1644 (1997).

[41] M G Mason, C W Tang, L S Hung, P Raychaudhuri, J Madathil, L Yan, Q T Le, Y Gao, S T Lee, L S Liao, L F Cheng, W R Salaneck, D A dos Santos, and J L Brédas, *J. Appl. Phys.*, **89**, 2756 (2001).

[42] A B Walker, A Kambili, and S J Martin, *J. Phys.: Condens. Matt.*, **14**, 9825 (2002).

[43] W H Press, B P Flannery, S A Teulolsky, and W T Vertterling, *Numerical Recipes in Fortran*, Cambridge University Press, Cambridge (1989).

[44] C M Snowden, *Semiconductor Device Modelling*, Peregrinus, London (1988).

[45] J M Lupton and I D W Samuel, *J. Phys. D.:Appl. Phys.*, **32**, 2973 (1999).

[46] J A Barker, C L Foden, and N C Greenham, *European Conf. On Molecular Electronics*, Presented paper available from www.cdtltd.co.uk (2002).

[47] P Lane, *Physics World*, **15**, 22 (2002).

[48] M N O Sadiku, *Elements of Electromagnetics*, second edition, Oxford University Press, Oxford (1995).

[49] M A Webster, *Unpublished data.*

[50] C M Wu, and E S Yang, *Solid State Electronics*, **22**, 241 (1979).

[51] M T Bernius, M Inbasekaran, J O'Brien, and W Wu, *Advanced Materials*, **12**, 1737 (2000).

[52] K Horio and H Yanai, *IEEE Trans. Electron Devices*, **37**, 1093 (1990).

[53] J C Scott and G G Malliaras, *Chem. Phys. Lett.*, **299**, 115 (1999).

Chapter 3

Single Layer Device Simulation

The operation of single layer OLEDs is relatively simple to understand using the rigid band model previously discussed; their current-voltage (J-V) characteristics are usually simple to interpret, aided by the fact that most single layer devices can be regarded as being unipolar. The J-V characteristics of such devices can be simulated using the drift-diffusion model discussed in Chapter 2, and then by the fitting of the parameters used in the simulation, more information relating to injection and transport in a given device can often be obtained. Despite several drift-diffusion models having been proposed e.g. [1][2][3][4], only a relatively small amount of work has been carried out using these models. Although good fits to experimental J-V data have been achieved these authors, the simulations have only been used to model a small number of devices. Furthermore, much of the literature on device models refers to theoretical calculations. It is therefore imperative to investigate the range of parameters for which these models are valid, and find any potential problems. The goal of the work presented in this chapter, therefore, is not only to validate the model presented in Chapter 2 and obtain good fits to the experimental data, but to assess the strengths and weaknesses of such a model and the fitting process.

The first aim of this chapter is to examine how sensitive the model is to variations in the material parameters. This may appear to be a somewhat trivial exercise, but given that most, if not all, of the material parameters are poorly characterised and certainly sample dependent, it is important to understand the effects of having incorrect or unknown material parameters on the results ob-

tained. Section 3.1 examines the role of material parameters on the simulated J-V characteristics obtained. This is done by taking typical material parameters from the literature, and simulating the J-V characteristics of an ITO/PPV/Al device, whilst systematically varying the material parameters to gauge the effect on the results obtained. The process of obtaining the best fit to experimental data is then outlined in section 3.1.13; as an example, the simulated J-V characteristics of a single layer PFO device are presented.

The second aim of the chapter is to demonstrate the validity and usefulness of the drift-diffusion model, as well as highlighting any potential problems with the model. Section 3.2 presents results from the simulation of the J-V characteristics of an ITO/MEH-PPV/Al device over a temperature range from 150K-300K. Section 3.3 contains the simulated temperature dependent J-V characteristics of an ITO/TPD/Al device. Finally, section 3.4 contains the results of simulating an single layer NPB device, with a PEDOT anode and a variety of cathodes.

Further sets of J-V characteristics have been successfully simulated with the model, but the experimental data was provided from single devices at specific temperatures (usually room temperature). This modelling yields values of the hole mobility μ_p, its field-dependence, E_0, and the hole barrier height, ϕ_{bp}. However, such information is of little use by itself, since the values obtained are highly sample dependent; no further insight into injection and transport is gained from these extra results. Such data is essentially a repetition of the work contained in the chapter and as such has been omitted for brevity and clarity.

3.1 Effects of material parameters on simulated J-V characteristics

In order to demonstrate the effects of varying the material parameters on the J-V characteristics of a single layer OLED, a typical ITO/PPV/Al device (Figure 3.1) has been simulated, with material parameters taken from the literature. Table 3.1 contains the parameters used in the device simulation. The device is essentially unipolar, owing to the very large barrier to electron injection ($\phi_{bn} = 1.7$eV) with a hole only device current flowing. The current is injection limited, owing to the value of ϕ_{bp} chosen, 0.5eV, which is a typical value [6].

The parameters in Table 3.1 were systematically varied in order to ascertain their effect on the J-V characteristics, and to investigate how inaccuracies in the values of material parameters used when simulating a specific device may affect the outcome of the simulation. For simplicity, the contribution from the tunnelling current has been neglected unless stated otherwise, and the PPV has been assumed to be trap-free [8] so as to allow the effects of varying each parameter to be unambiguous. Although the results described below have been obtained for a hole-only device, analogous results apply with equal validity to a single-layer electron-only device.

Parameter	Value	Units
T	300	K
d	100	nm
ϕ_{bn}	1.7	eV
ϕ_{bp}	0.5	eV
N_V	1×10^{27} [2]	m^{-3}
N_C	1×10^{27} [2]	m^{-3}
μ_{p0}	5×10^{-11} [8]	m^2/Vs
μ_{n0}	$0.01\mu_{p0}$ [9]	m^2/Vs
E_0	3.5×10^6 [8]	Vm^{-1}
N_A^-	1×10^{20} [10]	m^{-3}
ϵ_s	3.0 [2]	-

Table 3.1: Material parameters used to simulate an ITO/PPV/Al device.

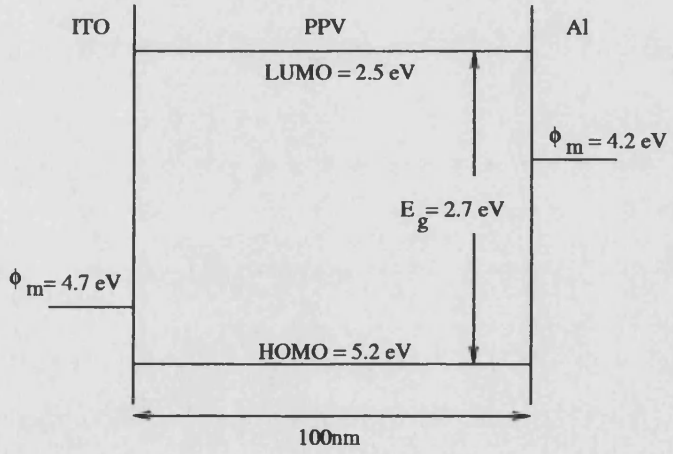

Figure 3.1: Schematic energy band diagram of the ITO/PPV/Al device. Energy levels of PPV taken from [5], ϕ_m Al taken from [11].

3.1.1 Temperature (T)

Since this device has an injection limited current, then clearly the device current will usually be very temperature dependent, since thermionic emission is by its very nature temperature dependent [18]. Figure 3.2 shows the effect of a slight variation in temperature, by a few Kelvin, on the device current.

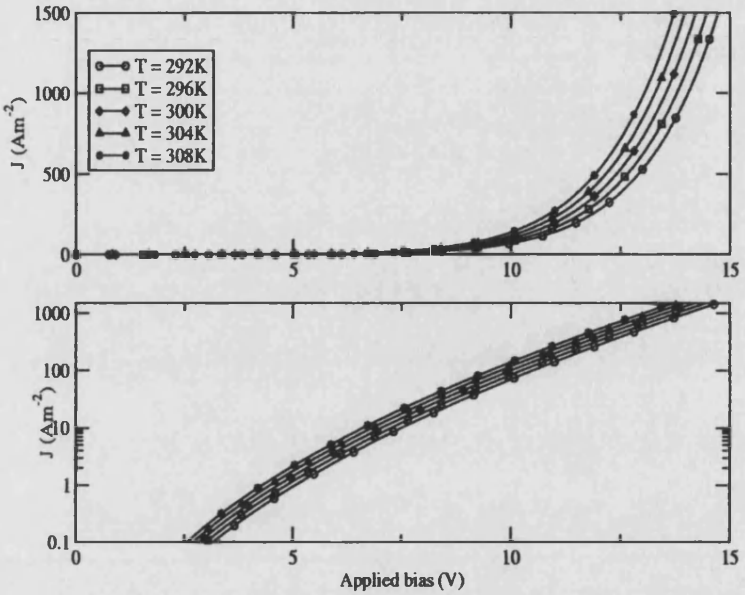

Figure 3.2: Effect of temperature variation on the J-V characteristics of an ITO/PPV/Al device.

As expected the current increases with temperature as the thermionic emission current increases, since more carriers have sufficient energy to surmount the barrier to injection, ϕ_{bp}. The hole mobility has been kept constant in Figure 3.2, but in reality the mobilities of carriers in organic semiconductors have been shown experimentally to vary with temperature e.g. [16][19], and so the difference between the device currents at the various temperatures would be different to that shown. Although the error in measuring the ambient temperature of operation when obtaining J-V data experimentally will be much smaller than the variation of temperature implemented in Figure 3.2, at low temperatures sample heating from the current flowing through a device can significantly alter the temperature at which a device is operating, and hence attempting model J-V characteristics at the measured ambient temperature can be somewhat misleading [20]. Temperature rises of up to 30K have been measured in typical devices at under typical operating conditions [21].

3.1.2 Thickness (d)

Figure 3.3 shows the effect on the J-V characteristics of varying the device thickness, d, from 98-102nm.

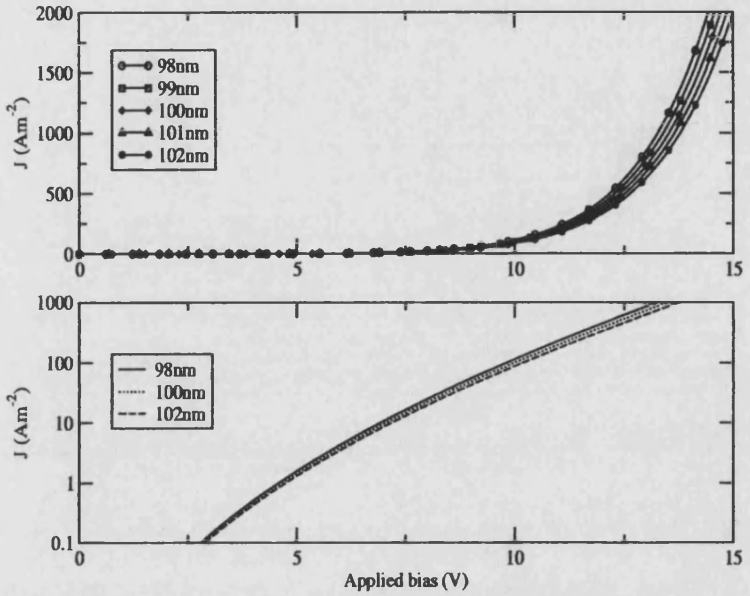

Figure 3.3: The J-V characteristics of the sample ITO/PPV/Al device for a range of thicknesses, d, from 98 to 102nm.

As can be seen from Figure 3.3, the current reduces with increasing thickness for a given voltage. This is because the current is injection limited, and the thermionic emission current is field-dependent. Hence for a given bias, an increase in device thickness results in a decrease in electric field at the contact, since the electric field in injection limited devices is constant across the device (see Figure 3.4), and a lower injection current. A very minor effect is that the mobilities will be slightly smaller at larger thicknesses since the mobilities are field dependent. Another subtle effect is that the barrier lowering also depends upon the electric field at the contact and hence a slightly reduced electric field will reduce the effect of the image barrier lowering on the J-V characteristics.

For purely injection limited J-V characteristics, the current at a constant field has no explicit thickness dependence i.e. J = J(E). For trap-free space-charge limited conduction (SCLC), with or without a field-dependent mobility, the current scales with d^{-1} at a constant field [14] (section 2.4).

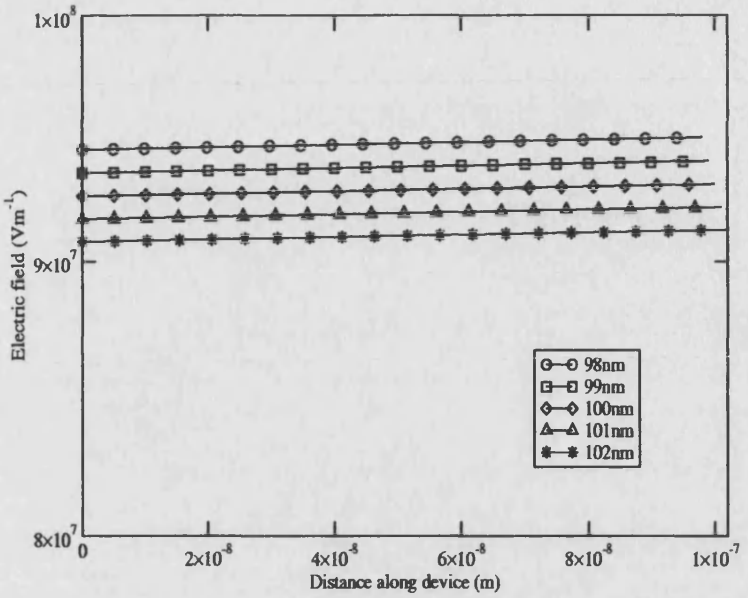

Figure 3.4: The electric field profile across the sample ITO/PPV/Al device for a range of thicknesses, d, from 98 to 102nm, at +10V.

3.1.3 Hole barrier height (ϕ_{bp})

In this and many other devices, the device current is injection limited, which is assumed to be primarily due to thermionic emission. Hence the device current depends upon the size of the barrier to hole injection, ϕ_{bp}. Figure 3.5 shows how the current varies as ϕ_{bp} is decreased from 0.6eV to 0.1eV.

As expected, the device current increases significantly as the barrier to hole injection is reduced, since the hole current is equal to the device current. Reducing ϕ_{bp} from 0.6eV to 0.1eV is achieved by increasing the workfunction of the ITO anode from 4.6eV up to 5.1eV, which is within the range of values for the workfunction of ITO. The built-in potential, which is equal to the difference between the workfunctions of the two electrodes (see section 2.3.1), actually increases with the increase in the ITO workfunction. Hence the effective field at a given applied bias is slightly reduced as ϕ_{bp} decreases, which has an effect on the mobility, barrier lowering and thermionic emission, but the increased current due to the reduction in barrier height more than compensates for this.

One particularly useful result which can be obtained from Figure 3.5 is that for larger values of ϕ_{bp}, the current varies strongly with the barrier height, but as the barrier is reduced below a value of 0.3eV, the current tends towards the space-

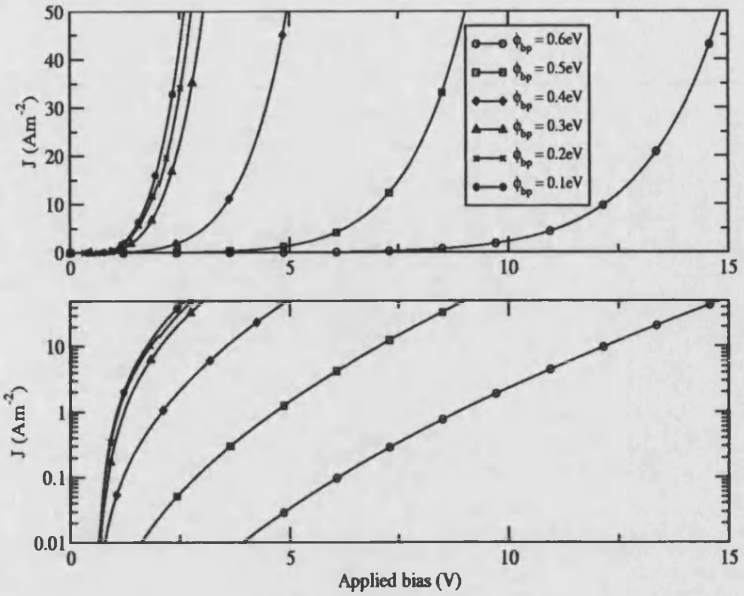

Figure 3.5: Effect of varying the barrier height to hole injection, ϕ_{bp}, on the J-V characteristics of an ITO/PPV/Al device.

charge limit (SCLC) (section 2.4), and hence the injecting contact is tending towards behaving Ohmically. A similar result has been obtained by Davids et al [2].

3.1.4 Electron barrier height (ϕ_{bn})

Although in the context of a unipolar hole-only device the concept of a barrier to electron (minority carrier) injection may appear redundant, the workfunction of the cathode plays a critical role in terms of the device operation. This point is often ignored in the analysis of J-V characteristics.

Figure 3.6 shows the effect on the J-V characteristics of the device of varying the electron barrier height, ϕ_{bn}, from 1.7 to 0.5 eV (this is equivalent to reducing the workfunction of the cathode, ϕ_m, from 4.2eV to 3.0eV). The current at a given applied bias decreases with the decrease in ϕ_{bn}. The explanation for this behaviour is that as the workfunction of the cathode is reduced, the built-in potential, V_{bi}, actually increases since the difference in the workfunctions of the electrodes increases (section 2.3), whilst the increase in the electron current is negligible due to the large values of ϕ_{bn} and/or the low value of μ_n. Hence the effective field at a given bias decreases with decreasing ϕ_{bn}, and the device current

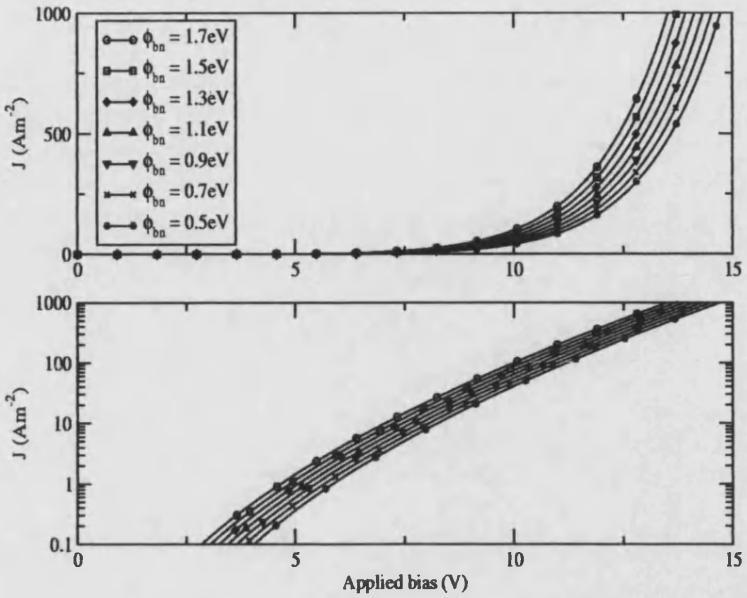

Figure 3.6: The effect of varying the barrier to electron injection, ϕ_{bn}, on the device's J-V characteristics.

consequently decreases.

Additionally, since V_{bi} is increased as ϕ_{bn} decreases, the bias at which carrier injection occurs increases, and the curves in Figure 3.6 are shifted to the right with increasing ϕ_{bn}; this is a very useful point of reference when fitting simulated J-V characteristics to experimental data. There are again also minor side effects in terms of the reduced field for the field-dependent mobilities and for barrier lowering.

3.1.5 Density of states (N_C, N_V)

Electron states in organic semiconductors are localised to molecules or to conjugated segments, and in the nondegenerate case the probability of a site being occupied by a hole or electron is much less than unity [22]. In this context, N_C and N_V are simply the density of localised sites multiplied by the number of ways it can be occupied i.e. its degeneracy. When using numerical models, most authors use a value of $1 \times 10^{27}\text{m}^{-3}$ for both N_C and N_V e.g. [2][4][23]. However, experimental estimates of N_C and N_V vary from 10^{25}m^{-3} to 10^{27}m^{-3} e.g. [8][25][26]. Figure 3.7 shows the variation in the J-V characteristics of the reference device as N_C and N_V are varied from $1 \times 10^{25}\text{m}^{-3}$ to $1 \times 10^{27}\text{m}^{-3}$.

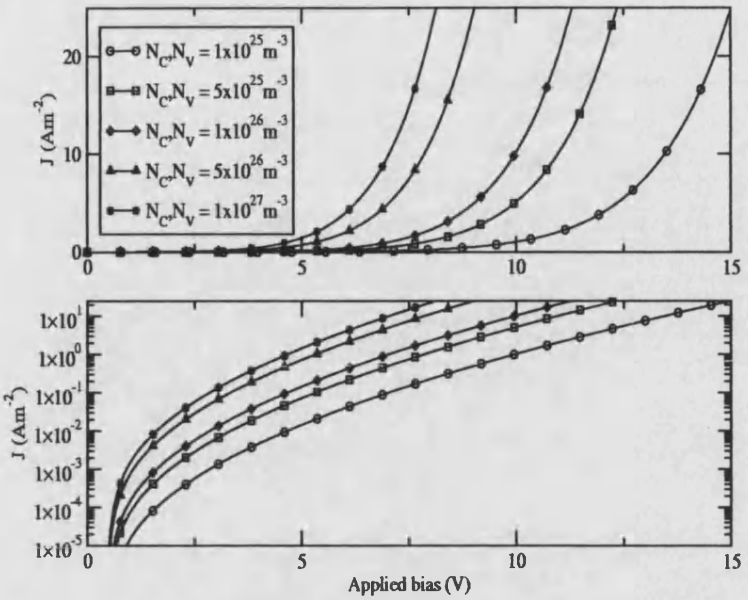

Figure 3.7: The variation in the J-V characteristics of an ITO/PPV/Al device as N_C and N_V are varied.

As expected, the current increases as the values of N_C and N_V increase, since the injected current depends on the density of carriers at the interface next to the metal contact, which itself depends upon the density of states (section 2.2.1).

3.1.6 Hole mobility (μ_p)

Figure 3.8 demonstrates the effect of varying the zero-field hole mobility, μ_{p0}, on the J-V characteristics of the device. As for the density of states, the injection current is determined by the material properties of the semiconductor, including μ_p (section 2.5). An increase in the hole mobility results in an increased injection current, and hence device current, since the injected carriers can be moved away from the contacts more efficiently. For lower mobilities, the backflowing current increases and the net injection current is reduced.

If the device was bulk rather than injection limited (i.e. SCLC) then the mobility would still be critical in determining the device current (section 2.4), with $J \propto \mu_p$.

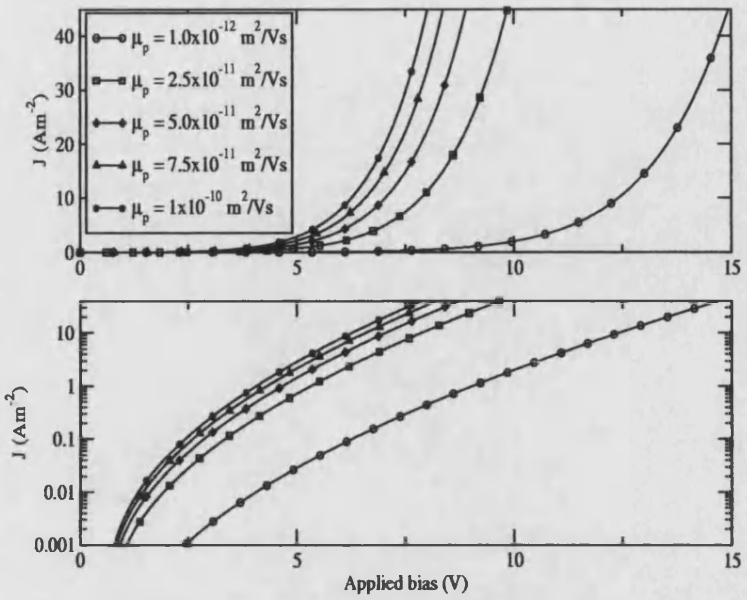

Figure 3.8: The effect of varying the zero-field hole mobility, μ_{p0}, on the J-V characteristics of an ITO/PPV/Al device.

3.1.7 Field dependence of mobilities (E_0)

Figure 3.9 shows the effect of the field dependence of the mobilities on the J-V characteristics of the sample device by varying E_0. At very low fields ($E < E_0$), the hole mobility, μ_p, is almost constant. However, as E increases, the mobility varies from its zero field value, and the currents vary accordingly (section 3.1.6).

As the value of E_0 is decreased, the field-dependence of the mobility increases (section 2.5) and hence the current increases more rapidly with applied bias. Conversely, the higher the value of E_0, the smaller the field-dependence of μ_p and the current varies less with increasing bias. The log-linear plot in Figure 3.9 shows that as the field-dependence of the mobility increases (i.e. E_0 decreases), the slope of the curve above V_{bi} increases. This is an important point of note as it means that when fitting simulated J-V data to experimental data, the value of E_0 can be obtained unambiguously since only one value of E_0 will give the correct slope in this portion of the J-V characteristic.

In the case of an Ohmic contact and the current being space-charge limited, then the field dependence of the mobilities will still be critical in determining the device current (see section 2.4).

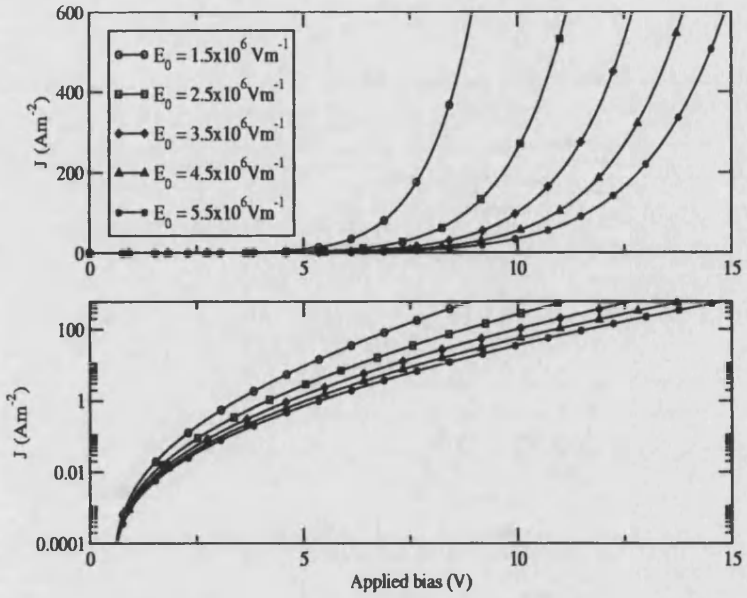

Figure 3.9: The effect of varying the field dependence of the hole mobility, E_0, on the J-V characteristics of an ITO/PPV/Al device.

3.1.8 Doping (N_A^-)

As previously mentioned, the majority of organic semiconductors, both polymeric and small molecule based, are assumed to be undoped, but in practice this is not the case [12], with doping often attributed to chemical reactions between the ITO substrate and semiconductor [13]. Doping is ignored by most authors when using either analytical models e.g. [14] or numerical models e.g. [2] of J-V characteristics, but experimental measurements have estimated the levels of acceptor doping to be less than $10^{22}m^{-3}$ in both polymers e.g. [15] and small molecules e.g. [16]. It is therefore of some importance to verify whether typical dopant concentrations significantly affect the J-V characteristics of a device.

Figure 3.10 shows the J-V characteristics for the reference ITO/PPV/Al device, when the acceptor doping, N_A^-, is varied from $1\times10^{10}m^{-3}$ to $1\times10^{23}m^{-3}$. It can be seen that for acceptor doping levels of up to $1\times10^{21}m^{-3}$, the J-V characteristics are unaffected, as the dopant carrier concentration is significantly smaller than the injected carrier density. Above this value, the doping increases the hole and hence device current, as the number of carriers present due to the dopants becomes comparable to, and greater than, the concentration of injected holes. Since acceptor levels have been assumed to be less than $1\times10^{22}m^{-3}$, then the value of the acceptor doping level, provided it is less than $1\times10^{22}m^{-3}$, can be arbitrarily

chosen without adversely affecting the simulated J-V characteristics in typical devices. This freedom to chose a relatively small value of the acceptor dopant concentration can be beneficial in terms of improving the numerical stability of the solver used in the drift-diffusion model presented here [17].

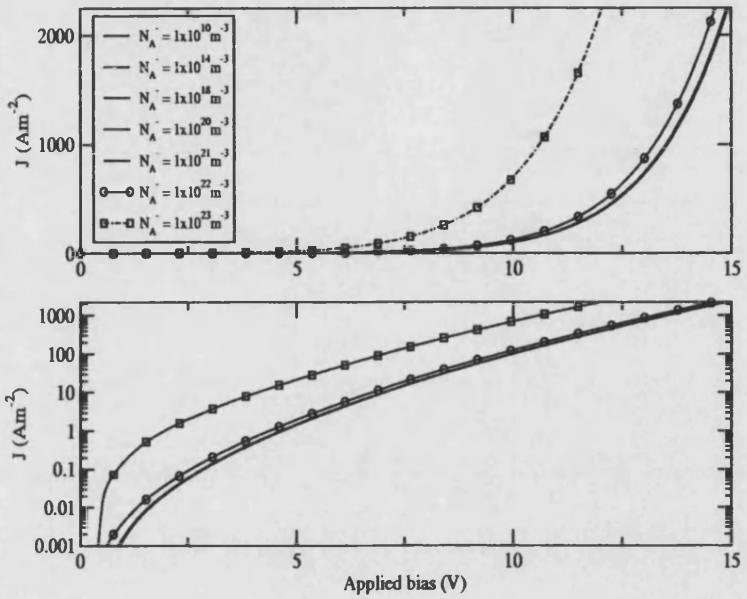

Figure 3.10: Effect of acceptor dopant density, N_A^-, on the J-V characteristics of an ITO/PPV/Al device.

3.1.9 Dielectric constant (ϵ_s)

The dielectric constant, ϵ_s, is another important material parameter, being involved in Poisson's equation (section 2.5), the recombination velocity, v_r (section 2.5), and image force barrier lowering (section 2.1.1). Figure 3.11 shows the effect on the J-V characteristics of varying ϵ_s.

As the dielectric constant is increased, the current decreases at a given bias. A small change in ϵ_s does not significantly change the electric field through Poisson's equation, nor vary v_{rp}. However, as mentioned in section 2.1.1, the magnitude of the barrier lowering through the Schottky effect is sensitive to the value of ϵ_s. The lower the value of ϵ_s, the greater the effect of the image force lowering, resulting in a larger injection and hence device current at a given field. Conversely, the larger the value of ϵ_s, the smaller the change in the barrier height and a smaller injection current flows at a given field.

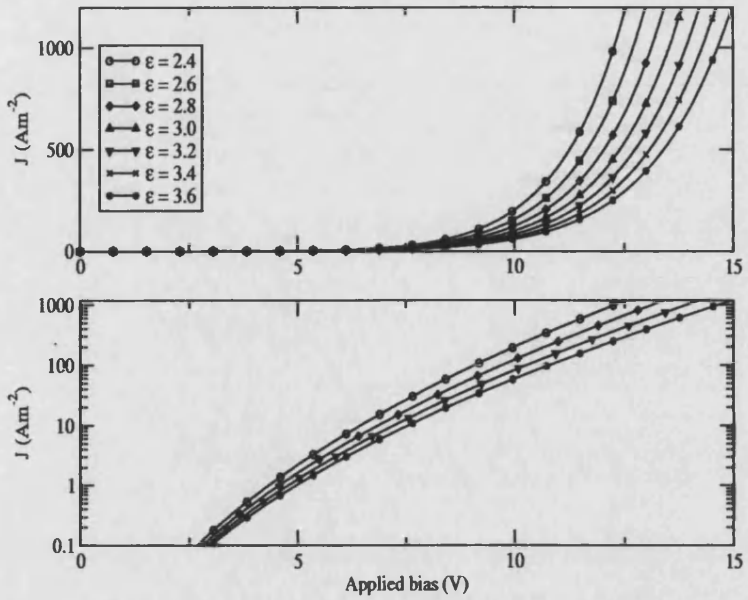

Figure 3.11: The effect of varying the dielectric constant, ϵ_s, on the J-V characteristics of the sample ITO/PPV/Al device.

3.1.10 Barrier lowering ($\Delta\phi_b$)

As mentioned in section 2.1.1, barrier lowering is a very important part of the injection process, and allows a current to flow across the reverse-biased Schottky contacts that would otherwise quickly saturate [18]. Figure 3.12 shows the J-V characteristics of the reference device with and without barrier lowering, and with and without a field dependent hole mobility (using the value of E_0 given in Table 3.1).

Without barrier lowering and without a field-dependent hole mobility, the current quickly saturates in the manner of a reverse-biased Schottky diode [18], as the barrier to injection into the semiconductor is a constant. The current as seen on the log-linear plot in Figure 3.12 is flat above V_{bi}. The addition of field-dependent mobilities can be seen to allow the current to increase with applied bias as although the barrier remains constant, the mobilities are increasing with field, and hence the drift current increases. This results in a positive gradient in Figure 3.12. Barrier lowering, without a field-dependent hole mobility, increases the current further, since the barrier to hole injection, ϕ_{bp}, is decreasing with increasing field, allowing an ever increasing injection current to be supplied. The gradient of the slope above V_{bi} is slightly steeper than in the previous case. Finally, in the device where both barrier lowering and field-dependent mobilities

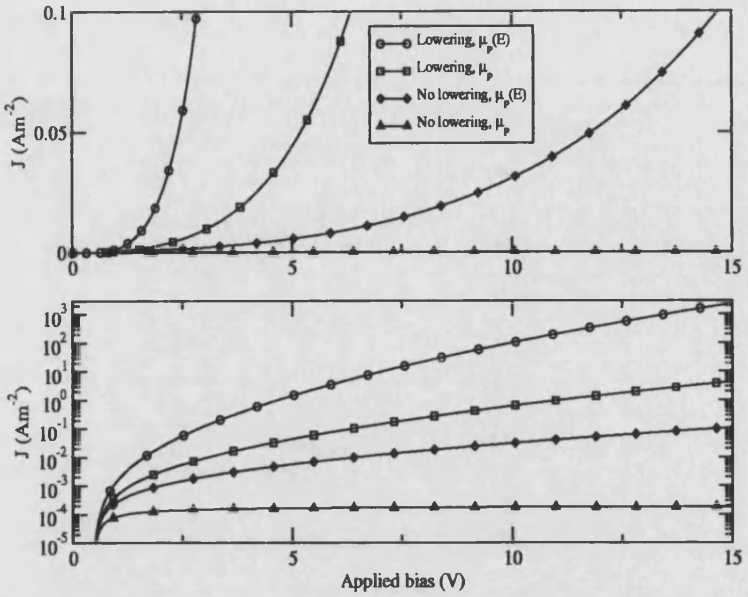

Figure 3.12: The J-V characteristics of the sample ITO/PPV/Al device with and without image barrier lowering, and with and without field-dependent mobilities.

are present, which would appear to be the situation in real devices, the current increases most rapidly as a superposition of the two previous cases, with a much steeper slope on the log-linear plot in Figure 3.12 above V_{bi}.

3.1.11 Tunnelling

As discussed in section 2.5, the Fowler-Nordheim tunnelling component of the injection current, has two scaling factors, α_1 and α_2, which determine the magnitude of the tunnelling current and the bias at which the tunnelling current becomes significant respectively [17]. Figure 3.13 shows the effect of the scaling parameter α_1 on the tunnelling contribution to the device current, whilst α_2 is set to 1.0, and Figure 3.14 shows the effect of varying the scaling parameter α_2 on the tunnelling contribution to the device current, whilst α_1 is set to 1×10^{-3}. In both figures, the J-V characteristic of the device without a tunnelling component is also shown for comparison.

It can be seen from Figure 3.13 that as the value of α_1 increases by an order of magnitude, the tunnelling current increases significantly. If the tunnelling current becomes large (for $\alpha_1 = 0.01, 0.1$), then the current can tend towards the space-charge limit. Figure 3.14 demonstrates that the value of α_2 determines at

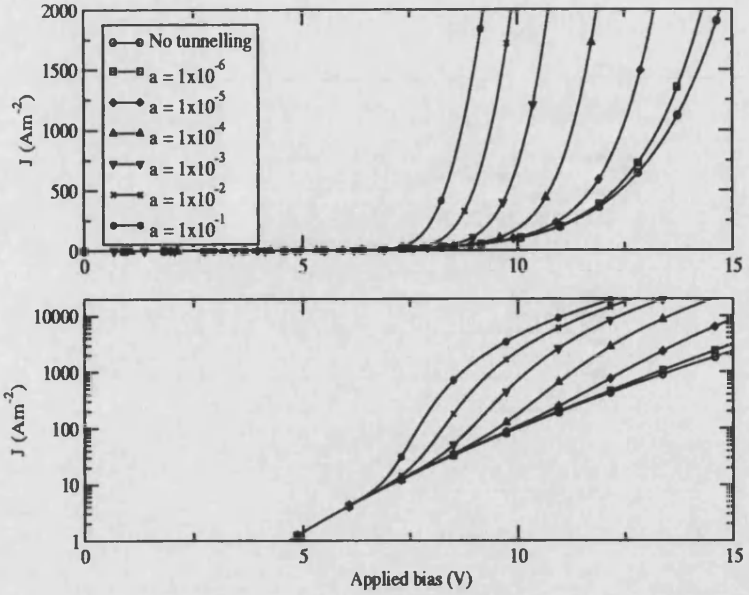

Figure 3.13: The effect of varying the tunnelling scaling parameter α_1 on the J-V characteristics of the sample device ($\alpha_2 = 1.0$).

what point the tunnelling contribution to the current becomes significant. For small values of α_2, the tunnelling current becomes significant at an early enough point that at moderately high biases the tunnelling current component is again large enough such that the current tends to the space-charge limit. As previously described, creating barriers thin enough to allow a significant tunnelling current is a practical solution to creating Ohmic contacts; this effect can be achieved through varying the parameters α_1 and α_2. However, this does not necessarily imply that the F-N tunnelling approach is valid.

3.1.12 Bipolar devices

Although many single-layer OLEDs can be considered to be unipolar for the purposes of analysing device currents, by their very nature OLEDs must be bipolar. Nevertheless, the electron current is usually negligibly small compared to the hole and hence device current. Figure 3.15 shows how the device's J-V characteristics varies as the barrier to electron injection is changed from 1.7eV to 1.2eV to 0.7eV. At each value of ϕ_{bn}, the zero-field electron mobility was set as $0.01\mu_{p0}$, $0.1\mu_{p0}$ and μ_{p0}. As discussed in section 3.1.4, lowering the value of ϕ_{bn} is equivalent to reducing the cathode workfunction, ϕ_m, and hence the built-in potential increases. Even with an increased electron mobility, the current at a given bias decreases

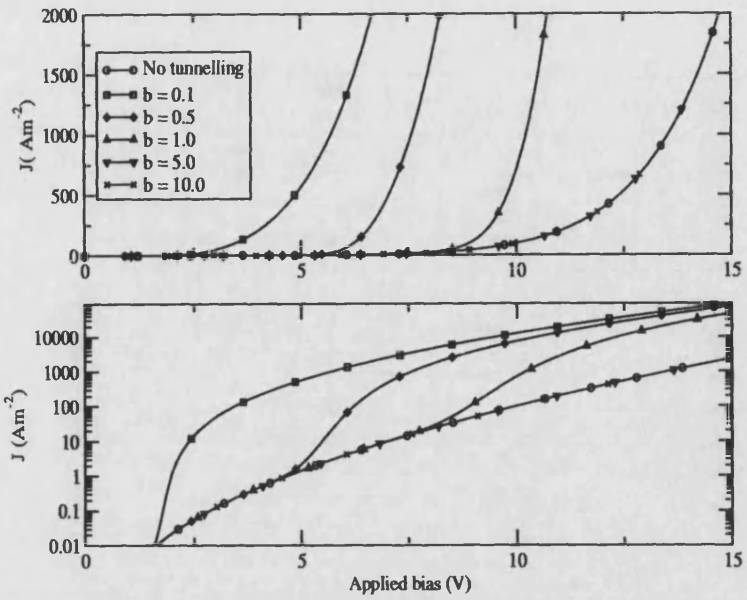

Figure 3.14: The effect of varying the tunnelling scaling parameter α_2 on the J-V characteristic of the sample device ($\alpha_1 = 1 \times 10^{-3}$).

as ϕ_{bn} decreases due to the increased built-in field, as the electron current is still very small.

Figure 3.16 shows the hole current, J_p, and electron current, J_n, profiles for the device at an applied bias of +15V, in the case where $\phi_{bn} = 0.7$eV, and the electron mobility is equal to $0.01\mu_{p0}$, $0.1\mu_{p0}$, and μ_{p0}. The electron current, J_n, is still many orders of magnitude lower than the hole current irrespective of the mobility of the electrons, and does not significantly contribute to the overall device current. However, it can be seen that for the higher values of the electron mobility ($\mu_{n0} = 0.1\mu_{p0}$ or μ_{p0}) the electron current profile is essentially constant across the device, whilst in the case where $\mu_{n0} = 0.01\mu_{p0}$, J_n decreases rapidly away from the cathode.

Figures 3.17, 3.18 and 3.19 show the optical recombination rate, R_{opt}, and hole and carrier density profiles for the device with barriers to electron injection of 1.7, 1.2 and 0.7eV respectively, at an applied bias of +15V. In each case, the zero-field electron mobility, μ_{n0}, was set to $0.01\mu_{p0}$, $0.1\mu_{p0}$, and μ_{p0}. In respect of each electron barrier height value, it can be clearly seen that the lower the barrier, the greater the injected electron density. The injected electron density increases by many orders of magnitude for each mobility as the barrier height is lowered. However, the electron density profile, and hence the recombination rate

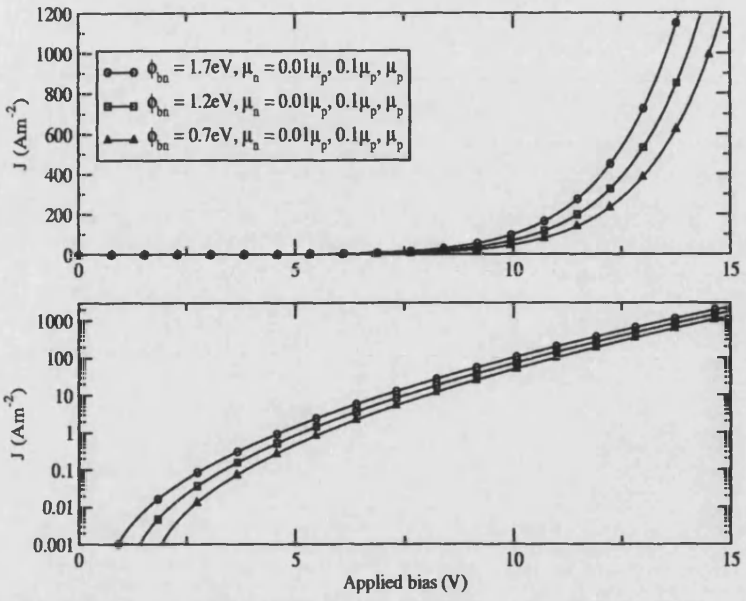

Figure 3.15: The J-V characteristics for the ITO/PPV/Al device with the barrier to electron injection, ϕ_{bn}, set to 0.7eV, 1.2eV, 1.7eV, and the zero-field electron mobility, μ_{n0}, set to $0.01\mu_{p0}$, $0.1\mu_p$ and μ_p.

profile, is also strongly affected by the electron mobility. In the lowest mobility case, the electrons injected are not transported away from the cathode particularly well, and accumulate near the cathode. This results in the recombination being confined to near the cathode, which is known to be undesirable since the electrodes can quench excitons e.g. [5]. As the mobility increases, the electrons are much better transported through the device and the electron density (and recombination profile) are much more uniform across the device.

Hence although the optical recombination rate is proportional to the carrier densities (section 2.5), it can be clearly seen that the magnitudes of the mobilities are also extremely important. The mobility of the minority carrier limits the recombination rate and the size of the recombination zone. It is thus necessary to try and balance both injection and transport in single layer OLEDS, although in practice this is difficult to achieve since organic semiconductors tend to favour transporting one carrier over another.

The internal quantum efficiency, η_{int}, can be calculated as follows [22]:

$$\eta_{int} = \frac{1}{4}\frac{J_r}{J} \tag{3.1}$$

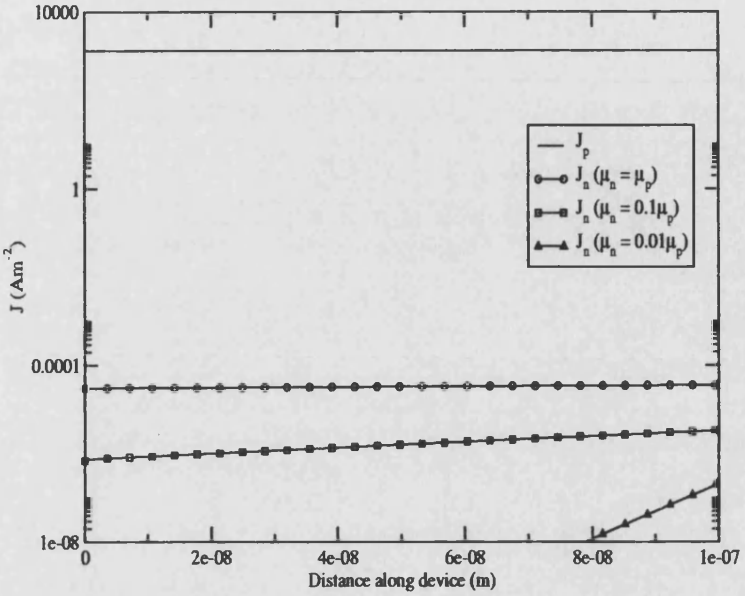

Figure 3.16: The hole current profile, J_p, and electron current, J_n, profiles for the device where $\phi_{bn} = 0.7$eV, and $\mu_{n0} = 0.01\mu_{p0}$, $0.1\mu_{p0}$, and μ_{p0}. V_{app}=+15V. The anode is on the left hand side.

where

$$J_r = J_p(d) - J_p(0) = J_n(0) - J_n(d) \tag{3.2}$$

J_r is the recombination current, which is equal to the difference in the magnitude of one of the carrier currents, either the hole current J_p or the electron current J_n, between the injecting and collecting electrodes, situated at either $x = 0$ or $x = d$. J is the device current, and the factor of $1/4$ assumes that the radiative singlet and non-radiative triplet excitons are formed in the ratio of 1:3.

In the case of $\phi_{bn} = 1.7eV$, the internal quantum efficiency increases by a factor of approximately 18 as the mobility is increased from $0.01\mu_{p0}$ to μ_{p0}, whilst the efficiency increases by a factor of approximately 17 and 15 in the cases of $\phi_{bn} =$ 1.2eV and 0.7eV respectively. Thus although the electron and hole densities will determine the magnitude of the recombination rate, the mobilities determine the device efficiency, which is of upmost importance.

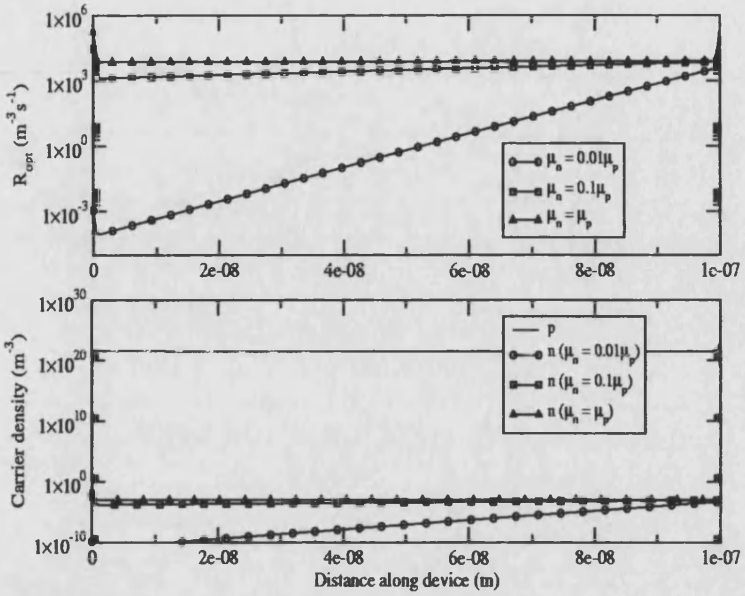

Figure 3.17: The optical recombination rate, R_{opt}, profile (top panel) and carrier density profiles (bottom panel) for the device in the case where $\phi_{bn} = 1.7$eV, and $\mu_{n0} = 0.01\mu_{p0}, 0.1\mu_{p0}, \mu_{p0}$. The hole injecting contact is on the left hand side. V_{app}=+15V.

3.1.13 Fitting method

Generally, the J-V characteristics of single-layer OLEDs can be considered to be unipolar since the magnitude of the barrier to minority carrier injection (usually ϕ_{bn}) is generally too large to allow significant minority carrier injection, and the minority carrier mobility (usually μ_n) is much smaller than the majority mobility, again reducing the contribution from the minority carrier current.

Although it has been demonstrated above that many of the material parameters affect the simulated J-V characteristics, most must be fixed to values obtained from experiment or in the literature, including ϕ_{bn}, N_C, N_V and ϵ_s. In order to obtain a best fit of the simulated J-V curve to the experimental data, one must vary ϕ_{bp}, μ_{p0} and E_{0p}. Values of μ_{p0}, ϕ_{bp} and E_{0p} obtained from the literature can also provide a useful starting point.

The barrier to minority injection, usually the electron barrier, is fixed and allows the other barrier to be varied such as to obtain the correct value of V_{bi}, as shown previously in this section. The mobility, μ_{p0}, can then be varied to obtain the correct magnitude of the current, and E_0 is varied to obtain the correct slope on a log-linear graph. By considering the shape of the experimental and simulated

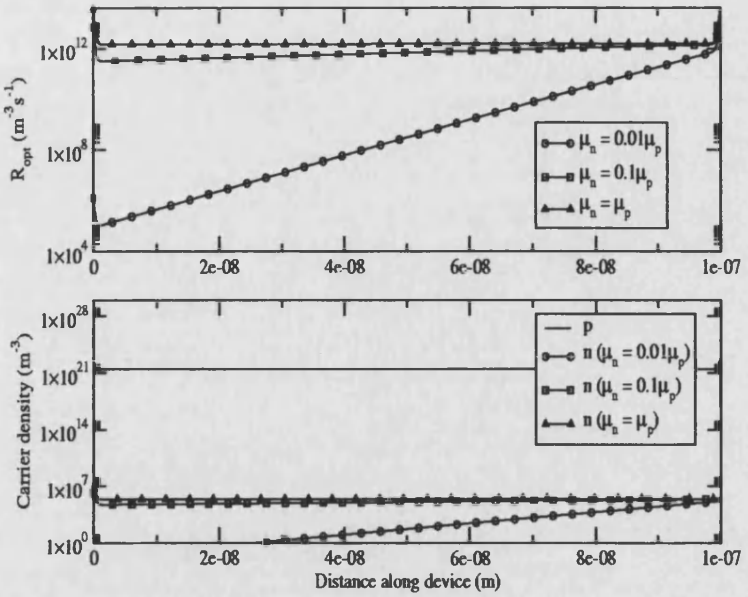

Figure 3.18: The optical recombination rate, R_{opt}, profile (top panel) and carrier density profiles (bottom panel) for the device in the case where $\phi_{bn} = 1.2$eV, and $\mu_{n0} = 0.01\mu_{p0}, 0.1\mu_{p0}, \mu_{p0}$. The hole injecting contact is on the left hand side. V_{app}=+15V.

J-V curves, it is then immediately apparent as to whether a tunnelling current component is required to improve the fit at high bias. If so then the scaling factors α_1 and α_2 can be adjusted to give the best fit.

Obtaining the best fit of a simulated bipolar device J-V curve to experimental data is essentially impossible, since there are 6 parameters to adjust. The only case in which fitting to a bipolar J-V curve may be practical is if hole only and electron only devices, with the same injecting contacts, have been fabricated along with the bipolar device. In this, case the values of ϕ_b, μ_0 and E_0 can be obtained for each of the carriers, making the job of fitting to a bipolar data possible. However, this assumes homogeneity of samples (in terms of mobilities and barrier heights), which in reality cannot be assumed.

As an example, the results of simulating an ITO/PFO/Au device (Figure 3.20) and an ITO/PEDOT/PFO/Au are presented below. The PFO layer is 1.6μm thick, and the Au cathode ensures the device is hole-only since ϕ_{bn}=2.3eV. The PFO was assumed to be trap-free [27]; Figure 3.21 shows the fit of the simulated data to the experimental data [29]. Unless stated, the parameters contained in Table 1.1 were used in the simulation.

The device with the PEDOT anode was simulated first, since the workfunc-

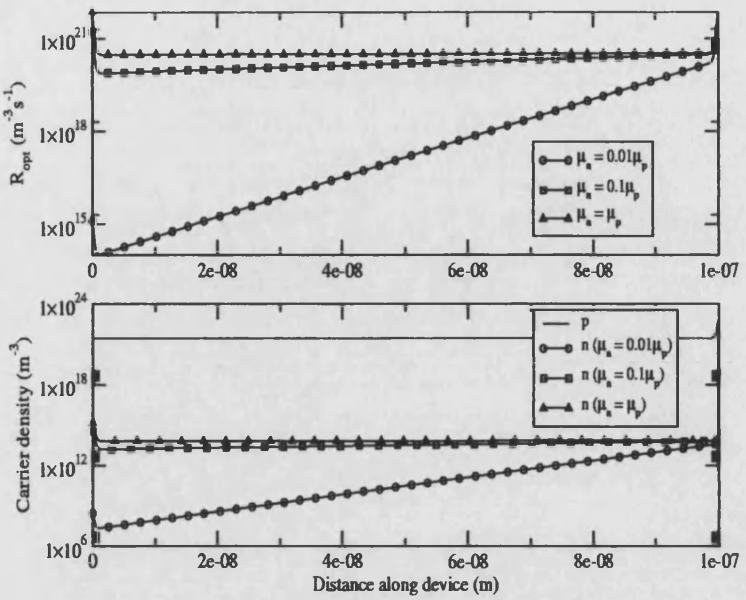

Figure 3.19: The optical recombination rate, R_{opt}, profile (top panel) and carrier density profiles (bottom panel) for the device in the case where $\phi_{bn} = 0.7$eV, and $\mu_{n0} = 0.01\mu_{p0}, 0.1\mu_{p0}, \mu_{p0}$. The hole injecting contact is on the left hand side. V_{app}=+15V.

tion of PEDOT is well known (ϕ_m=5.2eV e.g. [22]), giving a firm starting point for the value of the hole barrier height. The best fit to the data was obtained with ϕ_{bp}=0.6eV (confirming ϕ_m for PEDOT), $\mu_{p0} = 2.6 \times 10^{-9}$m^2/Vs, and E_0=1.6×10^{8}V/m. Using these values of μ_{p0} and E_0 for the ITO/PFO/Au device yielded a value of 0.8eV for ϕ_{bp}, corresponding to a workfunction of 5.0eV. The values of ϕ_{bp} and E_0 are in good agreement with experimentally obtained values e.g. [27][28][29].

The J-V characteristics in Figure 3.21 are very typical of those obtained from the simulation of many devices, where the unipolar device current is easily modelled by thermionic emission only, confirming injection limited behaviour which is consistent with the value of the barrier height calculated from the anode workfunction and HOMO energy level. No tunnelling current component is required as a result of the high temperature (allowing thermionic emission to dominate) and the large value of ϕ_{bp} means that the barrier is also thick, reducing the probability of tunnelling.

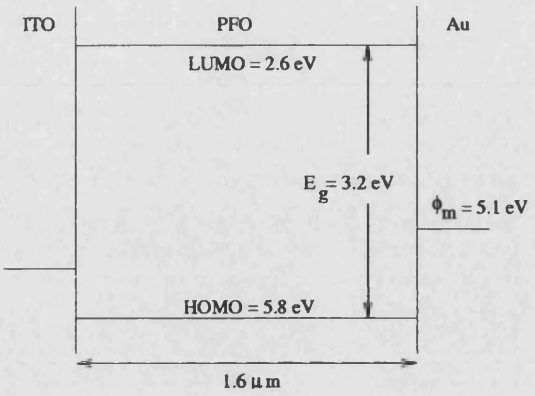

Figure 3.20: Schematic energy band diagram of an ITO/PFO/Au device. Energy levels of PFO taken from [27], ϕ_m Au taken from [5].

3.2 Temperature dependent J-V characteristics of an ITO/MEH-PPV/Al device

In this section, the results from modelling the temperature dependent (150-300K) J-V characteristics of a poly[2-methoxy,5-(2'-ethyl-hexyloxy)-1,4-phenylene vinylene] (MEH-PPV) conjugated polymer light emitting diode [30][31] are presented. The thickness of the MEH-PPV emissive layer is 95nm, and the anode and cathode materials are ITO and Al respectively. Details of the fabrication of the device and the experimental methods employed are contained in [32], which examined a similar device with a thicker emissive layer (160nm).

Figure 3.22 shows a schematic energy band diagram of the device; the HOMO and LUMO levels of MEH-PPV were assumed to be 5.4eV and 3eV respectively [19][36]. The workfunction of ITO is known to vary from by several tenths of an eV [33], depending upon the method of preparation. This results in a barrier to hole injection for this device from about 0.2-0.7eV, so the device current could potentially be either injection or space-charge limited. The barrier to electron injection ϕ_{bn} was found to be 1.2eV, by considering the workfunction of Al e.g. [11] and the LUMO level of MEH-PPV. The relatively large value of ϕ_{bn}, coupled with the fact that MEH-PPV is known to be a preferential hole transporting material [19], means that the electron current will make a negligible contribution to the overall device current, and the device is can be considered to be unipolar. The MEH-PPV was also assumed to be trap-free [19][32][35]. All other material parameters used were the same as in section 3.1.

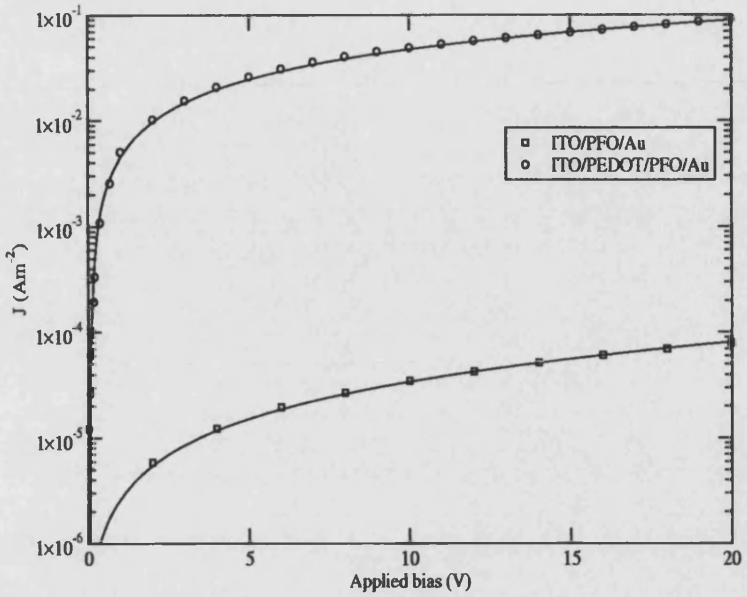

Figure 3.21: Simulated and experimental J-V characteristics of an ITO/PFO/Au and an ITO/PEDOT/PFO/Au device. Solid lines are simulated data, shapes are experimental data points.

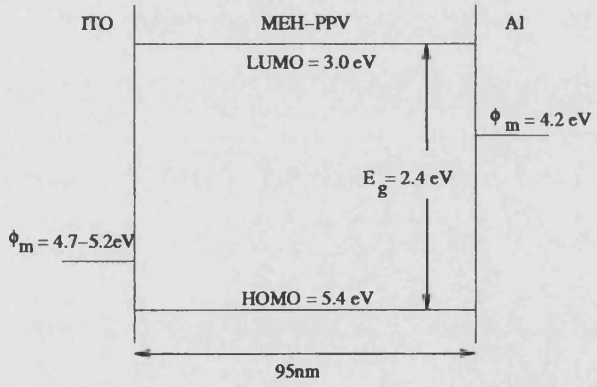

Figure 3.22: Schematic energy band diagram of an ITO/MEH-PPV/Al device.

Since the ITO/MEH-PPV contact could have been potentially quasi-Ohmic (<0.3eV), an initial fit to the data was attempted at 300K using a value of 0.2eV for ϕ_{bp}. This produced a space-charge limited J-V characteristic, the shape of which was found to be completely incompatible with the experimental data, and the fitted hole mobility was low ($< 10^{-11}m^2/Vs$) compared to published values e.g. [19][32]. The device current was therefore, as expected, considered to be injection limited, and in order to obtain the best fit of the simulated data to the experimental J-V curves, the fitting method described in section 3.1 was employed, varying μ_{p0}, ϕ_{bp}, and E_0, and α_1 or α_2 (the tunnelling scaling factors) as required. The J-V characteristics were simulated over the range of tempera-

tures from 150K-300K at 10K intervals. Figure 3.23 shows the experimental and simulated J-V curves for the device at temperatures of 150, 200, 250, and 300K.

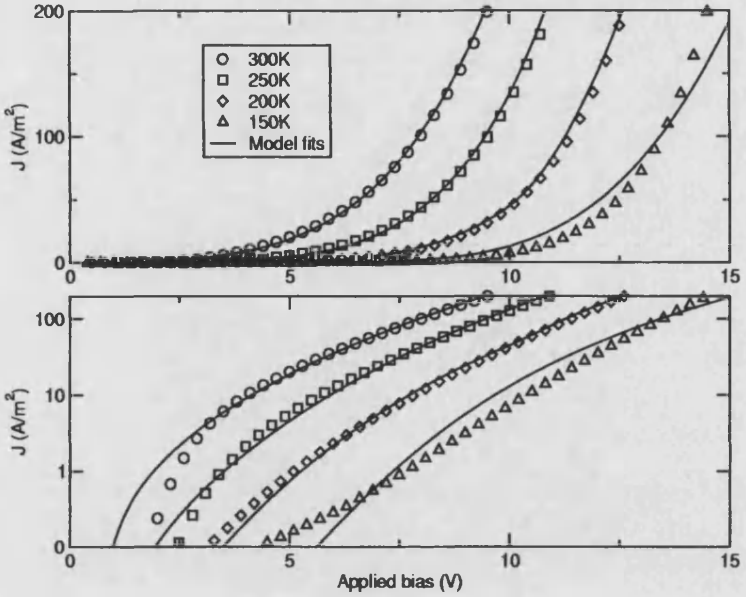

Figure 3.23: Experimental current densities (J) as a function of applied bias at temperatures of 150K (triangles), 200K (diamonds), 250K (squares), and 300K (circles). Solid lines represent the simulated J-V characteristics at these temperatures.

It was found that for temperatures in the range of 200-300K, good fits to the experimental data could be made across much of the voltage range. Below this, the fits became progressively worse as the temperature decreased, underestimating the current at low and high biases.

Figure 3.24 shows the fitted hole barrier height, ϕ_{bp}, as a function of temperature, whilst Figure 3.25 shows an Arrhenius plot of the fitted zero-field mobility, μ_{p0}, and the field-dependence of the mobility parameter, E_0. The tunnelling scaling factor, α_1 fitted at each temperature is shown in Figure 3.26 (α_2=1.0 for all T).

The values of μ_{p0} and E_0 given in Figure 3.25 were fitted over the temperature range of 200-300K to the empirical equation expressing the mobility as a function of electric field and temperature given by Gill [37]:

$$\mu(E,T) = \mu \exp\left(-\frac{\Delta}{k_B T}\right) \exp\left(\sqrt{\frac{E}{E_0}}\right) \tag{3.3}$$

where

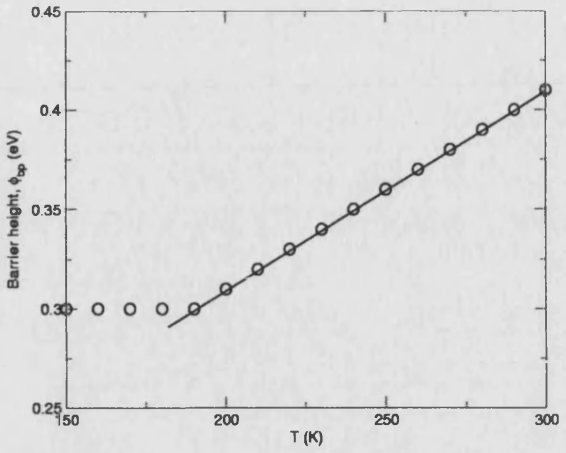

Figure 3.24: Fitted hole barrier height, ϕ_{bp}, (circles) as a function of temperature. The solid line is a linear fit to the data.

$$\mu_0 = \mu \exp\left(-\frac{\Delta}{k_B T}\right) \tag{3.4}$$

and

$$\frac{1}{\sqrt{E_0}} = B\left(\frac{1}{k_B T} - \frac{1}{k_B T_0}\right) \tag{3.5}$$

μ, Δ, B, and T_0 are material constants related to the degree of disorder in the material.

This yields the following parameters for the MEH-PPV in this sample: Δ = 0.27eV, $\mu = 1 \times 10^{-5} \mathrm{m}^2/\mathrm{Vs}$, $T_0 = 325\mathrm{K}$, and $B = 1.3 \times 10^{-5}$ eV/mV$^{1/2}$. Table 3.2 compares these values to those obtained experimentally in the literature for MEH-PPV. The results obtained are in good agreement with those in the literature; those obtained by Lupton and Samuel [32] were also obtained by modelling, but the values of Bozano et al [19] were obtained by analysis of experimental SCLC J-V characteristics of an MEH-PPV device. The good agreement with the results of Bozano et al is particularly encouraging since the two sets of values were obtained by entirely separate methods. The only significant disagreement between the two sets of results is over the value of T_0; however, this parameter was introduced by Gill and has no clear physical basis (see Chapter 5), making it difficult to interpret what this difference may be caused by. Since Δ, μ, T_0 and B are related to the disorder in the material, any small differences between

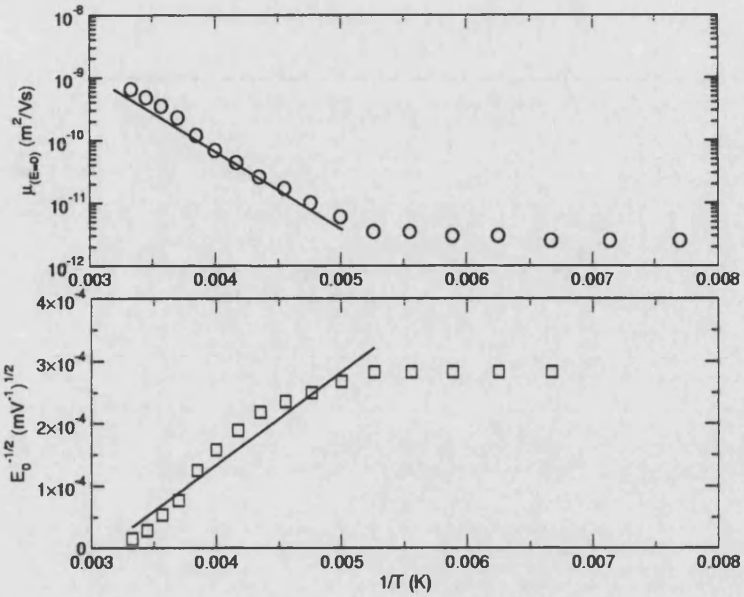

Figure 3.25: Arrhenius plot of μ_{p0} (top panel) and E_0 (bottom panel). The solid lines represent a best fit to the data points.

the values obtained and those published elsewhere are to be expected due to differences in the morphologies and purities of the samples.

Parameter	This work	Lupton and Samuel [32]	Bozano et al [19]
Δ (eV)	0.27	0.75	0.38±0.02
μ_0 (m^2/Vs)	1×10^{-5}	1.5×10^{-4}	1×10^{-5}
T_0 (K)	325	300	600±90
B (eV$(mV^{-1})^{1/2}$)	1.3×10^{-5}	5.5×10^{-5}	$2.3 \pm 0.2 \times 10^{-5}$

Table 3.2: Parameters obtained from Arrhenius plot for ITO/MEH-PPV/Al over range 200-300K, fitted to Gill's equation.

One particularly interesting result is the temperature dependence of the fitted barrier height (Figure 3.24). ϕ_{bp} decreases linearly with temperature down to about 200K, with a slope of 1meV/K; this is a significant variation in this parameter, yet there is little information in the literature regarding the variation of barrier heights with temperature. When attempting to model the temperature dependent J-V characteristics of an ITO/MEH-PPV/Al device, where the thickness of the MEH-PPV was 160nm, Lupton and Samuel [32] found that the fitted barrier height decreased with a slope of 1.2meV/K, also down to about 200K (starting with ϕ_{bp}=0.55eV at 290K). One explanation for the decrease in the value of ϕ_{bp} is the narrowing of the bandgap with temperature, as is evident from the absorption spectra of MEH-PPV [38]. However, the measured decrease

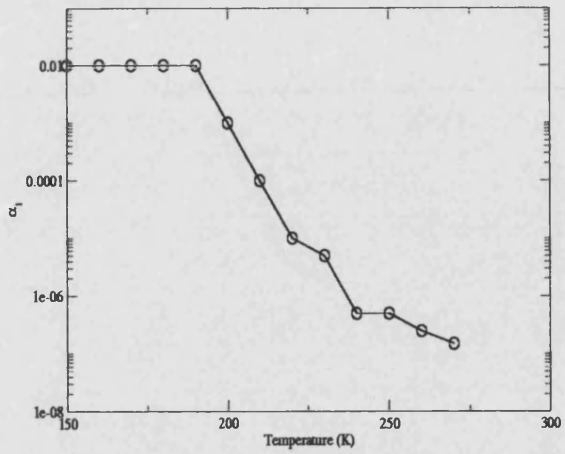

Figure 3.26: Fitted tunnelling scaling parameter, α_1, as a function of T. The solid line is a guide to the eye.

in the bandgap (~50meV) is less than predicted here by the variation in the barrier height; therefore some extra or alternative explanation is required. It is possible that the thermionic injection model is not entirely appropriate for dealing with injection into organic semiconductors, or is only appropriate over a certain temperature range. If the thermionic emission formalism used in the model is less strongly temperature dependent than the physical injection mechanism responsible in OLEDs, then the variation in barrier height found here may be required to compensate for this, although this does not explain the fitted value of ϕ_{bp} becoming constant below about 190K. Alternative injection mechanisms dealing with injection into a disordered hopping system have been proposed e.g. [39][40] and they exhibit characteristics which are qualitatively similar to those of thermionic emission. However, such injection mechanisms could not be coupled to a drift-diffusion model. More experimental data is required to be modelled for a variety of materials to see if this situation always occurs.

The linear decrease of the barrier height with temperature, down to 200K, has been suggested to be a product to the disorder inherent in the material [41]; once the ring torsions are frozen out e.g. [42], the band structure becomes relatively static, and hence the barrier height becomes constant. However, it is interesting to note that as the barrier height becomes constant at 190K, then the fitted values of μ_{p0} and E_0 also become approximately constant, and deviate from fitting to Gill's equation. In the literature, there is no data available for the behaviour of μ_p and E_0 for any materials below about 200K, making it difficult to decide whether this behaviour of the fitted values of μ_{p0} and E_0 is to be expected. It is unlikely that the mobility does become constant below a certain temperature,

given the thermally activated nature of hopping transport in organic semiconductors (see Chapter 5). It is possible that as the temperature decreases, the carrier mobility becomes increasingly dispersive, and as such the concept of a well-defined mobility, as required by the drift-diffusion model, cannot be applied in organic semiconductors at low temperatures.

The tunnelling pre-factor, α_1, also varies quite strongly with temperature. α_1 increases with decreasing temperature, indicating the presence of a larger tunnelling current contribution. This is consistent with the injection mechanisms at work here; as the temperature decreases, the thermionic emission component decreases and the tunnelling contribution to the injection current becomes more significant, particularly as the barrier height is also decreasing with increasing temperature, resulting in a thinner barrier. α_1 becomes constant at low temperatures, because owing to the low mobilities and the low barrier height, the current is actually tending to the SCLC limit and further increasing α_1 cannot increase the simulated device current. However, Fowler-Nordheim tunnelling is only weakly temperature dependent, with the temperature variation given as [45]:

$$J(T)/J(0) = \frac{\pi c_1 k_B T}{\sin(\pi c_1 k_B T)} \approx 1 + \frac{1}{6}(\pi c_1 k_B T)^2 \tag{3.6}$$

where J(T) is the tunnelling current at temperature T, and c_1 is a function of m^*, ϕ_b, and V. Koehler et al [46] have also argued that Fowler-Nordheim tunnelling is weakly temperature dependent through the changes with temperature of the Fermi distribution of the electrons in the metal contact. However, it is more likely that simply the fact that Fowler-Nordheim tunnelling is inappropriate for use in organic devices accounts for this strong temperature variation of α_1 (Chapter 2). In addition, sample heating is significant in OLEDs [21] and this may also account for the poor high-field fit to the experimental data at low temperatures. At steady state, as the sample heats up, the mobility will increase, and hence the current will be higher than predicted by the model at a given temperature.

In their modelling of a 160nm thick MEH-PPV device, Lupton and Samuel [32] postulated that their poor fits to the data at low bias, particularly at low temperature, was due to the fact that they had neglected diffusion in their model. They suggested that as the temperature decreases, the barrier to injection decreases, making the charge distribution less uniform, particularly as the contact becomes

quasi-Ohmic. Hence carrier gradients increase and diffusion is more important. However, the inclusion of the diffusion current in this model did not alleviate the poor fit to experimental data at low bias and temperature entirely.

In order to improve the fit between the simulated and experimental data at low biases and high temperatures, a discrete trap level was introduced into the MEH-PPV simulation [43][44]. A discrete trap level was placed at 0.3eV above the HOMO level, with a concentration of $3.5 \times 10^{22}\mathrm{m}^{-3}$; this level was found to significantly improve the fit to the experimental data at 300K (Figure 3.27). At low biases, the traps fill, and all injected carriers are trapped, reducing the current; this has the effect of shifting the low bias portion of the J-V characteristics to the right, as can be seen from the log-linear plot in Figure 3.27. As the bias is further increased, the traps are completely filled, and all injected carriers can then contribute to the device current, resulting in a J-V characteristic similar to that obtained without traps at high biases. However, at lower temperatures the model already underestimates the current at low biases, and the addition of the trap level makes this situation worse.

On the basis of these results, two conclusions can be reached. Firstly, there are no traps and the fit at low bias at 300K is simply not perfect, although no parameters could be varied to improve the fit. For example, it could be that the value of V_{bi} is incorrect (section 3.1). However, changing the built-in potential shifts the turn-on point of the curve, whereas the traps smooth the curve to the shape of the experimental data; this effect cannot be achieved with simply a change of V_{bi}. The other possible conclusion is that traps arise due to phase changes in the material occurring as the temperature changes [41].

Another characteristic of the device investigated was the internal quantum efficiency, η_{int}, which was calculated as shown in section 3.1.12. Taking the external quantum efficiency of the real device to be given by the light output divided by the device current, it was found that the efficiency increased by a factor of about 40 as the temperature was decreased from 300K to 11K [30]. The simulated internal quantum efficiency of the device was calculated over the temperature range of 200-300K, where the model was assumed to be valid. The electron mobility, μ_n, was set as both 0.01 and 0.1 μ_p. The relative quantum efficiencies of the experimental and simulated devices are shown in Figure 3.28; by taking the efficiencies relative to that at 300K, the fact that the experimentally obtained

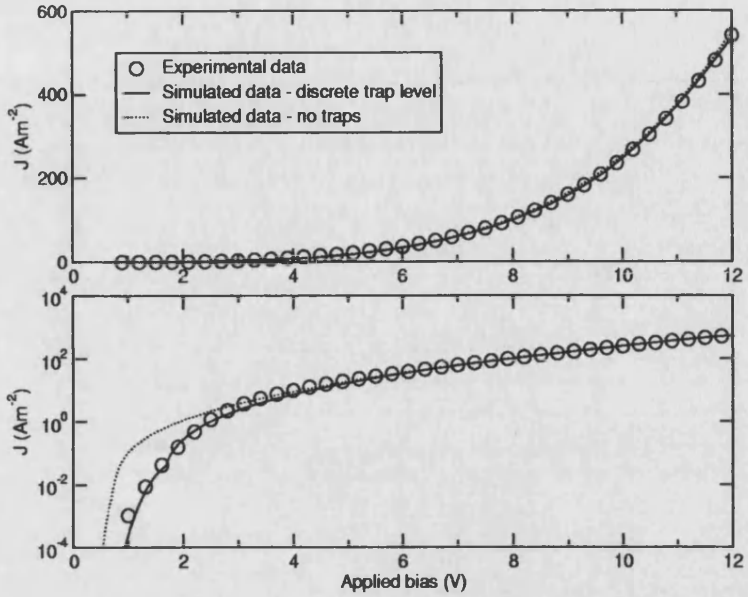

Figure 3.27: Comparison of simulated data, with and without a discrete trap level, to experimental data at 300K.

quantum efficiency is external and the simulated quantum efficiency is internal can be neglected, since the external quantum efficiency can be assumed to be a constant factor multiplied by the internal quantum efficiency e.g. [5].

It was found that in order to ensure that the efficiency increased at all in the simulated device as the temperature decreased, the barrier to electron injection, ϕ_{bn}, had to be decreased to at least the value shown in Figure 3.28, ignoring the actual increase in the efficiency in the experimental device. Although the model did exhibit increased efficiency as the temperature decreased, the slope of the variation of barrier height with temperature in Figure 3.28 is 5meV/K, much greater than the variation for the hole barrier height (1meV/K). A slope any smaller than this 5meV/K resulted in the efficiency decreasing with temperature. This indicates that although the bandgap does decrease with temperature, as previously mentioned, this cannot fully account for these observations since the sum of the changes in the barrier heights is significantly greater than the observed shrinkage. It was also found that varying the value of ϕ_{bn} at 300K had no effect, as the same slope of 5meV/K for ϕ_{bn} was still obtained.

In appears that in order to increase the calculated efficiency in the simulated device as T decreases, decreasing ϕ_{bn} causes a large build-up of electrons near the cathode, causing an optical recombination peak and hence improving the calculated efficiency. In practice, this could have an adverse affect on external

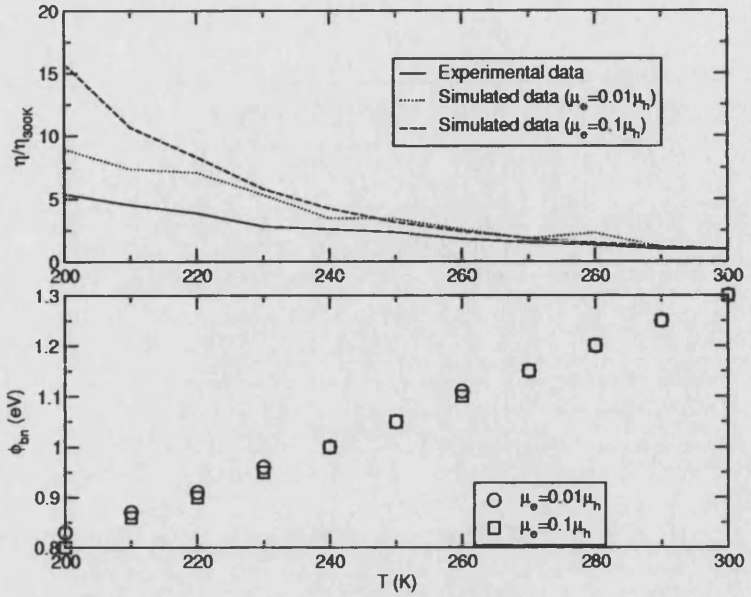

Figure 3.28: Experimental and simulated efficiencies (arb. units) as a function of temperature (top panel). Electron barrier height used in simulation (ϕ_{bn}) (bottom panel).

quantum efficiency since this recombination is occurring near the cathode, which can quench excitons e.g. [47]. Hence this increase in efficiency predicted by the model is unlikely to be the real reason for the increase in efficiency observed in the experimental data.

One potential explanation for the experimentally observed increase in efficiency as the temperature decreases is that the electron and hole mobilities tend to converge as the temperature drops, due to the electron mobility being more strongly field and temperature dependent [19]. This would cause the recombination current to rise as T decreases, as the electrons are spread more evenly through the device (as shown in section 3.1). The electron mobility was increased in the simulation relative to the hole mobility as the temperature decreased, but the fitted electron barrier height still had to be decreased by 5meV/K. It is therefore likely that the mobilities do indeed become more balanced as T decreases, but as well as increasing the recombination current as mentioned above, more recombination occurs in the bulk of the device away from the potentially exciton quenching cathode, further increasing the efficiency. This hypothesis cannot be tested by the model since the physics is simply not included.

3.3 Temperature dependent J-V characteristics of an ITO/TPD/Al device

In this section, the results of modelling a set of experimental J-V characteristics for a single layer ITO/TPD/Al OLED over a range of temperatures from 130K to 290K in 40K intervals [16] are presented. The thickness of the emissive layer, TPD (N,N'-diphenyl-N,N'-bis(3-methylphenyl)1-1'-biphenyl-4,4'-diamine), is 90nm. A schematic energy band diagram of the device is shown in Figure 3.29; the HOMO and LUMO levels of TPD are taken from [48], whilst the workfunction of Al is again taken as 4.2eV. The workfunction of ITO is a parameter to be determined via the fitting process. The TPD was assumed to be trap-free [16][48][49].

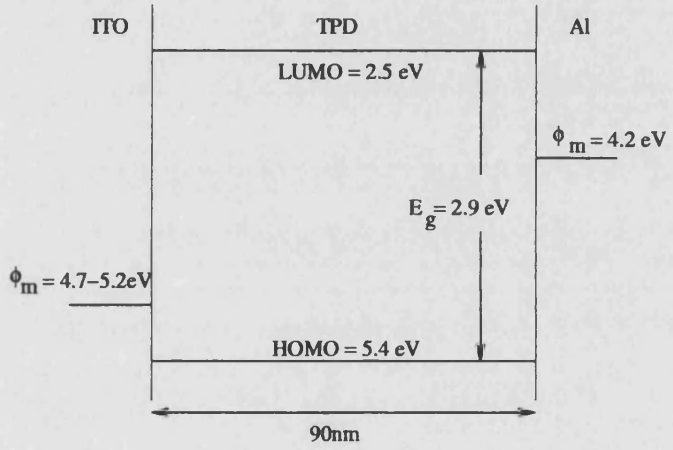

Figure 3.29: Schematic energy band diagram of an ITO/TPD/Al device.

Using the method described in section 3.1.13, the simulated data was fitted to the experimental data by varying μ_{p0}, E_0, ϕ_{bp}, and α_1, keeping all other parameters constant (as in Table 1.1). The device was known to injection limited, since the experimental data [16] showed the current was many orders of magnitude below that of TPD devices exhibiting SCLC. Additionally, an investigation of a series of devices which were identical except for the thickness of the TPD layer showed the current to scale with field, not thickness [16], a well-known property of injection limited devices e.g. [14].

Initially, it was found to be impossible to obtain anything approaching a satisfactory fit to the experimental data at any temperature. The gradient of the current above V_{bi} on a log-linear plot was too steep compared to the experimental data, even with field independent mobilities. As discussed in section 3.1, the gradient

Parameter	130K	170K	210K	250K	290K	Units
ϕ_{bn}	1.9	1.9	1.9	1.9	1.9	eV
ϕ_{bp}	0.21	0.28	0.32	0.38	0.45	eV
μ_{p0}	3.0×10^{-11}	4.0×10^{-11}	$4.4 \times^{-11}$	8.5×10^{-11}	5.1×10^{-10}	m^2/Vs
μ_{n0}	$0.01\mu_{p0}$	$0.01\mu_{p0}$	$0.01\mu_{p0}$	$0.01\mu_{p0}$	$0.01\mu_{p0}$	m^2/Vs
E_0	1.40×10^6	1.40×10^6	1.40×10^6	1.65×10^6	2.40×10^6	Vm^{-1}
ϵ_s	3.0	3.0	3.0	3.0	3.0	-
α	2×10^{-8}	2×10^{-8}	-	-	-	-

Table 3.3: Parameters used to simulate ITO/TPD/Al device, with no barrier lowering.

of the J-V characteristics above V_{bi}, for an injection limited device, is controlled by the field-dependence of the mobilities, E_0, and the presence of Schottky barrier lowering. Since the gradient was found to be too large without a field-dependent hole mobility, the only other explanation for the failure to fit the simulated J-V characteristics to the experimental data is that the barrier lowering effect was too great.

The J-V characteristics of the device were then modelled without any Schottky barrier lowering, using the parameters in Table 3.3; the simulated J-V characteristics are shown in Figure 3.30. Good fits to the experimental data were achieved, although a few discrepancies on the graphs are apparent. In the experimental data at 290K, there is a leakage current below 5V [41]. This actually makes the fitting process somewhat difficult since the position of V_{bi} cannot be ascertained from the experimental data, and hence obtaining the most accurate value of ϕ_{bp} is more difficult (section 3.1). The fit to the experimental data at 250K and 210K is quite poor at low fields. At high biases in the case of the device at 130K, the simulated current data is not quite as steep as the experimental J-V curve; at low temperatures, the tunnelling current component becomes more significant since thermionic emission is a temperature driven process, and the reduced barrier height fitted at 130K also increases the tunnelling current since the barrier is thinner. As in the previous section, it is likely that part of the reason for this difference is that the Fowler-Nordheim formalism is inappropriate for representing injection into OLEDs; sample heating may also play a part.

Figure 3.31 shows an Arrhenius plot of the μ_{p0} and $E_0^{-1/2}$ parameters used in the simulation, whilst Figure 3.32 shows the variation of the fitted hole barrier height, ϕ_{bp}, with temperature. The temperature variation of μ_{p0} is very low,

varying by just over an order of magnitude as the temperature decreases from 270K to 130K, whereas the temperature variation of mobilities in TPD (and all organic semiconductors) is much greater [50]. The value of μ_{p0} obtained from the simulation at 270K (5.1×10^{-10}m^2/Vs) is also about 3 orders of magnitude lower than published values e.g. [49]. E_0 is also smaller than published values by several orders of magnitude at all temperatures. However, it is interesting to note that both μ_{p0} decreases down to 210K before becoming approximately constant, and E_0 increases as T is decreased from 270K to 210K, also becoming approximately constant at lower temperatures. This behaviour is similar to that noted in the previous section.

The fitted value of ϕ_{bp} decreased linearly over the entire temperature range as the temperature decreased. At 270K, ϕ_{bp} was found to be 0.45eV, which is consistent with the conclusion of Campbell et al [16] that the device is injection limited. However, at low temperatures (130 and 170K), ϕ_{bp} was found to be less than 0.3eV, which is approximately the point where the contact tends to behave Ohmically. The implications of the fitted values of μ_{p0}, E_0, and ϕ_{bp} are discussed later in this section.

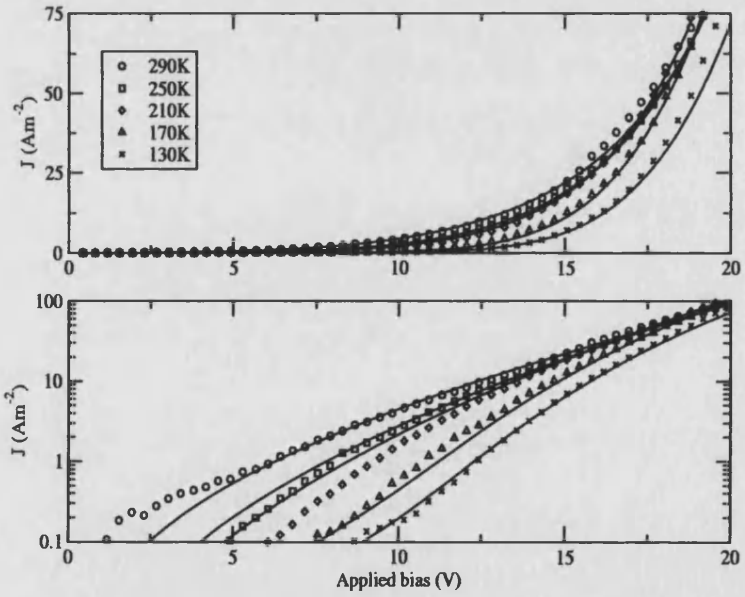

Figure 3.30: Simulated and experimental J-V characteristics for the ITO/TPD/Al device over a range of temperatures, with no barrier lowering. Shapes represent experimental data, solid lines represent simulated best fit.

As an alternative explanation, the J-V characteristics were then simulated using barrier lowering, but varying ϵ_s, since the value of this parameter significantly affects the magnitude of the barrier lowering (section 2.1.1). It was found that the

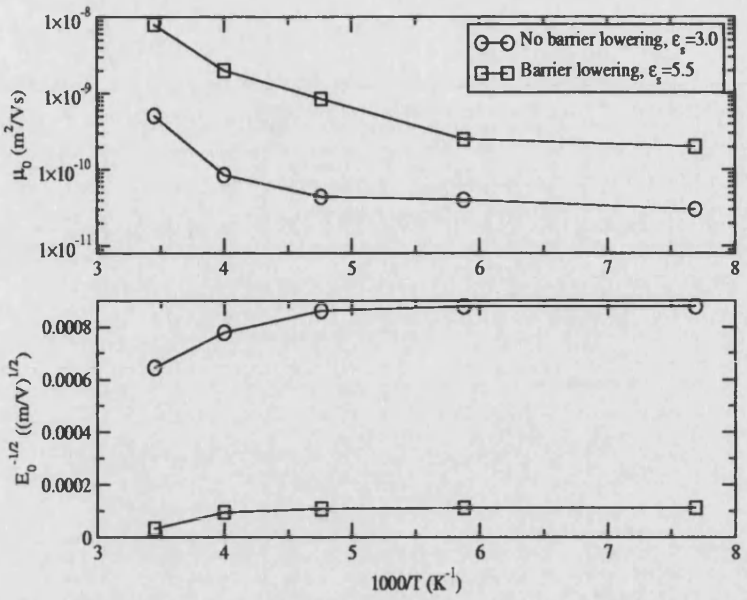

Figure 3.31: Arrhenius plot of $\mu_{p(E=0)}$ (top panel) and $E_0^{-1/2}$ (bottom panel) for the simulations with ($\epsilon_s = 5.5$) and without barrier lowering ($\epsilon_s = 3.0$).

Parameter	130K	170K	210K	250K	270K	Units
ϕ_{bn}	1.9	1.9	1.9	1.9	1.9	eV
ϕ_{bp}	0.32	0.36	0.42	0.48	0.54	eV
μ_p	2.0×10^{-10}	2.5×10^{-10}	$8.5\times^{-10}$	2.0×10^{-9}	8.0×10^{-9}	m^2/Vs
μ_n	$0.01\mu_p$	$0.01\mu_p$	$0.01\mu_p$	$0.01\mu_p$	$0.01\mu_p$	m^2/Vs
E_0	8.0×10^7	8.0×10^7	8.4×10^7	1.1×10^8	9.0×10^8	Vm^{-1}
ϵ_s	5.5	5.5	5.5	5.5	5.5	-
α	-	-	-	-	-	-

Table 3.4: Parameters used to simulate ITO/TPD/Al device, with barrier lowering.

lowest value of ϵ_s which would allow both barrier lowering and field-dependent mobilities to be used in the simulation was 5.5, somewhat higher than the value of 3.0±0.3 measured experimentally for the TPD sample [16], and higher than the typical values usually quoted for organic semiconductors, although some higher values have been reported e.g. 4.0 in [59]. Figure 3.33 shows the experimental and simulated J-V characteristics over the temperature range from 130K to 290K. The parameters used in the simulations are given in Table 3.4; Figure 3.31 shows an Arrhenius plot of the parameters μ_{p0} and E_0, and Figure 3.32 shows the fitted hole barrier height as a function of temperature.

It can be seen from Figure 3.33 that the simulated J-V characteristics obtained

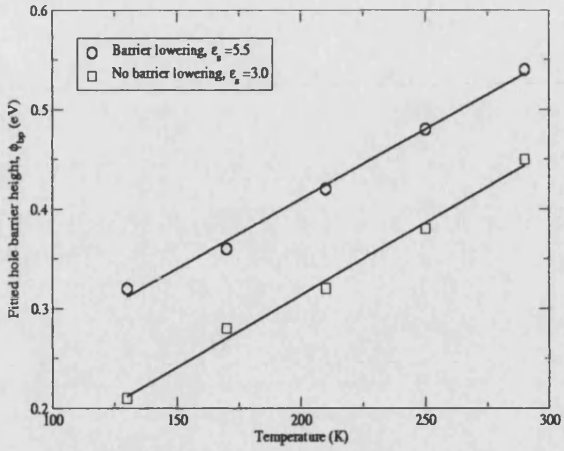

Figure 3.32: Fitted hole barrier height, ϕ_{bp}, as a function of temperature for the simulations with ($\epsilon_s = 5.5$) and without barrier lowering ($\epsilon_s = 3.0$).

using barrier lowering (ϵ_s=5.5) fit the experimental data better than those obtained from the simulation without barrier lowering (Figure 3.30). The fitted zero field hole mobility and field dependence of the mobility from this simulation are also more realistic, with $\mu_{p0} = 8.0 \times 10^{-9}$ m^2/Vs and $E_0 = 9.0 \times 10^8$ V/m at 270K. These values are much closer to published values e.g. $\mu_p = 3.2 \times 10^{-7}$ m^2/Vs and $E_0 = 1.48 \times 10^9$ V/m at 300K [49]. However, the temperature dependence of μ_{p0} is also much weaker than published values, again decreasing by just over an order of magnitude as the temperature was reduced from 270K to 170K, and then remaining approximately constant from 170K to 130K. E_0 also increased as T decreased from 270K down to 170K, but was constant from 170K to 130K. ϕ_{bp} was fitted to be 0.54eV at 270K, which clearly indicates the device is injection limited, but as for the previous case, decreased linearly with temperature.

Both approaches to modelling the experimental J-V characteristics yielded quite good fits, as can be seen in Figures 3.30 and 3.33, but clearly they cannot both be correct and one must examine the other factors in an attempt to understand the data.

Firstly, the fitted zero field hole mobilities vary by approximately an order of magnitude at 290K. The mobilities obtained from the simulation neglecting the contribution of barrier height lowering are lower than those obtained from the model by including the image barrier lowering, albeit with a higher dielectric constant, and are also much lower than those in the literature. This indicates that the fit using barrier lowering, with ϵ_s=5.5 is more realistic. However, the temperature dependence of μ_{p0} is quite similar for both simulations, with μ_p

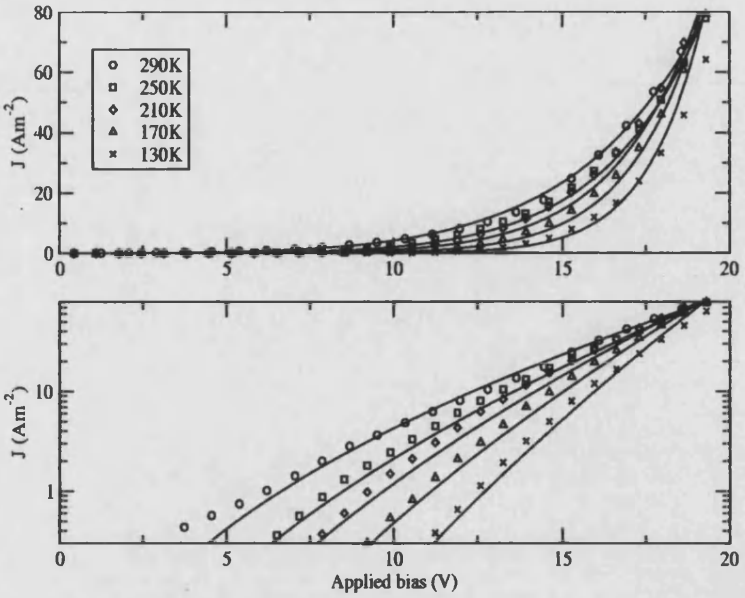

Figure 3.33: Simulated and experimental J-V characteristics for the ITO/TPD/Al device over a range of temperatures, with barrier lowering and ϵ_s=5.5. Shapes represent experimental data, solid lines represent simulated best fit.

decreasing at approximately the same rate with temperature in each case. In the case where barrier lowering was used. the mobility decreased with decreasing temperature down to 170K before becoming constant, whereas in the case where barrier lowering was not used, it becomes constant below 210K. In either case, the temperature dependence of the mobility is too small. Although in the previous section the fitted hole mobility in MEH-PPV became constant below about 200K, the temperature dependence of the fitted hole mobility between 200 and 300K was comparable to experimentally obtained values. Again this raises questions about the validity of the model over a wide temperature range, as the mobilities should continue to decrease with decreasing temperature.

The fitted field dependence of the hole mobility, E_0, also shows great variation between the two modelling approaches. In the case where barrier lowering is omitted, then the value of E_0 is much lower than in the case where it is included; this value of E_0 indicates that the mobility is strongly field-dependent and this determines the slope of the J-V curve above V_{bi} in the absence of barrier lowering (section 3.1). If barrier lowering is included (using ϵ_s=5.5), then E_0 is larger, since the barrier lowering also contributes to the slope of the J-V characteristics. However, in both cases, the fitted value of E_0 has a very small temperature dependence, whereas E_0 varies strongly with temperature not only in TPD e.g. [50], but in all organic semiconductors.

In the case of the simulation without barrier lowering, the fitted barrier heights, particularly at higher temperatures, are in good agreement with the conclusion of Campbell et al [16] that the current was injection limited, since the barrier height was >0.3eV above 210K; below this, the value of ϕ_{bp} was fitted to be less than 0.3eV, the region in which the contact can start to behave Ohmically, and SCLC can occur. When barrier lowering was used in the model the barrier heights were found to be >0.3eV for all temperatures, with a value of 0.54eV at 270K, indicating injection limited behaviour as suggested by Campbell et al [16]. Ultraviolet spectroscopy (UPS) has given the barrier between ITO and TPD to be 0.5eV at room temperature, in good agreement with the result obtained here of 0.54eV at 290K [51]. Campbell et al [16] used an analytic expression for thermionic emission which they fitted to their J-V characteristics, yielding a value of ϕ_{bp} of 0.24eV, which is a value which would normally lead to SCLC current flow, thus the contact behaves as an Ohmic contact, in stark contrast to their experimental findings suggesting that the device should be injection limited. However, in their analytical model, they neglected the back-flowing current at the interface, whereas Davids et al [2] have shown that the thermionic emission and interfacial recombination currents are similar in magnitude.

Although the fitted values of ϕ_{bp} in both simulations indicate that the device is injection limited, in agreement with the conclusions of Campbell et al [16], the temperature variation of ϕ_{bp} is interesting. The fitted barrier height decreases linearly over the entire temperature range for both simulations, decreasing by 0.24eV in the case without barrier lowering and 0.22eV in the case with barrier lowering. This variation corresponds to a variation of 1.7meV/K and 1.6meV/K in the simulations without and with barrier lowering respectively; this is larger than the 1meV/K found when fitting the temperature dependent J-V characteristics of the MEH-PPV device in the previous section. In fitting the barrier height to the MEH-PPV device in the previous section, ϕ_{bp} decreased linearly with decreasing temperature down to 190K before becoming constant. A potential explanation that was proposed for this behaviour was the freezing out of ring torsions in MEH-PPV. In TPD, such a situation does not occur [41], which could explain the fact that ϕ_{bp} decreases over the entire temperature range, although if this trend were to continue, the barrier height would become negligible at low temperatures. No data was found relating to the band gap shrinkage with temperature for TPD. As in the case for the MEH-PPV device in the previous section, this strong temperature dependence of ϕ_{bp} may well indicate that the

temperature dependence of the thermionic emission model is incorrect.

From the issues considered above, it would appear that the most likely explanation for the observed J-V characteristics is an increased value of ϵ_s, whilst retaining barrier height lowering, as opposed to completely disregarding barrier height lowering; however, a value as high as 5.5 has not been reported for ϵ_s in organic semiconductors. It is quite possible that an interfacial layer or dipole layer at the ITO/TPD interface could be responsible for the observed J-V characteristics e.g. [52][12], whether by locally causing changes in ϵ_s or by other mechanisms. For example, interfacial layers can alter the field next to the barrier, reducing the effect of Schottky lowering, but making the barrier height a function of bias e.g. [53]. If such an effect at the ITO/TPD interface is responsible, rather than ϵ_s being 5.5 for the entire TPD layer, then this could explain why although good fits to the J-V characteristics to the data could be obtained, the temperature dependences of μ_{p0}, E_0, and ϕ_{bp} do not appear to be correct. In the model a higher value of ϵ_s is being used than is actually present in order to reduce the effectiveness of Schottky barrier lowering at the ITO/TPD interface, replicating the true behaviour of the barrier in this case, but obscuring the transport physics in the device.

As for the MEH-PPV device in the previous section, the experimentally determined efficiency, calculated simply as L/I, was found to increase upon cooling at constant bias by a factor of approximately 20 as the temperature was decreased from 290K to 50K. As in the previous section, this was investigated using the model by varying ϕ_{bn}, using the previously fitted values of ϕ_{bp}, E_0, and μ_{p0}, in order to obtain an increase in internal quantum efficiency as T was decreased. This was repeated for $\mu_{n0} = 0.01\mu_{p0}, 0.1\mu_{p0}$ and μ_{p0}. Barrier lowering was used in the simulation, with ϵ_s=5.5. Figure 3.34 shows the fitted electron barrier height, ϕ_{bn}, required at each temperature in order to achieve an increase in efficiency at 15V, and the relative quantum efficiency obtained using this value of ϕ_{bn}.

It can be seen that in order to achieve even a small increase in efficiency, a large decrease in ϕ_{bn} is necessary; the fitted electron barrier height decreases at a rate of 7meV/K (compared to 5meV/K for the MEH-PPV device). This rate of decrease for ϕ_{bn} is much greater than the rate of decrease for ϕ_{bp}, again suggesting that other factors must also be responsible for the increase in efficiency. As concluded for the MEH-PPV device, it is likely that the rapid decrease of ϕ_{bn} in the

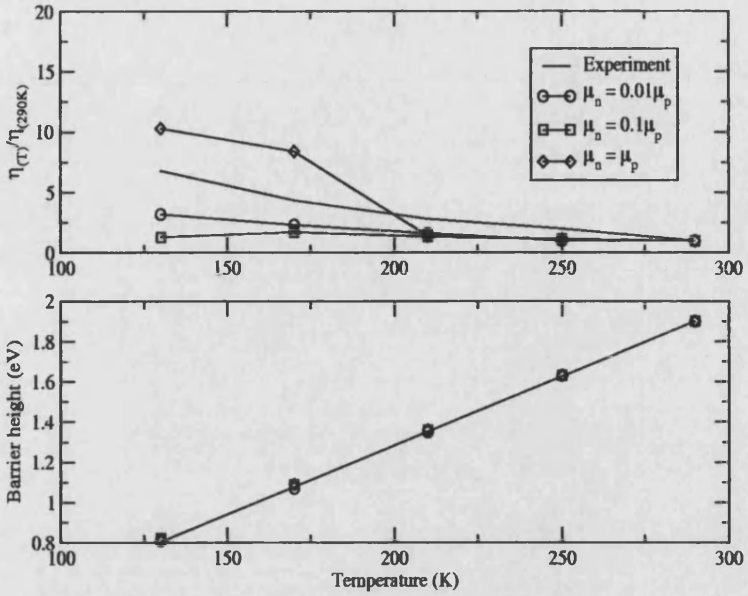

Figure 3.34: Relative efficiency compared to efficiency at 290K as a function of T at 15V (top panel), and the fitted electron barrier height, ϕ_{bn}, required to achieve an increase in efficiency at 15V (bottom panel).

model increases the electron density near the contact, increasing the recombination efficiency, whereas in the real device the carrier mobilities may converge, and the recombination zone is shifted away from the cathode as discussed in the previous section. It is possible that this larger rate of change for ϕ_{bn} compared to that found in the MEH-PPV device could be due to the reduced barrier lowering caused by the larger value of ϵ_s. Since barrier lowering is less effective in this case, the barrier height must be decreased more in order to inject a sufficient electron density in order to cause an increase in efficiency. This could be partial evidence for the dielectric constant being ~ 3 in the device, with other effects at the ITO/TPD interface being responsible for the observed J-V characteristics. However, due to the possibility of the parameters used in this simulation being incorrect as a result of trying to model interfacial effects, it is difficult to draw any firm conclusions from these results.

3.4 Cathode dependent J-V characteristics of a single layer NPB device

A set of J-V characteristics for devices having an ITO/PEDOT/NPB/Cathode structure, with the thickness of the NPB layer being 130nm [54], were investigated. The PEDOT layer was highly doped with PSS and can be considered to be essentially metallic [55]. PEDOT is used as a hole injecting electrode, owing to its large workfunction, and for the purposes of the simulation, the workfunction of the PEDOT layer is used as the workfunction of the anode; the ITO is simply ignored in the model. The cathodes used were Al, Al:Li, and LiF/Al, with LiF layer thicknesses of 2nm and 7nm. The measured electrode workfunctions are given below in Table 3.4. A schematic energy band diagram of the device is shown in Figure 3.35, and the experimentally obtained J-V characteristics are shown in Figure 3.36.

Electrode material	ϕ_m (eV)
PEDOT [56]	5.2
Al [54]	4.2±0.1
Al:Li [54]	3.8±0.1
LiF(2nm)/Al [54]	3.2±0.1
LiF(7nm)/Al [54]	2.9±0.1

Table 3.5: Workfunctions of the electrodes used.

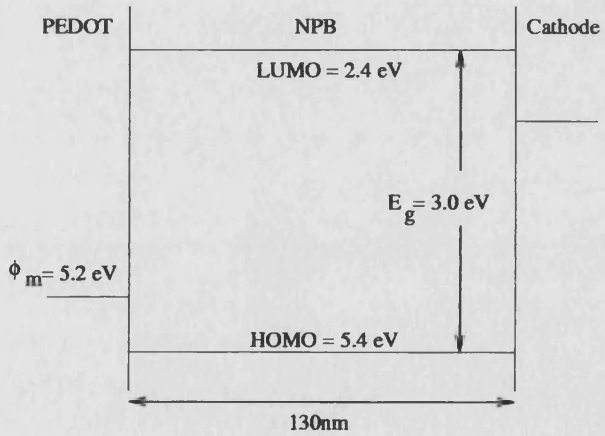

Figure 3.35: Schematic energy band diagram of an ITO/PEDOT/NPB/Cathode device, where Cathode = Al, Al:Li, LiF(2nm)Al, or LiF(7nm)Al. The ITO has been omitted for clarity; the PEDOT layer is considered to be the anode. The HOMO/LUMO levels are taken from [14]

In order to model the experimental data, the NPB was assumed to be trap-free [14][24][57]. The barrier to hole injection was set as 0.2eV, simply given

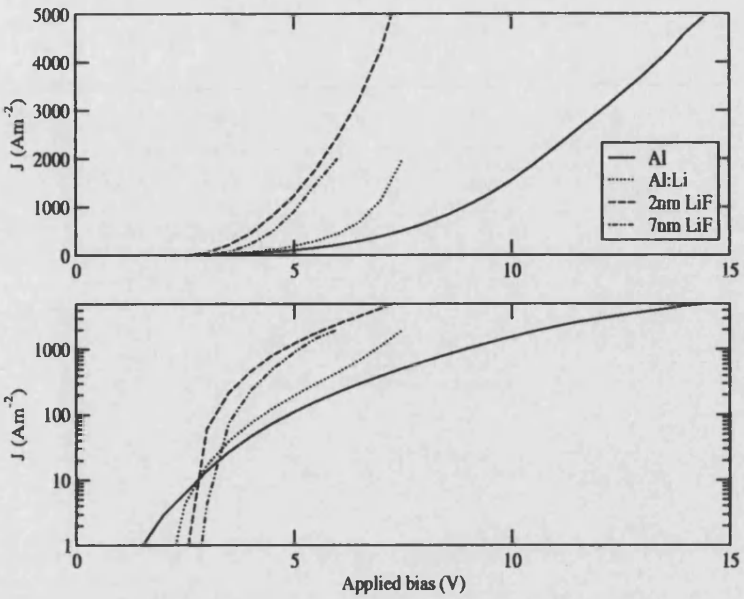

Figure 3.36: Experimentally measured J-V characteristics of an ITO/PEDOT/NPB/Cathode device, where Cathode = Al, Al:Li, LiF(2nm)/Al, or LiF(7nm)/Al.

by the difference of the workfunction of PEDOT and the HOMO level of NPB since PEDOT is well characterised and known to form good interfaces [41]. The barrier to electron injection, ϕ_{bn}, was also taken to be the difference between the workfunction of the cathode (Table 3.4) and the LUMO level of the NPB. The zero-field hole mobility and its field-dependence, μ_{p0} and E_0 respectively, were determined by fitting (as described in section 3.1). The electron mobility is not well known in NPB, but was assumed to be much lower than the hole mobility ($\mu_n = 0.01\mu_p$). All other parameters used were the same as those contained in section 3.1.

The first device simulated was the ITO/PEDOT/NPB/Al device, since the workfunction of Al is very well known, and because the very large barrier to electron injection (ϕ_{bn}=1.8eV) ensures that the device is hole-only. Figure 3.37 shows the best fit of the simulated curve to the experimental data, obtained using the following values: $\mu_{p0} = 9.0 \times 10^{-11}\text{m}^2/\text{Vs}$, $E_0 = 8.0 \times 10^6\text{Vm}^{-1}$, ϕ_{bp}=0.2eV.

It can clearly be seen from Figure 3.37 that the simulated J-V characteristics provide an excellent fit to the experimental data across almost the entire voltage range. Additionally, a field-dependent SCLC fit to the experimental data (equation 2.49), using the fitted parameters of $\mu_{p0} = 9.0 \times 10^{-11}\text{m}^2/\text{Vs}$ and $E_0 = 8.0 \times 10^6\text{Vm}^{-1}$, was also found to give an excellent fit to the data, and is

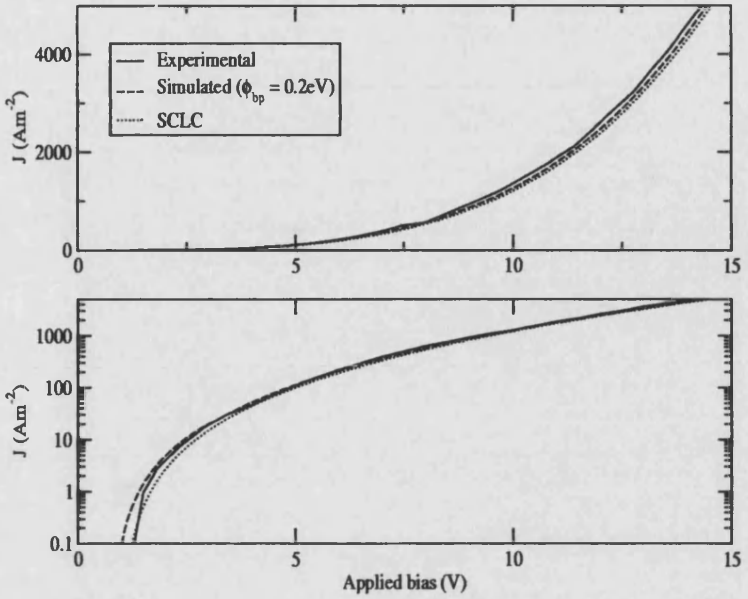

Figure 3.37: Simulated and experimental J-V characteristics of the ITO/PEDOT/NPB/Al device. Dotted lines indicate a field-dependent SCLC fit, corrected for V_{bi}, for the same parameters.

essentially an identical fit to the one provided by the simulation above V_{bi}. This result is not entirely unexpected; in section 3.1 it was noted that for small values of ϕ_{bp} (< 0.3eV), the J-V characteristics of a single layer unipolar device can tend towards the SCLC limit i.e. the injecting contact begins to behave as an Ohmic contact. In the literature, Brütting et al [14] obtained values of 1.0×10^{-8} m^2/Vs for μ_{p0} and 4.4×10^7 for E_0, whilst Giebeler et al [48] published a value of 1.0×10^{-7} m^2/Vs for μ_{p0}. The value of E_0 obtained from the simulation is acceptable and its difference to the published value could simply be due to the values being obtained from different samples. However, the value of μ_{p0} obtained from the simulation is several orders of magnitude lower than the published values; it is unlikely that this difference can be explained by the fact that the published and simulated values of μ_{p0} are for different samples of NPB.

The next device simulated, the ITO/PEDOT/NPB/Al:Li device, also has a very large barrier to electron injection ($\phi_{bn} = 1.4 \pm 0.1$eV). Hence, this device should also be unipolar and since the same PEDOT anode is used, the current should again tend towards the trap-free SCLC limit with the same parameters. The only difference between the devices is their built-in potentials; in the Al device, $V_{bi} = 1$V, whilst for the Al:Li device it is 1.4±0.1V. Therefore there should only be a very small difference in their J-V characteristics owing to this difference in the built-in potentials, as discussed in section 3.1. The first difference is that

of the turn-on voltage, where the applied voltage equals the built-in field; at this voltage, the flat-band condition is then reached and above this bias, carriers can be injected. On the log-linear J-V characteristics, this corresponds to the change from a steep slope to a shallower one at a bias approximately equivalent to V_{bi}. The second difference is that for the Al:Li device, the field drifting the carriers through the device at a given bias is slightly lower than that in the Al device, owing to the larger built-in field, and hence the current will be slightly lower. However, in the SCLC regime, this difference will be negligible even at modest voltages. Figure 3.38 shows the simulated J-V characteristics of the ITO/PEDOT/NPB/Al:Li device compared to those of the device with the Al cathode; the parameters used in the simulation are identical to those used for the ITO/PEDOT/NPB/Al device, except for the value of ϕ_{bn}, which was taken to be 1.4eV.

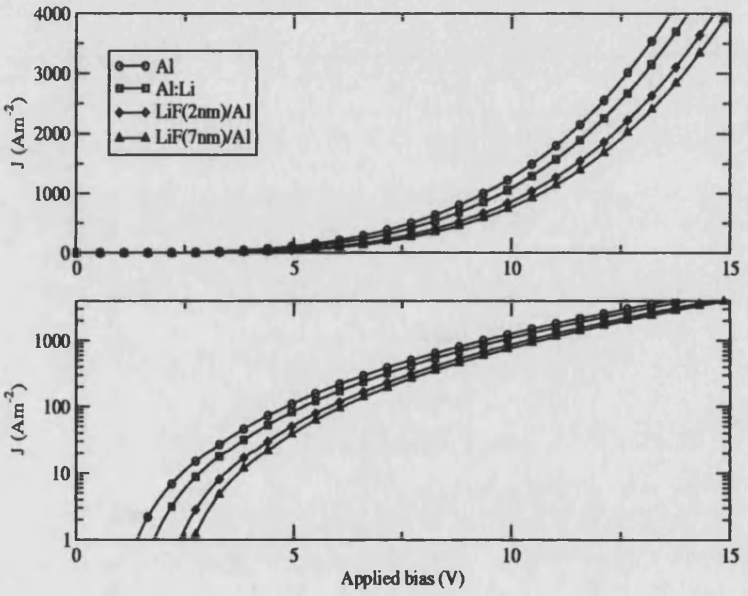

Figure 3.38: Simulated J-V characteristics of the ITO/PEDOT/NPB/Cathode device, where Cathode = Al, Al:Li, LiF(2nm)/Al, or LiF(7nm)/Al.

Figure 3.38 shows that the simulated J-V characteristics of the device with the Al:Li cathode behave as discussed above, with the current tending towards the same space-charge limit as for the device with the Al cathode at high fields. However, the simulated J-V curve does not correlate at all with the experimental data (Figure 3.36), being a factor of approximately 2 smaller than the experimental J-V curve at an applied bias of 5V, and an even greater factor at higher biases. An examination of the experimental data (Figure 3.36) confirms that the built-in potential is greater in the Al:Li device, due to the position of the turn-on point

on the log-linear J-V plot, as expected. However, the fact that the experimentally measured device current in the device with the Al:Li cathode is greater than that in the device with the Al cathode defies the explanation given above for the expected form of the J-V characteristics.

Simulated J-V characteristics of the ITO/PEDOT/NPB/LiF(2nm)/Al and LiF(7nm)/Al devices, keeping all parameters the same except for ϕ_{bn}=0.8 and 0.5eV respectively, are also shown in Figure 3.38. As expected, the current decreases with decreasing values of ϕ_{bn} due to an increase in V_{bi}. However, it can be seen that the current measured experimentally is largest in the device with the LiF(2nm)/Al cathode, followed by that in the device with the LiF(7nm)/Al cathode, followed by that in the device in with the Al:Li cathode, and finally by that in the device with the Al cathode, which is not what is expected assuming the devices to have trap-free space-charge limited currents and different values of V_{bi} (section 3.1). It is interesting to note, however, that the current in the device with the LiF(7nm)/Al cathode is lower than that of the device with the LiF(2nm)/Al cathode, which is expected by considering their relative built-in potentials. A number of potential explanations presented were considered, and are discussed below.

Perhaps the most obvious solutions involve the values of the carrier mobilities, μ_n and μ_p. If μ_p varied in each device, then since the devices have space-charge limited currents owing to the small hole barrier, ϕ_{bp}, an increase in μ_p would result in a larger device current. However, in order for this to be the explanation, the mobility would also have to vary by over an order of magnitude between the devices. This variation in μ_p could be due to sample preparation, which is unlikely since the samples were fabricated together in the same manner. The only other explanation for the variation in μ_p is that is a consequence of using different cathode materials; however, there is no evidence to suggest that this is the case. Neither of these explanations account for the low value of the hole mobility found in the device with the Al cathode compared to published values. Alternatively, it was considered that the electron mobility, μ_n, in NPB might be much greater than the value used in the solution ($\mu_n = 0.01\mu_p$); however, increasing the electron mobility to the extent that $\mu_n = \mu_p$ left the simulated J-V characteristics unchanged. This result is consistent with the device physics considered thus far, since for the devices with Al and Al:Li cathodes, the large barriers to electron injection ($\phi_{bn} = 1.8$ and 1.4eV respectively) mean that the

injected electron density is negligible compared to the hole density in the device, and hence a variation in the electron mobility will have no significant bearing on the device current. For the two devices with LiF/Al cathodes, the barriers to electron injection are still large (ϕ_{bn} = 0.8 and 0.5eV for LiF thicknesses of 2nm and 7nm respectively), but allow greater electron injection. However, compared to the SCLC hole current provided by the quasi-Ohmic PEDOT/NPB contact, the electron current is still negligible and varying μ_n cannot provide a significant increase in device current.

Space-charge neutralisation can occur when both contacts in a device are Ohmic and supply large numbers of electrons and holes to the bulk (section 2.4.3); this allows much higher charge densities to exist within the device, and hence the device can support a larger current than unipolar SCLC. As a device makes the transition from single carrier SCLC to double carrier SCLC, there will be an increase in the current, which is dependent upon the relative carrier mobilities, but may be as much as several orders of magnitude [58]. However, such an explanation cannot account for the observed variation in the experimental J-V characteristics with cathode material, since the barrier to electron injection, ϕ_{bn}, in all cases is too large ($\geq$ 0.5eV) for the electrode to be considered Ohmic. As previously mentioned, ϕ_b needs to be below 0.3eV for a contact to start behaving Ohmically. Hence the device current cannot be considered to be double carrier SCLC since the magnitude of the electron density is far too small compared to the hole density within the bulk to cause any appreciable charge neutralisation and subsequent increase in current density.

Murata et al [59] showed that a barrier to electron extraction in a device can cause an electron build up at the anode; an increased field is associated with this charge build-up, which in turn can enhance hole injection. Such a situation could not increase the device current, since the hole current is already space-charge limited, without significant space-charge neutralisation, which has already been rejected on the grounds that the values of ϕ_{bn} are too large in all the devices.

The final explanation is that of traps. Figure 3.39 shows a log-log plot of the experimental J-V curves for all of the devices.

Further inspection of Figure 3.39 reveals a form reminiscent of Figure 2.9 in section 2.4.2, for space-charge limited current with traps. It can be seen that at

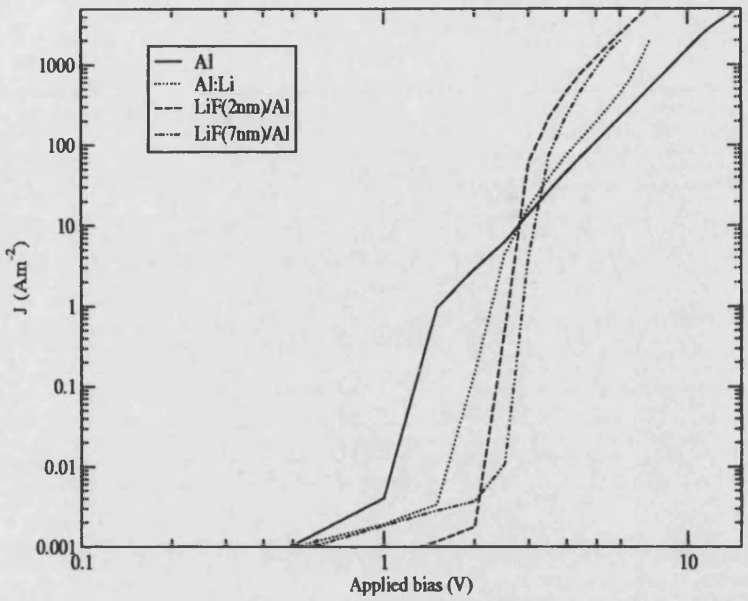

Figure 3.39: Experimental J-V characteristics for all the devices on a log-log plot.

V_{bi} (V_{bi}=1.0V, 1.4V, 2.0V and 2.3V for the devices with Al, Al:Li, LiF(2nm)/Al and LiF(7nm)/Al respectively), which corresponds to V_ω in section 2.4.2, the gradient changes from the Ohmic region as holes are injected, becoming very steep, and then following a SCLC form as the traps are filled (this also accounts for the deviation between the simulated and experimental J-V characteristics in Figure 3.37 at low biases). This sharp transition from the Ohmic to trap-filled limit SCLC is indicative of a discrete or narrow distribution of deep levels (section 2.4.2). The current at high fields is then the SCLC current, reduced by a factor determined by the ratio of free to trapped charge. This could explain why the J-V characteristics of the ITO/PEDOT/NPB/Al device simulated initially fitted the experimental data so well, yet yielded a much lower value of μ_p. In the trap free simulation, a reduced hole mobility compensated for the fact than in the real device, many holes were in fact trapped and unable to carry a current, whilst the form of the J-V curve was correct.

Therefore a possible explanation for the experimental J-V characteristics of these devices is given by the fact that if the hole trap concentration is high enough, it can severely reduce the hole current, J_p, flowing in the device. In this way, the electron currents, J_n, injected from the cathode, although small due to the relatively large values of ϕ_{bn}, can become comparable to the hole current. Hence the reduction of ϕ_{bn} with the variation of the cathodes increases the electron current, which is actually a significant fraction of the overall device current, increasing

the overall device current as observed in the experimental J-V characteristics. However, such a situation required a very high hole trap density ($> 10^{24}\mathrm{m}^{-3}$); even using a high value for μ_{p0} and setting $\mu_{n0} = \mu_{p0}$ in the simulation, the large values of ϕ_{bn} involved meant that the overall device current was very low, and many orders of magnitude lower than the experimentally obtained device current.

It is interesting to note from Figure 3.36 that whilst the current in the Al:Li device is greater than that in the Al device, which is unexpected in a trap-free device by considering V_{bi}, the current in the device with LiF(7nm)/Al cathode is lower than the device with the LiF(2nm)/Al device as expected. It was then postulated as to whether the devices with LiF/Al cathodes could be trap-free. Figure 3.40 shows fits to the experimental data for the devices with LiF(2nm)/Al and LiF(7nm)/Al cathodes, using all the parameters as previously discussed, but with $\mu_{p0} = 2.5 \times 10^{-9}$ m^2/Vs and $E_0 = 1.0 \times 10^7$ V/m for both devices.

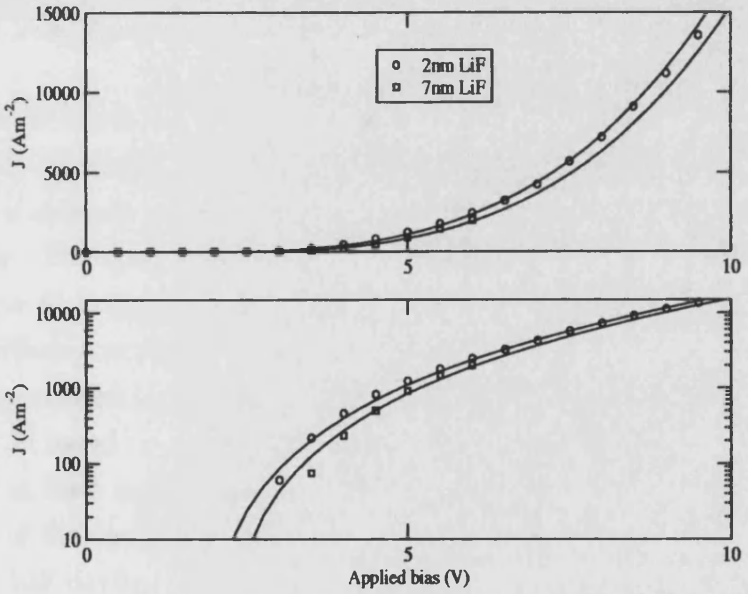

Figure 3.40: J-V characteristics of an ITO/PEDOT/NPB/LiF(2nm)/Al device and an ITO/PEDOT/NPB/LiF(7nm)/Al device. Shapes represent experimental data, solid lines represent simulated data. Fitted values: $\mu_{p0} = 2.5 \times 10^{-9}$ m^2/Vs, $E_0 = 1.0 \times 10^7$ V/m.

It can be seen from Figure 3.40 that these values provide excellent fits to the data, and are trap-free SCLC curves. The value of μ_{p0} is much more reasonable for a hole transporting material, although still a bit low compared to the published values. A discrete level of traps was then introduced into the ITO/PEDOT/NPB/Al device, with $N_t = 2.5 \times 10^{23}$ m^{-3} and E_t=2.7eV. Figure 3.41 shows the fit to the experimental data with these trap parameters, and the values of μ_p and E_0 used for the LiF/Al devices.

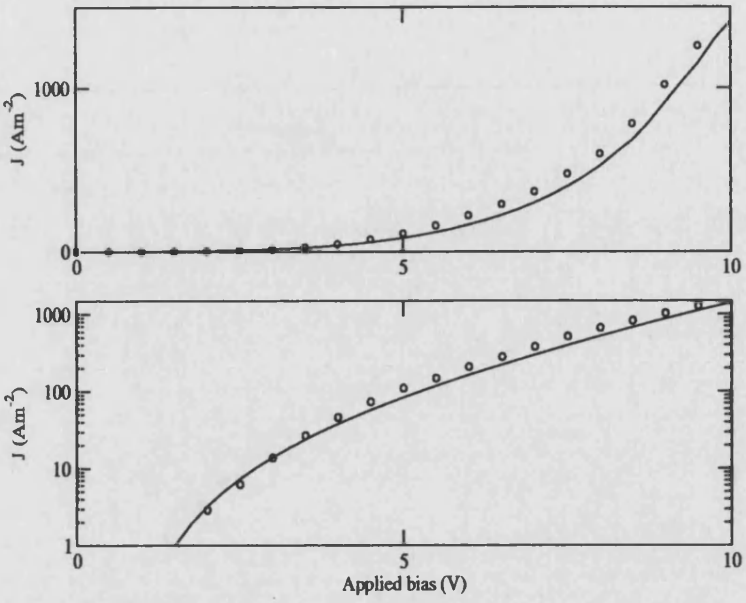

Figure 3.41: J-V characteristics of an ITO/PEDOT/NPB/Al device. Shapes represent experimental data, solid lines represent simulated data. Fitted values: $\mu_p = 2.5 \times 10^{-9}$ m^2/Vs, $E_0 = 1.0 \times 10^7$ V/m, E_t=2.7eV, $N_t = 2.5 \times 10^{23}$ m^{-3}.

Although the fit is not as good as for the trap-free devices in the previous Figure, the fit is still reasonable and proves the concept; without more information on the traps it is difficult to fit exactly to the data by varying the trap parameters and mobility. The question that naturally arises, then, is as to why traps are present in the Al and Al:Li devices, but not the LiF/Al devices. One would not expect the different samples of NPB to be radically different in terms of trapping, so it could be related to the cathode. More information is needed to investigate whether the Al based cathodes could introduce traps, even if local to the NPB/Al interface, or at least more traps compared to LiF based cathodes. It could be the case that all of the devices had some hole traps, which would mean that the value of μ_{p0} in the LiF devices should actually be higher; this is reasonable considering the published values for μ_{p0} in NPB. The decrease in currents for the different devices could therefore be linked to an increase in hole trapping.

3.5 Conclusions

The first section of the chapter, section 3.1, demonstrates the sensitivity of the model to the variation of parameters, or the effects of having poorly characterised materials, a common problem with disordered organic semiconductors

and OLEDs themselves. Clearly, fitting to experimental data can only be done where there are just a few parameters to be discovered, normally ϕ_{bp}, μ_{p0} and E_0. Many parameters can produce similar effects on the simulated J-V characteristics; for example, varying the barrier to injection or carrier mobility can both similarly affect the current magnitude, but the value of ϕ_{bp} also affects the value of V_{bi} which can be seen on the experimental J-V characteristics. Therefore the knowledge of how different parameters can affect J-V characteristics is crucial when interpreting and fitting simulated to experimental data. The model is more useful than analytical expressions since it can be used to obtain the best fit to the experimental data without making decisions regarding the nature of the contacts. The model can be useful for obtaining values of the mobility, for example, especially when they cannot be obtained from experimental data such as time of flight measurements [22][60].

In section 3.2, the temperature-dependent J-V characteristics of an injection-limited ITO/MEH-PPV/Al device have been successfully modelled, yielding values of Δ=0.27eV, $\mu_{p0} = 1 \times 10^{-5}$ m ^{2} /Vs, T_0 =325K, and B = 1.3×10^{-5} eV/mV $^{1/2}$, in good agreement with values in the literature. This has shown that the energy band approximation to organic semiconductors, and the thermionic emission model used for injection, are applicable, at least at high temperatures (>200K). Below this, it is possible that the traditional concept of a mobility is invalid due to transport becoming more dispersive, and the injection model may have the wrong temperature dependence. Further work on the temperature dependence of both the barrier height and carrier mobilities through the modelling of temperature dependent J-V characteristics would be useful. Attempting to investigate the temperature dependence of the efficiency in this device required the electron barrier height, ϕ_{bn}, to decrease more strongly with temperature than ϕ_{bp} such that a large electron concentration at the cathode increases the calculated recombination current. This modelling has highlighted the fact that whilst the model includes a valid form for recombination, other factors such as the quenching of excitons are not included, and their absence makes predictions regarding anything other than the recombination efficiency impossible. The fitting of a discrete trap level in the MEH-PPV was found to improve the fit to the experimental data at low biases and high temperatures, but made the fit worse at low temperatures. It is impossible to draw any conclusions regarding the existence of traps from this evidence and without further information, but the presence of traps is certainly a strong possibility and cannot be discounted.

The modelling of the temperature-dependent J-V characteristics of the ITO/TPD/Al device in section 3.3 turned up some surprising results. The dielectric constant, ϵ_s, fitted was larger than has been measured for this device experimentally (5.5 instead of 3.0) or quoted elsewhere in the literature. There is no clear indication as to whether this might be a value for the bulk material, or whether it is perhaps local to the interface. Using this large value of ϵ_s in the simulation reduces the effectiveness of Schottky barrier lowering in the model, possibly replicating the behaviour caused by effects at the interface such as dipole or interfacial layers, which can affect injection and barrier lowering. Clearly, more work investigating the nature of electrode/organic semiconductors and their effect on OLED performance is required. It is therefore difficult to be confident about the fitted values of μ_{p0}, E_0 and ϕ_{bp} given that the injection mechanism may be altered by interfacial effects, and the large value of ϵ_s will have affected the transport in the model. Nevertheless, the simulation found a barrier height which was consistent with the experimental observation that the device was injection limited; Campbell et al [16] found that fitting an analytical expression to the experimental data yielded a value for ϕ_{bp} which was more likely to be Ohmic, which clearly could not be the case. The analytical expression used neglected the importance of backflowing current at the Schottky contact, and clearly could not highlight the issue which caused the value of ϵ_s in the simulation to be much greater than the measured value. This confirms the benefits of device models, which do not make such assumptions, and using the knowledge gained in section 3.1, such models allow other issues to be investigated. Again, attempting to investigate the increase of device efficiency with decreasing temperature required the electron barrier height, ϕ_{bn}, to decrease rapidly with temperature in order to create a recombination peak near the cathode to compensate for the omission of quenching and optical effects from the model.

Modelling the J-V characteristics of a set of NPB devices with different cathodes in section 3.4 points to the existence of deep trap levels as the cause for the observed J-V characteristics. More information is required regarding the existence of traps in NPB, both to aid the fitting of data by providing information about trap depths and concentrations, and to answer the questions of whether the traps are dependent on the cathode material. Simulating the ITO/PEDOT/NPB/Cathode series of devices in section 3.4 shows some of the potential problems of modelling data or using analytical expressions to analyse experimental J-V data. If only one device had been modelled, the traps would not have been such a likely ex-

planation for the low mobility. However, having a set of devices to characterise is useful for both testing and validating the device model, as well as investigating unexpected behaviour.

The drift-diffusion model can certainly be seen to work well in terms of simulating the J-V characteristics of single layer OLEDs, and as well as good fits to the data providing material parameters, the model can also be used to make qualitative explanations of device behaviour. The temperature dependent efficiency could not be properly explained using the model, but this is perhaps not unsurprising since essential parts of the recombination and emission process, including exciton diffusion and quenching, are not included in the model. A more accurate determination of the behaviour of the electron mobility could also help; this could be obtained by obtaining accurate values for ϕ_b, E_0, and μ_0 for each carrier by modelling an electron only device and a hole only device separately.

References

[1] C D J Blades, *Ph.D. Thesis*, University of Bath (1999).

[2] P S Davids, I H Campbell, and D L Smith, *J. Appl. Phys.*, **82**, 6319 (1997).

[3] G G Malliaras and J C Scott, *J. Appl. Phys.*, **83**, 5399 (1998).

[4] D J Pinner, R H Friend, and N Tessler, *J. Appl. Phys.*, **86**, 5116 (1999).

[5] G Hadziioannou and P F van Hutten (eds.), *Semiconducting Polymers: Chemistry, Physics and Engineering*, Wiley-VCH, Weinheim (2000).

[6] S J Martin, *Unpublished data.*

[7] P W M Blom, M J M de Jong, and J J M Vleggaar, *Appl. Phys. Lett.*, **68**, 3308 (1996).

[8] P W M Blom, M J M de Jong, and M G van Munster, *Phys. Rev. B*, **55**, R656 (1997).

[9] P W M Blom, H C F Martens, and J N Huiberts, *Synth. Met.*, **121**, 1621 (2001).

[10] T Aernouts, W Geens, J Poortmans, J Nijs, and R Mertens, *Synth. Met.*, **122**, 153 (2001).

[11] D Sainova, H Fujikawa, U Scherf, and D Neher, *Optical Materials*, **12**, 387 (1999).

[12] W R Salaneck, S Stafström, and J-L Brédas, *Conjugated polymer surfaces and interfaces*, Cambridge University Press, Cambridge, UK (1996).

[13] W Brütting, M Meier, M Herold, S Karg, and M Schwoerer, *Chem. Phys.*, **227**, 243 (1998).

[14] W Brütting, S Berleb, and A G Mückl, *Organic Electronics*, **2**, 1 (2001).

[15] W Brütting, M Meier, M Herold, S Karg, and M Schwoerer, *Synth. Met.*, **91**, 163 (1997).

[16] A J Campbell, D D C Bradley, J Laubender, and M Sokolowski, *J. Appl. Phys.*, **86**, 5004 (1999).

[17] C D J Blades, *Private communication.*

[18] S M Sze, *Physics of Semiconductor Devices*, 2nd. ed., Wiley Inter-Science, New York (1981).

[19] L Bozano, S A Carter, J C Scott, G G Malliaras, and P J Brock, *Appl. Phys. Lett.*, **74**, 1132 (1999).

[20] J M Lupton, *Private communication.*

[21] J M Lupton, *Appl. Phys. Lett.*, **80**, 186 (2002).

[22] I H Campbell and D L Smith, *Solid State Physics: Advances In Research and Applications*, **55**, 1 (2001).

[23] J M Lupton and I D W Samuel, *Synth. Met.*, **111-112**, 381 (2000).

[24] J Staudigel, M Stößel, F Steuber, and J Simmerer, *J. Appl. Phys.*, **86**, 3895 (1999).

[25] A J Campbell, D D C Bradley, and D G Lidzey, *J. Appl. Phys.*, **82**, 6326 (1997).

[26] P E Burrows, Z Shen, V Bulovic, D M McCarty, S R Forrest, J A Cronin, and M E Thompson, *J. Appl. Phys.*, **79**, 7991 (1996).

[27] A J Campbell, D D C Bradley, and H Antoniadis, *J. Appl. Phys.*, **89**, 3343 (2001).

[28] T Kreouzis, *Unpublished data.*

[29] A J Campbell, *Unpublished data.*

[30] J M Lupton, *Unpublished data.*

[31] S J Martin, J M Lupton, I D W Samuel, and A B Walker, *J. Phys.: Cond. Matt.*, **14**, 9925 (2002).

[32] J M Lupton and I D W Samuel, *J. Phys. D: Appl. Phys.*, **32**, 2973 (1999).

[33] F Cacialli, J S Kim, T M Brown, J Morgado, M Granström, R H Friend, G Gigli, R Cingolani, L Favaretto, G Barbarella, R Daik, and W J Feast, *Synthetic Metals*, **109**, 7 (2000).

[34] A K Mahapatro and S Ghosh, *Appl. Phys. Lett.*, **80**, 4840 (2002).

[35] I H Campbell, P S Davids, D L Smith, N N Barashkov, and J P Ferraris, *Appl. Phys. Lett.*, **72**, 1863 (1998).

[36] I H Campbell, T W Hagler, D L Smith, and J P Ferraris, *Phys. Rev. Lett.*, **76**, 1900 (1996).

[37] W G Gill, *J. Appl. Phys.*, **43**, 5033 (1972).

[38] A K Sheridan, J M Lupton, I D W Samuel, and D D C Bradley, *Chem. Phys. Lett.*, **322**, 51 (2000).

[39] V I Arkhipov, E V Emelianova, Y H Tak, and H Bässler, *J. Appl. Phys.*, **84**, 848 (1998).

[40] M A Abkowitz, H A Mizes, and J S Facci, *Appl. Phys. Lett.*, **66**, 1288 (1995).

[41] D D C Bradley, *Private communication.*

[42] Z G Yu, D L Smith, A Saxena, R L Martin, and A R Bishop, *Phys. Rev. Lett.*, **84**, 721 (2000).

[43] H L Gomes, P Stallinga, H Rost, A B Holmes, M G Harrison, and R H Friend, *Appl. Phys. Lett.*, **74**, 1144 (1999).

[44] A V Yakimov, V N Savvate'ev, and D Davidov, *Synth. Met.*, **115**, 51 (2000).

[45] R Stratton, *J. Phys. Chem. Solids*, **23**, 1177 (1962).

[46] M Koehler, J R de Lima, M G E da Luz and I A Hummelgen, *Phys. Status Solidi a*, **173**, 29 (1999).

[47] C Hochfilzer, G Leising, Y Gao, E Forsythe, and C W Tang, *Appl. Phys. Lett.*, **73**, 2254 (1998).

[48] C Giebeler, H Antoniadis, D D C Bradley, and Y Shirota, *J. Appl. Phys.*, **85**, 608 (1999).

[49] B Ruhstaller, S A Carter, S Barth, H Riel, W Riess, and J C Scott, *J. Appl. Phys.*, **89**, 4575 (2001).

[50] M Stolka, J F Yanus, and D M Pai, *J. Phys. Chem.*, **88**, 4707 (1984).

[51] K Sugiyama, K Seki, E Ito, Y Ouchi, and H Ishii, *Electrical, Optical and Magnetic Properties of Organic Solid-State Materials IV*, **488**, 719 (1988).

[52] H Ishii, K Sugiyama, E Ito, and K Seki, *Advanced Materials*, **11**, 605 (1999).

[53] H K Hensich, *Semiconductor Contacts*, Clarendon Press, Oxford (1989).

[54] G L B Verschoor, *Unpublished data.*

[55] R H Friend, R W Gymer, A B Holmes, J H Burroughes, R N Marks, C Taliani, D D C Bradley, D A Dos Santos, J L Brédas, M Löglund, and W R Salaneck, *Nature*, **397**, 121 (1999).

[56] T M Brown, J S Kim, R H Friend, F Cacialli, R Daik, and W J Feast, *Appl. Phys. Lett.*, **75**, 1679 (1999).

[57] L B Lin, R H Young, M G Mason, and P M Borsenberger, *Appl. Phys. Lett.*, **72**, 864 (1998).

[58] M A Lampert and P Mark, *Current Injection In Solids*, Academic Press, New York (1970).

[59] K Murata, S Cina, and N C Greenham, *Appl. Phys. Lett.*, **79**, 1193 (2001).

[60] N Tessler, Lecture notes available from http://www.ee.technion.ac.il/people/nir/Lectures.html

Chapter 4

Multi-layer Device Simulation

In order for an OLED to be practical, it needs to have a low operating voltage, and a large fraction of the injected carriers should recombine. As has been demonstrated in Chapter 3, in a single layer device it is difficult to achieve high internal quantum efficiency due to the imbalance in carrier injection and mobility. A large proportion of the majority carriers traverse the device without recombination, whilst the lower mobility of the minority carrier can reduce the width of the recombination zone; both of these factors reduce the recombination efficiency. In order to reduce the operating voltage, the film needs to be as thin as possible, whilst allowing many of the carriers in the film to recombine.

In order to improve the efficiency of OLEDs, multi-layer structures are employed; the different layers have different mobilities and energy levels, allowing more efficient devices to be fabricated by enhanced carrier transport and confinement. Indeed, the first thin-film small molecule OLED reported by Tang and VanSlyke [1] was a bi-layer device, and now polymeric and small molecule OLEDs with many layers e.g. [2][3] have been produced in order to obtain highly efficient devices emitting at desired wavelengths.

Since multi-layer devices are more efficient, there is consequently a lot of interest, particularly commercial [4], in the development of these devices. Hence it is of great importance that device models can be successfully used to simulate multi-layer devices. Although several models reported in the literature are able to model heterostructure devices [5][6][7], little work has been done to compare

experimental and simulated data of multi-layer devices. Partially this is due to the difficulty of modelling multi-layer devices where there are many undetermined material parameters, making it difficult to fit to experimental J-V characteristics. Aside from J-V characteristics, it is also difficult to find experimental data which can be compared directly to the simulated device characteristics. This chapter demonstrates that our model can be used to model bi-layer OLEDs by comparing our simulated results to experimental data.

In section 4.1, the principles behind the use of multiple layers to block or alternatively enhance the transport of carriers across the device are discussed; these concepts are used to understand the results in the subsequent sections. Section 4.2 uses the model to investigate how the efficiency of a bi-layer OLEDs varies with layer thickness, and compares these results to those obtained experimentally. Finally, section 4.3 contains the results obtained from an experimental investigation into the internal electric field distribution of a bi-layer OLED and those obtained from the model.

4.1 Bi-layer devices

4.1.1 Blocking layers

In single layer OLEDs, a large fraction of injected majority carriers will be transported across the device without recombining, due to an imbalance in injection and transport between the two carrier types, reducing the internal quantum efficiency. It is possible to reduce the number of carriers which traverse the device without recombining by the use of a blocking layer e.g. [8]. The blocking layer is a material possessing a different energy band structure to the original layer used in the device. This difference creates an energy barrier which carriers must overcome in order to traverse the device; otherwise, the carriers are blocked by this barrier and accumulate at the interface between the two layers. These carriers which are impeded by the heterojunction can then recombine with the minority carriers, increasing the recombination yield.

Figure 4.1 shows the energy band diagrams of a hole transporting layer (HTL),

on the left hand side, and a hole blocking layer on the right hand side. The HOMO and LUMO levels of the HTL are 5.4eV and 2.5eV respectively, whilst the blocking layer has the same LUMO level, but the HOMO level varies from 5.4eV to 5.9eV. Table 4.1 contains the material parameters of the HTL and blocking layer used in the simulation, which represent typical values.

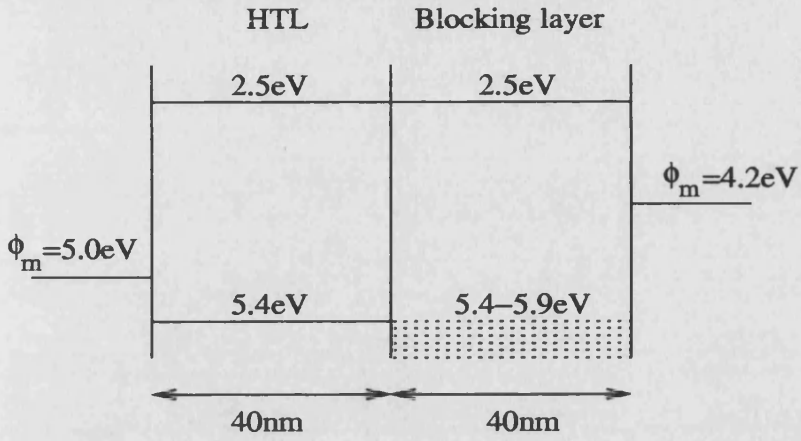

Figure 4.1: Schematic energy band diagram of the bi-layer device with the HTL on the left hand side, and the blocking layer on the right hand side.

Parameter	HTL	Blocking layer	Units
T	300	300	K
d	40	40	nm
ϕ_{bn}	-	1.7	eV
ϕ_{bp}	0.4	-	eV
N_V	1×10^{27}	1×10^{27}	m^{-3}
N_C	1×10^{27}	1×10^{27}	m^{-3}
μ_{p0}	1×10^{-10}	1×10^{-10}	m^2/Vs
μ_{n0}	$0.01\mu_p$	$0.01\mu_p$	m^2/Vs
E_0	1.0×10^8	1.0×10^8	Vm^{-1}
ϵ_s	3.0	3.0	-

Table 4.1: Material parameters used to simulate the bi-layer device.

The device is injection limited (ϕ_{bp}=0.4eV) and hole-only, since the electron barrier is very large (ϕ_{bn}=1.7eV); the presence of electrons is ignored in this discussion. Figure 4.2 shows the J-V characteristics of the device as the barrier for holes entering the blocking layer is increased from 0eV to 0.5eV. As the barrier increases, the device current (which is equivalent to the hole current in this case) decreases as more and more holes are blocked by the interface. A barrier height of just 0.1eV has a negligible effect on the current, as the holes are not significantly impeded by the barrier; for larger barrier heights, the effect becomes much more

pronounced, with a barrier of 0.5eV virtually blocking the entire hole, and device, current. As the blocking layer becomes larger, the voltage required to supply a given current, which is important in terms of the magnitude of the recombination rate, increases substantially.

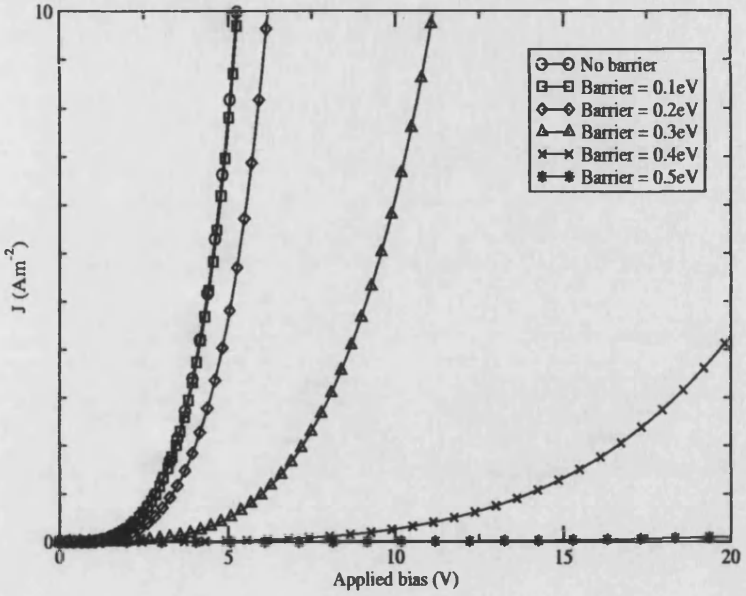

Figure 4.2: J-V characteristics for the bi-layer device as the barrier for holes crossing from the HTL into the blocking layer increases from 0eV to 0.5eV.

Figure 4.3 shows the hole density profile and electric field profile for the device at an applied bias of +10V as the barrier to hole transport from the HTL into the blocking layer is increased. When there is no barrier or the barrier is small (0.1eV), the hole density, and hence the electric field, is constant across the device, as the two layers are essentially identical and so the device behaves as a single HTL 80nm thick. As the barrier increases, the barrier becomes a significant obstacle to the holes' transport across the device and holes begin to accumulate at the HTL/blocking layer interface, on the HTL side. For a very large barrier (0.5eV), the hole density at the interface can be many orders of magnitude greater than in the rest of the HTL. The hole density in the blocking layer is drastically reduced by the presence of the barrier.

As the energy barrier between the layers increases, the large peak in the hole density at the interface between the two layers causes a rapid change in the electric field at the interface and the electric field in the blocking layer becomes much larger than in the HTL in order to satisfy Poisson's equation [9]. Since there are few holes in the blocking layer, the higher field ensures continuity of the hole

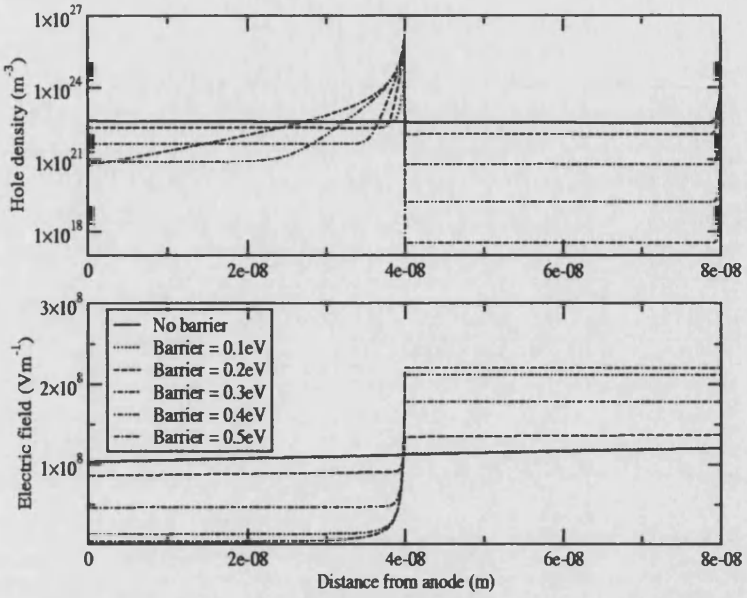

Figure 4.3: Hole density profile (top panel) and electric field profile (bottom panel) for the bi-layer device with the HTL on the left hand side and the blocking layer on the right hand side. The interface between the layers is located at x=40nm. Holes are injected into the HTL from the left hand side contact (x=0nm).

current across the device. This effect of charge accumulation causing a redistribution of the electric field in a bi-layer device has been measured experimentally using electroabsorption spectroscopy e.g. [10], and has been investigated using our drift-diffusion model (see section 4.3). Due to the presence of a high field in the blocking layer, this layer should be made as thin as possible to reduce the required driving voltage.

4.1.2 Transport layers

Blocking layers eliminate one source of inefficiency in OLEDs; the other major problem is that of unbalanced injection and transport. This problem can be solved by the use of a transport layer which improves the injection and/or transport of the minority carrier (usually electrons). To investigate the effects of transport layers on device performance, the same device as shown Figure 4.1 is considered, using the parameters in Table 4.1. In this case, the HOMO levels are equi-energetic i.e. there is no barrier to transport between the two layers, and the mobility in the right hand side layer varies by a factor of 1, 0.1, 0.01 or 0.001, such that the HTL (left hand side layer) is a better hole transporter than the right hand side layer.

Figure 4.4 shows the J-V characteristics of the device as μ_{p0} in the right hand side layer varies as μ_{p0}, $0.1\mu_{p0}$, $0.01\mu_{p0}$, and $0.001\mu_{p0}$. As the magnitude of the hole mobility in the right hand side layer decreases with respect to that in the hole transporting layer, the device current at a given bias decreases, although the effect is not as dramatic as for the case where a blocking layer is employed (Figure 4.2).

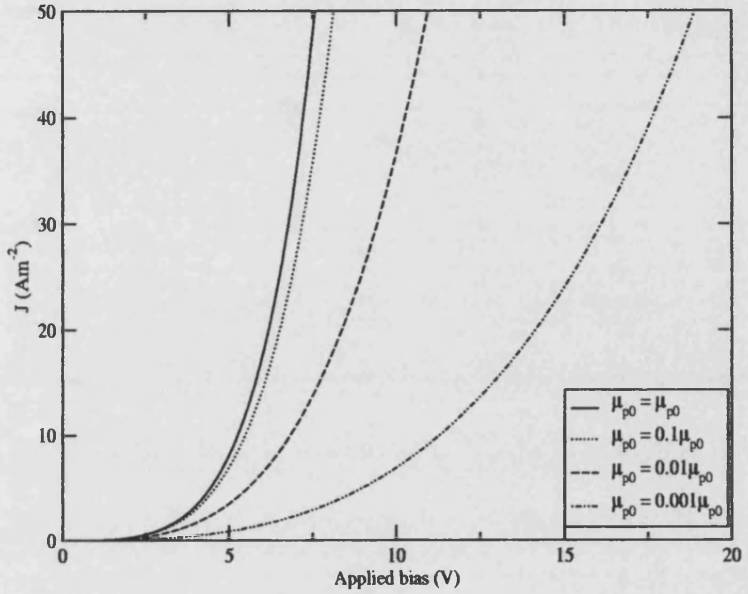

Figure 4.4: The J-V characteristics of the bi-layer device as μ_{p0} in the right hand side layer varies as μ_{p0}, $0.1\mu_{p0}$, $0.01\mu_{p0}$, and $0.001\mu_{p0}$.

Figure 4.5 shows the hole density profile and electric field profile across the device as the hole mobility in the right hand side layer varies with respect to the hole mobility in the hole transporting layer on the left hand side, at an applied bias of +10V. In order to maintain a constant current across the entire device, the electric field and carrier density increase in magnitude in the right hand side layer compared to that in the hole transporting layer on the left. The greater the ratio between μ_p in the HTL and μ_p in the right hand side layer, the greater the difference in the carrier densities and hence electric fields in the two layers. The use of an enhanced transport layer can thus be used to increase the carrier density in the other layer where the carrier mobility will be lower; this effect can increase the carrier concentration in the region of a device where the other carrier type is high, increasing the recombination yield. In practice, the material which preferentially transport one carrier type also tend to act as a blocking layer to the other carrier type owing to their energy band structure, and so typical bi-layer devices generally have a transporting and blocking layer for electrons and holes

e.g. [11].

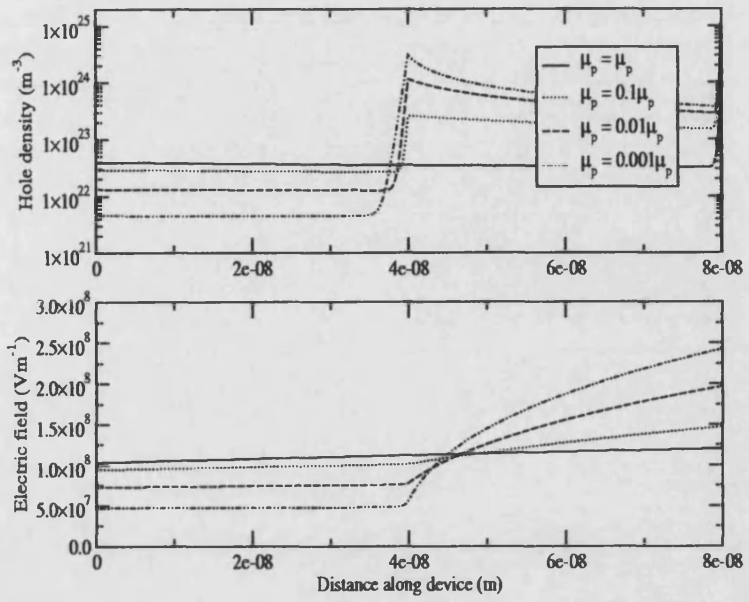

Figure 4.5: The hole density (top panel) and electric field profiles (bottom panel) of the bi-layer device as the mobility in the right hand side layer varies compared to that in the hole transporting layer on the left hand side. The applied bias is +10V. Holes are injected into the HTL on the left hand side at x=0m. The interface between the two layers is located at x=40nm.

4.2 Effect of layer thickness on the efficiency of a TPD/Alq device

The variation of the external quantum efficiency of a bi-layer TPD (N,N'-diphenyl-N,N'-bis(3-methylphenyl)1-1'biphenyl-4,4'diamine)/Alq (tris-(8-hydroxyquinoline) aluminium) device with Alq layer thickness has been investigated experimentally by Burrows and Forrest [12] and Schmitz et al [13][14]. Both groups independently concluded that there exists an optimum thickness of the Alq layer for achieving maximum efficiency; the essence of their results are shown in Figure 4.6.

Such a result appeared to be one that could be investigated, qualitatively at least, since the internal quantum efficiency, η_{int}, is easily obtained from the drift-diffusion model. A schematic energy band diagram of an ITO/TPD/Alq/Al is shown in Figure 4.7 and the parameters used in the simulation are given in Table 4.2. The barrier heights were calculated assuming the workfunction of Al again

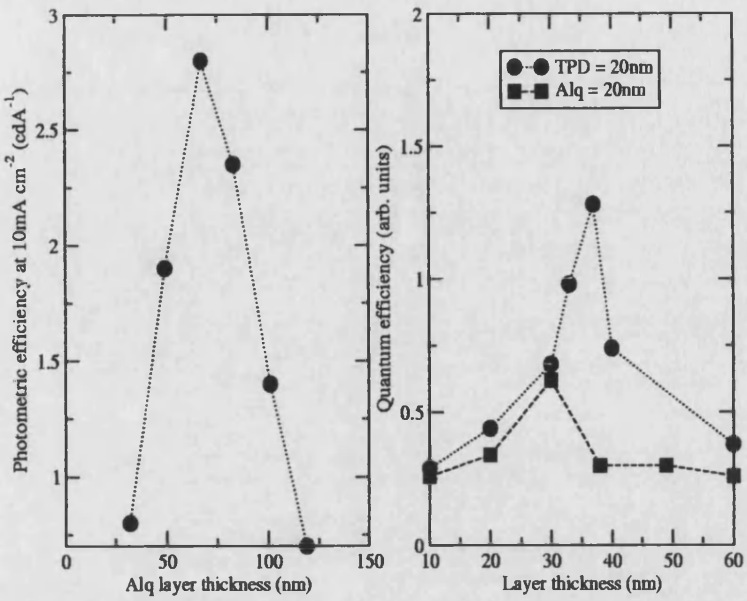

Figure 4.6: Efficiency of an ITO/TPD(40nm)/Alq/Al device as a function of Alq layer thickness reproduced from [13] (left panel) and efficiency of an ITO/TPD/Alq/Mg:Ag device as a function of Alq thickness when the TPD layer is 20nm thick, and as a function of TPD thickness when the Alq layer is 20nm thick, reproduced from [12]. The lines are simply a guide to the eye.

to be 4.2eV and that of ITO to be 4.8eV; this yields a value of 0.6eV for ϕ_{bp}, similar to that found for an ITO/TPD interface by fitting in Chapter 3.

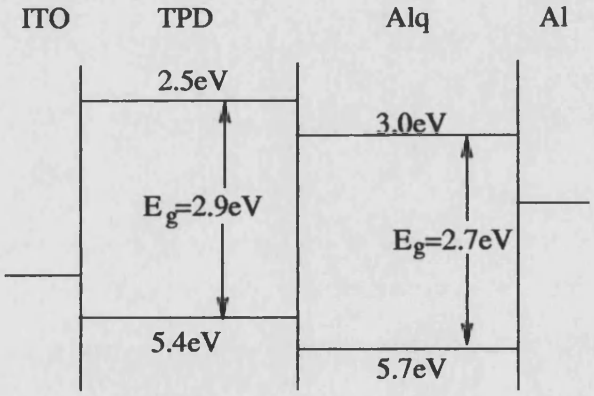

Figure 4.7: A schematic energy band diagram of an ITO/TPD/Alq/Al device. The energy levels are taken from [11][15].

The TPD layer thickness was set to be 40nm thick, and the Alq layer thickness was varied from 10-100nm, in an attempt to replicate the work of Schmitz et al [13][14]. Figure 4.8 shows the J-V characteristics of these devices.

As can be seen from Figure 4.8, as the Alq layer thickness increases, the driving voltage required to produce a fixed device current increases. Since the hole current

Parameter	TPD	Alq	Units
T	300	300	K
ϕ_{bn}	-	1.2	eV
ϕ_{bp}	0.6	-	eV
N_V [7][16]	1×10^{27}	1×10^{27}	m^{-3}
N_C [7][16]	1×10^{27}	1×10^{27}	m^{-3}
μ_{p0}	3.2×10^{-7} [6]	1.9×10^{-12} [7]	m^2/Vs
μ_{n0}	1.0×10^{-12} [6]	1.9×10^{-10} [7]	m^2/Vs
$E_{0,p}$	1.5×10^{9} [6]	7.1×10^{6} [7]	Vm^{-1}
$E_{0,n}$	1.5×10^{9} [6]	7.1×10^{6} [7]	Vm^{-1}
ϵ_s [16]	3.0	3.0	-
E_t [11]	-	0.14	eV
N_t [11]	-	1×10^{23}	m^{-3}

Table 4.2: Material parameters used to simulate an ITO/TPD/Alq/Al device.

in the TPD layer is injection limited, and the large value of ϕ_{bn} in the Alq layer means that the electron current injected into the Alq layer is small, the device is qualitatively similar to that in section 4.1.1. The Alq layer acts as a hole blocking layer, due to the offset between the HOMO levels in TPD and Alq (Figure 4.7), causing a build up of holes at the interface and hence the electric field is distributed such that the field is larger in the Alq layer. Hence to maintain a given current, a certain field must be maintained in the Alq layer and as the Alq thickness increases, the required driving voltage also increases.

The internal quantum efficiency, η_{int}, was calculated at a current of $20 Am^{-2}$ for each Alq layer thickness, and was taken to be given as:

$$\eta_{int} = \frac{1}{4}\frac{J_r}{J} \tag{4.1}$$

where 1/4 is the fraction of emissive singlet excitons created, and J_r is the net recombination current as detailed in section 3.1.12. Figure 4.9 shows the internal quantum efficiency as a function of the Alq layer thickness. Interestingly, in contrast to the findings of Schmitz et al [13] and Burrows et al [12], the efficiency was found to be completely invariant with the Alq layer thickness. The relatively low value of the calculated quantum efficiency is a consequence of the relatively large barrier to electron injection, ϕ_{bn}. Since the electron current is therefore small compared to the hole current, then owing to the imbalance in injection

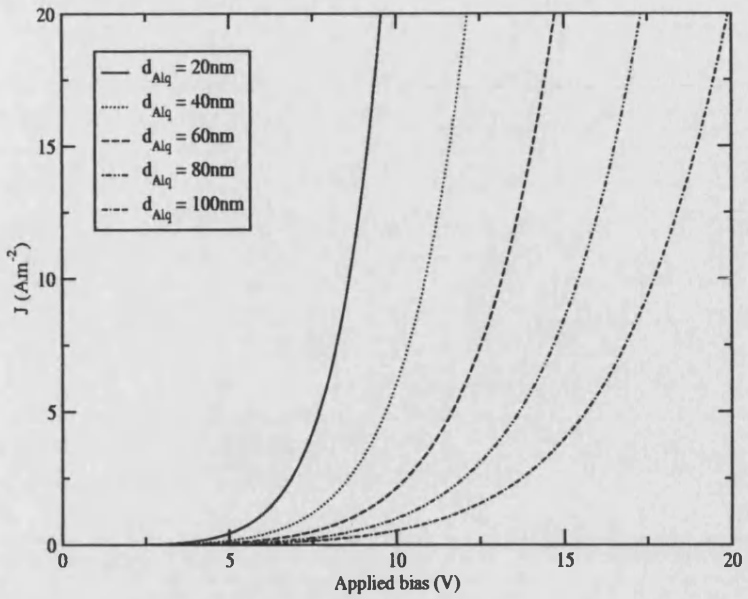

Figure 4.8: The J-V characteristics of a set of ITO/TPD/Alq/Al devices; the TPD layer thickness is 40nm, whilst the Alq layer thickness varies from 10-100nm.

caused by the different barrier heights, the recombination current will be small and hence the efficiency low. Figure 4.10 shows the carrier density, electric field and recombination rate profiles for the device with a 60nm thick Alq layer.

The carrier, recombination and field profiles were found to be identical for all of the devices at a constant current of 20Am^{-2}. The TPD layer acts as a blocking layer for electrons, due to the large mismatch between the LUMO levels of TPD and Alq, and the Alq layer acts as a blocking layer for holes, due to the mismatch between the HOMO levels of the two layers. Although a redistribution of the electric field might be expected as the blocking layers cause a build-up of carriers at the interface (section 4.1.1), this is not the case, as shown in Figure 4.10. In fact, the electric field is approximately constant across the device. The reason for this is at the relatively high current value being considered, the biases applied to the devices is quite high, and as such there is some electron injection from the Al cathode, despite the relatively large barrier height of 1.2eV. Although this injected electron current is quite small, the very large barrier for electrons going from Alq to TPD (0.6eV) causes a very large accumulation of electrons at the interface. This charge build-up opposes the hole build-up on the other side of the interface, and prevents any significant redistribution of the electric field.

Since both the electron and hole currents are injection limited, to achieve a given

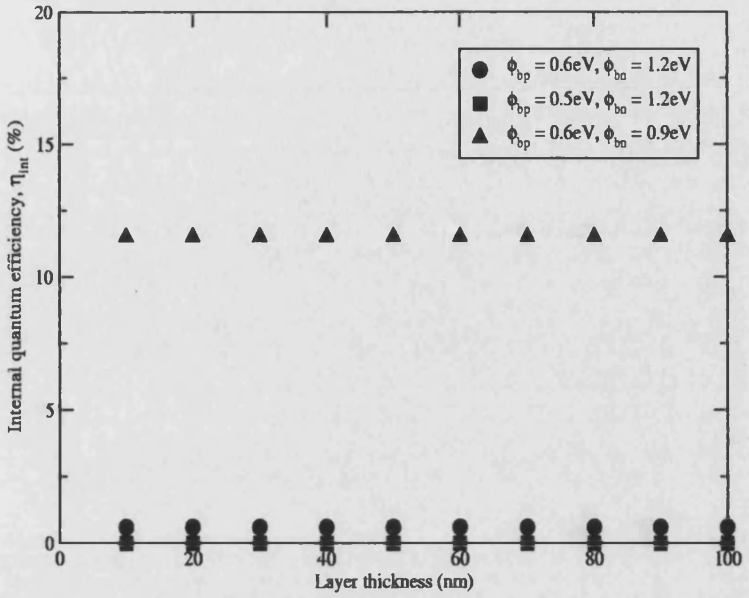

Figure 4.9: The internal quantum efficiency, η_{int}, as a function of Alq layer thickness at 20Am^{-2}. The TPD layer thickness is 40nm.

current, a certain field must be applied. The device current is dominated by the hole current, and so to obtain the same current for different Alq thicknesses, a varying bias must be applied. Since the electric field is constant across the device, this results in the same injection currents from both contacts, giving the same carrier and recombination profiles for all Alq thicknesses. The recombination rate peak at the interface dominates the recombination for the device, although there is some recombination in the Alq layer, and hence the efficiency is invariant with Alq layer thickness, a different result to that obtained by Schmitz et al [13][14] and Burrows et al [12].

Decreasing the hole barrier height, ϕ_{bp}, at the ITO/TPD interface meant that the hole, and hence device, current was larger, and so the recombination current became a smaller fraction of the device current, reducing efficiency. However, η_{int} was still invariant with Alq layer thickness. Figure 4.9 shows η_{int} as a function of Alq layer thickness for the case where ϕ_{bp}=0.5eV and ϕ_{bn}=1.2eV. Decreasing the value of ϕ_{bn} at the Alq/Al interface increased efficiency by improving the electron injection, allowing more electrons into the device to recombine. Again, however, the efficiency was found to be invariant with Alq layer thickness. Figure 4.9 shows the variation of η_{int} with Alq layer thickness for the case where ϕ_{bp}=0.6eV and ϕ_{bn}=0.9eV. In addition, varying the TPD layer thickness from 10nm to 100nm, with a fixed Alq layer thickness of 40nm, provided exactly the same results as for

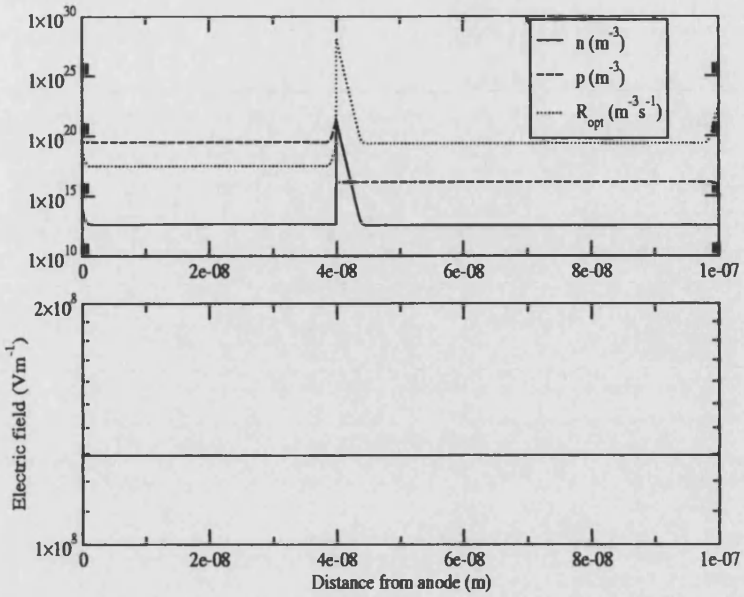

Figure 4.10: The carrier density and recombination rate profiles (top panel) and electric field profile (bottom panel) for the ITO/TPD(40nm)/Alq(60nm)/Al device, at a constant current of 20Am^{-2}.

a constant TPD layer thickness and varying the Alq layer thickness, for the same reasons as given above. It would appear that the observed dependence of the device efficiency on the Alq thickness may be caused by some effect not explicitly included within the model.

Schmitz et al [13][14] provided no explanation for the occurrence of an optimum Alq layer thickness for achieving maximum efficiency. Burrows et al [12] suggested that for thinner Alq layers, holes could cross the Alq layers without recombining, whilst for thicker Alq layers, electrons become trapped in the bulk before reaching the recombination zone at the heterojunction between the two layers. Hence they proposed that there exists an optimum Alq layer thickness where there is a common minimum for these two processes. However, Burrows et al also assumed that there were no barriers to either carrier type moving from the TPD and Alq layer and vice-versa; they completely neglected the role of the heterojunction in the recombination process. They also suggested that the current in the device was predominantly electron space-charge limited with traps, which is unlikely given that there is a significant barrier to electron injection (ϕ_{bn}) at the Alq/Mg:Ag interface, and that TPD acts as an electron blocking layer. Therefore their explanation is unlikely to be correct. Burrows et al also claimed that the efficiency was independent of TPD thickness, although it can be seen in Figure 4.6 that there is an optimum TPD thickness of 30nm. TPD is largely believed

to be trap-free e.g. [7][15] so the explanation of Burrows et al for the variation of the efficiency with Alq layer thickness cannot be applied to the variation of efficiency with TPD thickness. Schmitz et al also noted that an optimum layer thickness for TPD existed when repeating this experiment with layers of TPD derivatives, having different layer thicknesses, whilst keeping the thickness of Alq constant [14].

Yahiro and Tsutsui [17] obtained similar results to Schmitz et al and Burrows et al for an ITO/TPD(50nm)/Alq/Mg:Ag device (Figure 4.11), finding an optimum Alq layer thickness of 75nm. They explained such a variation in efficiency as a function of layer thickness as being due to a change in the out-coupling efficiency, caused by weak micro-cavity effects. The metallic cathode provides a mirror which can modify the pattern of the electromagnetic modes near the cathode, setting up standing-wave states [8]. Kahen [18] confirmed the conclusion of Yahiro et al via optical modelling.

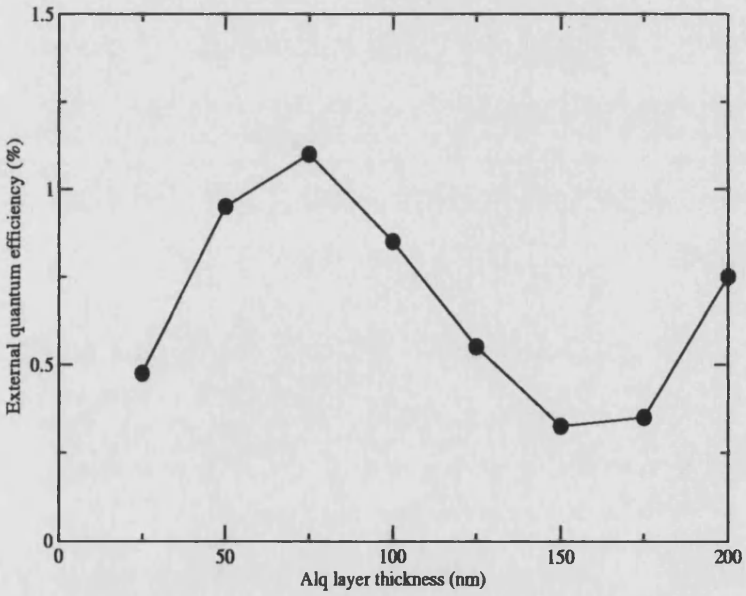

Figure 4.11: The measured external quantum efficiency of an ITO/TPD(50nm)/Alq/Mg:Ag device as a function of Alq layer thickness at a current of $10mAcm^{-2}$. Reproduced from [17]. The curve is a guide to the eye.

Another important effect is that of exciton quenching. Since the bulk of recombination occurs on the Alq side of the TPD/Alq interface, with some recombination also in the bulk of the Alq, then for very thin Alq layers the recombination zone is very close to the cathode. The quenching of excitons by electrodes is a well-known cause of reduced efficiency in OLEDs [19].

4.3 Internal electric field Distribution in an NPB/Alq OLED

In section 4.1, it was noted that the presence of a blocking or transporting layer could significantly change the electric field distribution from being essentially uniform in a single layer device, to varying greatly between the layers of a bi-layer device. One method of investigating the internal electric field distribution of a multi-layer device, and hence the accumulation of charges at interfaces, is to use the experimental technique of electroabsorption spectroscopy [20]. Electroabsorption (EA) spectroscopy uses an electric field to modulate the transmission of light through an organic thin film layer by perturbing the energy levels of the molecules; different layers react differently to an applied field and hence the electric field in a particular layer can be measured directly. EA spectroscopy has been largely used to evaluate the built-in field in single layer OLEDs e.g. [21], and to investigate the internal electric field distribution in bi-layer OLEDs [10][22][23].

In this section, the average electric field in each layer of a 4,4'-bis[N-(1-napthyl)-N-phenylamino]-biphenyl] (NPB)/tris-(8-hydroxyquinoline) aluminium (Alq) device obtained experimentally by EA spectroscopy is compared to that obtained using the drift-diffusion model. The NPB and Alq layers were 40nm thick, and the devices had either an Al or Al:Li cathode. Full details of the device fabrication and the experimental procedure are given in [22]. Figure 4.12 shows a schematic energy band profile of the devices.

Both devices were simulated using the parameters contained in Table 4.3. At each applied bias, the field profile for each device was obtained from the model. From this, the average electric field in each layer was calculated; the built-in field of the device (obtained from the simulation at 0V) was subtracted from this value to allow direct comparison with the experimental EA data.

Figure 4.13 shows the experimentally measured and simulated average fields in the layers of the ITO/NPB/Alq/Al device as a function of applied bias; good agreement between the experimental and simulated data can be seen. The barrier to hole injection, ϕ_{bp}, at the ITO/NPB interface used in the simulation was 0.7eV and the barrier to electron injection, ϕ_{bn}, at the Alq/Al interface was again taken as 1.2eV (its measured value was found to be 1.1±0.2 eV [22]). Although it is

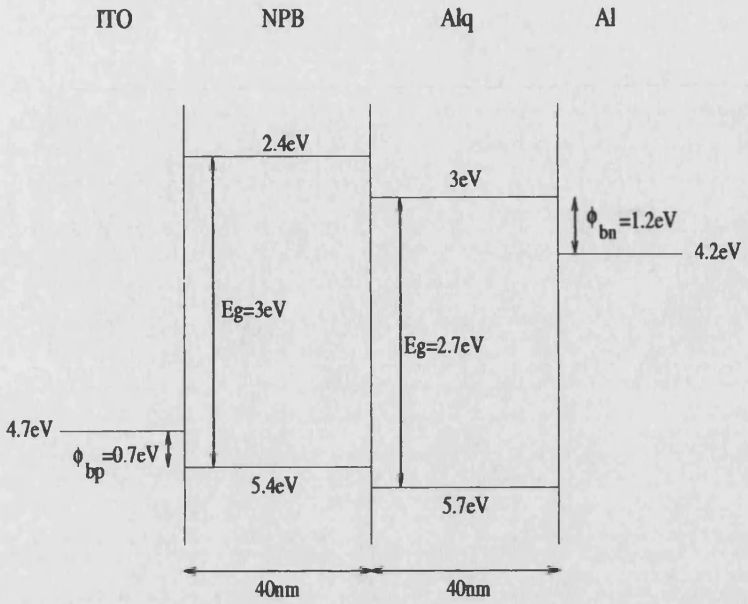

Figure 4.12: Schematic energy band diagram of an ITO/NPB/Alq/Al device.

Parameter	NPB	Alq	Units
ϵ_s[7]	3.0	3.0	-
μ_{n0}	6.1×10^{-10} [7]	1.9×10^{-10} [7]	m^2/Vs
μ_{p0}	6.1×10^{-8} [7]	1.9×10^{-12} [7]	m^2/Vs
E_{0n}	4.44×10^{7} [7]	7.1×10^{6} [7]	V/m
E_{0p}	4.44×10^{7} [7]	7.1×10^{6} [7]	V/m
N_C [7]	1×10^{27}	1×10^{27}	m^{-3}
N_V [7]	1×10^{27}	1×10^{27}	m^{-3}
E_t	-	0.15 [11]	eV
N_t	-	1.3×10^{23} [11]	m^{-3}

Table 4.3: Material parameters used in the simulation.

well known that the workfunction of ITO varies, the value of 4.7eV was chosen as it provided a good fit to the experimental data. The effect of changing the workfunction of ITO is discussed below.

Under small forward bias conditions, it can be seen from Figure 4.13 that the electric field is homogeneous across the device due to negligible charge injection from either contact since $V_{app} < V_{bi}$. As the applied bias is increased above V_{bi}, holes are injected into the NPB layer from the ITO contact; due to the large value of ϕ_{bn}, electron injection into the Alq layer from the Al contact is negligible. The holes injected into the NPB layer then build up at the NPB/Alq interface due to the offset between the HOMO bands; the Alq acts as a hole blocking layer.

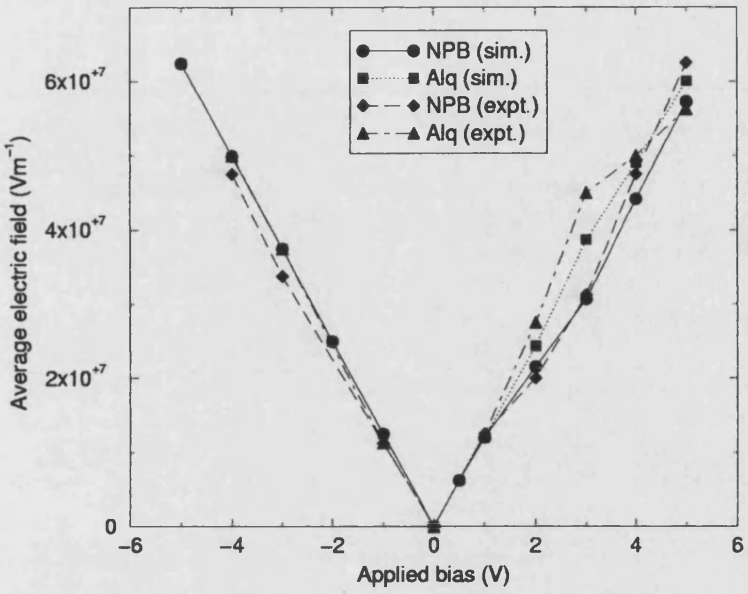

Figure 4.13: Comparison of simulated and measured average fields in the NPB and Alq layers of the ITO/NPB/Alq/Al device.

This charge build up causes the field to increase in the Alq layer in accordance with Poisson's equation, as outlined in the discussion of blocking layers in section 4.1.1. Figure 4.14, which shows the electric field and carrier density profiles obtained from the device simulation (V_{app}=+3V), demonstrates this point. Similar explanations for the experimentally obtained field distributions in similar bi-layer devices have been offered by Rohlfing et al [10] and Hiramoto et al [26], but without the confirmation provided by modelling. The presence of hole accumulation at an interface has been deduced from transient current measurements on a TPD/Alq device by Matsumura et al [27].

As the applied forward bias is increased further, the experimental curves in Figure 4.13 can be seen to converge and cross at about +4V; above this bias the average electric field in the NPB layer is larger than that in the Alq layer. At higher fields, electrons are injected over the barrier from the Al cathode into the Alq layer, and accumulate at the heterojunction (on the Alq side), where the offset between the LUMO levels is 0.6eV (see Figure 4.12) i.e. the NPB acts as an electron blocking layer. Although few electrons are injected relative to the number of holes, since $\phi_{bn} > \phi_{bp}$, the offset between the LUMO levels is twice as great as the offset between the two HOMO levels, resulting in significant electron build up at the heterojunction. This negative charge build up reduces the magnitude of the field in the Alq layer. A convergence of the curves is observed in the simulated data,

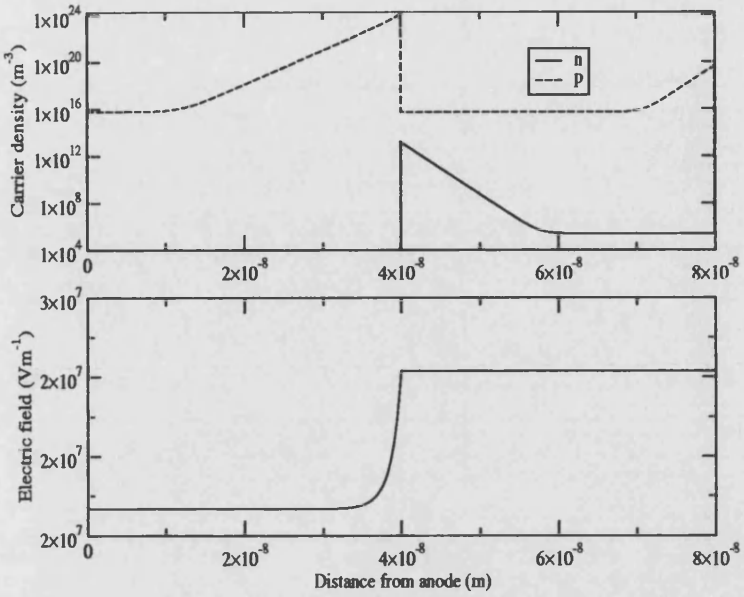

Figure 4.14: Electric field profile (top panel) and carrier density profiles (bottom panel) through the ITO/NPB/Alq/Al device at +3V. The ITO contact is located at x=0, and the interface between the NPB and Alq layers is located at x=40nm.

but they do not cross and the field in the Alq layer remains the greater, although the model does show increasing electron accumulation in the Alq layer at higher biases, which accounts for the convergence of the curves. Reducing the value of ϕ_{bn} in the model by several tenths of an eV did not significantly change the results. The offset between the LUMO levels was then increased to test whether greater electron confinement in the device, causing a large electron build-up, was responsible for the field-distribution obtained experimentally; however, no solution was possible with a larger LUMO offset due to numerical instabilities in the simulation and this theory could not be tested, although it remains quite probable.

Varying the workfunction of ITO from 4.7eV to 5.2eV results in a range of barrier heights to hole injection, ϕ_{bp}, ranging from 0.2-0.7eV. Since the barrier to electron injection, ϕ_{bn}, is much larger (1.2eV), the qualitative behaviour of the field distribution is unchanged, with significant hole injection, negligible electron injection, and the accumulation of holes at the interface resulting in the average field in the Alq layer being larger than that in the NPB layer. If the barrier to hole injection at the ITO contact is decreased, the average field in the Alq layer becomes even greater, as more holes would be injected into the system and hence accumulate at the interface. If ϕ_{bp} is increased, hole injection and consequently accumulation at the interface would decrease; the magnitude of the average field

in the Alq layer would be smaller than in the present situation, but it would still be the larger of the two average fields.

In reverse bias, the field across the simulated device is homogeneous, with the average fields in each layer being equal (see Figure 4.13), since no charge is injected and the device is fully depleted. This explanation holds for all three devices. The simulated curves lie exactly on top of each other, along with the experimental Alq curve. The experimental NPB curve sits slightly below the experimental Alq curve, but they are within experimental error [22].

Figure 4.15 shows the simulated and experimentally measured electric field distribution in the ITO/NPB/Alq/Al:Li device, again with good agreement between theory and experiment. In order to simulate this device, all parameters were unchanged except for the electron barrier, ϕ_{bn}, which was set as 0.6eV as this gave the best fit to the experimental data and is consistent with the measured value of 0.6±0.2eV [22].

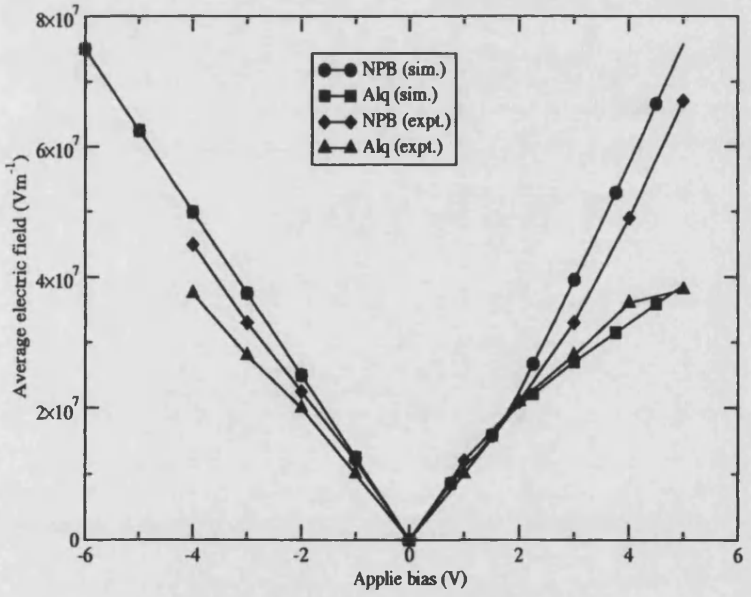

Figure 4.15: Comparison of simulated and measured average fields in the NPB and Alq layers of the ITO/NPB/Alq/Al:Li device.

As for the device with the Al cathode discussed above, there is little charge injection into the device at low forward biases ($< V_{bi}$) and so the field is homogeneous across the two layers. For larger forward biases, there is carrier injection from both electrodes. The electron barrier at the Al/Al:Li interface is smaller than the hole barrier at the ITO/NPB interface, and this coupled with the large LUMO

level offset at the NPB/Alq interface (0.6eV, see Figure 4.12), results in a large build up of electrons at the heterojunction (Figure 4.16). There is a also a large hole build up at the heterojunction in the NPB layer, but it is not of as great a magnitude as the electron build up in the Alq layer. This distribution of charges results in the average field in the NPB layer being greater than that in the Alq layer, again in accordance with Poisson's equation. As the bias is increased, the curves do not converge as in Figure 4.13 but in fact diverge; as the bias increases, ever larger numbers of electrons are injected from the cathode and build up at the heterojunction in greater numbers, increasing the difference between the field in the two layers.

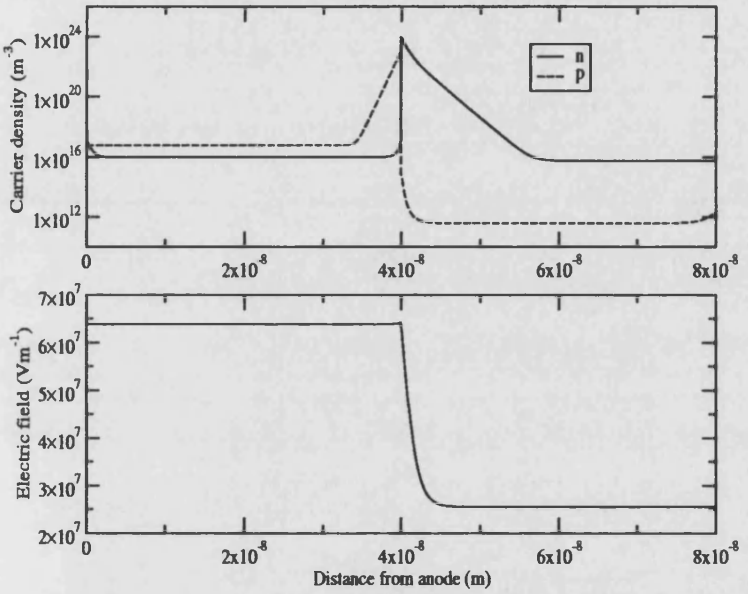

Figure 4.16: Electric field profile (top panel) and carrier density profiles (bottom panel) through the ITO/NPB/Alq/Al:Li device at +5V. The ITO contact is located at x=0, and the interface between the NPB and Alq layers is located at x=40nm.

In the simulation of this device, the values of the electrode workfunctions used are critical. Since the barrier height to electron injection ϕ_{bn} at the Alq/Al:Li interface is smaller than for the previous device, it now injects a significant number of electrons. These electrons accumulate at the organic-organic interface and can determine which layer has the greater average value of the electric field. If $\phi_{bp} \ll \phi_{bn}$, a larger number of holes than electrons will be injected, accumulate at the interface and cause a larger field to form in the Alq layer; the reverse situation occurs if $\phi_{bn} < \phi_{bp}$. If the barrier heights are equal, the field will be greater in the NPB layer as the band offset between the LUMO levels in the materials is greater than that for the HOMO levels, causing a greater confinement of electrons at the heterojunction, reducing the field in the Alq layer.

Rohlfing et al [10] also used EA spectroscopy to investigate the internal electric field distribution in an ITO/NPB/Alq/Mg:Ag device with layer thicknesses of 100nm and 200nm for the NPB and Alq layers respectively; it was decided to attempt to replicate their results. They also investigated the electric field distribution using EA spectroscopy for ITO/NPB/Alq/Mg:Ag devices with various thicknesses of Alq and NPB [28], and they found that the thicknesses of the layers made a quantitative difference to the average fields in each layer, but qualitatively the behaviour was found to be the same, indicating that the fields are primarily determined by the barriers to carrier injection and the accumulation of carriers at the interface.

The parameters used to simulate this device were unchanged except for the layer thicknesses and ϕ_{bn}. The value for the barrier to electron injection, ϕ_{bn}, at the Mg:Ag contact used in the simulation was set at 1.1eV. Although this is larger than published values of 0.7eV e.g. [29], this produced an electric field distribution in agreement with Rohlfing et al, with the field in the Alq layer being greater than in the NPB layer. Using smaller values for ϕ_{bn} in the device simulation produced an average electric field in the NPB layer greater than that in the Alq layer, due to significant electron injection and accumulation, cf the ITO/NPB/Alq/Al:Li device shown in figure 4.15.

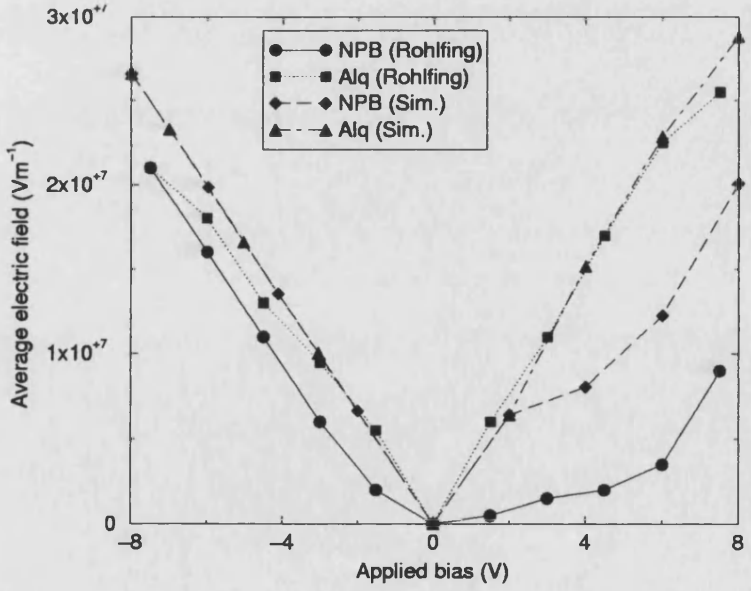

Figure 4.17: Comparison of simulated and experimentally measured [10] average fields in the layers of an ITO/NPB(100nm)/Alq(200nm)/Mg:Ag device.

Under forward bias conditions, it can be seen from Figure 4.17 that there is good

agreement between the experimental and simulated values of the average electric field in the Alq layer, and both show that the average field in the NPB layer is smaller than in the Alq layer. As can be seen from the carrier density and field profiles at V_{app}=+4V in Figure 4.18, the electron density in the Alq layer is considerably smaller than the hole density in this layer. Combined with the accumulation of holes in the NPB layer at the interface, this accounts for the field in the Alq exceeding that in the NPB layer.

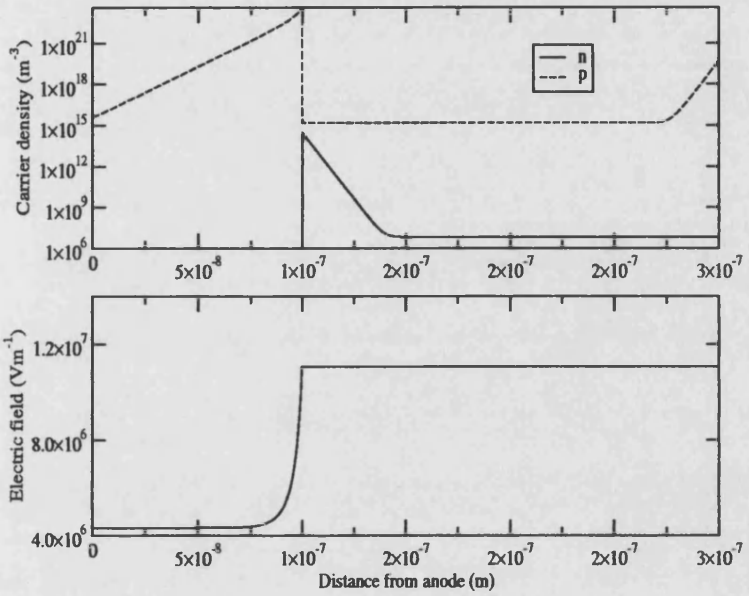

Figure 4.18: Simulated electric field profile (top panel) and carrier density profiles (bottom panel) for the ITO/NPB(100nm)/Alq(200nm)/Mg:Ag device at +4V. The anode is located at x=0.

However, the agreement between the experimental and simulated average electric field values in the NPB layer is disappointing. Although they both exhibit similarly shaped curves, the magnitudes of the curves vary considerably. The simulated NPB curve follows the simulated and experimental Alq curves under small forward bias conditions (V_{app} < 2V), as expected due to negligible charge injection; this situation occurred in the previous two devices. As the applied bias increases, the number of holes injected into the NPB layer increases, whilst few electrons are injected into the Alq layer, resulting in a larger average electric field value in the Alq layer for the reasons outlined above. The experimental data of Rohlfing et al [10] shows that even under small forward bias (including $V_{app} < V_{bi}$), the average field in the layer NPB is smaller than that in the Alq layer. In fact, the field in the NPB layer is shown by Rohlfing et al [10] to be smaller for $V_{app} < V_{bi}$ in forward bias than under the corresponding reverse bias. One might expect the field in each layer to be equal for all reverse biases and

forward biases below V_{bi} due to the negligible injection of charge. This situation is observed in the simulations of the devices with Al and Al:Li cathodes (above). At an applied bias of +4V, the average field in the Alq is a factor of about 10 times greater than in the NPB according to Rohlfing et al, whereas a factor of about 2 is obtained from the Al device.

Again, under reverse bias, a homogeneous electric field distribution across the device was simulated, for reasons previously outlined. Rohlfing et al [10] state that under reverse bias, the average field in both layers is identical within the accuracy of the experiment and the distribution is due to negligible charge injection. In this case, the agreement between the simulated average field values and their measured average field values is good (Figure 4.17).

4.4 Conclusions

Multi-layer devices, employing blocking and transport layers (section 4.1), are a useful method for creating efficient devices. Being able to model these devices is of great importance if device models are to be used more extensively for simulating OLEDs. Models such as the drift-diffusion one presented in this thesis can be used in order to understand device physics, and also predictively, to test various device architectures without having to fabricate a whole series of devices for characterisation.

Experimentally, it has been shown that the thicknesses of the layers in a bi-layer TPD/Alq device affect the measured efficiency [12][13][14], and that there exists an optimum layer thickness for maximising device efficiency. However, the drift-diffusion model showed the internal quantum efficiency to be invariant with the thickness of the Alq and TPD layers (section 4.2). This does not indicate that the model cannot successfully simulate bi-layer devices; the comparison of the internal electric field distribution provided by the model agrees with values obtained by electroabsorption spectroscopy (section 4.3), indicating that charge is correctly blocked and transported within the model. The findings of Yamada et al [28] that the electric field distribution is independent of the thickness of the organic layers suggests that the charge distribution is largely unaffected by the thickness of the layers, confirming the results obtained when investigating the effect of thickness

on device efficiency using the drift-diffusion model. The discrepancy with the experimentally obtained electric field distribution of Rohlfing et al [10] in an NPB/Alq device is puzzling, although it has been suggested that the analysis of their EA data may be incorrect [4], and so no conclusions can be safely drawn on this matter.

It is highly likely that in order to compare the simulated internal quantum efficiency calculated from the model with the external quantum efficiency measured experimentally, the outcoupling of the light and other factors must be accounted for. Although some drift-diffusion models include a singlet density term, which accounts for the diffusion and decay of singlets e.g. [30], the quenching of excitons at the electrodes and other sites and optical outcoupling must be included in a complete optical and electrical model in order to allow direct comparison with experiment. In order to use the model in a predictive manner, this optical part of the model is a necessity; it is no use using the electrical model to investigate which device configurations yield the maximal internal quantum efficiency if optical effects then waste a larger proportion of emitted light than necessary.

More experimental data would of course be useful to further test the model in the case of multi-layer devices, but it is more difficult to obtain experimental data for several reasons. Firstly, J-V characteristics cannot be easily modelled due to the large number of unknown parameters which need to be fitted; even if parameters are known for one layer, it is impossible to ascertain whether the resultant J-V curve is due to the presence of blocking or transport layers, or both. Another problem is that besides EA data, there is little data that can be directly modelled. Much of the data in the literature regarding multi-layer devices is focused on emission spectra or efficiencies, neither of which can be obtained from the electrical model. It is therefore likely that combined electrical and optical models are necessary in order for device modelling to become a more integral part of OLED fabrication.

References

[1] C W Tang and S A VanSlyke, *Appl. Phys. Lett.*, **51**, 913 (1987).

[2] J-H Lee, S-W Kim, S-H Ju, W-G Lee, J-S Choi, Y-K Kim, and W Y Kim, *Synthetic Metals*, **111-112**, 63 (2000).

[3] M T Bernius, M Inbasekaran, J O'Brien, and W Wu, *Advanced Materials*, **12**, 1737 (2000).

[4] G L B Verschoor, *Private communication.*

[5] B K Crone, P S Davids, I H Campbell, and D L Smith, *J. Appl. Phys.*, **87**, 1974 (2000).

[6] B Ruhstaller, S A Carter, S Barth, W Riess, and J C Scott, *J. Appl. Phys.*, **89**, 4575 (2001).

[7] J Staudigel, M Stössel, F Steuber, and J Simmerer, *J. Appl. Phys.*, **86**, 3895 (1999).

[8] R H Friend, R W Gymer, A B Holmes, J H Burroughes, R N Marks, C Taliani, D D C Bradley, D A Dos Santos, J L Brédas, M Löglund, and W R Salaneck, *Nature*, **397**, 121 (1999).

[9] U Albrecht and H Bässler, *Chemical Physics*, **199**, 207 (1995).

[10] F Rohlfing, T Yamada, and T Tsutsui, *J. Appl. Phys.*, **86**, 4978 (1999).

[11] W Brütting, S Berleb, and A G Mückl, *Organic Electronics*, **2**, 1 (2001).

[12] P E Burrows and S R Forrest, *Appl. Phys. Lett.*, **64**, 2285 (1994).

[13] C Schmitz, P Pösch, M Thelakkat, and H-W Schmidt, *Phys. Chem. Chem. Phys.*, **1**, 1777 (1999).

[14] C Schmitz, M Thelakkat, and H-W Schmidt, *Advanced Materials*, **11**, 821 (1999).

[15] C Giebeler, H Antoniadis, D D C Bradley, and Y Shirota, *J. Appl. Phys.*, **85**, 608 (1999).

[16] P S Davids, I H Campbell, and D L Smith, *J. Appl. Phys.*, **82**, 6319 (1997).

[17] M Yahiro and T Tsutsui, *Mat. Res. Soc. Symp. Proc.*, **660**, JJ5.27.1 (2001).

[18] K B Kahen, *Mat. Res. Soc. Symp. Proc.*, **660**, JJ4.2.1 (2001).

[19] G Hadziioannou and P F van Hutten (eds.), *Semiconducting Polymers: Chemistry, Physics and Engineering*, Wiley-VCH, Weinheim (2000).

[20] F Rohlfing and D D C Bradley, *Chemical Physics*, **227**, 133 (1998).

[21] T M Brown, R H Friend, I S Millard, D J Lacey, J H Burroughes, and F Cacialli, *Appl. Phys. Lett.*, **77**, 3096 (2000).

[22] S J Martin, G L B Verschoor, M A Webster, and A B Walker, *Organic Electronics*, **3-4**, 129 (2002).

[23] I H Campbell, M D Joswick, and I D Parker, *Appl. Phys. Lett.*, **67**, 3171 (1995).

[24] S Berleb, W Brütting, and G Paasch, *Organic Electronics*, **1**, 41 (2000).

[25] C Giebeler, H Antoniadis, D D C Bradley, and Y Shirota, *Appl. Phys. Lett.*, **72**, 2448 (1998).

[26] M Hiramoto, K Koyama, K Nakayama, and M Yokoyama, *Appl. Phys. Lett.*, **76**, 1336 (2000).

[27] M Matsumura, A Ito, and Y Miyamaw, *Appl. Phys. Lett.*, **75**, 1042 (1999).

[28] T Yamada, F Rohlfing, and T Tsutsui. *Jpn. J. Appl. Phys.*, **39**, 1382 (2000).

[29] M A Baldo, D F O'Brien, M E Thompson, and S R Forrest, *Phys. Rev. B*, **60**, 14422 (1999).

[30] D J Pinner, R H Friend, and N Tessler, *J. Appl. Phys.*, **86**, 5116 (1999).

Chapter 5

Hopping Transport Models

Although the application of the energy band formalism to modelling OLEDs (Chapter 2) has been successful, as is evident from the results presented and reviewed in Chapters 3 and 4, such an approach does not necessarily aid the investigation of the fundamental questions regarding transport in disordered organic semiconductors. In addition, it is questionable as to whether it really makes sense to treat a thin semiconducting polymer film in the same manner as a conventional crystalline semiconductor. Inevitably, a model which completely captures all of the correct physics, such as injection, transport, and recombination, of the operation of an OLED by considering the texture of the film and the correct nature of the charge carriers must be the ultimate aim [1][2].

A disordered organic semiconductor can be considered as consisting of a collection of hopping sites, i.e. molecules or conjugated segments, which vary in terms of their energies and positions; hence the intersite distance and coupling varies. Transport occurs by charge carriers hopping from one site to another; the term hopping actually refers to phonon-assisted tunnelling, and so hopping occurs from a site i to a site j with the aid of a phonon, as depicted in Figure 5.1. The energy of a hopping site may be affected by the conjugation length (particularly in conjugated polymers [1]), chemical structure and the presence of any defects. The spatial distribution of these sites, in terms of both distance and relative orientation, affects the coupling between sites (the wavefunction overlap) and hence the likelihood of tunnelling [3]. Hence the transfer rate, and ultimately mobility, depends upon the phonon frequency, the tunnelling probability, and the probability

of phonon absorption [3], as well as spatial and energetic considerations.

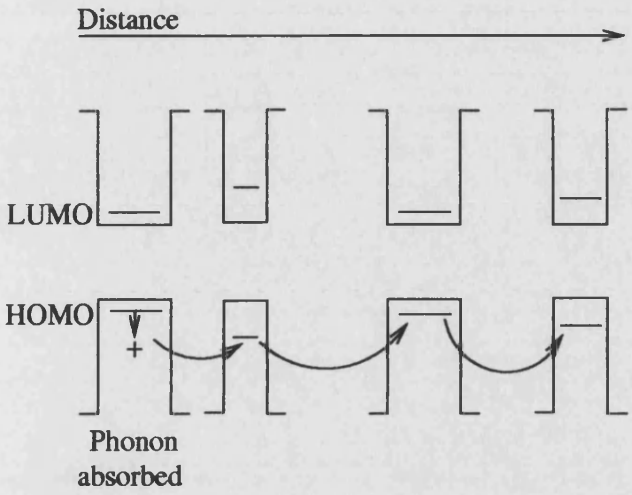

Figure 5.1: Schematic illustration of hopping transport in a disordered organic semiconductor. Molecules have different sizes, denoted by their width, and hence different energies; they are also separated by various distances.

Much experimental (section 5.1) and theoretical work has been carried out to investigate mobility in organic semiconductors. Hopping models, which attempt to account for the observed behaviour of the mobilities by considering purely polaronic effects e.g. [4], the effects of spatial and energetic disorder e.g. [5], or a combination of both e.g. [6][7], have been developed. Section 5.2 briefly reviews perhaps the most frequently cited model of hopping transport in disordered molecular materials, the Gaussian Disorder Model (GDM), which is concerned with the effects of spatial and energetic disorder on transport. For detailed reviews of hopping transport models, see [5][8][9][10].

Recently, there has been considerable interest in how the morphology of semiconducting organic thin films can affect the magnitude and field dependence of the mobilities, as well as the dispersive nature of charge transport e.g. [11][12][13]. Section 5.3 describes a Monte-Carlo disorder hopping model which was developed for this thesis with the express intention of explicitly including specific film morphologies in order to examine transport in specific classes of organic semiconductors, unlike the conventional GDM e.g. [5]. The model was initially devised in order to investigate transport in highly-aligned liquid-crystalline polymers e.g. PFO [14], but could be adapted to model other structures, such as non-rigid rod polymers, small molecules or dendrimers.

5.1 Carrier mobilities

The field and temperature dependence of the carrier mobilities in many organic semiconductors have been widely investigated experimentally, using methods such as the the time-of-flight (ToF) technique (section 5.1.1). The carrier mobilities in both conjugated polymers e.g. [15][16] and small molecules e.g. [17][18]. have invariably been found to be field dependent:

$$\mu(\mathrm{E}) = \mu_0 \exp\left(\sqrt{\frac{\mathrm{E}}{\mathrm{E}_0}}\right) \tag{5.1}$$

where μ_0 is the zero-field mobility of a carrier, E is the electric field, and E_0 is a constant determining the field-dependence of the carrier mobility. Furthermore, the field and temperature dependence of the carrier mobility has been found to fit Gill's empirical equation [19], where:

$$\mu_0 = C \exp\left(-\frac{\Delta}{k_B T}\right) \tag{5.2}$$

$$\frac{1}{\sqrt{\mathrm{E}_0}} = B\left[\frac{1}{k_B T} - \frac{1}{k_B T_0}\right] \tag{5.3}$$

where Δ is an activation energy, k_B is Boltzmann's constant, and T is temperature. C, B and T_0 are constants related to the degree of disorder in the material; the inclusion of these parameters, which are empirical, does not aid the understanding of transport in these materials [8].

5.1.1 Time-of-flight technique

The ubiquitous, but not unique, method for determining carrier mobilities in organic semiconductors, and investigating their field and temperature dependence, is the time-of-flight (ToF) experimental technique e.g. [10][20]. A pulse of light, incident on one end of the sample of material in question next to an electrode, generates a very thin sheet (essentially a delta function) of non-equilibrium charge carrier pairs. Either holes or electrons, depending upon the sign of the applied

electric field, then drift through the sample to the collecting electrode; the other carriers quickly exit the sample at the nearby electrode. A typical experimental ToF apparatus is illustrated in Figure 5.2.

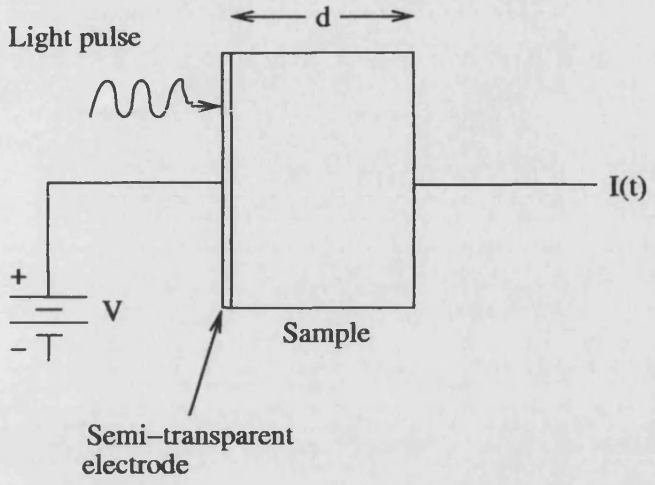

Figure 5.2: Schematic diagram of the time-of-flight (ToF) apparatus. A pulse of light generates a sheet of charge carriers, much narrower than the sample width d, which drift through the sample under the influence of the electric field (E= V/d).

The motion of the charge carriers gives rise to a time-dependent current, I(t), in the external circuit, which has two contributions: a conduction current, J_c, and a displacement current. Assuming the field (E=V/d) is constant, then integrating over the the sample thickness, d, yields [21]:

$$I(t) = \frac{1}{d}\int_0^d J_c(x,t)\mathrm{d}x + \frac{\epsilon_s}{d}\frac{\mathrm{d}V}{\mathrm{d}t} \tag{5.4}$$

where t is time, V is the voltage across the sample, and ϵ_s is the dielectric constant of the sample. If a constant voltage, V, is maintained, then $I(t)$ is the space-average of the conduction current. However, carriers do not have to exit the sample at the collecting electrode in order to generate a current in the circuit; changes in the field across the sample induced by the moving carriers generate a current as the battery attempts to maintain a constant voltage. Equation 5.4 can be expressed as [22]:

$$I(t) = \frac{\partial}{\partial t}\int_0^d \rho(x)\left(\frac{x}{d} - 1\right)\mathrm{d}x \tag{5.5}$$

where $\rho(x)$ is the charge density integrated over the y and z directions.

Figure 5.3(a) shows an idealised current-time plot which would result from the ToF technique if the sheet of charge generated moves with constant velocity across the sample; the current is constant until all of the carriers leave the sample at the transit time, t_τ, and they no longer contribute to the current. From this, a carrier drift mobility, μ, can be obtained:

$$\mu = \frac{d^2}{t_\tau V} \tag{5.6}$$

Alternatively, the time taken for the current to drop to half of its plateau value, $t_{1/2}$ (Figure 5.3), may be used in the above equation to calculate the mobility [15].

In reality, the shape of the current-time plot deviates from the ideal shape; Figure 5.3(b) depicts a typical experimentally obtained ToF plot from a sample of an organic semiconductor e.g. [16]. The main features of note are the initial peak in the signal, followed by a constant plateau region (all carriers are moving with constant velocity) followed by a tail; the length of the tail, or 'transition region' [21], is a measure of the spreading of the sheet of charge due to disorder [5]. The reason for this overall shape is the spreading of the charge packet from a delta-function to a broader Gaussian packet, due to the disorder present in organic semiconductors.

However, there are several points worth noting with regard to the ToF technique [8]. A major problem is that it is very difficult to a generate a sheet of carriers whose spatial extent is much less than the typical film thicknesses used in OLEDs ($\sim$100nm). Therefore ToF measurements are usually conducted on thicker films ($\sim$ 1μm); however, such thicker films may have different morphologies due to different fabrication techniques, thus producing films with differing amounts of disorder and hence different mobilities. Also, transport in a random hopping system is a relaxation process and the mobility of a carrier is not well defined until the carrier has relaxed within the density of states. Therefore the mobility obtained from measurements on thick films may well not correspond to the concept of mobility in thin films.

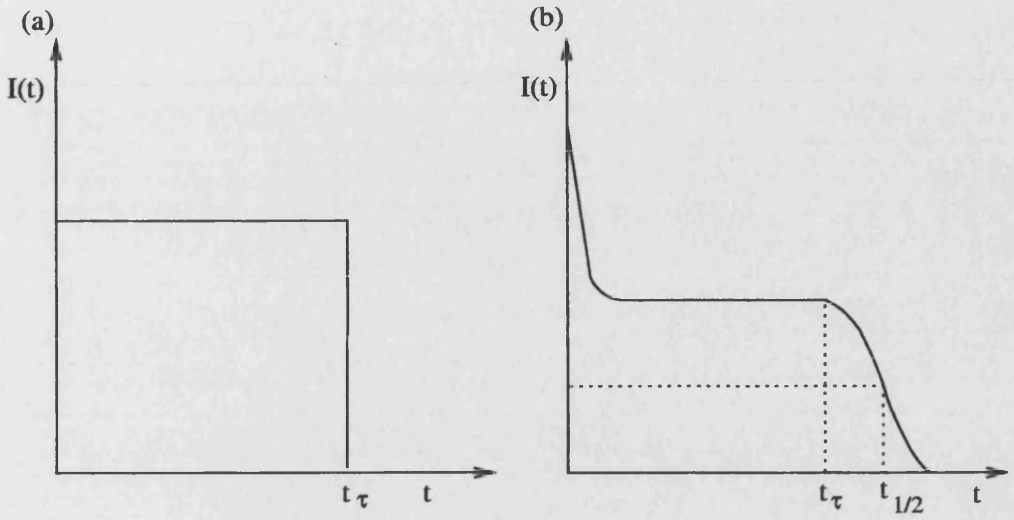

Figure 5.3: Schematic diagrams of (a) an idealised current-time plot, and (b) a typical current-time plot, both obtained from the ToF technique.

5.1.2 Dispersive transport

Transport in amorphous materials is frequently described as being dispersive [21]. The term dispersive, however, can mean many different things [23]. In the context of carrier transport in organic semiconductors, it is generally defined in two ways. Firstly, it can refer to transport in which the mean carrier velocity decreases with time i.e. the plateau region in Figure 5.3 is not constant. Secondly, it may mean that there is no point of inflexion on the current-time plot at which the current begins to decay away from its plateau value from which a transit time, t_τ, may be deduced e.g. [24][25]; this definition is generally accepted. Hence the current-transients illustrated in Figure 5.3 are both non-dispersive, with a constant current plateau region, and a well-defined transit time visible.

In the case of non-dispersive (or Gaussian) transport, there is still broadening of the tail of the current-time plot, as shown in Figure 5.3. The dispersion, W, of a sheet of carriers migrating through the sample is defined as [26]:

$$W = \frac{t_{1/2} - t_\tau}{t_{1/2}} = \sqrt{\frac{\pi k_B T}{qV}} \tag{5.7}$$

where t_τ and $t_{1/2}$ are as defined above, k_B is Boltzmann's constant, T is temperature, q is the electronic charge, and V is the applied voltage. This relationship

is only valid provided the Einstein relation is valid i.e. $qD = \mu k_B T$ [27].

It is found that W is larger than predicted for Gaussian transport; the broadening of the tails of the current-time plots is due to the Gaussian distribution of the transport states [26].

However, the traditional concept of mobility e.g. [27] must be used with some caution in this context. Once the sheet of charge in the ToF experiment has been generated (a delta function), the charges initially move together in a straight line. As time elapses and the packet moves through the film towards the collecting electrode, the packet broadens to a Gaussian (Figure 5.4). How, therefore, is the mobility of a carrier defined?

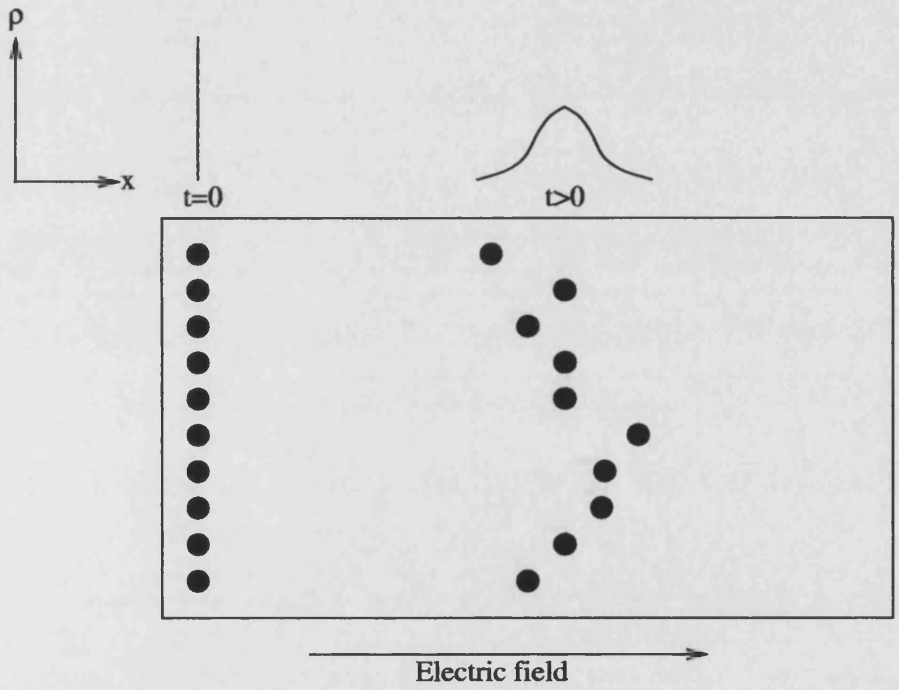

Figure 5.4: Schematic illustration of the broadening of the carrier packet from a delta function at t=0 (generation) to a Gaussian at some later time (t>0).

One possible measure of mobility is to take that of the fastest carrier. In this case, the transit time, t_T, is taken to be when the front of the packet reaches the collecting electrode i.e. the asymptotic 'shoulder' of the I(t) plot, as often used when performing ToF measurements. Another measure is the average velocity; if the carriers have travelled far enough to acquire a Gaussian shape then the transit time would be taken to be the time when the centre of the packet reaches the collecting electrode. For this reason, $t_{1/2}$ is often preferred as a measurement

of mobility to t_τ. However, it is quite possible that if the spreading of the packet is too great, i.e. the transport is dispersive, then it is impossible to define a mobility for the carriers (as discussed above), even though they do move under the influence of the electric field [3].

5.2 Gaussian Disorder Model (GDM)

Disorder models make the assumption that hopping charge transport is dominated by the effects of both spatial and energetic disorder, and much theoretical work has been carried out to investigate transport in organic molecular systems within the framework of the Gaussian Disorder Model (GDM) [5] [26][28]. Amorphous organic solids, including molecularly doped crystals, molecular glasses and conjugated polymers, are characterised by having small mean free paths for the charge carriers as a consequence of the high degree of disorder present in the system. The fundamental step is the transfer of charge between transporting sites, which may be molecules or segments in a conjugated polymer separated by topological defects. The energies of such transport sites are assumed to have a Gaussian distribution:

$$\rho(\epsilon) = \left(2\pi\sigma^2\right)^{-1/2} \exp\left(\frac{-\epsilon^2}{2\sigma^2}\right) \tag{5.8}$$

where ϵ is the on-site energy measured relative to the centre of the Gaussian density of states (DoS), and σ is the standard deviation of the distribution, which determines the degree of energetic disorder. Within the distribution, all of the states are localised. The rationale behind the choice of a Gaussian DoS is the existence of a Gaussian profile of the excitonic absorption band [5].

In the GDM, the jump rate, v_{ij}, from a site i to a neighbouring site j neglects polaronic effects [8], and assumes a Miller-Abrahams [29] form:

$$v_{ij} = v_0 \exp\left(-2\gamma R_{ij}\right) \begin{cases} \exp\left(-\frac{\epsilon_j - \epsilon_i}{k_B T}\right) & : \quad \epsilon_j > \epsilon_i \\ 1 & : \quad \epsilon_j < \epsilon_i \end{cases} \tag{5.9}$$

where v_0 is a prefactor, R_{ij} is the intersite distance, ϵ_i and ϵ_j are the energies of sites i and j respectively, and 2γ is an overlap parameter, consisting of separate site-specific contributions i.e. $2\gamma = \Gamma_i + \Gamma_j$. Allowing the overlap parameter to vary, again according to a Gaussian distribution of variance Σ, can be used to investigate the effects of geometric disorder e.g. variations in overlap due to varying the intersite distances and mutual molecular orientations. The energetic disorder, described by σ, is referred to as diagonal disorder, whilst the geometric disorder described by Σ, is referred to as off-diagonal disorder. However, the Miller-Abrahams approach neglects phonon emission for downhill hops [30].

The GDM is implemented using a Monte-Carlo approach, in which charge transport is treated as an incoherent random walk. The carriers are initially placed in random sites close to one edge of the sample system, and then move through the sample, following a trajectory specified by the following constraint that the probability, p, of hopping from a site i onto a neighbouring site j is given by:

$$p_{ij} = \frac{v_{ij}}{\sum_{i \neq j} v_{ij}} \tag{5.10}$$

Using this model, ToF measurements can be simulated, and hence carrier mobilities can be extracted by finding the transit time from the resulting current-time plot. The interplay between energetic and positional disorder was investigated by Bässler et al [5][31]; the essential results obtained by this approach can be summarised as follows.

For purely energetic disorder ($\hat{\sigma} > 0.0, \Sigma = 0.0$, where $\hat{\sigma} = \sigma/k_BT$), the application of an electric field reduces the activation energy required for forward hopping due to the carrier's gain in electrostatic energy. For a Gaussian DoS, the mobility at low fields was found to be independent of the applied field. As the field is increased, the mobility acquires the $\ln \mu \propto \mathrm{E}^{1/2}$ dependence characteristic of transport in disordered organic semiconductors e.g [20]. If the amount of energetic disorder present is small, then further increasing the field strength can result in the saturation of the mobility as a function of field, or even a decrease in mobility (i.e. negative field dependence), since here the electrostatic energy overcomes any activation energy and the carriers can always take the shortest path. Hence the $\ln \mu \propto \mathrm{E}^{1/2}$ dependence is only observed over a limited range of applied fields. If $\hat{\sigma}$ is large, the electric field is important for overcoming energetic

barriers at all temperatures, and as E increases, greater barriers can be overcome. Hence increasing the field allows shorter paths to be taken through the sample, increasing the mobility. Geometric (off-diagonal) disorder can introduce dead ends for the carriers; avoiding these dead ends may involved jumps against the field. Hence the mobility may decrease with increasing fields where Σ is large.

In a system containing both positional and energetic disorder, the behaviour of the mobility as a function of the electric field is a superposition of both effects. The positional disorder means that at low fields, carriers can choose an energetically easier route (possibly involving jumps against the field), but such routes are unlikely at high fields. At higher fields, the effect of field-lowering of the potential barriers becomes more important, and the competition between the two effects means that there will be a minimum mobility at some applied field value (see Figure 5.5). The simulation predicts that there will be a region of $\ln \mu \propto E^{1/2}$ within a finite field range. The slope, $S = \partial \ln \mu / \partial E^{1/2}$, will change sign when positional disorder exceeds energetic disorder.

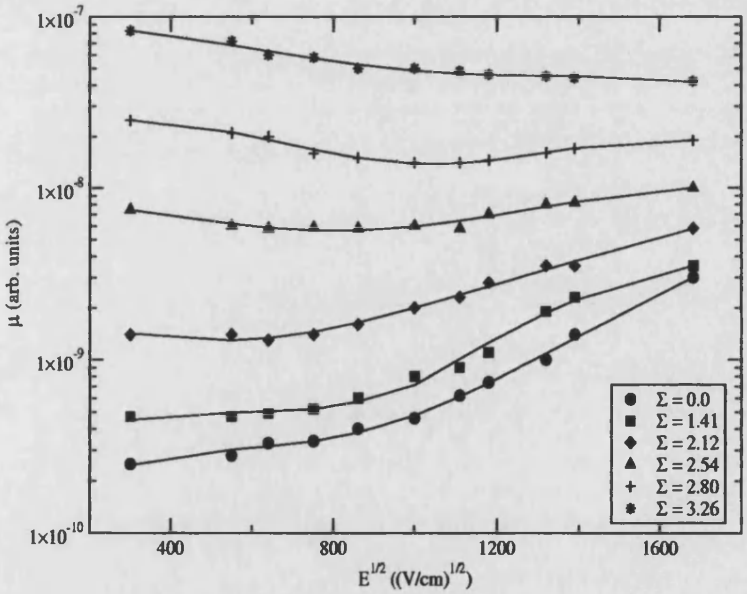

Figure 5.5: μ as a function of E for a large amount of energetic disorder ($\hat{\sigma} = 3.0$) and varying amounts of positional disorder (Σ). The lines are simply a guide to the eye. Reproduced from [5]

Bässler et al [5][31] formulated a law relating the mobility to the degree of diagonal, $\hat{\sigma}$, and off-diagonal, Σ, disorder:

$$\mu\left(\hat{\sigma},\Sigma,\mathrm{E}\right)=\mu_0\exp\left[-\frac{4\hat{\sigma}^2}{9}\right]\begin{cases}\exp\left(C\left(\hat{\sigma}^2-\Sigma^2\right)\sqrt{\mathrm{E}}\right) & : \quad \Sigma\geq 1.5\\ \exp\left(C\left(\hat{\sigma}^2-2.25\right)\sqrt{\mathrm{E}}\right) & : \quad \Sigma<1.5\end{cases} \tag{5.11}$$

where $C=2.9\times10^{-4}(\mathrm{cm}/V)^{1/2}$ is an empirical constant. Some authors prefer to fit this expression to experimental data rather than the empirical expression of Gill (equation 5.3), since the parameters Σ and $\hat{\sigma}$ are more meaningful [32].

5.2.1 Variations of the GDM

Through the fitting of equation 5.11 to experimental data, it has been shown that the GDM does describe transport in disordered organic semiconductors quite well, including reproducing the $\ln\mu\propto\mathrm{E}^{1/2}$ behaviour and yielding a physical value of μ_0. However, two of the main criticisms of the model are the failure to reproduce the $\ln\mu\propto\mathrm{E}^{1/2}$ dependence of the mobility over a larger range of fields, and the way in which positional disorder has been incorporated into the model [8]. The choice of a Gaussian distribution for off-diagonal disorder is not theoretically justified, unlike the case for diagonal disorder. In an attempt to rectify these problems, many additions have been made to the basic GDM (see [9][10] for an overview); the most important results are outlined below.

Gartstein and Conwell [37] showed that a spatially correlated site energy distribution could increase the field range over which the GDM predicts a $\ln\mu\propto\mathrm{E}^{1/2}$ dependence to a range which is similar to that observed experimentally. Strong field dependence occurs when the potential drop, given by qEl across a length scale l, is comparable to k_BT. If site energies are uncorrelated, as in the original GDM, the only relevant length scale is the inter-site distance. The introduction of spatially correlated site energies introduces a new larger length scale, over which the site energies are correlated. Thus spatial correlations can cause the mobility predicted by the GDM to show field dependence over a larger field range.

Dunlap et al e.g. [38] postulated that the origin of spatially correlated site energies was the existence of large permanent dipole moments in the dopant molecules used in molecularly doped polymers. There is a long-range interaction between

charge carriers and these dipole moments, and in this model, the energetic disorder is caused by different electrostatic potentials at the various sites, due to the random distribution in orientation in the dipole moments of nearby dopant molecules. Because the dipole-charge interaction is long-range, sites that are spatially close have similar energies and hence the site energies are spatially correlated, as suggested by Gartstein and Conwell [37]. Although this explanation was devised for the carrier mobility in molecularly doped polymers, it is believed to be valid for some organic semiconductors, such as Alq, which also have large permanent dipole moments [10].

However, many organic semiconductors used in OLEDs, such as the conjugated polymers PPV and PFO, do not have permanent dipole moments and thus the explanation of Dunlap et al [38] does not apply to these materials. Yu et al [6][39] stressed the importance of film morphology in producing correlated site energies. They suggested that fluctuations in the molecular geometry, such as the phenylene ring-torsion in PPV, could also cause spatially correlated site energies in materials without permanent dipoles. The spatial energy correlation is the result of strong inter-molecular restoring forces for ring-torsion fluctuations in dense films of closely packed polymers. Because the restoring force is intermolecular, ring-torsions on neighbouring chains will tend to move together. If an extra electron or hole is added to the polymer chain, the energy of the chain will depend on the torsion angle; hence there is a strong relation between a carrier at a site and the ring orientation at the site. Because the rings move together on nearby sites, there is a correlation between site energies. This approach has yielded a very similar field-dependence of the mobility to the charge-dipole interaction model of Dunlap et al [38], despite the different origins of the energetic disorder. However, the temperature dependence of the mobility predicted by the two models is different, since charge-dipole interactions are temperature independent, whilst in the molecular geometry fluctuation model of Yu et al, disorder is strongly temperature dependent. However, the temperature dependence of the mobility predicted by the model of Yu et al [6], which is not investigated in their publication, does not agree with experimental data [32].

The molecular geometry fluctuation model has also shown that there is a correlation between the strength of the field-dependence of the mobility and the magnitude of the mobility i.e. larger amounts of energetic disorder lead to a greater field-dependence of the mobility and a lower zero-field mobility. Figure

5.6 shows the experimental and simulated mobilities of PFO and MEH-PPV; it can clearly be seen that the field-dependence is lower in the PFO than in the MEH-PPV, whilst the magnitude of its mobility is much higher. This is because in MEH-PPV, the phenylene rings can easily rotate, whilst in PFO they are joined by bridging bonds so they can only rotate together, and hence the intermolecular restoring force to ring-torsion is increased, because two rings collide with a neighbouring molecule rather than one. Additionally, the the coupling of the ring-torsion to site energy is reduced in PFO because the charge can delocalise on two rings more easily, and hence the energetic disorder is reduced.

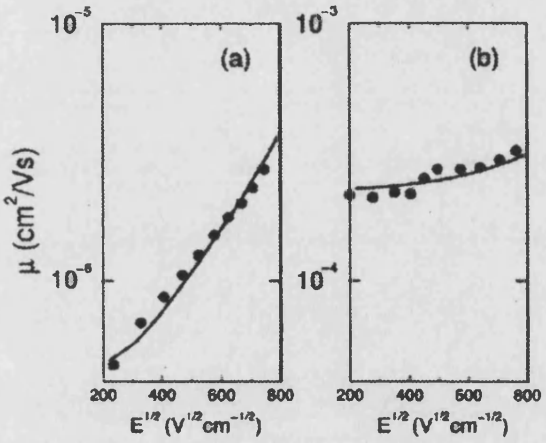

Figure 5.6: Hole mobility as a function of $E^{1/2}$. Left hand panel shows experimental (dots) and calculated (solid line) results for MEH-PPV. Right-hand panel shows experimental (dots) and calculated (solid line) results for PFO. Reproduced from [6]

It has also been suggested that variations in film morphology may have a significant effect on energies [40]. In polymer films, there may exist crystalline and amorphous regions, the former corresponding to lower energies as a result of larger polarisation energies, and the latter characterised by higher energies. Hence, within a polymer film, regions of disorder of varying degrees should cause similar site energies.

In order to investigate the effects of spatial disorder on transport, two approaches to counter the criticism of how the original GDM treats spatial disorder have been utilised [9]. The first approach taken uses the original GDM, but replaces the Gaussian distribution of site contributions to coupling, which are unphysical and cause correlations between hops, with more realistic approximations. For example, Gartstein and Conwell [33] introduced positional and orientational order via fluctuations in the bonds adjoining the transport sites, rather than having site fluctuations. Equation 5.9 is modified such that the elementary jump rate

becomes:

$$v_{ij} = \exp(\xi_{ij}) \exp(-2\gamma R_{ij}) \tag{5.12}$$

where ξ_{ij} is a uniformly distributed random variable which refers to the bonds.

An alternative approach, which is taken in this thesis, is to explicitly include the spatial disorder in the model. As mentioned in previous chapters, balanced mobilities are desirable for efficient OLEDs and thus investigations into how mobility varies with film morphology and composition are becoming more widespread e.g. [41][42]. It is therefore useful to have hopping models which can calculate mobilities for certain materials, along with the field and temperature dependence of these mobilities [2]. Stephan et al [7] introduced spatial disorder and anisotropy into the GDM. Spatial disorder was introduced by randomly varying the lattice spacing, whereas anisotropy was introduced by varying the lattice constant perpendicular to the field direction. If disorder exists only in the field direction, then the carrier may take a path around a forbidden jump at low fields, enhancing the mobility. As the field increases, the mobility decreases as such paths are against the field. If disorder exists perpendicular to the field, then the mobility is reduced at all fields since paths avoiding forbidden jumps in the field direction are also unlikely. For spatial disorder in three dimensions, the mobility behaves as a combination of the two factors. At low fields, the mobility is enhanced as more easy paths are available but at high fields these easy paths are against the field and hence cannot be taken; therefore there exists a critical field value below which μ increases with increasing disorder, and above which μ decreases with increasing disorder. Investigations of anisotropy show that for a reduction of the lattice spacing perpendicular to the field, the mobility increases except at high fields. Again, the anisotropy allows the carriers to move around difficult paths, except at high fields when they cannot jump against the field. Increasing the lattice spacing reduces the mobility at all fields, since few paths are open which avoid energetically costly jumps in the field direction.

Ramos and Stoneham [1][43] represented the polymer segments by straight strands or varying lengths on a regular lattice, with fluctuations in their orientations. Charges injected into the lattice hopped through the sample according to an algorithm similar to equation 5.9, and could be trapped if voids prevented

them from hopping or the local electric field (due to space charge) was too small. However, they focused on investigating on properties other than transport, and concluded that the competition between trapping, transport and recombination leads to systematic trends which can be used to aid OLED design.

5.3 Modelling transport in liquid-crystalline conjugated polymers

As mentioned in the previous section, there is considerable interest in how film morphology and composition affects transport. The systems initially chosen to be studied were films of liquid-crystalline conjugated polymers. Such conjugated polymers do not have correlated on-site energies arising from either permanent dipole moments or molecular geometry fluctuations, since they are structurally rigid, and hence they are also weakly energetically disordered. These factors also simplify the simulation of transport in these materials since less information is required. The main area of interest is the geometric disorder i.e. the effect of the composition of a film of liquid crystalline conjugated polymers on transport [44]

The hopping transport model described below is similar to the Gaussian Disorder Model in some respects; in its description of the transporting sites' energies, and it performs numerical simulations of the time-current plots obtained using the time-of-flight technique (section 5.1.1). The model itself comprises two areas: the creation of the polymer films (section 5.3.1), and the Monte-Carlo routine for charge transport (section 5.3.2).

5.3.1 Polymer film structures

Based on the premise that the extended backbone conjugation of liquid-crystalline polymers (e.g. PFO) makes them very stiff [10], the polymer chains themselves can be described as rigid rods [44]. They are represented within the simulation as straight lines, of length l, with the end points having co-ordinates (x, y, z) and (x', y', z'). These chains are subdivided into a number, n, of conjugated segments to mimic a real polymer chain, with each segment representing an individual

transport site. In reality, the conjugation along the polymer's carbon chain backbone may be interrupted by kinks or broken bonds, creating a number of hopping sites.

The chains are then distributed within a three-dimensional film according to the desired morphology. The film has a thickness, d, 1μm, similar to conventional ToF samples. This thickness is taken to be along the x-direction, which is also the direction of the applied field, and hence the electrodes are situated at $x = 0$ and $x = d$. In the y and z directions, periodic boundary conditions are imposed. The z-direction is chosen to be slightly larger than the chain length, l, to allow hopping in the z-direction, whilst the dimension of the y-direction must be sufficiently large that a reasonably large density of chains can be formed to give a realistic sample, whilst being small enough that the simulation time is not too great.

The first possible film composition to be considered is one in which the chains are chosen to be regularly spaced, and are all aligned parallel to the electrodes, so the end-point co-ordinates are (x, y, z) and (x, y, z'). The chains are on a lattice, with each chain placed in the $x-y$ plane such that it has four nearest neighbours, (except those closest to the electrodes), each separated by a distance equal to the lattice spacing, a (see Figure 5.7). In addition, the z-dimension is chosen to be equal to l plus the lattice constant, with the centre of the chain being located at $(x, y, z/2)$, so that each chain can hop from one end of itself to the other end. In this case, the exact number of chains to be created is known in advance.

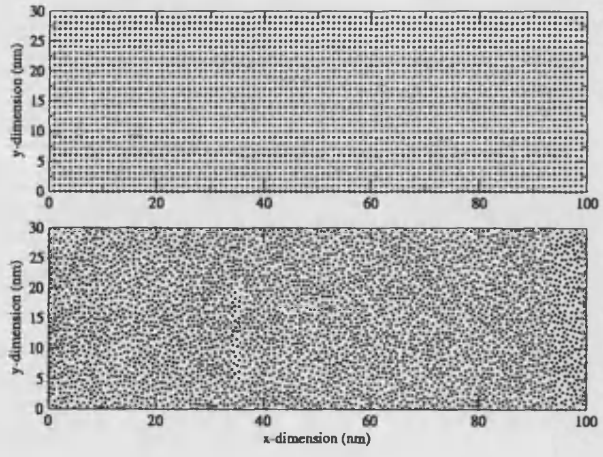

Figure 5.7: Plan view of the positions of the rods in the regularly spaced case (top panel) and irregularly spaced case (bottom panel). In both cases, all of the chains are aligned parallel to the electrodes. Only a portion of the films have been illustrated.

The next film composition considered has all of the chains aligned parallel to

the electrodes, but place the chains in randomly selected positions within the x-y plane; the chains are no longer on a lattice (Figure 5.7). This is achieved by multiplying the x and y dimensions by a random number, drawn from a uniform distribution between 0 and 1.0, to obtain the x and y co-ordinates of the chain's end points. The chains are placed subject to the condition that no two chains are closer than a specified minimum distance, r_{min}, to apply the so-called excluded volume condition, allowing for periodic boundary conditions. The end point co-ordinates of chain 1 are (x_1, y_1, z_1) and (x_1, y_1, z_1'), whilst the end point co-ordinates of chain 2 are (x_2, y_2, z_2) and (x_2, y_2, z_2') and so forth. However, since the chains are aligned in the z-direction, then $z_1 = z_2$ and $z_1' = z_2'$. Hence, the excluded volume condition can be expressed as:

$$|(x_2 - x_1, y_2 - y_1, 0)| \geq r_{min} \tag{5.13}$$

This means that although the chains are represented by lines, they still occupy a finite amount of space and hence cannot touch or cross directly through each other. Eventually, a situation will be reached whereby a new chain cannot be placed within the film and still satisfy the excluded volume condition, and a maximum chain density is reached.

The final film composition to be investigated is that in which the chains are not aligned parallel to the electrodes, but instead are randomly aligned i.e. they all point in different directions. A start position in the x, y plane for the chain is chosen as above, and then the end point is calculated as:

$$x' = x + l\sin\theta\cos\phi \tag{5.14}$$

$$y' = y \pm l\sin\theta\sin\phi \tag{5.15}$$

$$z' = z \pm l\cos\theta \tag{5.16}$$

where l is the chain length, and θ and ϕ are the polar and azimuthal angles (see Figure 5.8). The maximum values of θ and ϕ are specified initially; for each chain, the values of θ and ϕ used to calculate the end points of the chain (equations 5.14-5.16) are selected by multiplying their maximum values by a random number

between 0 and 1.0, again drawn from a uniform distribution.

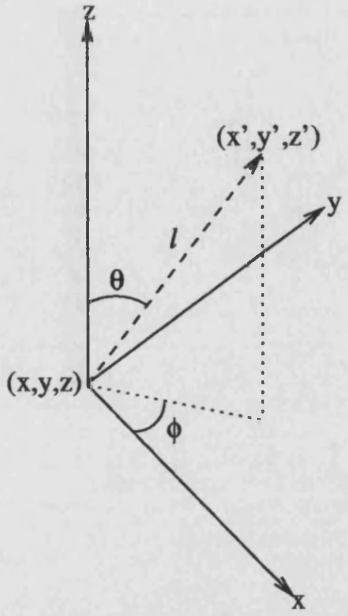

Figure 5.8: End points of the randomly aligned chains. The dashed line represents the polymer chain. θ and ϕ are the polar and azimuthal angles respectively.

The end point of the chain is chosen to be in the $\pm y$ and $\pm z$ direction by generating a random number; if the random number > 0.5, then $y' > y$ or $z' > z$. Similarly, if the random number < 0.5, then $y' < y$ or $z' < z$. In this manner, a chain pointing in any direction (within the limits of θ and ϕ) can be created. Again, a minimum interchain distance is specified to apply the excluded volume condition. This is a more complex calculation than in the previous case, and more computationally intensive, as it requires the chains to be represented as vectors, so that vector formulae can be applied to calculate the shortest distance between two finite skew lines.

Once the chains have all been created, the conjugated segments are created. This is performed by dividing the line created by the two end-points into the number of required segments, and then recording the co-ordinates of the mid-points of these sections.

The next element of this part of the program is to find the nearest-neighbour segments for each transporting site i.e. segment. Each segment can only have one transporting site to which it can hop per neighbouring chain. In the case of the regularly spaced chains, aligned parallel to the electrodes, then each site has four neighbours. Since the chains, and hence segments, are aligned in the

z-direction, these neighbours are the equivalent segments on neighbouring chains in the $+x, -x, +y$, and $-y$ directions. The distance to these sites is equal to the lattice constant, a. In addition, the end segments can also hop to the segment at the opposite end of the same chain across the periodic boundary condition.

Where the chains are aligned parallel to the electrodes but randomly distributed, again the neighbouring segments are within the $x-y$ plane. Only segments which exist within a specific cut-off distance, r_c, of a specific segment on a particular chain will be considered for hopping i.e.:

$$|(x_2 - x_1, y_2 - y_1, 0)| \leq r_c \tag{5.17}$$

where the cut-off distance is pre-specified. The cut-off distance is typically of the order of magnitude of the minimum inter-chain distance, and limits the number of possible hopping sites to a relatively small number.

Finally, in the case of the randomly aligned chains, the neighbouring segments are again selected to be those within a fixed hopping distance, r_c, by considering the distances between the mid-points of the segments:

$$|(x_{k,l} - x_{i,j}, y_{k,l} - y_{i,j}, z_{k,l} - z_{i,j})| \leq r_c \tag{5.18}$$

where i and k are neighbouring chains, and j and l are segments on those chains.

In all of the above situations, neighbouring segments across the periodic boundary conditions in the $+y$ and $-y$ directions must also be considered. When a segment on a nearby chain is deemed to be a suitable neighbouring transport site, the distance to the segment and the direction of the hop to the segment with respect to the field direction (i.e. the angle made with the $x-$direction), must be recorded.

The final stage of the generation of a specific polymer film is to assign on-site energies to each chain; the segments on a chain are considered to be iso-energetic. The on-site energies are taken from a Gaussian distribution (section 5.2); for

each chain an energy is selected by multiplying $k_B T_0$ by a random number chosen from a Gaussian distribution [45], having standard deviation σ, where k_B is Boltzmann's constant and T_0 is chosen to be 300K.

5.3.2 Hopping algorithm

Charge carriers, assumed to be holes since electron transport in PFO is highly dispersive e.g. [12], are initially placed within a thin region, δx, close to the left-hand side of the film; this is analogous to the way in which charge carrier pairs are generated by a pulse of light in the ToF technique (section 5.1.1). The width of the region is chosen arbitrarily, but should be very thin compared to the overall film thickness. The number of carriers placed between $x = 0$ and $x = \delta x$ is also chosen arbitrarily. However, factors which influence this choice are that the larger the number the carriers used in a sample, the smoother and more accurate the simulated ToF plot will be, but if only one charge is allowed per segment at any time (due to Coulombic repulsion considerations [47]), then if δx is large, the carriers near $x = 0$ are forced to remain in their initial positions until the carriers on the right hand side of the charge packet have moved further into the film, causing an unphysical broadening of the charge packet.

The hopping motion of the charge carriers under the influence of an applied electric field can be both inter- and intra-chain [8]. Intra-chain motion has been included in a very approximate fashion by allowing charges on a segment to hop to a neighbouring segment on either side, chosen at random, on the same chain at the beginning of the Monte-Carlo timestep, immediately preceding the inter-chain transport step. The most important aspect of the transport is assumed to be the inter-chain hopping, and the probability of a charge hopping from a segment to one of its neighbouring segments is given by either a Miller-Abrahams type hopping rate:

$$p_{ij} = \begin{cases} \gamma \exp\left(-\frac{\epsilon_j - \epsilon_i - q\mathrm{E}\cdot r_{ij}}{k_B T}\right) & : \quad \epsilon_j - \epsilon_i > q\mathrm{E}\cdot r_{ij} \\ \gamma & : \quad \epsilon_j - \epsilon_i \leq q\mathrm{E}\cdot r_{ij} \end{cases} \tag{5.19}$$

or a symmetric hopping rate:

$$p_{ij} = \gamma \exp\left(-\frac{\epsilon_j - \epsilon_i - q\mathrm{E}\cdot r_{ij}}{2k_BT}\right) \tag{5.20}$$

where p_{ij} is the un-normalised probability of hopping from site i to j, γ is a wave-function overlap factor, ϵ_j and ϵ_i are the energies of chains j and i respectively, q is the electronic charge, $\mathbf{E}$ is the electric field vector, $\mathbf{r}_{ij}$ is the vector for hopping from site i to j, k_B is Boltzmann's constant, and T is temperature. In the immediate work, γ has been neglected, and the cut-off distance r_c described above is employed to limit hopping to nearest neighbours; hence the tunnelling probability does not diminish with distance, and the hopping probability is based solely on energetic considerations. Calculations are in progress to deduce the tunnelling rates between polymer chains using the Bardeen formalism [46], which can then be implemented in the model.

The factor of 2 in equation 5.20 is a consequence of detailed balance [6]; both of these hopping algorithms satisfy the principle of detailed balance such that:

$$\frac{p_{ij}}{p_{ji}} = \exp\left(-\frac{\epsilon_j - \epsilon_i}{k_BT}\right) \tag{5.21}$$

The probabilities are then normalised such that:

$$P_{ij} = \frac{p_{ij}}{\sum_{i\neq j} p_{ij}} \tag{5.22}$$

The path taken is then selected by generating a random number, ran, and comparing it to the normalised probabilities. For example, if $0 \leq ran \leq P_{ij}$ then the charge hops to site j, else if $P_{ij} \leq ran \leq (P_{ij} + P_{i,j+1})$, then the charge hops to site $j+1$ and so on.

As the carriers hop through the sample, they generate a displacement current (section 5.1.1), which is calculated using equation 5.5. In practice, several simulations are usually run for the same type of sample in order to obtain an average $I(t)$ profile; the number of runs required depends upon the number of carriers used and simply the time available. As energetic and spatial disorder increases,

the simulation run time increases dramatically. From this $I(t)$ profile, a transit time and hence mobility can be established and the mobility investigated as a function of energetic and spatial disorder. Such results are presented in Chapter 6.

5.4 Conclusions

Treating charge transport in disordered organic semiconductors as hopping transport within the Gaussian Disorder Model provides a good description of the observed field and temperature dependence of the mobilities obtained experimentally. Extensions to the basic GDM to address the issues of spatially correlated energies, and positional disorder have also been made successfully, further improving the validity of the results obtained from the GDM.

A model based on the principles of simulating hopping transport in the GDM has been proposed in which the morphology of a film of liquid crystalline conjugated polymers is explicitly represented. Such systems do not have correlated energies and are weakly energetically disordered; hence the effect of varying the morphology of the film by varying the position and alignment of the polymer chains can be investigated with relative ease. The results of such an investigation, for small and varying amounts of energetic disorder, where the chains are either all aligned parallel to the electrodes, and either regularly or irregularly spaced, or randomly aligned within specific limits, to mimic spatial disorder, are contained within Chapter 6.

References

[1] A M Stoneham and M M D Ramos, *J. Phys.:Condens. Matt.*, **13**, 2411 (2001).

[2] A M Stoneham, M M D Ramos, A M Almeida, H M G Correia, R M Ribeiro, H Ness, and A J Fisher, *J. Phys.:Condens. Mat.*, Forthcoming publication (2002).

[3] N Tessler, Lecture notes available from: http://www.ee.technion.ac.il/people/nir/Lectures.html

[4] L B Schein, D Glatz, and J C Scott, *Phys. Rev. Lett.*, **65**, 472 (1990).

[5] H Bassler, *Phys. Stat. Sol. (b)*, **175**, 15 (1993).

[6] Z G Yu, D L Smith, A Saxena, R L Martin, and A R Bishop, *Phys. Rev. B.*, **63**, 085202-1 (2001).

[7] J Stephan, A Liemant, F Albrecht, and L Brehmer, *Synth. Met.*, **109**, 327 (2000).

[8] G Hadziioannou and P F van Hutten, *Semiconducting Polymers: Chemistry, Physics and Engineering*, Wiley-VCH, Weinheim, Germany (2000).

[9] A B Walker, A Kambili, and S J Martin, *J. Phys.: Condens. Matt.*, **14**, 9825 (2002).

[10] I H Campbell and D L Smith, *Solid State Physics*, **55**, 1 (2001).

[11] C H Tan, A R Inigo, W Fann, P K Wei, G Y Perng, and S A Chen, *Organic Electronics*, **3**, 81 (2002).

[12] M Redecker, D D C Bradley, M Inbasekaran, and E P Woo, *Appl. Phys. Lett.*, **74**, 1400 (1999).

[13] H Sirringhaus, R J Wilson, R H Friend, M Inbasekaran, W Wu, E P Woo, M Grell, and D D C Bradley, *Appl. Phys. Lett.*, **77**, 406 (2000).

[14] M Grell, D D C Bradley, M Inbasekaran, and E P Woo, *Advanced Materials*, **9**, 798 (1997).

[15] A J Campbell, D D C Bradley, and H Antoniadis, *Appl. Phys. Lett.*, **79**, 2133 (2001).

[16] M Redecker, D D C Bradley, M Inbasekaran, W W Wu, and E P Woo, *Advanced Materials*, **11**, 241 (1999).

[17] C Giebeler, H Antoniadis, D D C Bradley, amd Y Shirota, *Appl. Phys. Lett.*, **72**, 2448 (1998).

[18] R G Kepler, P M Beeson, S J Jacobs, R A Anderson, M B Sinclair, V S Valencia, and P A Cahill, *Appl. Phys. Lett.*, **66**, 3618 (1995).

[19] W D Gill, *J. Appl. Phys.*, **55**, 5033 (1972).

[20] K C Kao and W Hwang, *Electrical Transport In Solids: with particular reference to organic semiconductors*, Pergamon Press, Oxford (1981).

[21] H Scher and E W Montroll, *Phys. Rev. B*, **12**, 2455 (1975).

[22] G F L Ferreira, *Phys. Rev. B.*, **16**, 4719 (1976).

[23] J C Scott, B A Jones, and L T Pautmeier, *Mol. Cryst. Liq. Cryst.*, **253**, 183 (1994).

[24] A J Campbell, D D C Bradley, and H Antoniadis, *J. Appl. Phys.*, **89**, 3343 (2001).

[25] A R Inigo, C H Tan, W Fann, Y S Huang, G Y Perng, and S A Chen, *Advanced Materials*, **13**, 504 (2001).

[26] D Hertel, H Bässler, U Scherf, and H H Hörhold, *J. Chem. Phys.*, **110**, 9214 (1999).

[27] S M Sze, *Physics of Semiconductor Devices*, 2nd ed., J. Wiley and Sons, New York (1981).

[28] M Abkowitz, H Bässler, and M Stolka, *Phil. Mag. B*, **63**, 201 (1991).

[29] A Miller and E Abrahams, *Phys. Rev.*, **120**, 745 (1960).

[30] I I Fishchuk, D Hertel, H Bässler, and A K Kadashchuk, *Phys. Rev. B*, **65**, 125201-1 (2002).

[31] P M Borsenberger, L Pautmeier, and H Bässler, *J. Chem. Phys.*, **94**, 5447 (1991).

[32] T Kreouzis, *Private communication.*

[33] Y N Gartstein and E M Conwell, *J. Chem. Phys.*, **100**, 9175 (1994).

[34] B Hartenstein, H Bässler, S Heun, P Borsenberger, M van der Auweraer, and F C De Schryver, *Chem. Phys.*, **191**, 321 (1995).

[35] A Kambili and A B Walker, *Phys. Rev. B*, **63**, 012201 (2001).

[36] P E Parris, *J. Chem. Phys.*, **108**, 218 (1998).

[37] Y N Gartstein and E M Conwell, *Chem. Phys. Lett.*, **245**, 351 (1995).

[38] D H Dunlap, P E Parris, and V M Kenkre, *Phys. Rev. Lett.*, **77**, 542 (1996).

[39] Z G Yu, D L Smith, A Saxena, R L Martin, and A R Bishop, *Phys. Rev. Lett.*, **84**, 721 (2000).

[40] S V Rakhmanova and E M Conwell, *Synth. Met.*, **116**, 389 (2001).

[41] T-Q Nguyen, R C Kwong, M E Thompson, and B J Schwartz, *Appl. Phys. Lett.*, **76**, 2454 (2000).

[42] H C F Martens, P W M Blom, and H F M Schoo, *Phys. Rev. B.*, **61**, 7489 (2000).

[43] M M D Ramos and A M Stoneham, *Comp. Mat. Sci.*, **17**, 260 (2000).

[44] D D C Bradley, *Private communication.*

[45] W H Press, B P Flannery, S A Teulolsky, and W T Vertterling, *Numerical Recipes In Fortran*, Cambridge University Press, Cambridge (1989).

[46] A Kambili and A B Walker, *Unpublished data* (2002).

[47] A M Stoneham, *Private communication.*

Chapter 6

Simulating Hopping Transport In Liquid Crystalline Conjugated Polymers

In this chapter, results are presented for the field and temperature dependence of the mobilities of carriers, assumed to be holes, in a film of a liquid-crystalline conjugated polymer, PFO [1] (Figure 6.1), a blue light emitting polymer. PFO exhibits non-dispersive hole transport, has a high hole mobility compared to many other less ordered conjugated polymers, and has a weakly field dependent hole mobility e.g. [2][3]. Figure 6.2 shows an experimentally obtained set of mobilities at different temperatures [4].

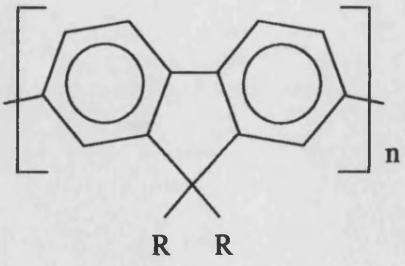

Figure 6.1: Chemical structure of poly(9,9-dioctylfluorene) (PFO). R=C_8H_{17}.

A negatively field dependent hole mobility (i.e. the mobility decreases with increasing field) has also been observed [5][6], indicating very high levels of purity and order. PFO does not have a permanent dipole moment and is structurally rigid; hence no spatially correlated site energies, due to either charge-dipole in-

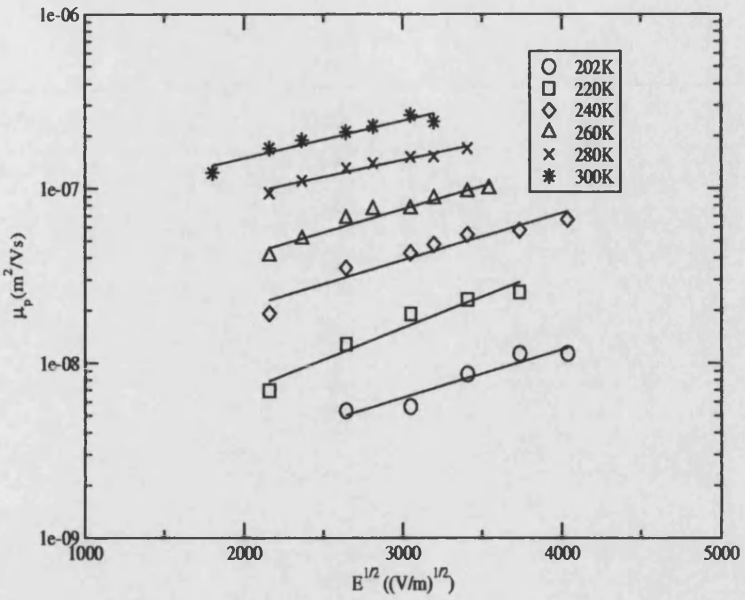

Figure 6.2: Logarithm of the hole mobility, μ_p, in PFO as a function of $E^{1/2}$, obtained by time-of-flight technique [4]. The shapes represent experimental data points, and the lines represent a best fit to the data points.

teractions or molecular geometry fluctuations are expected to be present in the system [6]. The transport in these films has been investigated using the Monte-Carlo simulation described in Chapter 5.

In all of the samples simulated to obtain these results, the film thickness, d, was taken to be 1μm, and the length of the chains, l, was assumed to be uniform and was set at 100nm. Each chain was assumed to have 5 segments [6]. The symmetric hopping algorithm given in Chapter 5 was used to describe the transport in these results, although this choice is somewhat arbitrary, with other authors reporting that the different rates yield similar results at low fields, with some deviation at high fields as the mobility calculated using the symmetric hopping rate becomes greater than that calculated using the M-A hopping rate e.g. [8][9]. Section 6.1 examines the results obtained from the sample when all chains are aligned parallel to the electrodes, and all of the chains are regularly spaced with a lattice constant, a, of 1nm. Section 6.2 examines the results obtained from a film of chains which are still all aligned parallel to the electrodes, but are randomly placed within the film rather than being positioned on a regular lattice, subject to the excluded volume condition. Finally, section 6.3 contains the results obtained from a sample of chains which are distributed randomly throughout the sample, and have a distribution of orientations as opposed to being aligned to the electrodes.

The mobilities have been calculated in each case for a range of applied fields from $14 \times 10^6 - 50 \times 10^6 \mathrm{Vm}^{-1}$, which are values typically used in experiments. The time used to calculate the mobility is $t_{1/2}$, defined as the time taken for the current taken to fall to half of its plateau value, as outlined in Chapter 5.

6.1 Regularly spaced and aligned polymer chains

The first system to be examined was one in which all the chains were aligned parallel to the electrodes, and were regularly spaced within the film i.e. spatially ordered. This system was chosen to allow the effects of purely energetic disorder to be examined, to facilitate the understanding of later systems which were not spatially ordered. Different amounts of energetic disorder were applied to the system, ranging from $\hat{\sigma}$=0.0 to 2.0, where $\hat{\sigma} = \sigma/2k_BT$. Figure 6.3 shows a set of current-time plots obtained at a temperature of 300K, with $\hat{\sigma}$=0.5.

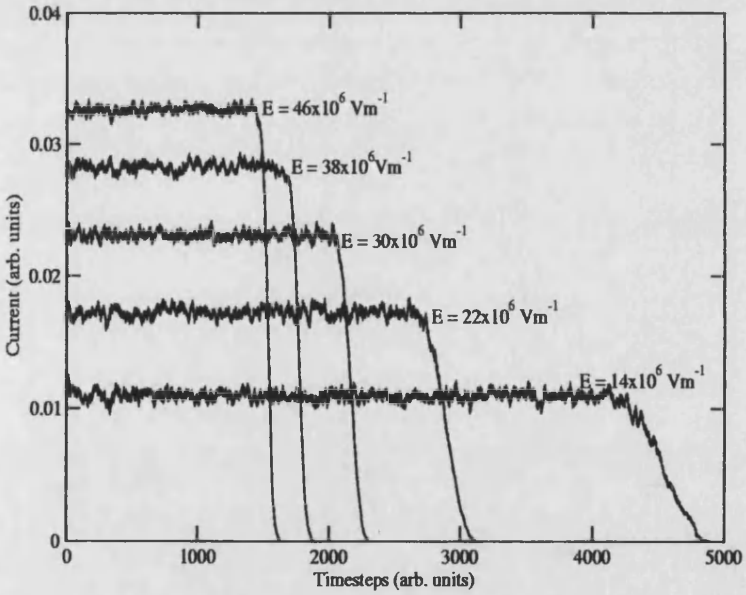

Figure 6.3: Current-time plots for a film of regularly spaced liquid crystalline polymer chains at 300K, $\hat{\sigma}$=0.5.

The current-time plots appear qualitatively very similar to those obtained from the experimental time-of-flight technique [10], with a distinctive well-defined plateau region and a decaying tail, indicative of non-dispersive transport [11]. As the applied field is increased, the magnitude of the current in the plateau

region can be seen to increase as the carrier packet moves with increased average velocity, and the time at which the tail is observed becomes smaller, corresponding to the earlier arrival of the carriers at the collecting electrode as the field is increased. Two other features can also be observed upon closer inspection; firstly, at t=0, a small initial current spike at low fields, and secondly, as the applied field increases in magnitude, the spread of the tail region decreases. These two features are explained below in section 6.1.1.

6.1.1 Profile of current-time plot

Although time-of-flight current-time traces follow a general shape, as previously discussed in Chapter 5 [10], the specific details of a such a trace vary from material to material, and also the temperature and applied field. Figure 6.4 shows a simulated current-time plot obtained from the system of regularly spaced liquid crystalline polymers with no energetic disorder at 100K, with an applied field of $42\times10^{6}\mathrm{Vm}^{-1}$; the current packet is also illustrated at several times during the simulation. Figure 6.5 shows the same information for the same system when $\hat{\sigma}$=1.0 and the applied field is $42\times10^{6}\mathrm{Vm}^{-1}$.

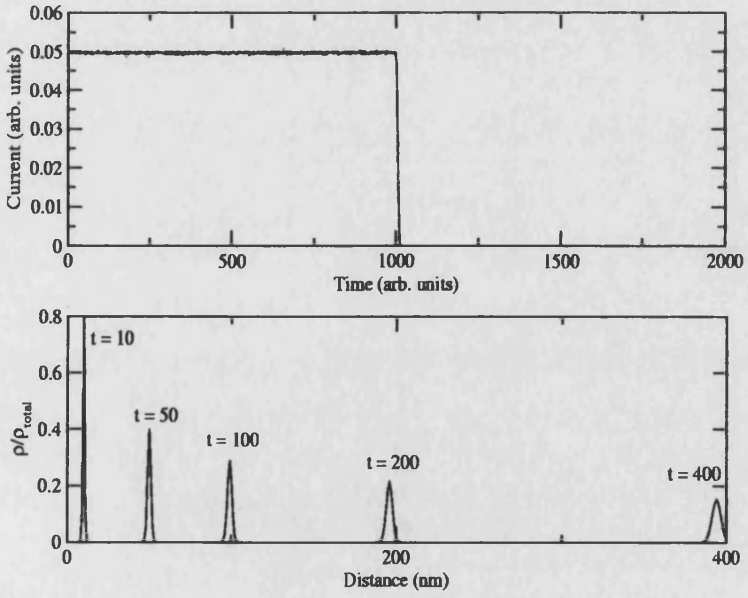

Figure 6.4: Simulated current-time plot (top panel) for a film of regularly spaced liquid crystalline polymer chains with no energetic disorder at 100K, E=$42 \times 10^{6}\mathrm{Vm}^{-1}$. The bottom panel shows the profile of the charge packet at various times during the simulation.

The current-time trace shown in Figure 6.4 closely resembles that of the idealised

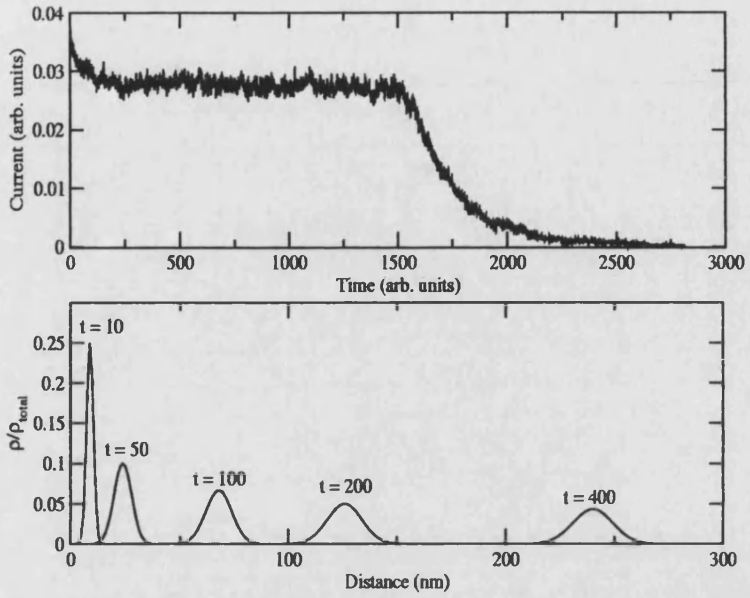

Figure 6.5: Simulated current-time plot (top panel) for a film of regularly spaced liquid crystalline polymer chains at 100K, $\hat{\sigma}$=1.0, and E=42 $\times$ $10^6 Vm^{-1}$. The bottom panel shows the profile of the charge packet at various times during the simulation.

time-of-flight trace depicted in Figure 5.3, in which the sheet of charge generated moves through the sample with a constant velocity; all carriers leave the sample at the transit time, t_τ. Inspection of the charge packet profile in Figure 6.4 confirms that a similar situation exists here too; initially, the charges are all in a line next to the left-hand electrode. As a field is applied, they all hop forward to the next row of transport sites without hindrance. Hence at t=10, the packet still resembles a delta-function. As the packet moves across the sample, it does spread to a Gaussian, whose width increases with time. However, it can be seen that the centre of the packet moves with a uniform velocity of approximately 1nm/timestep. Consideration of equation 5.4 to calculate the current verifies that for such a packet, the current is almost constant. As the packet of carriers arrives at the collecting electrode, the carriers almost all leave the sample simultaneously and the current suddenly drops to zero; the very small spreading of the tail of the trace in Figure 6.4 indicates that the packet had spread during its traversal of the film.

The situation in Figure 6.5 is somewhat different; the simulated current-time plot has a different shape to that in Figure 6.4. Firstly, the current-time plot exhibits an initial spike, which quickly drops down to the plateau current value. This initial spike is observed in all time-of-flight experiments conducted on organic semiconductors. The charge packet profile in Figure 6.5 shows that although the

charges are all initially lined up next to the left hand electrode, once the field is applied, the charges do not all move forward together; even at t=10, some spreading can be seen and the packet is Gaussian. The energetic disorder prevents all carriers from moving forward in the field direction and some carriers hop in directions away from the field. In this way, some carriers move forward initially, followed by the rest over subsequent time steps. This behaviour causes the formation of the Gaussian propagating charge packet, which then moves through the sample. As the packet moves through, a constant current is generated, corresponding to the plateau region of the time-of-flight plot. Once the packet reaches the collecting electrode, the carriers at the front of the packet exit first, reducing the magnitude of the current. However, the rest of the carriers in the packet are still in the sample generating a current. As more and more carriers reach the electrode and exit, the current drops further until all carriers leave the sample and the current tends to zero. Hence it can be seen that the greater the disorder, the broader the packet will be and hence the larger the initial spike and width of the tail on the current-time plot. The strength of the electric field and the temperature will also affect the shape of the plot, since these factors determine how strong the effect of disorder is on the carriers, as will be seen below.

6.1.2 Carrier mobilities for $\hat{\sigma}$=0.0

Initially, the mobility of carriers in the system was investigated for the case where $\hat{\sigma}$=0.0 i.e. where all the chains are equi-energetic. In practice, such a situation cannot actually exist since the existence of a polaron on a chain will alter its energy [12], but this system provides an understanding of transport in the absence of spatial and energetic disorder. Figure 6.6 shows the how the logarithm of the hole mobility, $\ln \mu$, varies with the applied electric field (from 14-50$\times 10^6$ Vm^{-1}) over a range of temperatures (from 50-350K).

Figure 6.6 shows that in this system, the mobility, μ, decreases with both increasing temperature and increasing electric field strength. This can be understood by considering the un-normalised probability for hopping between two sites (equation 5.20), which in the absence of any energetic disorder can be expressed as:

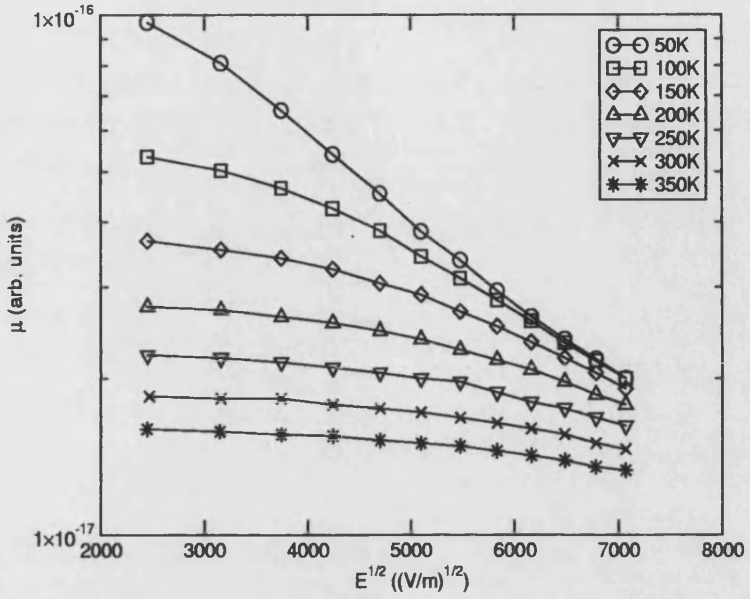

Figure 6.6: Logarithm of hole mobility, μ, as a function of $\sqrt{\mathrm{E}}$, for various temperatures. The chains are regularly spaced and there is no energetic disorder in the system.

$$p_{ij} = \exp\left(\frac{q\mathrm{E}\cdot\mathbf{r}}{k_B T}\right) \tag{6.1}$$

where p_{ij} is the probability of hopping between sites i and j, q is the electronic charge, $\mathbf{E}$ is the electric field, $\mathbf{r}$ is the hopping vector between the two sites, k_B is Boltzmann's constant, and T is the temperature.

Due to the regular positioning of the chains, the neighbouring transport sites which they may hop to are in the $+x$, $-x$, $+y$, and $-y$ directions, where x is the field direction and the y direction is perpendicular to the field direction. Hence the un-normalised probabilities, p, of hopping in the various directions are:

$$p_{+x} = \exp\left(\frac{q\mathrm{E}a}{k_B T}\right) \tag{6.2}$$

$$p_{-x} = \exp\left(\frac{-q\mathrm{E}a}{k_B T}\right) \tag{6.3}$$

$$p_{+y} = 1 \tag{6.4}$$

$$p_{-y} = 1 \tag{6.5}$$

where a is the lattice spacing. Hence the probability of hopping in the field direction ($+x$) is much larger than the probability of hopping in the other directions, and increases exponentially with the applied field. The probability of hopping against the field (-x direction) is small, and decreases exponentially with the applied field. The probability of hopping perpendicular to the electric field is fixed at 1. As the probabilities are normalised, the probability of hopping in the field direction is always large and increases as the field increases. At a constant field, as the temperature increases, the probability of hopping in the x-direction is actually slightly decreased.

In this system, thermal energy dominates, hence at low temperatures, even at low fields, the probability of hopping in the field direction is high and the majority of carriers will move in the $+x$ direction; this is illustrated in Figure 6.7, which illustrates the path of a carrier across the sample at 100K. As the field increases, virtually all carriers will move forward in the $+x$ direction at each timestep, and the carriers move essentially as a delta function of charge, as discussed in section 6.1.1. Therefore the transit time of the carriers quickly saturates to a constant value, which corresponds to the minimum number of time-steps required to traverse the lattice i.e. hopping in the $+x$ direction each time, for all fields, and hence the drift velocity saturates. Given that the mobility is the ratio of the drift velocity to field for a constant thickness, then μ varies as E^{-1} at high fields, as can be seen from Figure 6.6.

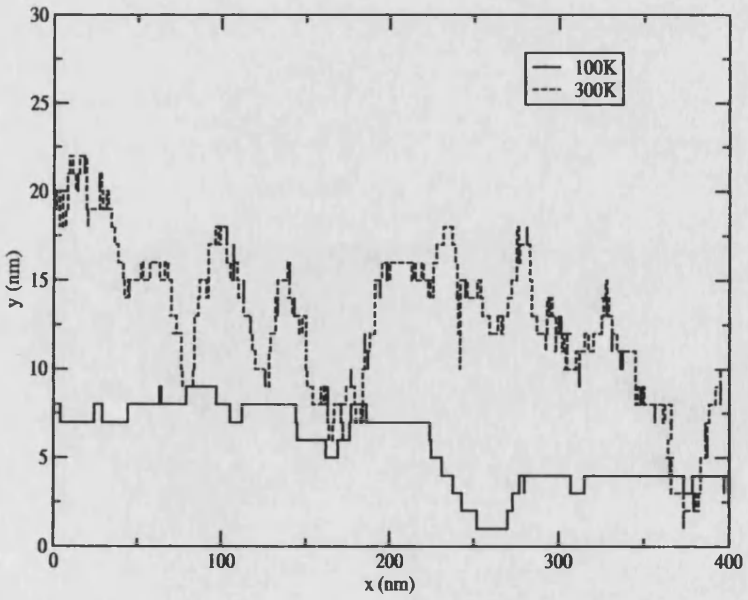

Figure 6.7: Typical paths for carriers across a film of regularly spaced chains with no energetic disorder at 100K and 300K, with an applied electric field of 30×10^6 Vm^{-1}.

As the temperature increases, then as mentioned above, the probability of hopping forward at a specific electric field strength actually decreases slightly, and so the carriers take a slightly less straightforward path across the sample; this is analogous to phonon scattering in crystalline semiconductors. The path of a typical carrier at 300K is shown in Figure 6.7. Hence, at a given field, the mobility decreases with increasing temperature since the transit time has increased. Additionally, at higher temperatures, the carrier transit time does not saturate as it does for lower temperatures, and so even at high fields, the mobility is lower for a given field than at lower temperatures, and the mobility-field curve does not attain an E^{-1} slope.

6.1.3 $\hat{\sigma} > 0.0$ (energetically disordered)

In a real system, there will inevitably be some energetic disorder, as the energy of the polymer chains varies for a variety of reasons including different conjugation lengths and chain lengths, and chemical and topological defects e.g. [13]. However, films of liquid crystalline conjugated polymers are more energetically homogeneous than other polymers [6], and so only a small amount of energetic disorder should be required to simulate a real sample.

Figure 6.8 shows the logarithm of the hole mobility as a function of the square root of the electric field for a very small amount of energetic disorder when $\hat{\sigma}$=0.5, for a range of temperatures from 100-350K. Qualitatively, this graph looks similar to that in Figure 6.6; however, there are several differences. Firstly, it can be seen that at low temperatures (100-200K), the mobility exhibits a positive field dependence i.e. $\ln \mu$ increases with $\sqrt{E}$ for low fields. This situation arises because although the energetic disorder is relatively low, at low temperatures the carriers do not have sufficient thermal energy to overcome energetic barriers between hopping sites, and have to take lower energy paths which may well be longer (see Figure 6.9). As the electric field is increased, the carriers can overcome more energetic barriers due to increased electrostatic energy, and they can take shorter paths as they can make more forward hops (in the field direction), resulting in a higher mobility, and the mobility increases with the field. At low fields, the mobilities of carriers are lower than in the case for $\hat{\sigma}$=0.0 as they are taking longer paths through the sample.

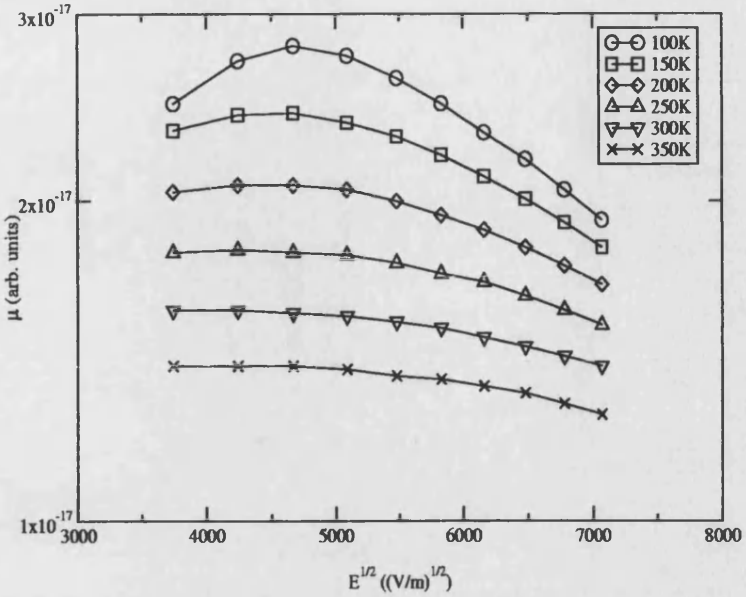

Figure 6.8: Logarithm of hole mobility, μ, as a function of $\sqrt{E}$ for a system of regularly spaced liquid crystalline polymers with $\hat{\sigma}$=0.5.

Once the field reaches a critical value, carriers at low temperatures can overcome all energetic barriers by virtue of their increased electrostatic energy; above this value, they can take a route that approaches the shortest route for $\hat{\sigma} = 0.0$ for all applied fields and so the transit time tends to a saturation value, as in the previous case for $\hat{\sigma} = 0.0$, and the mobility decreases with applied field.

At higher temperatures (>200K), the carriers have sufficient thermal energy to overcome virtually any barrier even without electrostatic energy. For these carriers, their mobilities are very similar to the case where $\hat{\sigma} = 0.0$, and $\ln \mu$ decreases with $\sqrt{E}$ at all fields for the same reasons.

Figure 6.10 shows the variation of the logarithm of the carrier mobility as a function of $\sqrt{E}$ for $\hat{\sigma} = 1.0$. Two important features are readily observed from Figure 6.10. Firstly, the carrier mobility increases for nearly all values of E at all temperatures, with the curves only flattening out at high fields. The second important feature is that there exists a cross-over behaviour; below certain values of the electric field, the mobility increases with increasing temperature, but above these fields, the mobility decreases with increasing temperature, as in the previous cases. Such behaviour has also been observed by Yu et al [7].

At low fields, the carriers do not have sufficient thermal energy to overcome

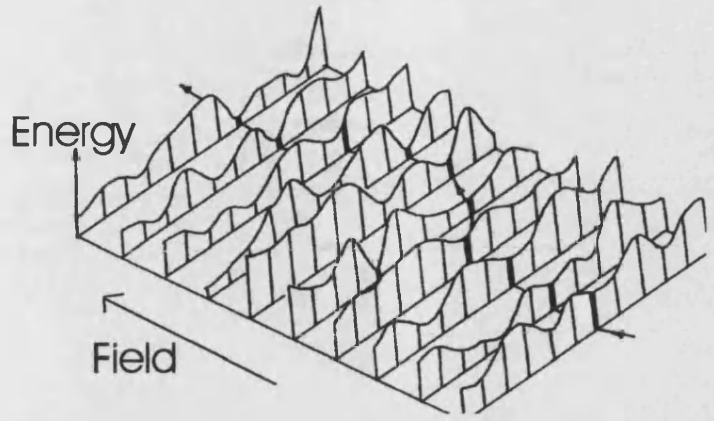

Figure 6.9: Schematic illustration of a carrier taking a low energy path through an energetically disordered system.

the larger barriers, and consequently the mobility increases with increasing temperature; having increased thermal energy allows shorter paths to be followed and hence the higher temperature carriers have higher mobilities. In fact, at low temperatures and low fields, the carrier transport becomes very dispersive, which is indicated by the lack of data points in Figure 6.10. As the electric field is increased, the carriers gain more electrostatic energy and can overcome larger barriers and hence can take shorter paths, resulting in higher mobilities. At lower temperatures, the mobility increases more rapidly with the electric field since the increase in electrostatic energy opens up more paths which were not available at lower fields. As the field is further increased, the carriers have enough energy (electrostatic and thermal) to overcome practically all barriers, and so a cross-over occurs, and the mobility then reduces with increasing temperature as in the previous cases. The lower the temperature, the higher the field that is required for this cross-over to occur, since more and more of the carrier's energy for overcoming barriers is provided by electrostatic energy from the applied field. Eventually, at very high fields, the transit times start to tend towards a saturation value as the carriers have sufficient energy to overcome all barriers; however, the transit times do not completely saturate as the mobility only marginally decreases with increasing field. Owing to the longer paths lengths caused by carriers taking lower energy pathways through the sample, the mobilities of the carriers in this case are lower than in the previous cases.

Figures 6.11 and 6.12 show the logarithm of the hole mobility as a function of $\sqrt{E}$ for $\hat{\sigma}$=1.5 and $\hat{\sigma}$=2.0 respectively. When $\hat{\sigma}$=1.5, the mobility increases as a function of both increasing field and increasing temperature for all but high

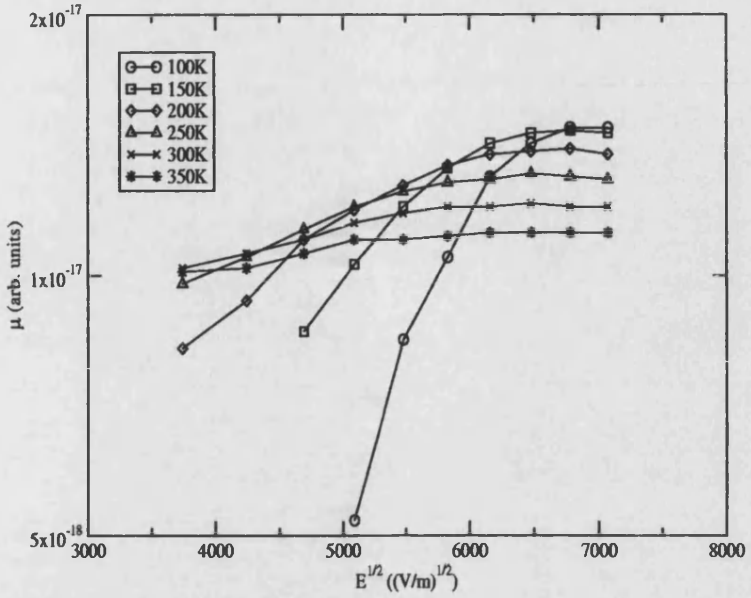

Figure 6.10: Logarithm of hole mobility, μ, as a function of $\sqrt{E}$ for a system of regularly spaced liquid crystalline polymers with $\hat{\sigma}$=1.0.

fields, as the disorder is greater than the thermal energy, and the electrostatic energy is ever more crucial for overcoming energetic barriers. At very high fields, the mobility starts to decrease with increasing temperature as the addition of large amounts of electrostatic energy provide enough energy to overcome most energetic barriers, even at lower temperatures. When $\hat{\sigma}$=2.0, it can be seen from Figure 6.12 that the mobility increases both with increasing temperature and increasing electric field, as is observed experimentally (see Figure 6.2). With such a large amount of energetic disorder present in the system, the thermal energy is small in comparison, and electrostatic energy is required to overcome barriers. As E increases, ever larger barriers can be surmounted, hence shorter paths can be taken and μ increases.

In the case for $\hat{\sigma}$=2.0, which most closely resembles experimental results in Figure 6.2, the values of E_0 obtained from Figure 6.12 are 5.47×10^6 Vm^{-1} at 250K, 8.57×10^6 Vm^{-1} at 300K, and 1.44×10^7 Vm^{-1} at 350K. This field dependence decreases with increasing temperature, as is observed experimentally in all organic semiconductors. At 300K, the value obtained from the experimental data in Figure 6.2 is 4.11×10^6 Vm^{-1}, which is in good agreement with the values obtained here. The mobility at a field of 38×10^6 Vm^{-1} obtained from the simulation at 300K is a factor of 1.33 larger than at 250K. From the experimental data in Figure 6.2, at a field of 10×10^6 Vm^{-1}, the measured value of μ_p at 300K is 2.75

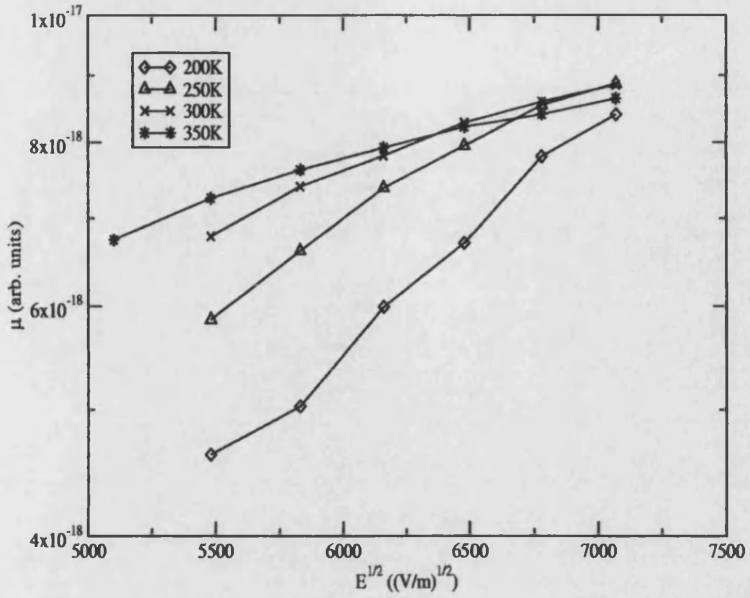

Figure 6.11: Logarithm of hole mobility, μ, as a function of $\sqrt{E}$ for a system of regularly spaced liquid crystalline polymers with $\hat{\sigma}$=1.5.

times larger than that at 260K and 5 times larger than that 240K. Data for fields larger than this is unavailable, but at much higher fields, the mobilities become much close due to increased field dependence at lower temperatures, and so the temperature variation of the simulated carrier mobility may also show good agreement with experimental values.

As the energetic disorder i.e. $\hat{\sigma}$ increases, the transport becomes more and more dispersive at low temperatures and/or low fields and no transit times, and hence no mobilities, can be obtained from the current-time traces.

6.2 Irregularly spaced, aligned chains

Although the polymer chains may be well aligned within the film, it is unlikely that they will be regularly spaced within the film [14], as if on a lattice as discussed in the previous section. It is more likely that the chains will be packed in the film so as to achieve a maximum density, but this may involve them being irregularly spaced such that each chain has neighbours which are at slightly different relative positions and distances; this is termed here as spatial disorder. This configuration was examined, again with varying amounts of energetic disorder.

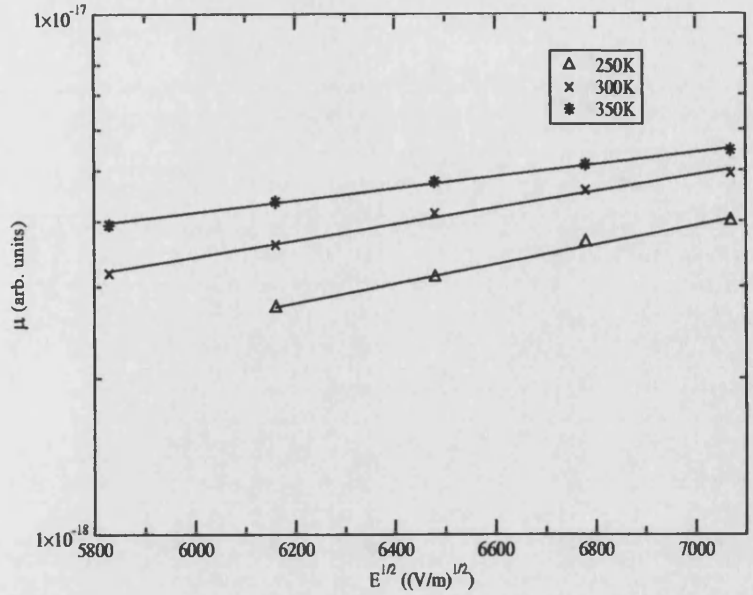

Figure 6.12: Logarithm of hole mobility, μ, as a function of $\sqrt{E}$ for a system of regularly spaced liquid crystalline polymers with $\hat{\sigma}$=2.0. The lines represent a best fit to the data points.

Figure 6.13 shows how the logarithm of the hole mobility varies as a function of the square root of the electric field in the case where there is no energetic disorder i.e. $\hat{\sigma}$=0.0, for temperatures from 150K to 350K.

Figure 6.13 appears qualitatively very similar to Figure 6.6; however, the mobilities in the two cases cannot be compared directly since in this case, the minimum interchain distance was set to be 0.7nm, whereas in the regularly spaced case (section 6.1), the chains were spaced 1nm apart. Hence in this case, a charge carrier will have to perform more hops to traverse the sample than in the regularly spaced case, resulting in a longer transit time and hence mobility.

The same basic explanation applies to this sample for $\hat{\sigma}$=0.0 as to the regularly spaced sample for $\hat{\sigma}$=0.0. In this case the sample is subject to some positional disorder, resulting in less direct paths, carriers at all temperatures and fields will be subject, on average, to a similar amount of positional disorder. In the regularly spaced case the neighbouring transport sites to which a carrier could hop were very straightforward, with the hop in the field direction dominating even at low fields. However, in this case, several neighbouring sites might involve a hop which moves the carrier forward, even slightly, in the field direction, which is quite favourable in terms of energy. This means that at lower fields, the path which might be taken is not quite as straightforward as in the regularly spaced

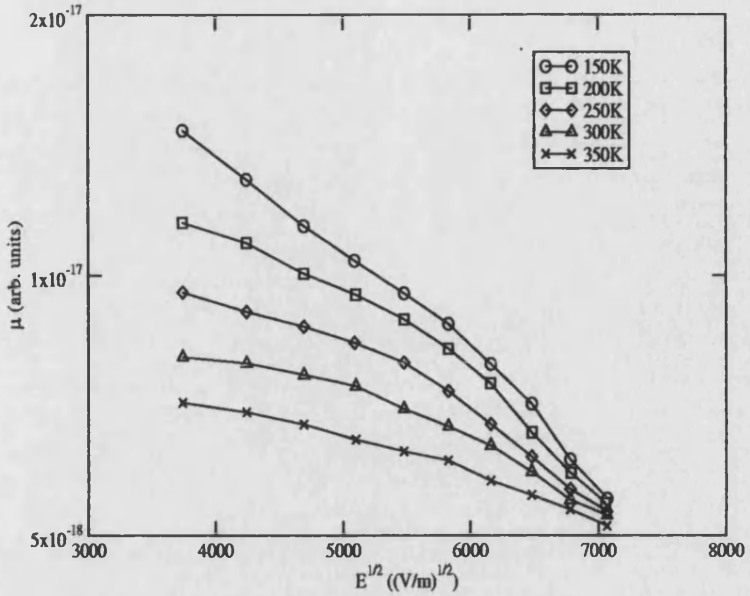

Figure 6.13: Logarithm of hole mobility as a function of the square root of the applied electric field for carriers in a sample of aligned but irregularly spaced chains. $\hat{\sigma}$=0.0.

case since the probabilities are similar, and so the hops which involve moving furthest forward in the field direction do not dominate until the field strength is larger. Consequently, the transit time does not saturate at all, or not until very large fields are applied, and so the mobility does not decrease quite as rapidly with field as it does in the regularly spaced case. As the temperature is increased, the carriers are again effectively scattered, leading to the mobility decreasing with increasing field as in the regularly spaced case.

Figure 6.14 shows the logarithm of the hole mobilities as a function of the square root of the electric field, for the case where $\hat{\sigma}$=0.5. It can be seen that at 150K, the mobility is lower than at 200K for low fields. This is because energetic disorder is greater than the thermal energy, but the spatial disorder means that the hops to neighbouring transport sites move the carrier less in the field direction compared to the regularly spaced case so the carrier cannot gain as much electrostatic energy. Hence at low fields even for this relatively small amount of energetic disorder, the thermal and electrostatic energy is insufficient for overcoming most energetic barriers, and longer low energy paths must be taken. The mobility increases with electric field at low fields at 150K, as the increase in electrostatic energy in this region opens up more straight forward paths through the sample for the carriers. Clearly, the effect of energetic disorder is more pronounced in this case compared to in the case where the chains are all regularly aligned (section

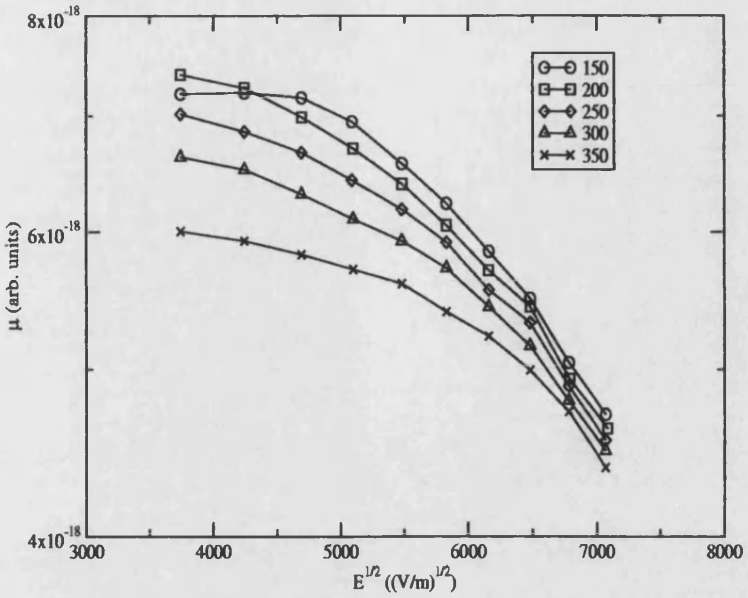

Figure 6.14: Logarithm of hole mobility as a function of the square root of the applied electric field for carriers in a sample of aligned but irregularly spaced chains. $\hat{\sigma}$=0.5.

6.1).

Figure 6.15 shows how the logarithm of the hole mobility varies with the square root of the electric field when the energetic disorder is further increased, to $\hat{\sigma}$=1.0. The effect of this amount of energetic disorder is significantly more pronounced than for when the chains are regularly spaced. The mobility increases with increasing temperature for all values of the electric field, and the mobility increases with increasing electric field except at 350K, when the mobility decreases slightly with field. This illustrates how the thermal energy alone is insufficient to overcome energetic barriers, and as the field is increased, the electrostatic energy allows ever shorter paths to be take, and the mobility increases with $E^{1/2}$, except at 350K, where the temperature allows most barriers to be overcome, and the reduction in transit time afforded by an increase in electrostatic energy is not sufficient to increase the mobility. At low temperatures, the combined thermal and electrostatic energy is not sufficient to overcome many of the barriers and the transport is very dispersive; hence no transit times and mobilities could be determined for carriers below 200K.

Finally, Figure 6.16 shows how μ varies with $E^{1/2}$ when the energetic disorder is increased still further, with $\hat{\sigma}$=1.5; due to the dispersive nature of the transport, results were only possible for temperatures of 300K and 350K. The mobility

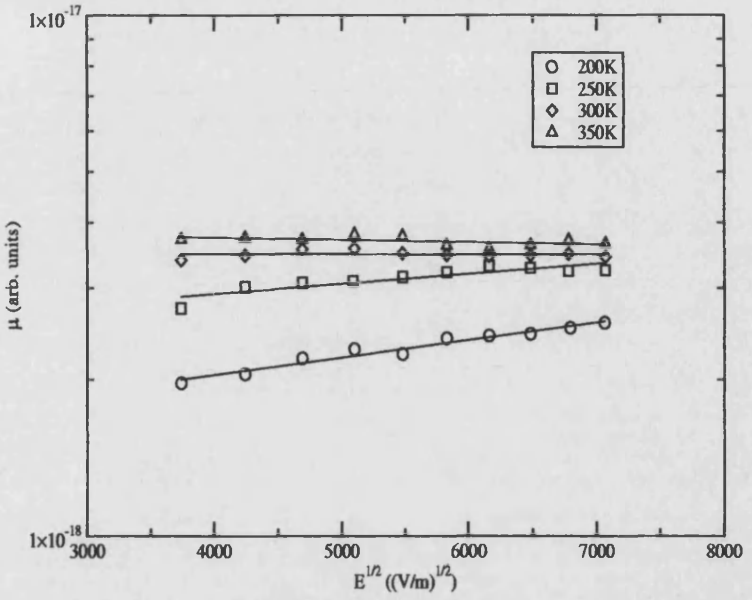

Figure 6.15: Logarithm of hole mobility as a function of the square root of the applied electric field for carriers in a sample of aligned but irregularly spaced chains. $\hat{\sigma}$=1.0. The lines are a best fit to the data points.

increases with both increasing electric field and increasing temperature for all applied fields; the values of E_0 calculated from Figure 6.15 are 7.67×10^7 Vm^{-1} at 300K and 2.23×10^8 Vm^{-1} at 350K. Although these values are higher than the value of 4.11×10^6 Vm−1 at 300K calculated from Figure 6.2, such values are still comparable with those reported elsewhere for PFO. However, the values of the mobilities simulated at 300K and 350K are very similar.

6.3 Chains with a distribution of orientations

The final structural configuration to be investigated was that in which all of the chains are rigid, but are not aligned to the electrodes or to each other. In this case, the values of the angles θ and ϕ (section 5.3.1) were allowed to vary randomly in the range from 0 to 5°. This relatively small amount of mis-alignment within the chains was chosen to mimic the situation in which chains which are not entirely aligned; this situation may occur in thick films which are aligned by rubbing, where only a certain number of layers of chains can be fully aligned [6].

In this configuration, the packing density within the simulated sample is altered; less chains can be fitted in the sample whilst conserving the condition of a min-

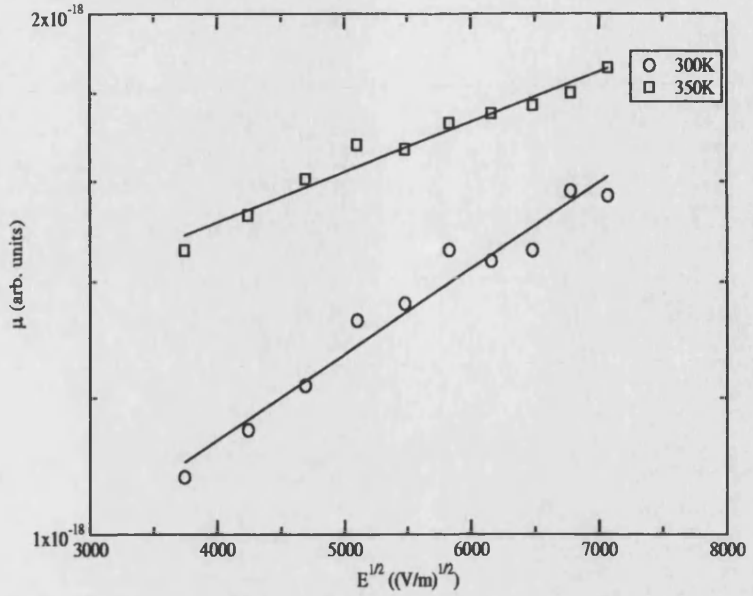

Figure 6.16: Mobility as a function of the square root of the applied electric field for carriers in a sample of aligned but irregularly spaced chains. $\hat{\sigma}$=1.5. The lines are a best fit to the data points.

imum inter-chain distance of 0.7nm. Consequently, the cut-off distance which limits the distance a carrier can hop from one site to another had to be increased to 1.3nm in order to allow conduction. As a result of this situation, the mobilities calculated for this configuration are higher since there are less polymer chains in the sample and hence the carriers cross the sample in fewer Monte-Carlo timesteps. Thus the mobilities calculated in this section cannot be directly compared to the values obtained in previous sections.

A further problem is also caused by the use of a rigid cut-off distance in this situation. As the amount of misalignment is increased, the average interchain spacing is increased, and so the cut-off distance must be increased. However, if the cut-off distance is increased to a value which just allows conduction through the film, the number of neighbouring transport sites to which a carrier may hop may be small, and hence the paths taken and hence the calculated mobilities can be very similar, even for large variations of energetic disorder, electric field, and temperature. If the cut-off distance is increased too much, carriers can gain large amounts of electrostatic energy which can allow them to overcome even large energy barriers, thus masking the effects of the electric field, temperature and energetic disorder on transport in a sample. The cut-off distance is found by trial and error, and for these reasons, no results could be obtained for the case where θ and ϕ were allowed to vary between 0 and 10°. The cut-off distance required

to obtain accurate results is also affected by then number of segments in a chain, due to geometric considerations.

Figure 6.17 shows the logarithm of the calculated hole mobilities, μ, as a function of $E^{1/2}$ for temperatures from 200K to 350K; the system is energetically pure i.e. $\hat{\sigma}$=0.0. As in the previous two cases, the mobility decreases with both increasing temperature and increasing field, for the reasons previously outlined.

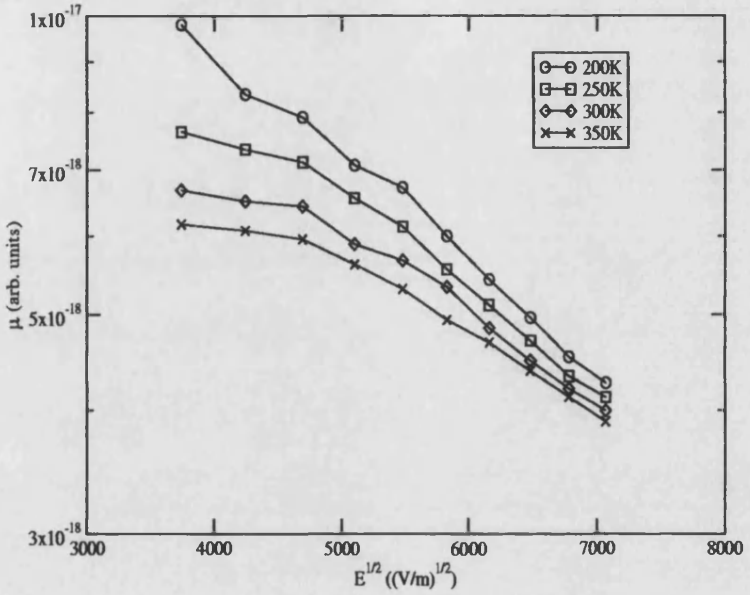

Figure 6.17: Logarithm of hole mobility, μ, as a function of $E^{1/2}$ for a sample of liquid crystalline conjugated polymers which are misaligned. $\hat{\sigma}$=0.0.

Figures 6.18 and 6.19 show the logarithm of the calculated mobility, μ, as a function of $E^{1/2}$ for $\hat{\sigma}$=0.5 and 1.0 respectively. For the case where $\hat{\sigma}$=0.5 (Figure 6.18), it can be seen that at low fields, the mobility at 200K is lower than that at 250K, and it also increases with increasing field before the mobility becomes larger than the mobility at 250K and decreases with increasing field for larger fields. This indicates that at low T and E, the energetic disorder is greater than the thermal energy and requires electrostatic energy to overcome the energetic barriers. Such a situation occurs in the irregularly spaced case for $\hat{\sigma}$=0.5, but at 150K. This shows that the effect of energetic disorder is slightly more pronounced in this case. The reason for this is that now the carriers hop in 3-d, rather than in 2-d (i.e. the x-y plane) in the previous two cases. The hops to neighbouring sites now involve slightly less of a jump in the field direction, reducing the contribution from the electrostatic energy available for overcoming energetic barriers.

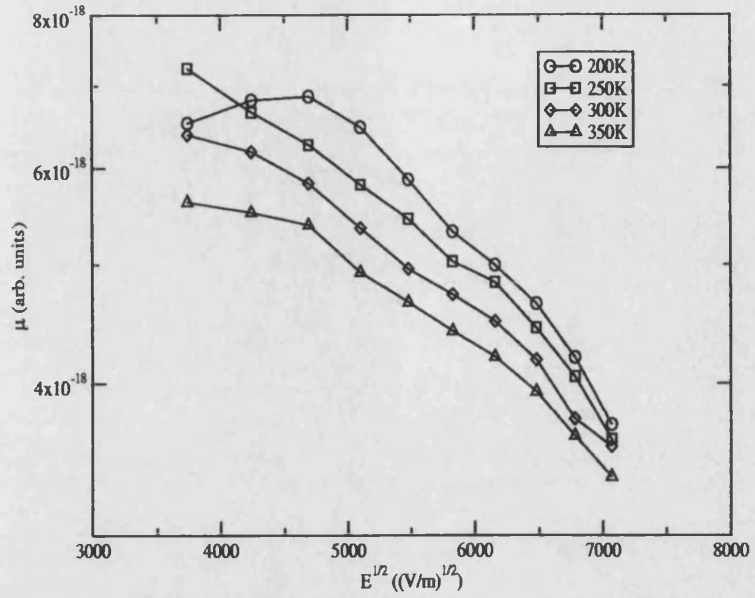

Figure 6.18: Logarithm of hole mobility, μ, as a function of $E^{1/2}$ for a sample of liquid crystalline conjugated polymers which are misaligned. $\hat{\sigma}$=0.5.

Similarly, in Figure 6.19, it can be seen that the mobility increases with increasing E and T at all temperatures, whereas in the irregularly spaced case (section 6.2, μ was almost constant at 300K and actually decreased with increasing E at 350K. E_0 calculated from Figure 6.19 yields values of 7.81×10^8 Vm^{-1} at 200K, 9.32×10^9 Vm^{-1} at 250K, 3.26×10^{11} Vm^{-1} at 300K, and 9.29×10^{11} Vm^{-12} at 350K. These values of E_0 are very large, corresponding to a very small field dependence of the mobilities, and the mobilities are very similar at a given field as T varies. $\hat{\sigma}$ could not be further increased in this case as the transport became too dispersive to determine mobilities.

6.4 Conclusions

Preliminary results from this model of hopping transport in a film of liquid crystalline conjugated polymers indicate that mobilities which exhibit behaviour which is qualitatively comparable with observed experimental behaviour e.g. Figure 6.2, with the mobility increasing with both increasing temperature and electric field, can be produced, provided a certain amount of energetic disorder is present. The amount of energetic disorder required to make the mobilities increase with field and temperature depends upon the degree of spatial disorder

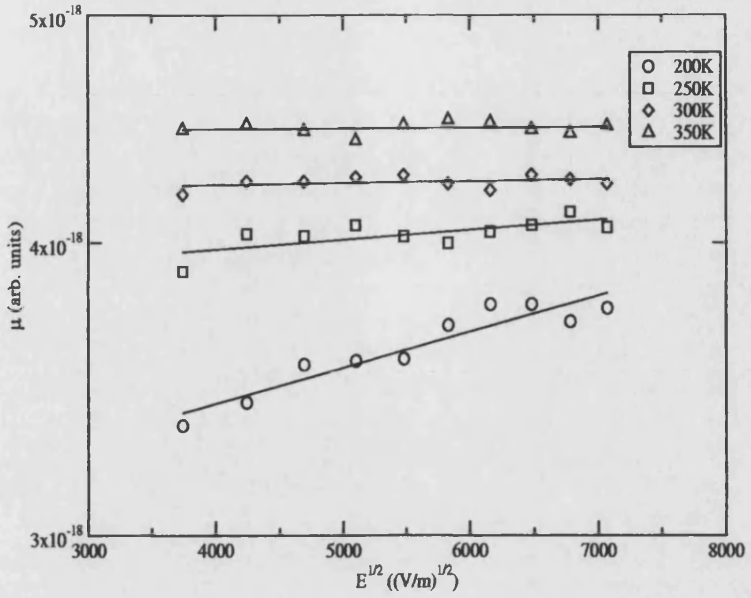

Figure 6.19: Logarithm of hole mobility, μ, as a function of $E^{1/2}$ for a sample of liquid crystalline conjugated polymers which are misaligned. $\hat{\sigma}$=1.0. The lines are a best fit to the data points.

present, but must be greater than the thermal energy, and is the cause of the field and temperature dependence of the mobilities. When the energetic disorder is greater than the thermal activation energy, increasing the electrostatic energy allows larger barriers to be overcome and hence shorter paths can be taken. Thus the mobility increases with both field and temperature. Increasing amounts of spatial disorder have the effect of decreasing the amount of energetic disorder required to cause the mobilities to increase with field and temperature by reducing the contribution from the electrostatic energy provided by the field.

In systems with no spatial disorder, large amounts of energetic disorder are required to produce mobilities which increase with both field and temperature; for low amounts of energetic disorder, the mobilities can decrease with field due to a saturation of transit times. Other authors have also shown that for a spatially ordered system, large amounts of energetic disorder (large $\hat{\sigma}$) can produce a mobility that increases with field, but at large fields the drift velocity can saturate, yielding an E^{-1} dependence of the mobility [15][16]. As spatial disorder is introduced by first allowing chains to be regularly spaced, and then allowing the rods to have a distribution of orientations, less energetic disorder is required to produce qualitatively similar trends, owing to a reduced contribution from the electrostatic energy.

The results obtained show the field dependence of the mobility, E_0, to be in good agreement with published parameters for the regularly and irregularly spaced cases, and that the temperature dependence of the mobility in a given system to be also reasonable. However, the observed behaviour can be produced by either a very large amount of energetic disorder in a spatially ordered system, or by a combination of both energetic and spatial disorder; the spatial disorder can be seen to effectively enhance the energetic disorder. Without further information on the degree of either type of disorder, no firm conclusions can be drawn by relating the experimentally measured mobilities to the behaviour observed in the model. Fitting the experimental data in Figure 6.2 to the law formulated by Bässler (equation 5.11) yields a value of $\sim$ 0.1eV for σ [17], which corresponds to a value of $\hat{\sigma} \sim 2.0$ in these results. Similar values have been reported by other authors in various organic semiconductors e.g. [18][19].

A value of $\hat{\sigma} = 2.0$ in the regularly spaced and aligned sample (section 6.1) produced mobilities which increased with both E and T, and produced a value of E_0 which is physically reasonable. However, it is impossible to confirm that this structural formation is indeed present in the experimental sample, as the model uses a fixed hopping rate; in reality the hopping rate could vary with field and temperature. It is possible that the inclusion of realistic tunnelling rates could allow firmer conclusions to be reached, and could also allow actual mobility values to be calculated. The inclusion of such tunnelling rates with a wavefunction overlap factor would also eliminate the problems of using a rigid cut-off distance for intersite hopping as described in section 5.3.2, allowing more complex systems to be studied.

References

[1] U Scherf and E J W List, *Advanced Materials*, **14**, 477 (2002).

[2] M Redecker, D D C Bradley, M Inbasekaran, and E P Woo, *Appl. Phys. Lett.*, **73**, 1565 (1998).

[3] M Redecker, D D C Bradley, M Inbasekaran, W W Wu, and E P Woo, *Advanced Materials*, **11**, 2451 (1999).

[4] T Kreouzis, *Unpublished data* (2002).

[5] M Redecker, D D C Bradley, M Inbasekaran, and E P Woo, *Appl. Phys. Lett.*, **74**, 1400 (1999).

[6] D D C Bradley, *Private communication* (2002).

[7] Z G Yu, D L Smith, A Saxena, R L Martin, and A R Bishop, *Phys. Rev. B.*, **63**, 085202-1 (2001).

[8] H Cordes, S D Baranovskii, K Kohary, P Thomas, S Yamasaki, F Hensel, and J-H Wendorff, *Phys. Rev. B*, **63**, 094201-1 (2001).

[9] D H Dunlap, P E Parris, and V M Kenkre, *Phys. Rev. Lett.*, **77**, 542 (1996).

[10] H Scher and E W Montroll, *Phys. Rev. B.*, **12**, 2455 (1975).

[11] J C Scott, B A Jones, and L T Pautmeier, *Mol. Cryst. Liq.*, **253**, 183 (1994).

[12] A M Stoneham, *Private communication* (2001).

[13] G Hadziioannou and P F van Hutten, *Semiconducting Polymers: Chemistry, Physics and Engineering*, Wiley-VCH, Weinheim (2000).

[14] T Kreouzis, *Private communication* (2002).

[15] D M Goldie, *J. Non-Cryst. Solids*, **266-269**, 294 (2000).

[16] H Bässler, *Phys. Stat. Sol.(b)*, **175**, 15 (1993).

[17] D Poplavskyy, T Kreouzis, A J Campbell, J Nelson, and D D C Bradley, *Materials Research Society 2002 Spring Meeting*, Paper P1.4, MRS Proceedings, **725** (2002).

[18] I H Campbell and D L Smith, *Solid State Physics*, **55**, 1 (2001).

[19] A Ioannidis, E Forsythe, Y Gao, M W Wu, and E M Conwell, *Appl. Phys. Lett.*, **72**, 3038 (1998).

Chapter 7

Conclusions and Further Work

7.1 Drift-diffusion model

The drift-diffusion model developed and presented in Chapter 2 models electrical charge transport in organic light emitting diodes using a band continuum model, more usually associated with the modelling of charge transport in crystalline inorganic semiconductors. Such a model describes charge transport via the drift-diffusion current equations and the current continuity equations coupled to Poisson's equation. The model developed uses physics appropriate to organic semiconductors: charge injection is generally dominated by thermionic emission, which has an organic recombination velocity describing current backflowing at the metal-semiconductor interface, transport includes field-dependent carrier mobilities, and recombination is via a Langevin bimolecular mechanism.

In Chapter 3, results obtained from using the drift-diffusion model to simulate the J-V characteristics of single layer OLEDs were presented. As a tool for quickly modelling the J-V characteristics of individual devices, the model is very useful, and good fits to experimental data are easily obtained, yielding values for the majority carrier mobility and its field dependence, and the size of the barrier to majority carrier injection. These values are always in good agreement with values published in the literature. Such modelling must be undertaken with the proviso that several of the material parameters may be unknown and hence must be taken from the literature as typical values. Section 3.1 shows that the

variation of certain material parameters can have a significant effect on the J-V characteristics of a device, and this must be borne in mind when modelling device characteristics.

Section 3.2 contains the results of simulating the temperature dependent J-V characteristics of a 95nm thick ITO/MEH-PPV/Al device. By obtaining a best fit to the data for temperatures $\geq$200K, values of Δ, μ, T_0 and B for holes were obtained, and calculated to be 0.27eV, 1.0×10^{-5} m^2/Vs, 325K, and 1.3×10^{-5} $(eV(mV^{-1})^{1/2})$ respectively. Such values are in very good agreement with the literature [1][2]. The linear decrease in the fitted hole barrier height, ϕ_{bp}, with decreasing temperature (above 200K) may well be partially due to the variation in the bandgap of MEH-PPV with temperature, but other factors must also be involved to explain such a strong variation. In addition, the fitted values of μ_{p0} and E_0 also varied with temperature, but again only down to 200K. The reason for this apparent breakdown in the model below 200K is unclear, but may be due to the temperature dependence of the injection mechanism, or perhaps the increasingly dispersive nature of charge transport at low temperatures, and needs further investigation. It would be interesting to compare the temperature dependence of a microscopic hopping injection model e.g. [3] to the thermionic emission used in the model, to see if this can account for the strong variation of ϕ_{bp} with temperature.

Section 3.3 presented results from the investigation into the temperature dependent J-V characteristics of an ITO/TPD/Al device. This device was very interesting because unlike all of the other devices investigated here and elsewhere, initially a fit to the data couldn't be obtained using barrier height lowering and field-dependent carrier mobilities, two very important aspects of OLED operation. It was found that increasing ϵ_s to a value of 5.5, compared to an experimentally measured value of 3.0$\pm$0.3 [4], which is a typical value for organic semiconductors, allowed the best fit to the data to be obtained using both barrier lowering and field-dependent mobilities. However, fitting μ_{p0} and E_0 over the temperature range yielded values which were nowhere near as strongly temperature dependent as they should be, but it is likely that this is related to the high value of ϵ_s used in the simulation. It appears probable that using a higher value of ϵ_s to reduce the effectiveness of Schottky barrier lowering replicates the behaviour caused by other factors, such as interfacial layers, but it is unlikely that this larger value of ϵ_s is correct, at least not for the bulk of the device. It is certainly possible that

interfacial layers and states may play a role in the operation of, at least some, OLEDs, but this aspect of metal-organic semiconductor contacts has been largely ignored thus far.

In both sections 3.2 and 3.3, the model was used to investigate the increase in device efficiency with decreasing temperature, as observed experimentally in both of these devices. It was found that in order to obtain an increase in the simulated device efficiency as the temperature decreased, the barrier to electron injection, ϕ_{bn}, had to be decreased at a greater rate than the fitted hole barrier height, ϕ_{bp}. This increase in electron injection creates an electron build-up and consequently a recombination peak near the cathode in the model, increasing device efficiency. In reality, recombination near to an electrode is undesirable since the metal can quench excitons, reducing the external quantum efficiency of the device. It is possible that the actual cause of the increase in efficiency is that as the temperature decreases, the electron and hole mobilities become comparable, spreading the recombination throughout the device and away from the potentially quenching cathodes. Increasing the electron mobility as the temperature was decreased in the simulation did not change the value of the barrier height required to increase the efficiency. Therefore the efficiency is not only increased due to the existence of a wider recombination zone, but also because less exciton quenching is occurring. Such physics is of course not included in the model and this idea cannot be tested.

Finally in Chapter 3, in section 3.4, the results from simulating a series of NPB devices with different cathodes were presented. Again, simulating these devices provided some interesting results. It was found that fitting to the ITO/PEDOT/NPB/Al device, which has a hole only current and an essentially Ohmic hole injecting PEDOT/NPB contact, yielded a SCLC fit, but with a zero-field hole mobility of $\mu_{p0} = 9.0 \times 10^{-11}$ m^2/Vs, several orders of magnitude lower than published values e.g. [5]. Furthermore, reducing the electron barrier height, ϕ_{bn}, as the cathode was varied should have had only a small effect on the J-V characteristics, owing to an increase in V_{bi}. However, the current actually increased by an order of magnitude as the cathode was changed from Al (ϕ_{bn}=1.8eV) to LiF(2nm)/Al (ϕ_{bn}=0.8eV). It was found that the best explanation for this behaviour was that the LiF/Al cathode devices were trap free, yielding a hole mobility of 2.5×10^{-9} m^2/Vs, closer to published values, and that the Al device had hole traps in, with E_t=2.7eV, and N_t=2.5×10^{23} m^{-3}. NPB

is generally assumed to be trap free e.g. [5], so further work is required here to investigate the presence of traps in NPB, and whether they could be cathode dependent, perhaps due to reactions between NPB and the cathode metals.

Chapter 4 contains results from multi-layer device modelling using the drift-diffusion model. It has been shown that the use of multi-layer devices employing transport and/or blocking layers can significantly increase device efficiency. Section 4.2 used the model to investigate whether the efficiency of a bi-layer TPD/Alq device was dependent upon the thickness of the emissive Alq layer, as reported experimentally [6][7]. It was found using the model that the efficiency was invariant with layer thickness, as the build-up of carriers at the heterojunction, with the Alq acting as a hole blocking layer and the NPB acting as an electron blocking layer, controls the emission. The variation in efficiency with thickness is almost certainly due to the outcoupling of the light, micro-cavity effects and exciton quenching. As with the investigation into the variation of efficiency with temperature in single layer devices, this result shows the complexity of the recombination and emission processes present in OLEDs, and that an electrical transport model cannot be used to investigate device efficiency in any detail.

Finally, in section 4.3, the electric field distribution in an NPB/Alq bi-layer device was compared to that obtained experimentally by electroabsorption (EA) spectroscopy. The results obtained from the model show good agreement with the experimental results, verifying the assumptions that the electric field distributions are a consequence of the presence of blocking layers, where a large build-up of carriers at the interface can cause a rapid change in the electric field. The relative amounts of carrier injection are also critical. The ITO/NPB/Alq/Al device is essentially hole-only, and the holes being blocked by the Alq layer change the field distribution, with the field in the Alq layer being greater than in the NPB layer until at high biases, electrons are injected and are build-up in greater concentrations at the interface, changing the field-distribution again. In the ITO/NPB/Alq/Al:Li device, the barriers ϕ_{bp} and ϕ_{bn} are comparable, and injection of both electrons and holes occurs above V_{bi}. However, the NPB blocks electrons more effectively than Alq blocks holes, and the electron build up at the interface dominates the field distribution, with the field in the NPB always being the greater of the two. The discrepancy between the simulated data and the experimental data of Rohlfing et al [8] is puzzling, and needs further investigation.

7.1.1 Further work

The drift-diffusion model presented here is complete in the sense that it contains all the necessary physics to produce valid results. However, there are some additions which could be made to the model:

Improving the stability of the software, so that it can be easily used by people unfamiliar with the code/solver (some work has been done using alternative numerical solvers [9]).

Include the ability to model exponential or Gaussian trap distributions.

Couple with the drift-diffusion transport model to an optical model to allow the efficiency to be calculated accurately, thus allowing the model to be used as a design tool.

In reality, though, simply more data sets are required to be modelled, to look for trends in device behaviour, and to further investigate some of the issues which have occurred so far. For example, in the instance of temperature-dependent J-V characteristics, it would be interesting to see if the model always breaks down below a certain temperature, and to see how the fitted barrier height varies with temperature in different materials.

7.2 Hopping transport Monte-Carlo model

In Chapter 5, a model to investigate the effects of the morphology of thin film OLEDs on carrier mobilities was presented, initially with a view to investigating transport in liquid-crystalline conjugated polymer films. This model explicitly represents the morphology of the conjugated polymers by treating them as rigid rods and allowing various different types spatial disorder to be introduced. The energies of the chains are chosen from a Gaussian distribution, whose width determines the energetic disorder present in the system. Charges placed on polymer chains on one side of the film then propagate through under the influence of an electric field, generating a current-time plot, similar to that obtained from the experimental time-of-flight technique, from which a mobility can be obtained.

In Chapter 6, the mobilities of carriers in systems of liquid crystalline conjugated polymers having varying amounts of spatial and energetic disorder were investigated as a function of both electric field and temperature. The main conclusions that can be drawn from these preliminary results is that there is a minimum amount of energetic disorder required such that the mobilities increase with increasing electric field and temperature, as observed experimentally. This level of energetic disorder exceeds the thermal energy available to carriers and hence electrostatic energy is required to overcome barriers. Increasing the field allows the carriers to overcome larger barriers, and hence they take shorter paths through the film resulting in increased mobilities. However, the degree of energetic disorder required to produce this behaviour depends on the degree of spatial disorder within the film.

For spatially ordered films, with the chains all aligned to the electrodes and regularly spaced within the film, the presence of a small amount of energetic disorder results in the mobilities decreasing with both increasing temperature and field, as the transit times can saturate, or come close to saturating, due to the dominance of the thermal energy in the system. As more energetic disorder is added to the system, there is a cross-over behaviour, whereby at low fields, the mobility increases with both increasing field and temperature; due to the enlarged amount of energetic disorder, thermal energy is insufficient for overcoming barriers and electrostatic energy becomes important for transport. At high fields, the electrostatic energy once again becomes comparable to the energetic disorder and the mobility decreases with increasing electric field and temperature. Such behaviour has not been observed experimentally, as such a spatially ordered film is unlikely to exist. Finally, with the application of a large amount of energetic disorder, the mobility increases with increasing field and temperature, as observed experimentally, although at low temperatures, the transport is dispersive. This behaviour is a result of the energetic disorder being much greater than the thermal energy available to carriers, and hence electrostatic energy is always required to overcome barriers. The field dependence of the mobilities in this system are comparable to experimental values.

Increasing the amount of spatial disorder in the system from aligned and regularly spaced chains to aligned and irregularly spaced chains, to chains with a variety of orientations, reduces this critical value of energetic disorder required to achieve $\mu \propto (\mathrm{E}, T)$, owing to a decreased contribution from the electric field. Again, the

field dependence of the mobilities in these systems are physically reasonable.

From the results obtained so far, it is impossible to separate the effects of spatial and energetic disorder and compare any qualitative trends with experimental data which might give information on the relative contributions from spatial and energetic disorder in real systems i.e. one cannot at present predict whether a system is spatially ordered with a high amount of energetic disorder present, or spatially disordered with a smaller amount of energetic disorder by examining experimental mobilities. Since the hopping rate is constant, it is also difficult to come to any conclusions regarding the field and temperature dependence of the mobilities simulated by this model. If the hopping rate is in fact field or temperature dependent, then the field and temperature dependence of the mobilities will of course be different to those predicted here.

7.2.1 Further work

The preliminary results obtained from the model are very encouraging, but the model needs further development to enable this work to progress, and the following items need to be addressed:

Eliminate the use of a cut-off distance and replace it with a wavefunction overlap factor. This would make it much easier to investigate more spatially disordered structures without having to try and find a cut-off distance by trial and error.

Implementing calculated tunnelling rates [10] may allow Monte-Carlo timesteps, to be replaced with real time steps, allowing actual mobilities to be calculated. Additionally, the tunnelling rates should confirm whether the hopping rate is uniform, or whether it is field, and possibly temperature, dependent. If the hopping rate does depend on other factors, this will affect the results obtained so far; for example, if the hopping rate does depend upon the electric field, then the amount of energetic disorder required to obtain a desired field-dependence of the mobilities may be reduced.

Rather than using the transit time (or $t_{1/2}$) obtained from the current-time plot to determine the mobility, use the current integration mode to obtain t_τ [11], since it is unaffected by dispersion.

Investigate and add realistic intra-chain transport [12].

In the longer term, the following areas could be investigated:

The model could be used to progress beyond transport, and exciton creation and diffusion could be modelled using explicit structures.

The model could be used to investigate transport in other structures; for example, transport in polymer blends could be investigated by implementing different hopping rates between different polymers.

References

[1] J M Lupton and I D W Samuel, *J. Phys. D.:Appl. Phys.*, **32**, 2973 (1999).

[2] L Bozano, S A Carter, J C Scott, G G Malliaras, and P J Brock, *Appl. Phys. Lett.*, **74**, 1132 (1999).

[3] V I Arkhipov, E V Emelianova, Y H Tak, and H Bässler, *J. Appl. Phys.*, **84**, 848 (1998).

[4] A J Campbell, D D C Bradley, J Laubender, and M Sokolowski, *J. Appl. Phys.*, **86**, 5004 (1999).

[5] W Brütting, S Berleb, and A G Mückl, *Organic Electronics*, **2**, 1 (2001).

[6] C Schmitz, P Pösch, M Thelakkat, and H-W Schmidt, *Phys. Chem. Chem. Phys.*, **1**, 1777 (1999).

[7] P E Burrows and S R Forrest, *Appl. Phys. Lett.*, **64**, 2285 (1994).

[8] F Rohlfing, T Yamada, and T Tsutsi, *J. Appl. Phys.*, **86**, 4978 (1999).

[9] M A Webster, *Unpublished results.*

[10] A Kambili and A B Walker, *Unpublished data.*

[11] A J Campbell, D D C Bradley, and H Antoniadis, *Appl. Phys. Lett.*, **79**, 2133 (2001).

[12] A M Stoneham, M M D Ramos, A M Almeida, H M G Correia, R M Ribeiro, H Ness, and A J Fisher, *J. Phys.:Conden. Matt.*, Forthcoming publication (2002).